Electro-optic photonic devices based on epitaxial barium titanate thin films on silicon

Stefan Abel

UNIVERSITÉ DE GRENOBLE

THÈSE

Pour obtenir le grade de

DOCTEUR DE L'UNIVERSITÉ DE GRENOBLE

Spécialité : **Optique et Radiofréquence**

Arrêté ministériel : 7 août 2006

Présentée par

Stefan ABEL

Thèse dirigée par **Alexei TCHELNOKOV**

préparée au sein du **IBM Research – Zurich laboratory**
dans **l'École Doctorale de Electronique, Electrotechnique, Automatique et Traitement du signal**

Dispositifs électro-optiques à base de Titanate de Baryum épitaxié sur Silicium pour la photonique intégrée

Electro-optic photonic devices based on epitaxial barium titanate thin films on silicon

Thèse soutenue publiquement le **21 février 2014**,
devant le jury composé de :

Dr. Jean-Emmanuel Broquin
Professeur, INPG, Grenoble, France, Président
Dr. Alex DEMKOV
Professeur, The University of Texas at Austin, USA, Rapporteur
Dr. Delphine MARRIS-MORINI
Maître de conférences, University Paris Sud, France, Rapporteur
Dr. Chiara MARCHIORI
Research staff member at IBM, IBM Research – Zurich, Suisse, Membre
Dr. Frédéric BOEUF
Ingénieur R&D, STMicroelectronics, France, invité
Dr. Thomas SCHRÖDER
Professeur, IHP, Allemagne, Membre
Dr. Alexei TCHELNOKOV
Ingénieur R&D, CEA-Leti, France, Directeur de thèse

dates of submission

to referees:	20.12.2013
to jury:	07.02.2014
final version:	09.03.2014

Abstract

English

A novel concept of utilizing electro-optical active oxides in silicon photonic devices is developed and realized in the frame of this thesis. The integration of such oxides extends the silicon photonics platform by non-linear materials, which can be used for ultra-fast switching or low-power tuning applications. Barium titanate is used as active material as it shows one of the strongest Pockels coefficients among all oxides. Three major goals are achieved throughout this work:

First, thin films of $BaTiO_3$ are epitaxially grown on silicon substrates via molecular beam epitaxy (MBE) using thin $SrTiO_3$ buffer layers. A shuttered co-deposition growth technique is developed in order to minimize the formation of defects in the $BaTiO_3$ films by achieving a 1:1 stoichiometry between barium and titanium. The layers show a tetragonal symmetry and are therefore well-suited for electro-optical applications. The orientation of the long c-axis of the $BaTiO_3$ crystal can be tuned to point perpendicular or parallel to the film surface, depending on the growth conditions. In addition, thin MBE-grown seed layers are combined with rf-sputter deposition. With this hybrid growth approach, rather thick ($> 100\,\mathrm{nm}$), epitaxial $BaTiO_3$ layers on silicon substrates are obtained with a commercially available, wide spread deposition technique.

As a second goal, a strong Pockels coefficient of $r_{\mathrm{eff}} = 148\,\mathrm{pm/V}$ is determined in the epitaxial $BaTiO_3$ films. This first experimental result on the electro-optical activity of $BaTiO_3$ layers on silicon shows a clear enhancement compared to alternative non-linear materials such as lithium niobate with $r_{\mathrm{eff}} \sim 31\,\mathrm{pm/V}$. By means of the electro-optical

characterization method, also the presence of ferroelectricity in the films is demonstrated.

Third, the electro-optical active $BaTiO_3$ layers are embedded into silicon photonic devices. For this purpose, a horizontal slot-waveguide structure with a $\sim$50 nm-thick $BaTiO_3$ film sandwiched between two silicon layers is designed. With this design, the optical confinement in the active $BaTiO_3$ layer is enhanced by a factor of 5 compared to Si-waveguide structures with a standard cross section and $BaTiO_3$ as cladding. Straight $BaTiO_3$ slot-waveguides with propagation losses of $50 - 100$ dB/cm as well as functional passive devices such as Mach-Zehnder-interferometers, couplers, and ring resonators are experimentally realized. Additionally, first active ring resonators with Q-factors of $Q \sim 5000$ are fabricated. The physical origin of the observed resonance shift as a function of the applied bias voltage, however, can not be conclusively clarified in the present work.

The combination of high-quality, functional $BaTiO_3$ layers with silicon photonic devices as demonstrated in this thesis offers new opportunities by extending the design palette for engineering photonic circuits with the class of electro-optical active materials. The integration of oxides such as $BaTiO_3$ enables novel device concepts for tuning, switching, and modulating light in extremely dense photonic circuits. The integration also opens exciting challenges for material scientists to tailor the electro-optical properties of those oxides by strain engineering or fabrication of superlattice structures, which could ultimately lead to another boost of their electro-optical properties.

Français

Dans le cadre de cette thèse, un nouveau concept de dispositifs pour la photonique sur silicium est abordé. Ce concept est basé sur l'utilisation d'oxydes électro-optiquement actifs, monocristallins et directement intégrés sur silicium. Dans la cadre de la photonique sur silicium, l'ajout de tels matériaux rend possible l'exploitation d'effet non-linéaires dans un large champ d'application, que ce soit pour des modulateurs ultra-rapides ou bien pour des dispositifs d'ajustement fonctionnant à très basse puissance. Le titanate de baryum $BaTiO_3$, avec un coefficient de Pockels parmi les plus larges existant, a été particulièrement utilisé dans ce travail au cours duquel trois résultats essentiels ont été obtenus.

En premier lieu, des couches minces épitaxiales ont été obtenues sur des substrats de silicium grâce à l'utilisation de l'épitaxie par jets moléculaire et de couches tampons de titanate de strontium $SrTiO_3$. Une technique de croissance par co-déposition a été développée de manière à obtenir un rapport Ba:Ti proche de la stœchiométrie, et ce afin d'éviter la formation de défauts cristallins dans la couche de $BaTiO_3$. Le matériau déposé cristallise dans une structure de symétrie quadratique, ce qui est un pré-requis pour l'obtention de propriétés électro-optiques. De plus, selon les conditions de croissance, l'axe c de la maille élémentaire quadratique a pu être ajusté de manière à être aligné parallèlement ou perpendiculairement à la surface du substrat. L'utilisation d'une mince couche tampon de nucléation a également permis de croitre des films minces $BaTiO_3$ épitaxiées par pulvérisation, technique largement répandue en milieu industriel.

Un coefficient de Pockels élevé a par la suite été obtenu sur de telles couches épitaxiées. La valeur mesurée de 148 pmV est clairement supérieure aux valeurs admises dans la littérature pour d'autres matériaux non-linéaires tels que le niobate de lithium, pour lequel un coefficient de 31 pmV est rapporté. La méthode de caractérisation électro-optique développée à cette occasion révèle également le caractère ferroélectrique des couches de $BaTiO_3$, observé pour la première fois dans de tels matériaux épitaxiés sur silicium.

Finalement, ces couches minces électro-optiquement actives ont été intégrées dans des dispositifs photoniques sur silicium. Dans cette optique, une structure de guide d'onde à fente a été utilisée en insérant 50 nm de $BaTiO_3$ entre deux couches de silicium. Dans ce type de structure, le confinement optique est 5 fois supérieur à celui obtenu pour des guides d'onde en silicium avec une gaine à base de $BaTiO_3$. Des guides d'ondes rectilignes ont tout d'abord été fabriqués, pour lesquels des pertes optiques de l'ordre de $50 - 100$ dB/cm ont été mesurées. Par la suite, des composants passifs fonctionnels ont été fabriqués, tels que des interféromètres type Mach-Zehnder, des résonateurs circulaires et des coupleurs. Finalement, la fonctionnalité de composants actifs a été démontrée pour la première fois, en se basant notamment sur des résonateurs ayant un facteur de qualité Q d'environ 5000, et pour lequel la résonance varie en fonction du champ électrique transverse. L'origine physique de cette variation n'a cependant pas pu être expliquée sur la seule base de l'effet Pockels.

Cette thèse démontre que l'utilisation de nouveaux matériaux électro-optiquement actifs au cœur de dispositifs photoniques sur silicium crée de nouvelles opportunités pour la conception et l'ingénierie de circuits photoniques. L'intégration d'oxydes tels que barium titanate permet d'envisager de nouveaux concepts de dispositifs pour ajuster, moduler ou commuter la lumière au sein de circuits photoniques denses. De nouveaux défis et perspectives s'ouvrent également aux scientifiques pour modifier artificiellement les propriétés électro-optiques de ces matériaux, que ce soit par contrainte, dopage ou par l'ingénierie de multicouches. De telles avancées pourront sans aucun doute fortement améliorer les performances des dispositifs.

Contents

List of Abbreviations

abbreviation	description
a-axis	tetragonal long axis parallel to film surface
ac	alternating current
APB	anti phase boundaries
a-Si:H	hydrogenated amorphous silicon
BF	bright-field
BHF	buffered-HF
BOX	buried oxide
BTO	barium titanate
c-axis	tetragonal long axis perpendicular to film surface
clad	cladding
c-Si	crystalline silicon
dc	direct current
DF	dark-field
EDX	Energy-dispersive x-ray
EELS	electron energy-loss spectroscopy
FDTD	finite-difference time-domain
FE	fully etched waveguide (see fig. 4.6)
$FE^{\parallel}$	FE-waveguide with in-plane electric field
FWHM	full width at half maximum
HAADF-STEM	High-angle annular dark-field scanning transmission electron microscopy
HE	halfway etched waveguide (see fig. 4.6)
$HE^{\parallel}$	HE-waveguide with in-plane electric field (see fig. 4.14)
$HE^{\perp}$	HE-waveguide with out-of-plane electric field (see fig. 4.14)

HRTEM	high-resolution transmission electron microscopy
HSQ	hydrogen silsesquioxane
ICP	inductively coupled plasma
MBE	molecular beam epitaxy
MFIS	metal-ferroelectric-insulator-semiconductor
ML	monolayer
MOS	metal-oxide-semiconductor
MZI	Mach-Zehnder interferometer
ox	oxide
PE	partially etched waveguide (see fig. 4.6)
PECVD	plasma enhanced chemical vapor deposition
$PE^{\perp}$	PE-waveguide with out-of-plane electric field (see fig. 4.14)
per	perovskite
PFM	piezo force microscopy
QCM	quartz crystal micro-balance
QCSE	quantum-confined Stark effect
RC	rocking curve
rf	radio-frequency
RHEED	reflection high electron energy diffraction
RIE	reactive-ion etching
SEM	scanning electron microscopy
SOI	silicon-on-insulator
STO	strontium titanate
TE	transverse-electric (main electric field component parallel to surface of wafer)
TEM	transmission electron microscopy
TEOS	tetraethoxysilane
TM	transverse-magnetic (main magnetic field component parallel to surface of wafer)
TMAH	tetramethylammonium hydroxide
UC	unit cell
UHV	ultra high vacuum
VHF	very high frequency
WG	waveguide
XRD	x-ray diffraction

List of Symbols

symbol	unit	description
a	Å	lattice parameter
c	Å	lattice parameter (tetragonal, long axis)
$a^{\parallel}$	Å	lattice parameter, parallel to surface
$a^{\perp}$	Å	lattice parameter, perpendicular to surface
α_{b}	dB/cm	bending losses in a curved waveguide
α_{g}	dB	insertion loss of one grating coupler
α_{p}	dB/cm	propagation losses
$\boldsymbol{D}$	V/m	displacement field
d	nm	layer thickness
d_{el}	µm	distance between electrode and waveguide
δ	°	rotation of polarization, induced by electric field
δ'	°	field-normalized rotation of polarization
δ'_{max}	°	maximal δ for a specific orientation of the electric field
E	V/m	electric field
$\hat{E}$	V/m	mean electric field in $BaTiO_3$ layer
E_{c}	V/m	coercive field
$\boldsymbol{E}_{\mathrm{ext}}$	V/m	externally applied electric field
ϵ		relative permittivity; strain
$\hat{\eta}$		optical indicatrix
f	Hz	frequency
FSR	nm	free spectral range of a resonator
$\Delta\gamma$	°	rotation of optical axis due to applied electric field
Γ_{xy}		confinement factor of the optical mode in a waveguide in the region xy
g	nm	gap between two coupled waveguides
$\boldsymbol{k}$	m^{-1}	wavevector
L	µm	length

λ	nm	wavelength
λ_0	nm	center wavelenth of a resonace
$\delta\lambda$	nm	full width at half transmission of a resonance
L_c	µm	coupling length in a directional coupler to transfer all optical power from one waveguide to the other one
n		refractive index
$\hat{n}$		refractive index tensor
n_b		birefringence (difference between ordinary and extraordinary refractive index)
n_eff		effective mode index
n_eo		extra-ordinary refractive index
n_g		group index
n_o		ordinary refractive index
ν		relative volume fraction of domains
P	W	optical power
p	mbar	pressure
P_el	W	electric power
φ_E	°	angle between applied electric field and crystalline axis
P_s	W	optical power of laser source
Q		quality factor of resonator
Q_cr		quality factor of critically coupled resonator
r	µm	bending radius of waveguides
r	pm/V	Pockels effect
r_{ij}	pm/V	Pockels coefficient, element ij in reduced tensor notation
r_c	pm/V	Pockels coefficient along c-axis
r_e	dB	extinction ratio
r_eff	pm/V	effective Pockels effect
ρ	$\Omega\,\mathrm{cm}$	resistivity
T	°C	temperature
T		transmission through integrated device
T_C	°C	Curie temperature
t_xy	µm	thickness of layer xy
2θ	°	diffraction angle (in x-ray diffraction)
θ_a	°	orientation of analyzer in electro-optical characterization
θ_i	°	incident polarization
$\theta_\mathrm{i}\vert_{\delta'_\mathrm{max}}$	°	incident polarization which results in the maximal δ' for a specific orientation of the electric field
V	V	applied voltage

V_{ac}	V	applied electric ac-field, peak-to-peak value
V_{off}	V	offset of applied electric field
V_{π}	V	voltage applied to a Mach-Zehnder interferometer that yields a phase shift of π between both arms
ω	°	rocking angle (in x-ray diffraction)
$\Delta\omega$	°	FWHM of rocking curve
w_{WG}	nm	width of waveguide

CHAPTER 1

Introduction

1.1 Advancements and challenges in silicon photonics

Silicon technology has experienced tremendous progress since the first transistor was developed in 1947 at *Bell Labs* and the concept of integrated circuits (ICs) has evolved in the late 1950s. Decades of research and development resulted in highly efficient silicon microprocessors, which can be produced in large volumes and at low costs. The key to the success of this technology was to reduce the size of the transistors, as it reduced the power consumption, while the speed was increased. The scaling follows the empirical Moore's law, which anticipates a doubling of the transistor count every ∼18 months. At last, this resulted in 22 nm-small feature sizes of current circuits with more than a billion transistors per microprocessor.

One of today's main challenges when combining a high integration density with clocking speeds of several GHz lies in interconnecting the individual units within the circuits. This "interconnect bottleneck" will eventually limit the performance of the next technology nodes. Using current state-of-the-art technology, electrical interconnects are fabricated with multiple metal layers, which are connected to each other through vias in the back-end-of-line (BEOL) [1]. Further down-scaling of the critical dimensions gives however rise to two main problems for electrical interconnects:

- Increasing propagation delay. For feature sizes in the µm-range the delay of electric signals is rather small ($< 2\,\mathrm{ps/mm}$) as the propagation is mainly limited by the speed of the electro-magnetic wave [1]. In contrast, smaller node sizes ($< 32\,\mathrm{nm}$) have an increased resistance of the connection lines

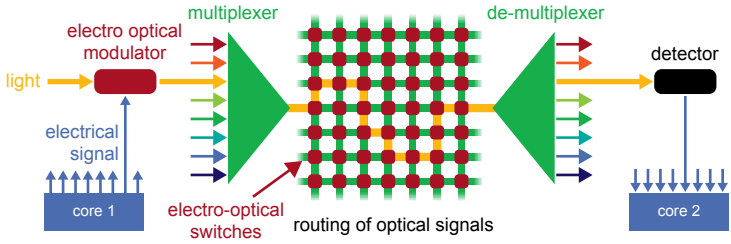

Fig. 1.1 Illustration of a potential silicon photonic transceiver system to connect different cores of a microprocessor. An electric signal from the first core is encoded into the optical domain using an electro-optical modulator. Wavelength-division multiplexing (WDM) is used to combine and, after routing the signal through the optical network, split several optical frequency ranges. A detector finally converts the optical into an electrical signal which is delivered to the target core.

and the signal propagation is therefore limited by the larger RLC-time constant. The estimated propagation delay for electrical connections is up to ∼40 ps/mm in the 22 nm node [2], hence, causing signal delays in the order of the clock cycle for connections across the full chip [1, 3].

- Increased power consumption. Due to different scaling laws, the ratio of the power dissipation of electrical interconnects and transistors increases by a factor of ∼30 when scaling down feature sizes from 1 µm to 32 nm [1]. By now, interconnects have become a significant contribution to the overall power consumption of integrated circuits, and are one of the primary constraints on the clock speed of the processors [4].

One possible solution to overcome these fundamental limitations of electrical interconnects is to transfer them from the electrical into the optical domain. Fiber optics have been used for long-haul communication for decades, motivated by the negligible heat dissipation in transparent media, low cross talk, and, most importantly, the high carrier frequency of > 100 THz which enables bandwidths of $>$ Tb/s [1, 5]. The excellent performance of optical links, the transparency of silicon at important telecommunication wavelengths of 1.3 µm and 1.55 µm, and the low-cost fabrication in current CMOS (complementary metal-oxide-semiconductor) lines triggered the development of silicon photonics. Indeed, shorter interconnect delay times, advantages in the total power consumption, and an increased bandwidth compared to electrical interconnects have been predicted for integrated photonics [2, 4, 5]. Manifold novel devices were designed to guide, couple, filter, or modulate light [6–8] - all based on silicon. A co-

integration of such optical links with electric circuits envisions the fabrication of ultra-fast electro-optic transceiver systems for intra-chip data communication with high bandwidth when exploiting multiplexing schemes, as explained in fig. 1.1. A concept that is close to reality, as indicated by first silicon photonic links with $> 100\,\mathrm{Gb/s}$ that are already commercially available [9].

Despite these great advancements in the field of silicon photonics, many challenges still need to be solved. On the system level, an advanced design methodology is required to engineer such complex, highly integrated photonic networks with methods similar to those used for electronic design processes [10]. Also, strict alignment tolerances when connecting photonic networks with optical fibers during the packaging process need to be met [10]. On the device level remaining challenges are the search for non-reciprocal structures for optical isolation [11], integrated light sources [12], and efficient detectors at a wavelength of $\lambda = 1.55\,\mu\mathrm{m}$ [13]. Although first implementations of modulators operating at high speeds of more than $40\,\mathrm{Gb/s}$ have been shown [8, 14], the ideal compromise between bandwidth, insertion loss, power consumption and footprint has not yet been found. Additional device challenges arise from the fact that resonant photonic devices are extremely sensitive to changes in the optical path length. Such changes can occur during fabrication or can be induced by temperature variations. For example, if the radius of a ring resonator varies by only $3\,\mathrm{nm}$ around a target value of $5\,\mu\mathrm{m}$, its resonance frequency at $\lambda \approx 1.55\,\mu\mathrm{m}$ shifts by $\sim$100 GHz, which is more than the typical spacing between two channels in systems using dense wavelength division multiplexing. Furthermore, due to the thermo-optic effect of silicon [15], local and global temperature variations will change the refractive index and thus the optical path length and the resonance frequencies in resonators. Different approaches to address these issues have been shown, such as using claddings with a negative thermo-optic effect [16], active tuning by locally heating the structures [17, 18], or moving to non-resonant structures. However, the drawbacks of these approaches lie in difficult additional processing steps, increased power consumption, or larger footprints.

The examples show that despite the recent progress in silicon photonics, plenty of limitations still have to be solved. A large community is therefore focused on combining silicon with new materials to enrich the variety of properties available in the photonic platform for new device concepts. Examples are the integration of III/V materials for integrated lasers [10], Ge for photodetectors [13] and SiGe for future modulators [19]. Surprisingly, the class of electro-optical materials, which is critical for state-of-the-art telecommunication links, has hardly been considered for silicon photonic devices.

1.2 Barium titanate thin films for silicon photonics

The great potential of materials showing a strong linear electro-optical effect (Pockels effect) in optical communication systems is visible in the example of lithium niobate ($LiNbO_3$). Lithium niobate has been used for decades to modulate light at high frequencies [20] and until today, it is a major component of most telecommunication networks [21]. The Pockels effect, which describes the change of the refractive index of a material when exposed to an electric field, occurs even at very high frequencies (> THz) [22]. The linearity of the effect has been crucial for exploiting advanced modulation formats such as quadrature amplitude modulation (QAM) that further increase the bandwidth of optical links [21, 23]. However, all these devices are based on bulk $LiNbO_3$ crystals and are therefore incompatible with silicon photonics.

Yet, the presence of a strong electro-optically active material in optical circuits in silicon would offer several opportunities: first, it would allow the replication of the previously developed, mature modulation technique of $LiNbO_3$, second, due to a change of the refractive index without current flow it would enable novel devices such as zero-power tuning elements and third, by exploiting the ferroelectric nature of many electro-optically-active material, non-volatile optical memories could be envisioned. Silicon itself cannot be used for such devices because its Pockels effect vanishes due to the centro-symmetric crystalline structure of silicon [24]. Even though this symmetry can be broken by applying strain gradients [25, 26], the resulting Pockels coefficients in silicon are by a factor of ∼20 smaller than in $LiNbO_3$. Therefore, the heterogeneous integration of another material is essential in order to obtain efficient devices based on the Pockels-effect.

Barium titanate ($BaTiO_3$) represents an excellently suited-material system for integration into silicon photonics, since it fulfills three main criteria:

1. Bulk $BaTiO_3$ has one of the highest Pockels coefficients ($r_{BTO} > 1000$ pm/V [28]) among all well-known materials (fig. 1.2a). In particular, the electro-optical properties of bulk $BaTiO_3$ are ∼30 times larger than in $LiNbO_3$ and ∼600 times larger than the ones of strained silicon.
2. The feasibility of using $BaTiO_3$ for high speed modulation has been demonstrated previously for thin films grown on magnesium oxide substrates [29, 31, 32] (fig. 1.2b).
3. Deposition routes have been shown to epitaxially integrate single-crystalline perovskite oxides, such as $BaTiO_3$ or strontium titanate ($SrTiO_3$), on silicon (fig. 1.2c) [33, 34].

In order to use $BaTiO_3$ integrated into silicon photonic devices, it is required to merge the above mentioned criteria, which so far have been investigated only

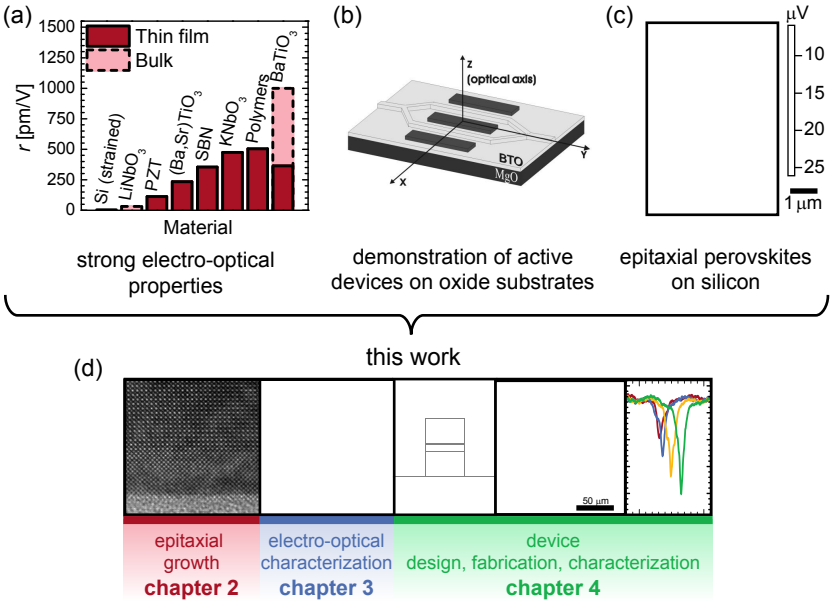

Fig. 1.2 (a) Comparison of Pockels effect for various material systems from literature [26–28], barium titanate shows extremely high values in bulk crystals. (b) Demonstration of $BaTiO_3$-based optical modulators on MgO substrates [29] (reproduced by permission of AIP Publishing LLC). (c) Demonstration of epitaxial growth of ferroelectric $SrTiO_3$ on silicon [30] (reproduced by permission of The American Association for the Advancement of Science). (d) Scope of this thesis, and outline of the chapters.

individually. The route from bare silicon wafers to integrated, electro-optically-active photonic devices are the scope of this thesis. In particular the following points are addressed in different chapters, as illustrated in fig. 1.2d:

- Epitaxial growth. Different routes to grow high-quality, single-crystalline $BaTiO_3$ thin films on silicon substrates by means of molecular beam epitaxy are developed. Focus is put on investigating the symmetry of the crystals and finding ways to enhance the crystalline quality since the electro-optical properties are strongly linked to the $BaTiO_3$ crystalline structure. Additionally, a hybrid growth approach is established that utilizes a commercially wide-spread deposition method (rf-sputtering) for obtaining epitaxial $BaTiO_3$ films on silicon substrates (chapter 2).

- Electro-optical characterization of $BaTiO_3$ thin films. The properties of thin films can significantly vary from those of bulk crystals. An example is the presence of ferroelectricity in thin layers of $SrTiO_3$, which is non-ferroelectric as bulk crystal (see fig. 1.2c). The electro-optical properties of $BaTiO_3$ typically degrade when deposited on oxide substrates, compared to bulk crystals [27]. Furthermore, no investigation of the Pockels coefficients of $BaTiO_3$ on silicon substrates has been made so far. In order to characterize $BaTiO_3$ thin films, an electro-optical setup is built and a systematic study on the response of $BaTiO_3$/Si samples is performed (chapter 3).
- $BaTiO_3$-based, silicon photonic devices. In a final step, a concept for embedding electro-optically active $BaTiO_3$ thin films into silicon photonic structures is developed. This development included the engineering of slot-waveguides with strong confinement of the optical mode in the $BaTiO_3$ region, the design of photonic components such as couplers and resonators, and the benchmarking of the estimated performance with state-of-the-art active silicon photonic elements. Passive and active $BaTiO_3$-based devices are fabricated, and optically and electro-optically characterized (chapter 4).

CHAPTER 2

Fabrication of thin films

2.1 Background

2.1.1 Epitaxial film deposition

The monolithic integration of high quality crystalline films on host substrates like silicon paves the way to the realization of devices and systems with a broad range of applications. A key enabler is *epitaxy*, the process of growing a crystalline material on top of a crystalline substrate where both crystal lattices have well-defined orientations in respect to each other. Discovered already in the 19th century [35], the physical phenomenon of epitaxy has been theoretically as well as experimentally investigated throughout the decades. Epitaxially grown layers have been used for many important applications, such as the fabrication of opto-electronic devices using epitaxial combinations of GaAs and $Al_xGa_{1-x}As$ thin films [36].

When growing an epitaxial film on a substrate of different composition and structural parameters (heteroepitaxy), one of the crucial steps is the arrangement of the first deposited atoms on the host crystalline surface. Generally, numerous options exist of how the new elements will stabilize on the substrate, ranging from amorphous, polycrystalline to single crystalline layers. Even a re-evaporation of the atoms can occur. Physically, the process and product of the deposition is described by the laws of thermodynamics, statistics, and quantum mechanics, as excellently reviewed by Herman *et al.* [35]. The complexity of the atomistic aspects of the deposition process provides a large opportunity for scientists to create novel crystalline structures that naturally do not exist.

The key in achieving such structures is to influence the reaction kinetics by carefully choosing the process conditions in order to enforce or block desired chemical reactions.

The structure of the grown heteroepitaxial layers is strongly dependent on the first atomic layers that are deposited on the substrate. The atoms can for example nucleate and grow in small islands, each having a slightly different crystalline orientation, or homogeneously wet the surface and arrange regularly to the crystalline lattice of the substrate. Due the mismatch of lattice constants between substrate and film in many cases, strain is created in the film that relaxes by the formation of crystalline defects. The number of such defects can either increase when the film grows, or they can be reduced by annihilation between different defects. Furthermore, a mismatch in the thermal expansion coefficient between the materials will have an impact on the final layer quality.

All of these examples show parameters that can artificially be varied during the deposition process: The wetting is influenced by adhesion layers, the lattice constant is often tunable by the film composition, and the influence of the thermal expansion can be varied by selecting the growth temperature. Understanding, controlling, and fine-tuning these numerous parameters represent the challenges and opportunities in the research field of epitaxial growth.

2.1.2 Functional oxides on silicon

Perovskites on silicon The epitaxial growth of complex oxides on silicon substrates is an excellent example of a structure that naturally does not exist, but could only be realized by thoroughly choosing the process conditions and using advanced deposition tools. The main issue to be solved is that Si tends to oxidize in the presence of oxygen: the consequent formation of an amorphous interfacial SiO_2 layer hinders then epitaxial growth. The research field was pioneered by McKee *et al.* [33] who for the first time epitaxially deposited a perovskite material, barium titanate ($BaTiO_3$), on silicon substrates. They defined a process which relies on the formation of ordered alkaline earth metal-silicide structures (i.e. SrSi, BaSi) at high temperature, fully commensurate to Si and stable upon cooling. The layer-by-layer thermodynamic equilibrium which is maintained at atomic level during the process allows a stable, heteroepitaxial transition from the Si to the crystalline oxide. The precision at the atomic level required by this process is achieved using molecular beam epitaxy (MBE) with tools working in an ultra high vacuum (UHV) environment (see section 2.1.4).

Due to the numerous properties of perovskite oxides that are absent in silicon such as ferro- and piezoelectricity, a large research community explored the integration path with the vision of enabling new devices and functionalities for silicon-based electronics [34, 37]. However, the interest in this research

field has mainly been motivated by the use of oxides in the electronic domain, in particular as high permittivity gate dielectric in field-effect transistors [38]. Therefore, the growth process of perovskites has been carefully optimized [39] and single crystalline layers of strontium titanate ($SrTiO_3$) were fabricated even on large-scale 8 inch substrates [40]. Lately, it has also been claimed that the perfection of epitaxially grown $SrTiO_3$ surpasses those of bulk crystals [41] due to the very high quality of nowadays available silicon substrates and epitaxial processes. The feasibility of epitaxially combining such virtual oxide substrates with many other perovskite materials opened the door for realizing novel material systems, such as two-dimensional electron gases at $SrTiO_3/LaAlO_3$ interfaces on silicon substrates, which can ultimately be used for all-oxide electronics [42].

Barium titanate on silicon $BaTiO_3$ (BTO) is a well-studied perovskite material, that undergoes a transition from a ferroelectric tetragonal phase to a paraelectric cubic phase when heated above its Curie temperature of $T_c = 123\,°C$ [43]. In the cubic phase the Ti atoms are octaedrally coordinated by six O atoms. In the tetragonal phase atoms are displaced along the z-direction and the unit cell is elongated along the c-axis (fig. 2.1a). Tetragonal $BaTiO_3$ has a variety of functional properties such as piezoelectricity [44], ferroelectricity [45], and electro-optic activity [27, 46], which originate from a displacement of the Ti atoms along the c-axis with respect to their centrosymmetric position in the unit cell (fig. 2.1b). These properties can be exploit for manufacturing active devices, such as piezoelectric actuators [47], or nonvolatile ferroelectric memories [48]. Owing to its excellent electro-optical bulk properties, $r_{BTO} > 1000\,pm/V$ [49], $BaTiO_3$ is also a promising candidate for modulating and tuning components in silicon photonics [27, 29, 46]. The integration of such oxide on Si enables the fabrication of functional devices in the silicon CMOS and photonics platform using high volume low cost production methods.

The functional properties of $BaTiO_3$ are absent in the cubic phase [24]. Although the tetragonal phase is stable at room temperature in bulk $BaTiO_3$ [50], thin films consisting of polycrystalline $BaTiO_3$ tend to stabilize in the cubic symmetry [51, 52]. It is therefore important to ensure epitaxial growth conditions during the monolithically integration of $BaTiO_3$ thin films onto Si substrates in order to control the crystalline structure of the perovskite. Indeed, thin layers of tetragonal $BaTiO_3$ can be grown on Si but their orientation with respect to the substrate varies with the growth parameters due to the lattice and thermal coefficient mismatch between the two materials. During the epitaxial growth of $BaTiO_3$ on silicon substrates, the huge lattice-mismatch of $\sim 26\,\%$ is reduced to $\sim 4° - 5\,\%$ by a rotation of the $BaTiO_3$ crystalline lattice

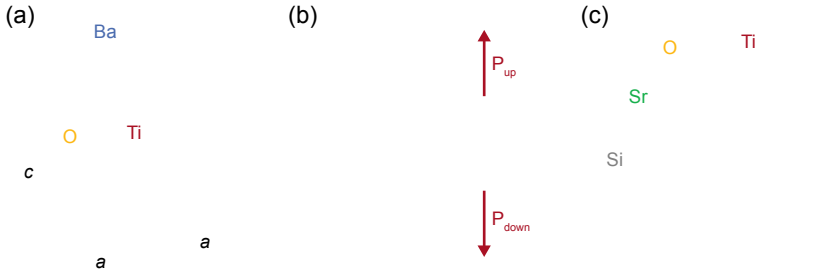

Fig. 2.1 (a) Tetragonal unit cell of $BaTiO_3$ with one long *c*-axis and two shorter *a*-axes. (b) Two ferroelectric polarization states in tetragonal $BaTiO_3$ due to different positions of the Ti atom relative to the O atoms. (c) Epitaxial growth of $SrTiO_3$ on silicon: The perovskite unit cell is rotated by 45° in respect to the silicon unit cell. The interface between the two layers is simplified in the illustration compared to first-principle calculations [53, 54].

by 45° [33] to form the epitaxial relationship $[100]_{BTO} \parallel [110]_{Si}$ (fig. 2.1c). The orientation of the long axis of the tetragonal lattice is determined by the different thermal expansion coefficients of silicon and $BaTiO_3$ (table 2.1): at high growth temperatures, relaxed $BaTiO_3$ layers crystallize in a cubic structure. Due to the smaller thermal expansion coefficient of Si, $BaTiO_3$ layers are subjected to biaxial tension when cooled through the Curie temperature. To relieve such biaxial tensile strain the films tend to orient with their longer *c*-axis in the plane of the substrate and the short *a*-axis out-of-plane, resulting in an in-plane ferroelectric polarization of the $BaTiO_3$ films.

Since for many applications *c*-axis oriented films are preferred, alternative $BaTiO_3$ growth paths on specific buffer layers have been explored. For instance, the growth of pure tetragonal *c*-axis oriented $BaTiO_3$ on Si has been reported using $10 - 30\,nm$ thick $Ba_{0.7}Sr_{0.3}TiO_3$ buffer layers [55]. In the current work, it will be discussed (section 2.3) how purely *c*-axis oriented $BaTiO_3$ layers can be grown onto Si substrates using much thinner $SrTiO_3$ buffers (4 nm), similar to recently published work [48, 56]. The evolution of the crystalline orientation of $BaTiO_3$ thin films as a function of their thickness has been found to provide a way to tune the crystalline orientation of the films.

Towards thicker $BaTiO_3$ layers The thickness range of the functional oxide layer as required for optical [27, 29] and piezoelectric [61–63] applications ($50\,nm - 1\,\mu m$) is rather broad. It is hardly covered by MBE deposition, which

is the standard method for growing epitaxial perovskites on silicon and which is operated at rather low deposition rates ($< 100\,\mathrm{nm/h}$). It was previously shown that thin MBE-grown seed layers can be combined with pulsed laser deposition to obtain thicker, but still epitaxial films [48]. A new hybrid growth process is developed in the framework of this thesis: It consists of the growth of a seed $BaTiO_3/SrTiO_3$ layer onto a Si substrate by MBE, followed by the deposition of a thicker $BaTiO_3$ layer by radio-frequency (rf) sputtering. The influence of the MBE seed layer thickness, as well as the sputtering and post-sputtering annealing conditions on the crystalline structure of the hybrid layers are thoroughly analyzed (section 2.4).

2.1.3 Properties of barium titanate

Barium titanate has been heavily investigated since the 1940s in the form of bulk crystals [50, 64, 65], and more recently in the form of thin films on various substrates [45, 66, 67]. Some of the properties which make $BaTiO_3$ interesting for fundamental science [68] as well as more application driven research [69] are reviewed in the following section.

Structural properties As previously mentioned, the origin of most functional properties lies in the crystalline structure of $BaTiO_3$ (fig. 2.1), which is described in the non-centrosymmetric tetragonal P4*mm* space group at room temperature with one long *c*-axis and two short *a*-axes (table 2.1). Barium

Table 2.1 Crystal symmetry, lattice constants, and linear thermal expansion coefficient α of $BaTiO_3$ [57, 58], $SrTiO_3$ [59] and silicon [60] at different temperatures. For silicon, the distance between the atoms along the [110] direction is given in brackets, as it is the the relevant parameter for the perovskite growth due to the rotation of the crystal lattice by 45° (fig. 2.1c). For $BaTiO_3$ and $SrTiO_3$, the lattice mismatch relative to Si is given in brackets. The crystalline structure of Si and $SrTiO_3/BaTiO_3$ is diamond (diam.) and perovskite (perov.), respectively.

material	crystal symm.	lattice parameter [Å] 25 °C	lattice parameter [Å] 600 °C	α [$10^{-6} \times 1/\mathrm{K}$] 25 °C	α [$10^{-6} \times 1/\mathrm{K}$] 600 °C
silicon	diam.	5.431 (3.840)	5.443 (3.849)	2.55	4.2
$BaTiO_3$	perov.	a=3.994 (+4.0%) c=4.038 (+5.2%)	4.031 (+4.7%)	16.9 (a) -13.9 (c)	13.2
$SrTiO_3$	perov.	3.905 (+1.7%)	3.978 (+3.4%)	32.3	31.7

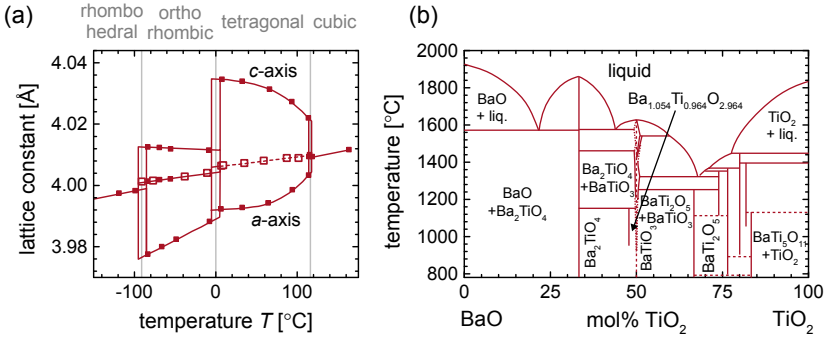

Fig. 2.2 (a) Lattice parameters and crystalline symmetry measured for bulk-$BaTiO_3$ at different temperatures. Transitions between the different crystalline phases are indicated by gray lines. Open symbols and the dashed line correspond to calculated values assuming a cubic structure with constant cell volume. All data replotted from ref. [50]. (b) Phase diagram for different compositions of BaO and TiO_2 (replotted from ref. [72]). Only the major phases are labeled. The full diagram can be found in ref. [72].

titanate experiences several phase transitions when varying the temperature (fig. 2.2a). The most important one for many applications is the highest one at $T_C = 123\,°C$ [43] to the cubic phase where many properties such as ferroelectricity or electro-optic activity disappear. The actual transition temperature in thin films can however vary significantly from the bulk transition temperature due to clamping and strain effects, or microstructural defects such as grain boundaries. For example, a cubic symmetry for thin, polycrystalline $BaTiO_3$ films has already been reported at room temperature [51], while an increase to $T_C \approx 177\,°C$ has been observed in epitaxial films on MgO substrates [70].

The compositional phase diagram between BaO and TiO_2 (fig. 2.2b) shows a variety of different compositions and crystalline symmetries, with $BaTiO_3$ as the special case for the exact ratio of 1:1. If the ratio is slightly off, typically solid solutions of two different phases will form, for example a mixture of $BaTiO_3$ and $BaTi_2O_5$ for Ti-rich crystals. Therefore, in order to obtain high quality single crystalline films, the composition of Ba:Ti has to be controlled carefully. Keeping the proper stoichiometry during the perovskite deposition is a challenge for most thin film deposition methods [71].

Functional properties The exploration of the functional properties of $BaTiO_3$ started with the discovery of the ferro- and piezoelectric properties [64, 73] and is

still being continued. It has for example recently been shown by calculations that $BaTiO_3$ can exhibit a piezoelectric response comparable to PZT (lead zirconate titanate), on of the most common materials used for piezoelectric applications [74]. The first electro-optical measurements of $BaTiO_3$ were performed in the 1970s and revealed very high Pockels coefficients of $r_{42} \approx 1640\,\mathrm{pm/V}$ and $r_c = r_{33} - r_{31} \approx 108\,\mathrm{pm/V}$ at room temperature at a wavelength of 546.1 nm [75, 76]. Calculations taking into account the coupling of different physical effects such as the elasto-optic, piezo-electric and electro-optic effect, show a slight decrease of the response in the infrared wavelength region, and illustrate the different electro-optical effect for clamped and unclamped crystals [28, 77]. In the clamped situation (constant strain), the electro-optic effect is typically by a factor of ∼2 smaller than in the unclamped case (constant stress), where elasto-optic contributions add to the pure electro-optic effect. The elastic deformations are caused by the piezo-electric effect, which vanishes at high frequencies.

Applications and recent development The interest in $BaTiO_3$ has been high for more than half a century, and still nowadays, new understanding of fundamental physics is gathered and novel devices are realized by using $BaTiO_3$. For example, an ultra low critical thickness for ferroelectricity of ∼2.4 nm [66], an enhanced remanent polarization and coercive field due to strain-effects [45], and ferroelectric superlattices of $BaTiO_3$ and $SrTiO_3$ [67] were demonstrated. Insight into the ferroelectric ordering of nano-scale crystals were recently obtained by investigating $BaTiO_3$ crystals as small as 5 nm. Furthermore, $BaTiO_3$-based plasmonic modulators [69] and drastically improved tunneling barriers by using $BaTiO_3$ thin films [78] represent recent work on $BaTiO_3$-based devices and illustrate the still very present interest in the material system barium titanate.

2.1.4 Growth and characterization methods

Molecular beam epitaxy

Principle of MBE Molecular beam epitaxy (MBE) is a deposition method to grow high quality epitaxial films in a very clean environment, often with very low pressures in the ultra-high vacuum (UHV) regime ($p < 1 \times 10^{-9}$ mbar) [35, 79]. The mean free path length of atoms is in the order of several kilometers at these low pressures. Therefore, solid materials such as metals can locally be evaporated and, in a properly-designed chamber, directed as an atomic or *molecular beam* towards a specific position where the sample is mounted (fig. 2.3a). The atomic compositions at the sample surface can be controlled by blocking the beams of different sources by mechanical shutters. Cryopanels

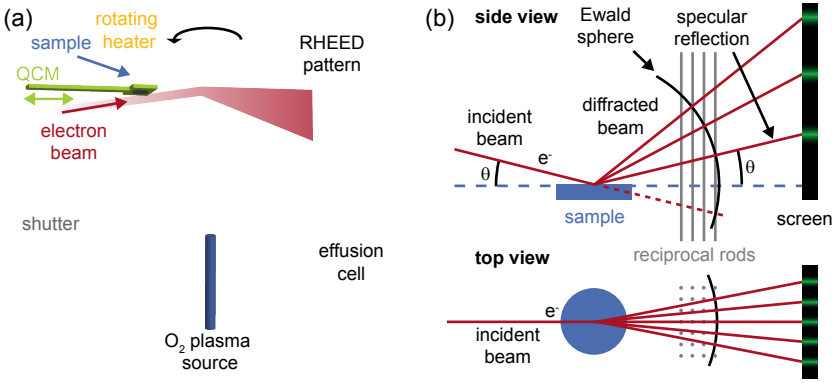

Fig. 2.3 (a) Schematics of a MBE system (after [79]). (b) Physical principle of RHEED (after [80]). Due to the gracing incidence, the electrons only penetrate into the top few atomic layers of the sample. The reciprocal space of such a 2D-lattice is represented by rods whose intersection with the Ewald sphere is line-shaped due to the finite extension of the rods. A streaky diffraction pattern is therefore typically observed, as shown in (a).

cooled with liquid nitrogen typically cover the walls of the growth chamber to prevent atoms from re-evaporation. Sub-monolayer (ML) coverages can be well controlled by using low atomic fluxes. The rates are determined using a quartz crystal micro-balance (QCM) prior to the deposition process. The QCM is placed at the sample position, and the shift of the quartz resonance frequency is monitored. The resonance frequency depends on the material coverage on the quartz, which allows to calculate the evaporation rates of the sources.

Gases such as oxygen can be introduced into the chamber in either a molecular or in a more reactive radical form by plasma-cracking the molecular bonds. By means of MBE, process conditions can be created that lead to growth mechanisms controlled by surface kinetics and that result in crystalline structures far from the thermodynamic equilibrium.

RHEED The high vacuum in MBE reactors allows for the utilization of RHEED (reflection high energy electron diffraction) as a technique to characterize the sample surface during the growth [35, 80]. As indicated in fig. 2.3a, an electron beam is pointed at a gracing incident angle onto the sample. Since the wavelength of the electrons ($\sim 10 - 20\,\mathrm{keV}$) is in the order of the atomic spacing, a diffraction pattern of the crystal is monitored on a fluorescent screen. Due to

the gracing incidence, the electrons only penetrate into the top-most atomic layers, making the technique very surface sensitive. The reciprocal space of a 2-dimensional crystalline surface layer consists of infinite rods extending perpendicular to the sample surface which create a typically line-shaped diffraction pattern. Figure 2.3b illustrates the construction of the diffraction lines, which are defined by the intersection of the Ewald's sphere (having a large radius for electrons) with the reciprocal space (rods). A more precise and mathematical description of the physics of RHEED can be found in ref. [80].

The reflected electron beam provides additional information to the diffraction pattern: When following the intensity of the reflected electrons (specular spot), the coverage of the currently growing monolayer can be estimated if the film grows two-dimensionally. Each full period of the oscillating intensity corresponds to the deposition of one single monolayer: while the minima correspond to a surface covered with atoms of half a monolayer where the reflected electrons between the upper and the lower surface regions interfere with each other [80], the maxima correspond to a completely, homogeneously covered surface.

Chambers used in this thesis Two different MBE reactors with base pressures of $\sim 5 \times 10^{-10}$ mbar are used to fabricate epitaxial films, a 2 inch *Riber* system (MBE32), and a 8 inch *DCA* reactor. The latter is also capable of handling 2 inch substrates. The relevant sources in both chambers are strontium effusion cells, typically operated at ∼350 °C, and titanium ebeam evaporation cells. The titanium cell is controlled by the filament current in the *DCA* system, while a mass spectrometer monitoring the Ti-signal is used to stabilize the emitted Ti-flux in the *Riber*. A barium effusion cell, typically operated at ∼500 °C, is used in the *Riber* system to grow $BaTiO_3$ layers. In specific cases, after $SrTiO_3$ deposition, the sample is transferred from the *DCA* to the *Riber* system for subsequent $BaTiO_3$ growth. The quality of the $SrTiO_3$ template layer is not degraded by the short exposure to air as observed in unchanged RHEED patterns. Both systems are equipped with plasma gas sources to create atomic oxygen, QCMs for calibrating the deposition rates, and RHEED systems by *k-space*.

The sample temperature is determined by a pyrometer operating at a wavelength of ∼10 µm (*Riber* system). The readout value of the pyrometer depends on many parameters such as the emissivity of the sample (surface), the angle of incidence, the focus of the pyrometer, and internal reflections for samples consisting of multiple layers (for example SOI substrates). Those parameters are difficult to determine, which thus prohibits a precise absolute temperature determination for comparing different MBE systems. In addition, since silicon is transparent below ∼ 300 °C in the infrared wavelength region, the pyrometer

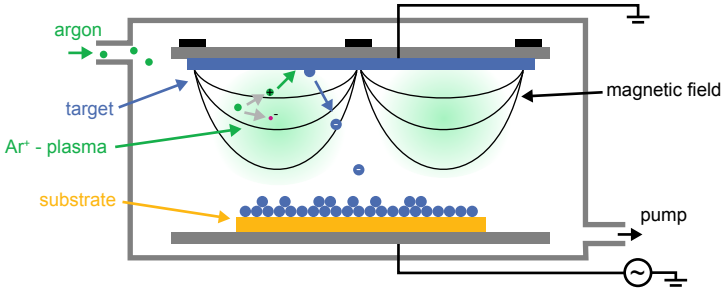

Fig. 2.4 Illustration of a rf-sputtering system: Ar-atoms are ionized in a rf-electric field, and confined in a region close to the target by a magnetic field. Atoms from the target are released by collisions with Ar-ions, and accelerated to the substrate [79].

cannot be used at low temperatures. Instead, a thermocouple mounted at the sample manipulator has to be used. The real temperature of the sample can however strongly deviate from the manipulator temperature, in particular during heating and cooling processes. In the *DCA* system, no pyrometer but solely a thermocouple is used for controlling the temperature.

RF sputtering

A rf-magnetron sputtering system *Von Ardenne CS 320S* operating at a a rf-frequency of 13.56 MHz is used for the hybrid growth of epitaxial $BaTiO_3$ films on MBE-grown seed layers (section 2.4). For the deposition, Ar-ions are created in a plasma and accelerated with energies of $50 - 1000$ eV towards the ceramic $BaTiO_3$ target. A magnetic field confines the electrons closer to target, creating a larger concentration of Ar-ions. The bombardment causes surface atoms to be ejected from the target, which are then collected at the surface of the sample [79]. In particular for insulating substrates, such as $BaTiO_3$ as used in the experiments, an AC-bias is applied in order to avoid charging of the target. Figure 2.4 illustrates the sputtering process.

Annealing

The sputtered $BaTiO_3$ films require a post-deposition annealing step in order to fully crystallize. The annealing process is performed in a rapid thermal annealing system (*AS one* by *AnnealSyS*). Slow heating rates ($\sim$25 °C/min) are used in

order to reach the target annealing temperature of ∼650 °C within 20 min in O_2 atmosphere at ambient pressure. The temperature is hold for another 20 min before cooling down to room temperature. To study the change in crystallinity, some of the annealing experiments are performed with a XRD tool, equipped with a heating system and a dome to provide an oxygen atmosphere for the sample.

Material characterization tools

X-ray diffraction The crystalline structure of the epitaxial layers is characterized by means of x-ray diffraction (XRD) [81]. The physical principle of XRD is illustrated in fig. 2.5: The sample is exposed to x-rays with a wavelength similar to the atomic distances (1.54 Å for a Cu-anode as used in this work). The diffraction pattern of the x-rays scattered at the atoms of the crystal is recorded by varying the angle of incidence of the x-rays, as well as the angle of the detector relative to the crystal (fig. 2.5b). Mainly two modes of operation are applied throughout the experiments:

- In symmetric $\theta - 2\theta$-scans, the angle of incidence is equal to the angle between the detector and the sample. In this configuration, the recorded diffraction pattern is sensitive to atomic planes and their distances parallel to the sample surface (out-of-plane lattice constants). Epitaxial films have a well-defined crystalline orientation, and thus only a small set of all possible atomic planes contribute to the recorded diffraction pattern. In contrast, polycrystalline films are randomly oriented and all crystalline planes contribute to the diffraction pattern. Polycrystalline films can thus clearly be distinguished from epitaxial films.

  Samples are also analyzed in gracing incidence geometry in this work. In that case the x-rays are diffracted at atomic planes perpendicular to the sample surface, thus revealing the in-plane lattice constants.
- Rocking curves (RC) are used to judge the crystalline quality of an epitaxial layer: The angle between incident beam and detector (2θ) is fixed at a value corresponding to a specific diffraction line, while the angle of the sample ω relative to the incident beam (*rocking* angle) is slightly varied during the scan. For a perfect single crystal, the diffraction condition is only fulfilled for a single ω-position, resulting in a sharp rocking curve. If the sample consists of slightly misaligned crystalline domains, each domain contributes at a different ω to the diffraction pattern, resulting in a broader curve [81].

Throughout the work, a four circle *D8 Discover* X-ray diffractometer system from *Bruker AXS*, equipped with a Cu-rotating anode is used. Lattice

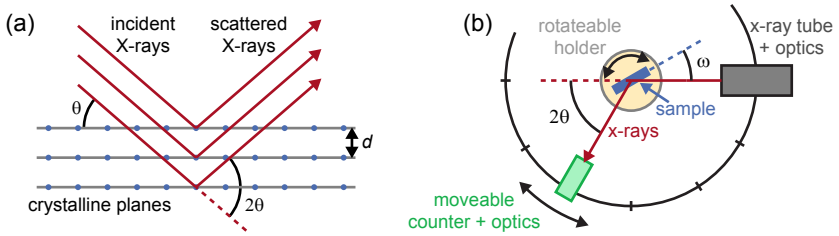

Fig. 2.5 (a) Scattering of x-rays at atoms of different crystalline planes. Since the wavelength of the x-rays is in the same order of magnitude as the distance of the atomic planes d, a diffraction pattern is visible. (b) Illustration of a XRD system (top view).

parameters are determined by fitting the diffraction peaks using pseudo-Voigt functions.

TEM Transmission electron microscopy (TEM) is used to study the microstructure of epitaxial films in cross-sectional and plan-view geometry. Electron diffraction, high-resolution transmission electron microscopy (HRTEM), high-angle annular dark-field scanning transmission electron microscopy (HAADF-STEM), electron energy-loss spectroscopy (EELS), and energy-dispersive X-ray (EDX) spectroscopy are performed using a *JEOL 2200FS* TEM/STEM microscope. The tool is operated at 200 kV and equipped with a *Gatan DigiScan* system and an in-column Omega-type energy filter. For STEM, the convergence and collection semiangles are set to 10.8 mrad and the inner semidetection angle of the annular dark field detector is calibrated at 100 mrad. For these operating conditions, the microscope provides a spatial resolution of about 1.6 Å. For cross-sectional geometry, the samples are cut parallel to the (011) planes of the Si substrate, while for plan-view samples are cut with an ultrasonic disk cutter into disks with a diameter of 3 mm. In both cases, the samples are then mechanically ground with a tripod polisher to a thickness of about 20 µm, followed by Ar ion milling until electron transparency. Alternatively, a focused ion beam tool is used to cut lamellae that are thinned down to ~ 100 nm.

Scanning probe microscopy The surface morphology of the films is investigated by conventional atomic force microscopy (AFM) operating in tapping mode in a *Dimension V* and *Dimension FastScan* tool by *Bruker*. To analyze the piezo-response of the $BaTiO_3$ films, the tools are operated in the PFM (piezo force microscopy) mode [82]: Therefore, a conductive tip (Pt-coated

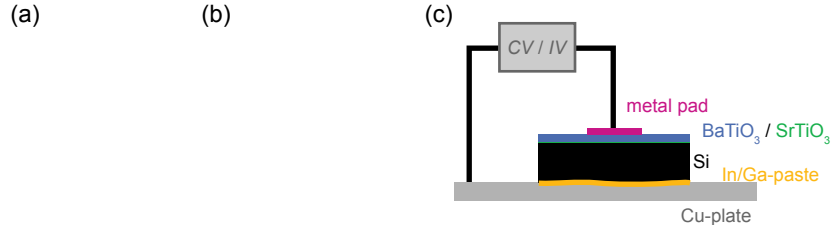

Fig. 2.6 (a) Working principle of a PFM: The topography causes a deflection of the laser beam when no electric field is applied. (b) The surface is deformed when a voltage V_{ac} is applied to the sample. Depending on the polarization P of the ferroelectric domains and the direction electric field, the cantilever is deflected differently [82] (Figure courtesy of Asylum Research, an Oxford Instruments company and Stephen Jesse, Oak Ridge National Laboratory). (c) Illustration of the setup used for I/V and C/V measurements. The sample is fixed on a copper block using a In/Ga paste.

silicon tip or PtSi tip) is scanned in contact over the sample surface. At the same time, an electric AC-field is applied between the tip and the grounded sample. For piezoelectric samples, the electric field deforms the surface, which results into a deformation of the cantilever. By using a lock-in amplifier, the modulated deformation can be separated from the surface topography. The working principle of a PFM is illustrated in figs. 2.6a and 2.6b.

In order to write patterns into the ferroelectric film, a DC voltage of $V_0 = \pm 10\,\mathrm{V}$ is applied to the tip while scanning over the surface. Highly doped Si-substrates ($\rho < 0.005\,\Omega\,\mathrm{cm}$) particularly used for these experiments serve as back electrode. After writing structures, a smaller AC voltage ($V_{ac} \sim 1\,\mathrm{V}$) is applied to the tip to read out the patterns. The operating frequency is chosen to be close to the cantilever resonance in order to enhance the sensitivity [82].

Electrical measurements

Platinum pads of different sizes (typically square-shaped, $40 \times 40\,\mu\mathrm{m}^2$, or circular shaped with a diameter of 225 µm) serve as top electrodes for electrical measurements. The silicon wafer mounted with an indium-gallium paste on a copper block serves as back contact, as illustrated in fig. 2.6c. An *Agilent 4284A LCR Precision Meter* is used for four point capacitance-voltage (C/V) measurements, during which a small sinusoidal ac signal and a larger dc bias is applied to the top electrode. Thus, the capacitance of the film can be analyzed for different band bending regimes of the metal-oxide-semiconductor (MOS)

structure, such as accumulation, flat-band, or depletion [36, 83]. Two-point current-voltage (I/V) measurements are performed in the same experimental geometry using an *Agilent 4155C* parameter analyzer.

2.2 Epitaxial growth of strontium titanate on silicon

Although the direct growth of epitaxial $BaTiO_3$ on silicon was reported first [33], the route of integrating epitaxial $SrTiO_3$ films has been explored in greater detail [37, 38, 41, 53, 84–86]. In the effort to replace SiO_2 with a high-dielectric-constant gate dielectric, $SrTiO_3$ represented a better candidate than $BaTiO_3$ due to the smaller lattice mismatch to Si (table 2.1). Indeed, thin $SrTiO_3$ layers were expected to better match the underlying Si crystalline structure and therefore to be characterized by a lower amount of electrically active interface defects. Regarding the applications targeted in this thesis, thin $SrTiO_3$ films represent an ideal buffer layer for accommodating the larger $BaTiO_3$ to silicon lattice mismatch and enable therefore the integration of high quality optically active $BaTiO_3$ layers (section 2.3).

In this chapter, two different growth routes to obtain $SrTiO_3$/Si are discussed, with focus on the crystalline quality of the oxide layers. The routes either rely on a single or on a multi-step crystallization process. Additionally, the growth process on other substrates than low-doped silicon wafers is explored, in particular SOI wafers as required for integrated photonic devices (chapter 4).

Deposition procedure

Sample preparation The preparation of the wafers prior to the growth is identical for all experiments: Before loading the typically slightly p-doped (boron), (001)-cut silicon wafers ($\rho = 0.1 - 0.5\,\Omega\,\mathrm{cm}$) into the UHV chamber, the surface is cleaned with an oxygen plasma, followed by a megasonic and ozone clean to remove particles and organic contaminants. The native SiO_2 is then removed by a buffered HF solution. The last step is repeated with an intermediate ozone clean, before loading the wafer with little delay ($\sim$5 min) into the MBE system. The HF dip creates a hydrogen terminated silicon surface that suppresses the oxidation of silicon in ambient environment.

Single-step crystallization process Because of the rather short process time compared to multi-step crystallization processes as discussed later in this section, a deposition route with only one single annealing step is explored to grow epitaxial $SrTiO_3$ layers on silicon. The process tries to minimize the

amount of SiO_2 forming at the $SrTiO_3$/Si interface during the growth [87], and consists of four major steps (visualized in fig. 2.7):

1. High temperature Sr. The deposition of 0.5 ML of Sr at a substrate temperature of ∼625 °C in UHV creates an interfacial strontium silicide layer. This silicide layer does not only prevent silicon oxidation in the subsequent steps [84, 88], but also represents the template for the following epitaxial growth being commensurate to the Si crystalline structure underneath. The high substrate temperature during Sr deposition is required to allow the Sr atoms to rearrange on the Si surface and to form a specific surface reconstruction which is the template for the subsequent epitaxial steps [53].

   The desorption of the hydrogen while heating is monitored by the RHEED pattern, which shows a transition from a 1x1 to a 2x1 periodicity of the Si-surface. During the Sr deposition, a 3x1 surface reconstruction is formed when reaching a coverage of 1/6 ML [53]. Monitoring the RHEED intensity at the position of the 3x1 diffraction line (fig. 2.7a) is used as a feedback to control the overall shuttering time and evaluating the Sr deposition process. The substrate temperature during Sr deposition is slightly reduced compared to the values of 650 °C to 700 °C as typically reported for similar process routes [84, 87, 88] to suppress the formation of SiC which is caused by a background contamination of the *Riber* MBE chamber.

2. Low temperature SrO. Additional 0.8 ML of metallic strontium are deposited at ∼100 °C to prevent the formation of SiO_2 during the introduction of O_2 into the growth chamber. 1.2 ML SrO_2 are then deposited under oxygen pressure of $\sim 5 \times 10^{-9}$ mbar. All steps are controlled by following the intensity of the specular spot in the RHEED system (fig. 2.7b). SrO is a strongly ionic oxide and grows epitaxial on the Sr-Si template at the low temperature and pressure reported above. This ensures that only a minimum amount of Si gets oxidized during the first $SrTiO_3$ deposition steps.

3. Amorphous $SrTiO_3$. $SrTiO_3$ is then deposited onto the SrO template. The Sr and Ti cells are first calibrated in oxygen ($\sim 5 \times 10^{-8}$ to 2×10^{-7} mbar). Higher oxygen pressure is required at this stage to oxidize Ti due to its ionic character. By keeping the substrate at the low temperature of ∼50 °C, again minimum substrate oxidation is ensured. 10 unit cells (UC) of $SrTiO_3$ are deposited in a layer-by-layer manner. The final film is in the amorphous state.

4. Crystallization of $SrTiO_3$. Finally, the amorphous $SrTiO_3$ is crystallized by solid state epitaxy when heating the sample above ∼480 °C. Typically,

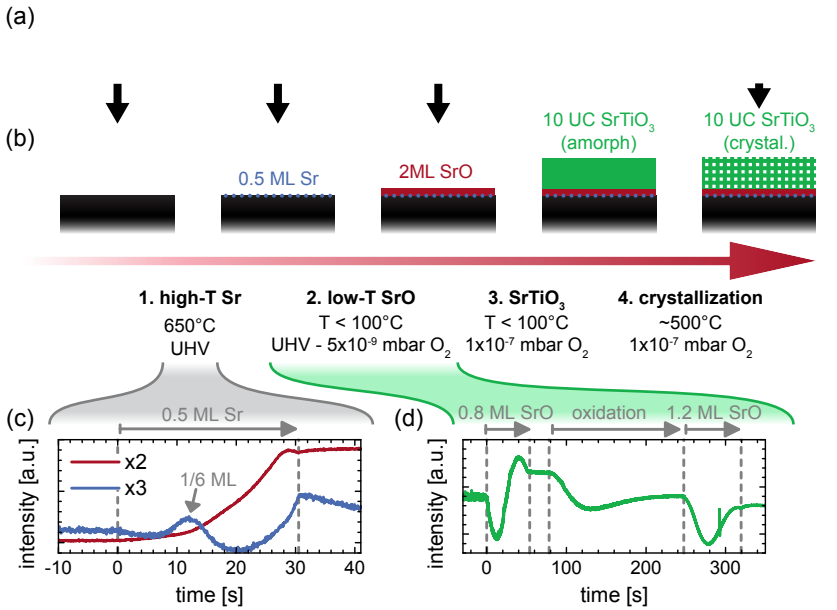

Fig. 2.7 Epitaxial growth of $SrTiO_3$ on silicon with a single crystallization step. (a) RHEED diffraction pattern at various stages during the growth. (b) Evolution of the layer stack of the sample, and process conditions for the four main deposition steps. (c) Intensity of the x2 and x3 diffraction lines during the initial deposition of 0.5 ML Sr. The maximum in the x3 line indicates a coverage of 1/6 of a monolayer. (d) Intensity of the specular spot during the deposition of 2 ML SrO. Oscillations are visible for different deposition steps as marked in the plot. The experimental data corresponds to a SOI wafer, but is similar to ordinary silicon substrates.

the oxygen is kept at the same pressure as used during the $SrTiO_3$ deposition.

Optionally, a direct deposition of $SrTiO_3$ at 500 to 550 °C is performed in oxygen ($\sim 2 \times 10^{-7}$ mbar) to obtain thicker $SrTiO_3$ layers.

Multi-step crystallization process Alternatively, the growth of $SrTiO_3$ is performed in multiple steps of depositing $2-4$ UC-thick amorphous $SrTiO_3$ layers and subsequently annealing them. Such multi-step crystallization process typically enhances the crystalline quality of the $SrTiO_3$ layer [88–90] in the

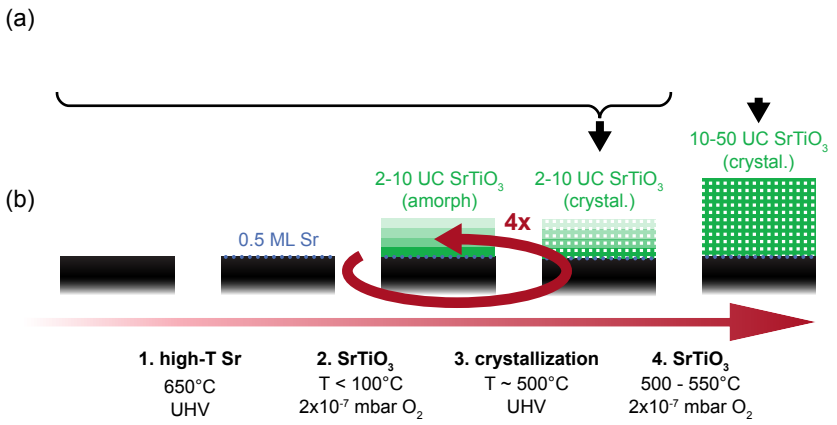

Fig. 2.8 (a) RHEED diffraction pattern of $SrTiO_3$ at different layer thicknesses. (b) Illustration of the multi-step crystallization deposition process. In contrast to the single-step crystallization process (fig. 2.7b), $SrTiO_3$ is directly deposited on the Sr/Si template at low temperature (step 2), followed by an annealing step in UHV. The process is cycled several times, before depositing $SrTiO_3$ at higher temperature to reach larger layer thicknesses. The samples are heated to 750 °C prior to step 1 to desorb any SiO_2 that might be created before loading the wafer into the MBE chamber.

expense of increasing the process time. A description of the individual process steps, and details of the pressure and temperature profiles are given in fig. 2.8 and the corresponding figure caption. As the major differences compared to the single-step crystallization process, the deposition of 2 ML of SrO is omitted because of its low thermal stability at higher temperatures [90], and the $SrTiO_3$ is deposited in several steps. All multi-step crystallization experiments are performed in the *DCA* MBE system which provides an active cooling system and consequently allows rather short annealing cycles ($\sim 30 - 60$ min per cycle).

Comparison of $SrTiO_3$ quality

As visible from the RHEED patterns for the first 10 UC (4 nm) of $SrTiO_3$ (figs. 2.7a and 2.8a), both deposition processes result in thin films with flat surface and epitaxial relationship to the silicon substrate. These features are maintained also in thicker $SrTiO_3$ layers (> 10 nm, figs. 2.9a and 2.9d). The surface roughness of such layers determined by AFM analysis is low for both growth methods ($\sim 0.3 - 0.4$ nm rms, figs. 2.9b and 2.9c), in agreement with

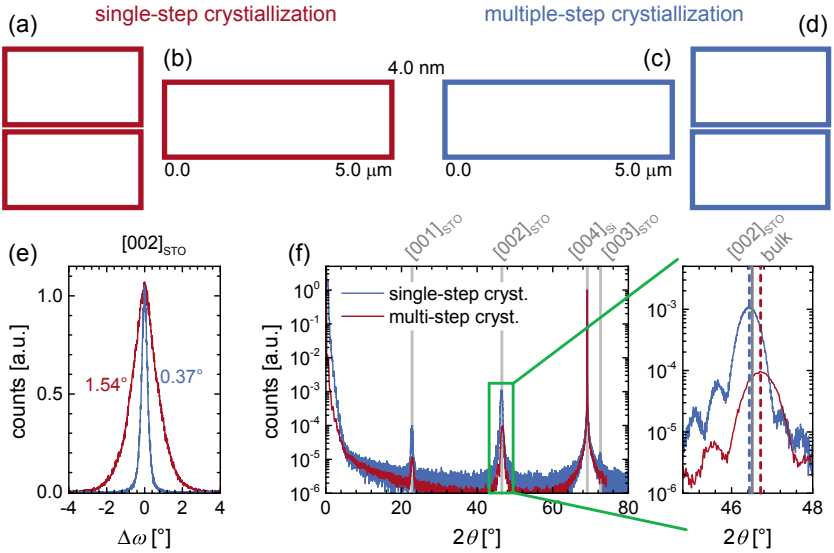

Fig. 2.9 Comparison of $SrTiO_3$ layers grown with a single recrystallization process (12 nm-thick, highlighted in red) and with a multi-step recrystallization process (20 nm-thick, blue). (a)/(d) RHEED patterns and (b)/(c) topography of the samples. The azimuthal orientation is indicated in the RHEED images. (e) Rocking curves of the $[002]_{STO}$ peak. (f) X-ray diffraction pattern in out-of-plan geometry, and magnification of the $[002]_{STO}$ peak. The lattice parameters are $a^{\perp}_{STO} = 3.890$ and $a^{\perp}_{STO} = 3.910$ for the sample grown with a single and with multiple crystallization steps, respectively. The positions of the bulk diffraction peaks are indicated in gray.

the RHEED patterns. The formation of small islands (fig. 2.9c) in some of the films could not be correlated to the deposition process. The islands might be due to small deviations from the 1:1 stoichiometry between Sr and Ti. The concentration of any crystalline phases other than $SrTiO_3$ is however small since no evidence was found in x-ray diffraction (fig. 2.9f) and RHEED investigations.

The major difference between both growth methods is the significantly higher crystalline quality of $SrTiO_3$ layers grown with the multi-step crystallization process, indicated by the sharper diffraction lines in the RHEED patterns (figs. 2.9a and 2.9d). The higher quality is evidenced by the smaller full width at half maximum (FWHM) of the rocking curve ($\Delta\omega_{STO} = 0.37°$) compared to

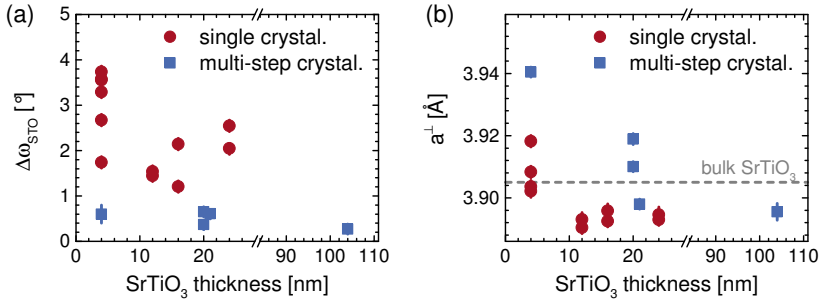

Fig. 2.10 (a) FWHM of the $[002]_{STO}$ rocking curve $\Delta\omega_{STO}$ and (b) out-of-plane lattice constant $a_{\perp}$ for $SrTiO_3$ thin films of different thickness grown with a single- and multi-step crystallization process, respectively.

the layer grown with a single crystallization step ($\Delta\omega_{STO} = 1.54°$) (fig. 2.9d). The analysis of several films confirms this trend of a reduced FWHM of the rocking curve independent of the layer thickness (fig. 2.10a). The comparison also reveals rather large sample-to-sample variations, which are the consequence of the strong impact of the chamber conditioning on the deposition process. A conclusive analysis of the dependence of layer thickness on the $SrTiO_3$ quality is thus not possible. Nevertheless, the highest crystalline quality among all samples is achieved with a relatively thick film (104 nm) grown by the multi-step crystallization process (fig. 2.10a). The FWHM of the RC is only $\Delta\omega_{STO} = 0.27°$ in that particular sample, which is close to values reported for bulk $SrTiO_3$ crystals ($0.035° - 0.108°$ [41]). The good quality of thick films is in agreement with a systematic study of $SrTiO_3$/Si films that shows an enhancement in the $SrTiO_3$ quality for an increasing film thickness [40].

The rather large FWHM of the rocking curve of the $SrTiO_3$ layer grown with the single crystallization method (fig. 2.9d) is caused by slightly misoriented crystalline domains. Such defects are formed in order to relax strain that originates from the lattice mismatch between silicon and $SrTiO_3$ (table 2.1). The relaxation already occurs in the 2 ML SrO and the first 4 nm of $SrTiO_3$, which are deposited amorphously and then crystallized in a single-step solid-state epitaxial process. Since the deposition is performed at low temperature, strain due to the mismatch of the thermal expansion coefficients is absent and a bulk-like $SrTiO_3$ lattice constant is observed (fig. 2.10b). Thicker (> 10 nm) $SrTiO_3$ layers grown at 500 °C are relaxed during the deposition. When cooling down to room temperature, tensile strain establishes due to the mismatch of the thermal expansion coefficients between Si and $SrTiO_3$ (table 2.1). The

crystalline symmetry is therefore slightly distorted. In particular, the out-of-plane lattice constant is compressed to values slightly smaller than the bulk lattice constant, as seen in fig. 2.9e.

In contrast, thin layers of $SrTiO_3$ grown with the multi-step crystallization method show a significantly larger out-of-plane lattice constant compared to bulk crystals (fig. 2.10b). The increased lattice parameter results from compressive strain in the $SrTiO_3$ crystal due to the lattice mismatch of ∼1.7 % (table 2.1) relative to the Si substrate. In agreement with sharper $SrTiO_3$ rocking curves (fig. 2.10a), less defects are created in strained $SrTiO_3$ layers at the interface to the high-quality silicon substrate compared to fully relaxed $SrTiO_3$ films. The large strain levels are however only present in thin $SrTiO_3$ layers (fig. 2.10b). Thicker layers grow relaxed at the growth temperature of 500 °C, and tensile strain originating from the thermal expansion mismatch causes a slightly reduced out-of-plane lattice parameter compared to bulk crystals (fig. 2.10b). A transition between layers with compressive and tensile strain is visible at a $SrTiO_3$ thickness of ∼20 nm (fig. 2.10b). More data for intermediate layer thicknesses would however be required to analyze the critical thickness in detail.

In conclusion, the multi-step crystallization process leads to a significantly better $SrTiO_3$ crystalline quality compared to the single-step crystallization method, mainly because the first monolayers grow highly strained and experience thus a reduced defect density compared to relaxed films. The introduction of periodic annealing steps might be the key to avoid defects in the very first unit cells, similar to methods developed for the growth of III/V semiconductor materials [91]. Additionally, the absence of 2 ML SrO between the $SrTiO_3$ crystal and the silicon surface might contribute to the improvement of the crystalline quality: Such SrO buffer layer mainly serves to avoid oxidation of the Si interface [39]. Due to the large lattice mismatch to the silicon substrate (a_{SrO} = 5.144 Å [92], ∼5.6 % mismatch), defects might form within the first SrO monolayers, which are continued in the successive $SrTiO_3$ layer.

The first monolayers on top of the Sr-terminated silicon surface are crucial for reaching a high quality epitaxial growth, and should therefore be further investigated, independently of the subsequent annealing procedure. Several methods have been reported to grow the initial oxide layer on silicon. As an example, Park *et al.* [41] deposited 3 ML SrO and subsequently 2 ML TiO_2, which interdiffuses into the SrO layer to form $SrTiO_3$ during the first annealing step. Their approach resulted in the currently smallest $SrTiO_3$ rocking curves of perovskite films on silicon substrates with a FWHM of $\Delta\omega_{STO} = 0.006°$ for the $[002]_{STO}$ peak.

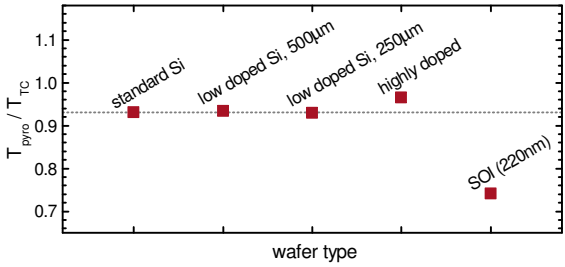

Fig. 2.11 Temperature calibration for different silicon substrates showing the ratio between the pyrometer readout temperature T_{pyro} and the thermocouple T_{TC}. The conductivity of the wafers is $\sim 0.5\,\Omega\,\mathrm{cm}$ for standard wafers, $\sim 10^4$ $\Omega\,\mathrm{cm}$ for high resistive wafers, and $\sim 10^{-4} - 10^{-3}\,\Omega\,\mathrm{cm}$ for high conductive wafers, respectively. The SOI wafer has a 220 nm thick silicon device layer and a 3 µm buried oxide layer.

Growth on different Si-substrates

In this work, the growth process is mainly investigated on low-doped silicon wafers, as previously described. Different substrates are however required for many applications, such as silicon-on-insulator (SOI) wafers for the fabrication of photonic devices (chapter 4). Furthermore, highly resistive Si-wafers are necessary for the electro-optic characterization (chapter 3) and, in some cases, highly doped silicon wafers are needed for determining the piezoelectric properties of the $BaTiO_3$ films. The main challenge in adapting the growth process to these different substrates is the adjustment of the temperature during the growth. In the MBE chamber, the wafers are heated via radiation from a hot filament. The actual temperature of the wafer at a specific heating power varies between different substrates for two reasons: First, the absorption of the wafer is dependent on the doping [93], and second, radiation is reflected at interfaces between the different layers in a SOI wafer. Such interfaces are not present in standard silicon substrates. Additionally, differently doped wafers show different emissivity values, which has an impact on the temperature readout of the pyrometer. Since a thermocouple to directly measure the surface temperature is not available, the actual temperature can not be determined consistently between different substrates.

In order to experimentally account for these differences in temperatures, a coarse calibration is performed in the *ASone* RTA, where a thermocouple as well as a pyrometer are installed. Figure 2.11 shows the ratio between both

temperature readouts for a sample temperature of 650 °C as determined by the thermocouple. Ideally, this ratio should be one for a well calibrated pyrometer. Significantly deviations from the low-doped silicon wafers are visible for the highly doped and the SOI wafer. Taking these deviations into account when performing the growth, $SrTiO_3$ films with good crystalline quality are achieved (see fig. 2.7 as example for SOI substrates).

2.3 Epitaxial deposition of barium titanate thin films

$SrTiO_3$/Si templates as described in the previous section are used for fabricating epitaxial $BaTiO_3$ thin films. The approach of depositing epitaxial $BaTiO_3$ on silicon was previously reported [55, 94–96], but is much less explored than the growth of $SrTiO_3$ layers. Generally, the larger lattice mismatch between $BaTiO_3$ and Si (∼4.0 %) compared to $SrTiO_3$ and Si (∼1.7 %, table 2.1) makes it more difficult to obtain barium titanate films of high structural quality on Si substrates. Additionally, the properties of $BaTiO_3$ thin films are influenced by anomalous distortions of the lattice parameters and strain, as observed in the presence of nano-scale $BaTiO_3$ grains [97, 98]. Achieving control over the sample morphology is therefore a key condition for obtaining high-quality films with bulk-like functional properties, as desired for most $BaTiO_3$-based devices.

Therefore, different growth processes and their impact on the crystalline quality and the microstructure of the films are discussed below (sections 2.3.1 and 2.3.2). A detailed analysis of the crystalline symmetry of the $BaTiO_3$ layers is given in section 2.3.3.

2.3.1 Layer-by-layer deposition

Growth process and epitaxial relationship

Barium titanate is deposited at ∼600 °C on top of 10 UC epitaxial $SrTiO_3$ on silicon grown by the single-step crystallization process (section 2.2). BaO and TiO_2 are therefore deposited sequentially to achieve a layer-by-layer growth with typical fluxes corresponding to ∼15 s/ML. Variations of the growth temperatures between 575 °C and 650 °C have no influence on the crystalline quality as determined by RHEED and rocking curve analyses and do not change the surface roughness of the films. The formation of oxygen vacancies in the perovskite layers is minimized by using atomic oxygen at a pressure of $p \approx 2 \times 10^{-5}$ mbar, which is close to the upper limit allowed in MBE systems. The evolution of the RHEED pattern during the $BaTiO_3$ deposition (figs. 2.12a and 2.12b) shows that the crystalline quality of the initial $SrTiO_3$

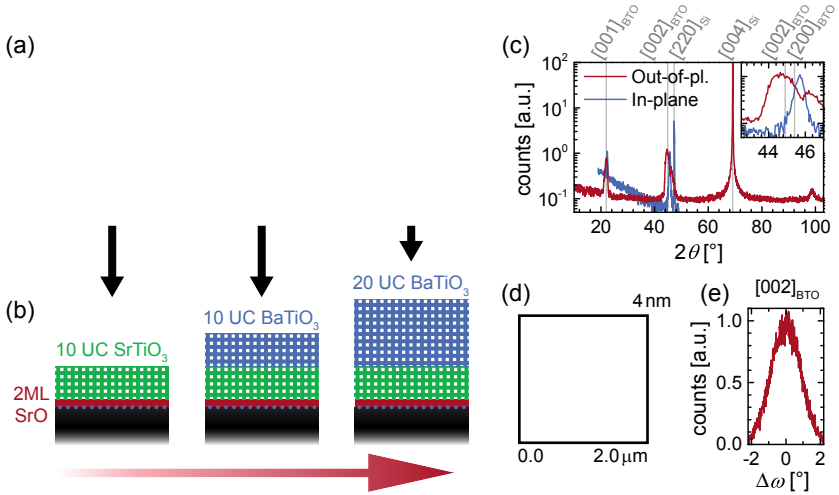

Fig. 2.12 (a) RHEED patterns at various stages during the growth process of a 8 nm-$BaTiO_3$ film on top of 4 nm-$SrTiO_3$, as illustrated in (b). (c) XRD diagram in out-of-plane and in-plane geometry, with magnification of the $[002]_{BTO}$ diffraction peak (inset). The main crystalline axes are labeled in gray. (d) Topgraphy measured by AFM and (e) rocking curve of the $[002]_{BTO}$ diffraction peak. The FWHM is $\Delta\omega_{BTO} = 2.1°$.

layer is maintained during the $BaTiO_3$ deposition. X-ray diffraction analysis (figs. 2.12c and 2.12e) confirm the epitaxial relationship, and reveal a similar FWHM of the RC as observed for $SrTiO_3$ layers grown by a single crystallization process (fig. 2.10a). Also, the low surface roughness of 0.4 nm of the $BaTiO_3$ layers (fig. 2.12d) matches the roughness of the $SrTiO_3$ seed layers (fig. 2.9).

The XRD diagrams for the in- and out-of-plane orientation (fig. 2.12c) show two clearly different lattice parameters, which is in accordance with a tetragonal crystal symmetry expected for $BaTiO_3$. For the specific sample shown in fig. 2.12, $BaTiO_3$ is oriented with the longer c-axis perpendicular to the sample surface ("c-axis" film). However, the orientation of the c-axis varies with the growth conditions, the layer thickness, and the chemical composition of the buffer layer [55, 94, 99], as discussed in more detail in section 2.3.3.

The atomic arrangement and epitaxial relationship of the $BaTiO_3$ layer relative to the $SrTiO_3$ layer is visualized by line scans in a HRTEM micrograph

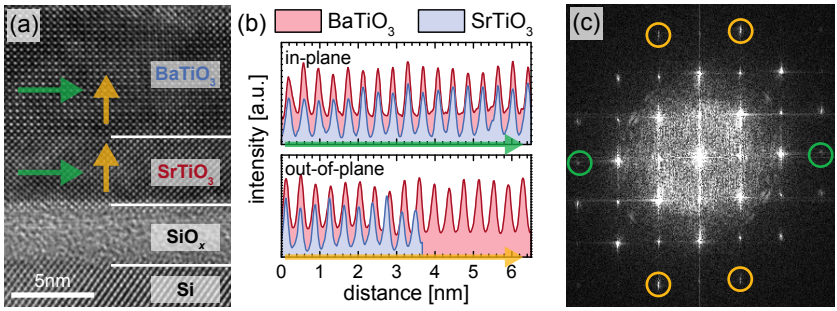

Fig. 2.13 (a) HRTEM image of the $BaTiO_3/SrTiO_3$ interface. The green and yellow arrows indicate the direction of line scans parallel and perpendicular to the interface (b). The scans reveal a commensurate growth of $BaTiO_3$ on $SrTiO_3$ with a different out-of-plane lattice constant. (c) The different splitting of the diffraction peaks in the FFT of the HRTEM image highlights the different out-of-plane lattice parameters (yellow circles), and confirms the identical in-plane constants (green circles).

of a $BaTiO_3/SrTiO_3/Si$ layer stack[1] (figs. 2.13a and 2.13b): Scans parallel to the interface show the identical in-plane registry of the atoms, in agreement to the presence of one single in-plane diffraction peak for the $BaTiO_3$ and $SrTiO_3$ films in the XRD pattern (fig. 2.12c). The in-plane lattice parameter $a^{\parallel}$ of both layers is identical, and the growth of $BaTiO_3$ is commensurate to the $SrTiO_3$ seed layer.

Contrary, the scans perpendicular to the interface show a different lattice spacing between the $BaTiO_3$ and the $SrTiO_3$ layers, again in agreement to two different out-of-plane lattice constants $a^{\perp}$ as seen in the XRD analysis (fig. 2.12c). The fast Fourier transform (FFT) of the HRTEM image (fig. 2.13c) visualizes the observations of different out-of-plane constants: a splitting of the diffraction spots is only visible in the out-of-plane direction (yellow circles). For the in-plane direction, only single diffraction peaks are present (green circles).

Thin $BaTiO_3$ layers which grow commensurately on the $SrTiO_3$ seed layer

1 In addition to the MBE-deposition as described above, 100 nm $BaTiO_3$ is sputtered on top of the stack at 500 °C, which results in an amorphous phase (details in section 2.4). The amorphous phase is preferentially milled away during the sample preparation and is thus not visible in the microscopy images. Since the thermal budged of the MBE deposition is not significantly increased by the sputter process, no influence on the MBE-layers by the sputtering process is assumed.

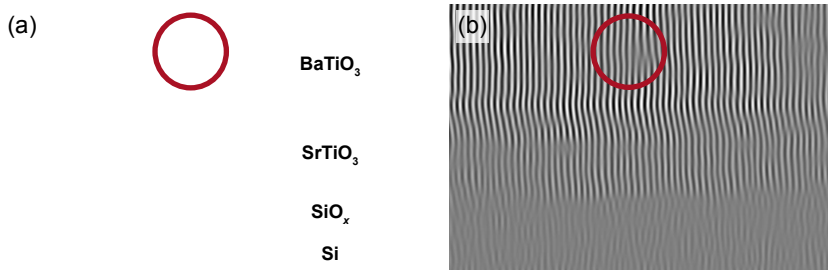

Fig. 2.14 (a) Edge dislocation in the $BaTiO_3$ layer, which is formed to relax the strain caused by the epitaxial growth on the $SrTiO_3$ buffer layer. (b) $[001]_{BTO}$ Bragg filtered version of (a). The missing lattice plane in the $BaTiO_3$ crystal compared to the $SrTiO_3$ film is highlighted in red.

are highly strained due to the lattice mismatch of ∼2.3% between both layers at room temperature (table 2.1). The strain is partially reduced by the formation of dislocations at the $BaTiO_3/SrTiO_3$ interface in order to minimize the energy of the films [56]. When the layer thickness is increased, strain is further released by the formation of dislocations within the $BaTiO_3$ layer. Figure 2.14 shows an example of an edge dislocation in the $BaTiO_3$ layer at a distance of ∼5 nm from the $BaTiO_3/SrTiO_3$ interface. As discussed in section 2.3.3, a layer thickness greater than ∼30 nm is required to fully relax the $BaTiO_3$ film. A way to avoid the formation of edge dislocations is the reduction of the strain by tuning the lattice constant of the buffer layer closer to the one of $BaTiO_3$. One option to experimentally realize such adjustment is by mixing barium into the buffer layer, and creating a $Ba_xSr_{1-x}TiO_3$ solid solution [55].

The commensurate growth of $BaTiO_3$ on $SrTiO_3$ seen in fig. 2.13 indicates that the $BaTiO_3$ crystalline quality is determined by the $SrTiO_3$ template. X-ray analysis with a similar FWHM of the $[002]_{BTO}$ rocking curve ($\Delta\omega_{BTO} = 2.1°$, fig. 2.12e) compared to the $[002]_{STO}$ rocking curve of $SrTiO_3$ layers grown with the single-step crystallization process (fig. 2.10) are in agreement with these TEM observations. Generally, the formation of dislocations to release strain (fig. 2.14) might result in a degradation of the crystalline quality in the $BaTiO_3$ film.

Analysis of interfacial layers

The high resolution STEM micrographs (figs. 2.13a and 2.14a) of the interfaces not only show the epitaxial ordering of the crystalline $BaTiO_3$ and $SrTiO_3$

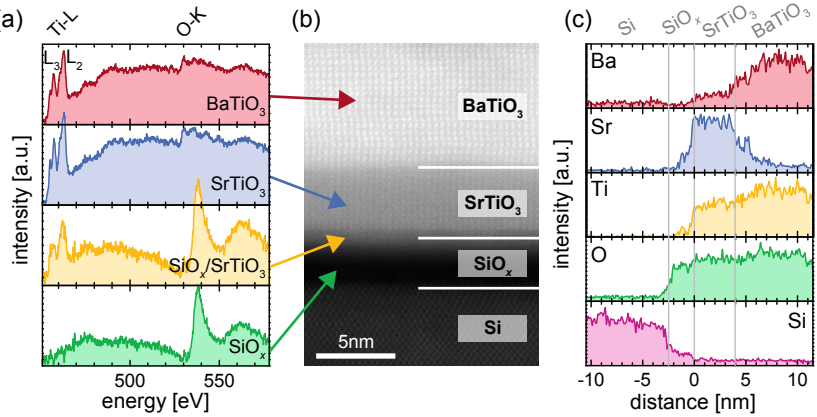

Fig. 2.15 (a) EEL+ spectra at different positions of the $BaTiO_3/SrTiO_3/Si$ layer stack[2], as indicated in the (b) ADF-STEM image. The spectra are calibrated with literature values for the Ti-L and O-K edge [102]. (c) EDX line profiles perpendicular to the interface. The distance is centered at the lower $SrTiO_3$ interface.

layers in respect to the silicon substrate. They also reveal an amorphous SiO_2 layer at the $SrTiO_3/Si$ interface with a thickness of ∼3 nm. Although $SrTiO_3$ growth process was originally designed to avoid any interfacial SiO_2 formation [39], the SrO/Si interface is rather unstable against high temperatures and high oxygen pressures [38, 100, 101]. In particular, the $BaTiO_3$ growth process with atomic oxygen is much more aggressive for the interface than the $SrTiO_3$ deposition only. Likely, oxygen diffuses through the $SrTiO_3$ layer at the high temperature used during the $BaTiO_3$ deposition and oxidizes the Si underneath. Since SiO_2 forms after the crystallization of $SrTiO_3$, it does not harm the epitaxial relationship of the subsequently deposited layers.

The assignment of the amorphous layer at the $SrTiO_3/Si$ interface (black layer in fig. 2.15b) to SiO_2 is justified by the EEL spectra, which show the typical oxygen edge of amorphous SiO_2 (fig. 2.15a). The spectra also show a crystal

2 The sample under investigation is identical to the one described in footnote 1 (page 30) with the exception of the top $BaTiO_3$ layer, which is sputtered at 600 °C. Since the thermal budged of the MBE deposition was not significantly increased by the sputter process, no influence on the MBE-layers by the sputtering process is assumed.

field splitting in the titanium L_2 and L_3 edge within the $BaTiO_3$ and $SrTiO_3$ layers as expected in crystalline layers. However, at the $SrTiO_3/SiO_2$ interface, the Ti-L edge shows no crystal field splitting, which indicates the presence of an amorphous interfacial species that contains Ti. It was previously reported that amorphous $TiSi_x$ silicide can form at temperatures higher than $> 450\,°C$ in Ti/Si multilayers [103]. Silicide may form also at the $SrTiO_3$/Si interface at high temperatures [100] and in oxygen deficient conditions. In oxygen rich conditions, more likely a Ti-rich silicate layer forms as previously observed at similar interfaces [101]. The Ti-rich amorphous phase is observed in several, similarly fabricated samples, and seems to be characteristic to the growth process. A systematic study, in particular using XPS (x-ray photoelectron spectroscopy) analysis, is required to identify the character and the cause for the formation of that interfacial layer.

The composition of the amorphous SiO_2 layer is in agreement with EDX line scans across the interface (fig. 2.15c), which show the presence of oxygen and silicon at the $SrTiO_3$/Si interface. The upper part of the amorphous layer appears clearly brighter in the STEM image (fig. 2.15b) indicating the presence of heavier elements that originate from the $SrTiO_3$ layer. Indeed, the EDX profiles confirm the interdiffusion of Sr into the SiO_2 layer. They also show a Ti-peak close to the $SrTiO_3$ interface, consistent with a Ti-rich silicate phase (fig. 2.15c). The diffusion of barium into the $SrTiO_3$ layer as observed in fig. 2.15c is not detected in the TEM analysis of similarly fabricated samples. The diffusion might be due to slight variations in the $BaTiO_3$ deposition temperature for the specific sample shown in fig. 2.15.

The role of the $BaTiO_3$ composition

Compared to the growth of $SrTiO_3$, which keeps a good crystalline structure even for off-stoichiometric Sr:Ti ratios by for example forming Ruddlesden-Popper phases [71], meeting a 1:1 ratio of Ba and Ti is very critical to obtain high quality $BaTiO_3$ films. This is in particular true for rather thick $BaTiO_3$ layers ($> 50\,nm$) as required in electro-optical devices (chapter 4). The comparison of three samples with different Ba:Ti ratio of 1.03:0.97, 1.00:1.00, and 0.97:1.03 (fig. 2.16) shows the strong impact of the film composition on the growth process: Between the streaky diffraction lines corresponding to the $BaTiO_3$ matrix, individual diffraction spots are visible in the RHEED patterns, indicating 3D crystalline features. These features are oriented at a specific crystalline direction relative to the $BaTiO_3$ crystal. For Ti-rich samples, such diffraction spots are not visible but the pattern is characterized by a rather blurry background which might be attributed to the presence of amorphous species. The spotty features in the diffraction patterns are most pronounced in the Ba-rich sample, but

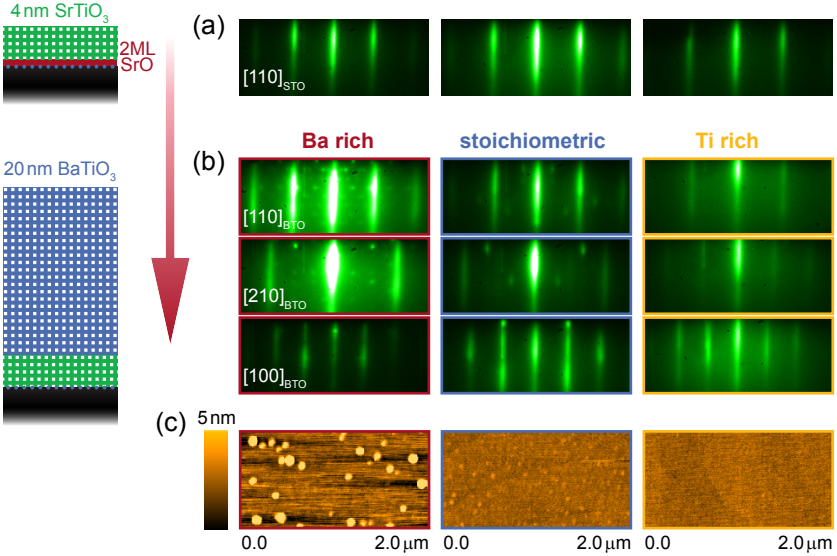

Fig. 2.16 Influence of the Ba:Ti ratio on the $BaTiO_3$ layer quality. (a) RHEED patterns of the initial $SrTiO_3$/Si templates grown by single-step crystallization. (b) Diffraction pattern after successively depositing 20 nm $BaTiO_3$ with Ba-rich (red, Ba : Ti = 1.03 : 0.97), stoichiometric (blue, Ba : Ti = 1.00 : 1.00), and Ti-rich (yellow, Ba : Ti = 0.97 : 1.03) conditions, respectively. 3D diffraction features are visible in addition to the 2D-streaks for some of the samples. (c) Topography measured by AFM. The cross section of the layer stack is illustrated on the left.

are also visible in the nominally stoichiometric sample. The real stoichiometry might be indeed slightly off, because the calibration of the fluxes via QCM is prone to systematic errors as discussed in section 2.3.2.

A clear trend for the formation of "precipitates" in Ba-rich samples is visible not only in the diffraction patterns, but also in the evolution of the surface topography with an increasing density of small islands (fig. 2.16c). According to the $BaTiO_3$ phase diagram (fig. 2.2), Ba_2TiO_4 or $Ba_{1.054}Ti_{0.964}O_{2.964}$ might form for Ba-rich growth conditions. Possibly due to their low volume fraction and thus low diffraction intensities, such phases are not observable by means of XRD investigations. In particular, no correlation could be made between the composition and the crystalline quality as determined by the FWHM of the $BaTiO_3$ rocking curves.

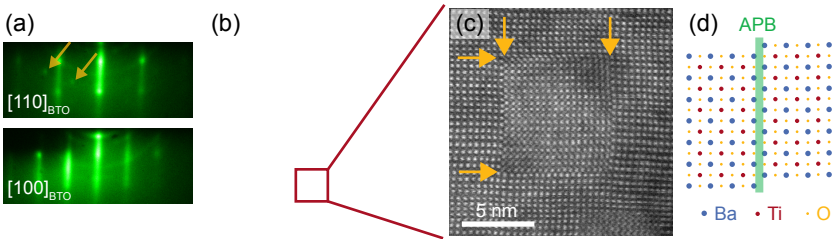

Fig. 2.17 (a) RHEED pattern of a 130 nm-thick $BaTiO_3$ layer grown with layer-by-layer deposition. Individual diffraction spots in addition to the streaky pattern of the two-dimensional, crystalline surface are indicated by arrows. (b) BF-STEM image showing small, rectangular shaped defects in the $BaTiO_3$ film. (c) Atomic resolution DF-STEM image revealing APBs with missing TiO_2 planes, likely caused by Ti-deficiency during the growth. (d) Schematics of an APB in $BaTiO_3$ with a missing TiO_2 plane.

To further understand the origin of the "preciptates", HRTEM analysis are performed on a rather thick (130 nm) $BaTiO_3$ film with similar RHEED patterns (fig. 2.17a). In these patterns, traces of polycrystalline domains are visible in addition to individual diffraction spots. The plan-view STEM analysis of the sample shows ∼5 nm-small, planar crystalline defects of rectangular shape (fig. 2.17b). These defects are indeed anti phase boundaries (APBs) as seen at atomic resolution (fig. 2.17c). In particular, the TiO_2 lattice plane is missing, indicating a Ti-deficiency of the film, which is equal to Ba-excess. As shown in fig. 2.16, the individual diffraction spots in the RHEED pattern are indeed characteristic for barium excess. Since the APBs are regularly embedded in the $BaTiO_3$ matrix, the local distortion of the lattice constant might give rise to additional diffraction features visible in the RHEED patterns.

As discussed for $La_{1-x}Ca_xMnO_3$ films grown on $SrTiO_3$ substrates [104], APBs can serve as origin for the formation of islands, which would also result in RHEED patterns with 3D diffraction features. The topography seen in off-stoichiometric, Ba-rich films (fig. 2.16c) as well as their RHEED patterns with individual diffraction spots are consistent with such island formation triggered by APBs due to Ba-excess.

In addition to small APB defects, the cross-sectional analysis shows columnar shaped features perpendicular to the surface (figs. 2.18a and 2.18b). The columns lead to domains with increasing mis-orientation towards the surface of the film, where some of the columns detach and small pores are formed. The columnar structure is confirmed in the plan-view geometry by the presence

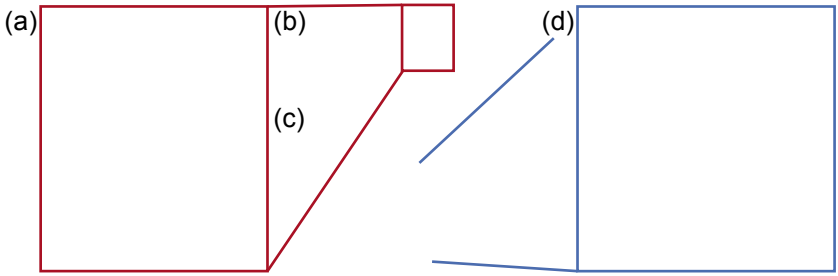

Fig. 2.18 TEM analysis of a 130 nm-thick MBE-grown $BaTiO_3$ layer showing a columnar structure and the formation of pores. (a) High and (b) low magnification cross-sectional DF-STEM images. (c) Rectangular-shaped columns are visible in the plan-view TEM images at low and (d) high magnification.

of rectangular defects which are surrounded by pores (figs. 2.18c and 2.18d). Electron diffraction patterns (not shown) reveal the same crystalline symmetry of the pores and the surrounding matrix with a slight rotation of the crystalline planes in the columns. No different composition between the columns and the matrix could be identified via EDX scans. It is therefore unlikely that the columns represent a different phase such as Ba_2TiO_4 that might form in non-stoichiometric $BaTiO_3$ (fig. 2.2).

Stress during cooling down as a consequence of the different thermal expansion coefficients between silicon and $BaTiO_3$ is unlikely to be the origin for the pore formation. First, because the $BaTiO_3$ films would only marginally be strained ($\epsilon \approx 0.5\%$), and second, because stress relaxation typically leads to cracks in the film which are not observed in MBE grown $BaTiO_3$ layers. If other phases than $BaTiO_3$ are locally established due to off-stoichiometric growth conditions, these phases might however have different elastic moduli and could thus act as breaking points of the film. As suggested by Lebedev *et al.* [104], also APBs might promote the formation of columnar structures that are separated by pores. Minimizing the creation of APBs by avoiding off-stoichiometric growth conditions would thus be a key for obtaining homogeneous and dense layers without pores.

2.3.2 Shuttered co-deposition

Challenges for controlling the Ba:Ti stoichiometry

In order to avoid the formation of other crystalline phases than $BaTiO_3$, a precise 1:1 ratio between Ba:Ti has to be obtained. Therefore, two main challenges have to be solved for the MBE deposition process:

- Systematic errors in the flux calibration have to be eliminated. One error arises from the assumption that the atoms evaporated from the sources have the same sticking coefficient on the quartz during the calibration and on the sample surface during the film growth. Since the quartz is kept cool at 25 °C and the sample is heated at ∼600 °C, the sticking coefficient might however differ between both cases. In addition, the choice of the shuttering cycles has an impact on the flux measurements: During the calibration, the shutters of the sources are typically opened and closed for 1 min each, while the real shuttering during the deposition is much faster. The calibrated rates for different shutter cycles vary by more than 10 % (fig. 2.19a). Reasons for that variation are the finite shutter closing/opening time during one cycle. Furthermore, heat is reflected back into the cell when the shutter is closed, which eventually varies the temperature of the cell core and the thermocouple in the cell. The calibration errors could be compensated by carefully varying the composition in various calibration samples, and thus determining corrected calibration curves.
- The titanium source exhibits a slow, long term drift which stabilizes only after several hours of operation (fig. 2.19b). Even though a short-term extrapolation of the flux is possible, the fabrication of a 50 nm thick $BaTiO_3$ film with a deposition time of $1 - 2$ h would require several recalibration steps during the process.

Due to these difficulties in properly determining the actual flux, the formation of precipitates as seen in the RHEED patterns for films with a thickness of > 20 nm (figs. 2.16b and 2.17a) is hardly avoidable. A way to overcome this lack of composition control is by co-depositing both metal oxides at the same time while using a fast shuttering sequence to compensate off-stoichiometry, as described in the following.

Concept of shuttered co-deposition

The simultaneous deposition of BaO and TiO_2 onto the sample provides several advantages compared to the $BaTiO_3$ layer-by-layer growth.

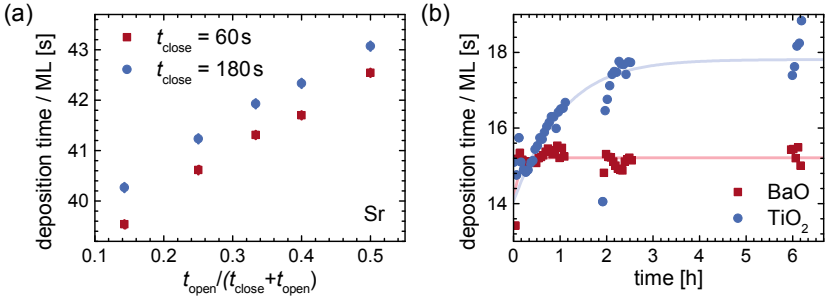

Fig. 2.19 (a) Deposition time for one monolayer of Sr for different calibration settings while keeping the cell temperature constant. The amount of Sr deposited on the QCM during one calibration cycle is measured in order to determine the Sr-flux. Therefore, the shutter is iteratively opened for the time t_{open} and closed for t_{close} to compensate temperature variations of the quartz due to thermal radiation from the hot Sr-cell. The Sr flux increases (reduction of deposition time per monolayer) when the relative shutter opening time is reduced. The increased rate is likely caused by back reflections of the thermal radiation of the cell at the closed shutter, which increases the cell core temperature. (b) Long-term drift of the TiO_2 and BaO deposition times per monolayer for fixed source settings. Solid lines are guides for the eye.

- Some studies report an improved layer quality in $SrTiO_3$ films grown by co-deposition compared to layer-by-layer deposition [105, 106]. The simultaneous deposition influences the growth kinetics as the presence of strontium promotes the oxidation of titanium [107]. The improved oxidation might also be valid for the chemically similar $BaTiO_3$.
- The deposition time is reduced by a factor of 2 which lowers the impact of drifting fluxes of Ba and Ti.
- As the key advantage, the stoichiometry is only determined by one parameter, namely the ratio of the fluxes of the two sources. The second parameter, the absolute magnitude of the fluxes, determines the total thickness of the film, where small deviations are less critical for most applications. In contrast, during a layer-by-layer deposition, both fluxes have to be known exactly to determine the deposition time of 1 ML for BaO and TiO, respectively.

Typically, both fluxes are set to identical rates when co-depositing both materials. During the growth, drifts of the fluxes have to be compensated to

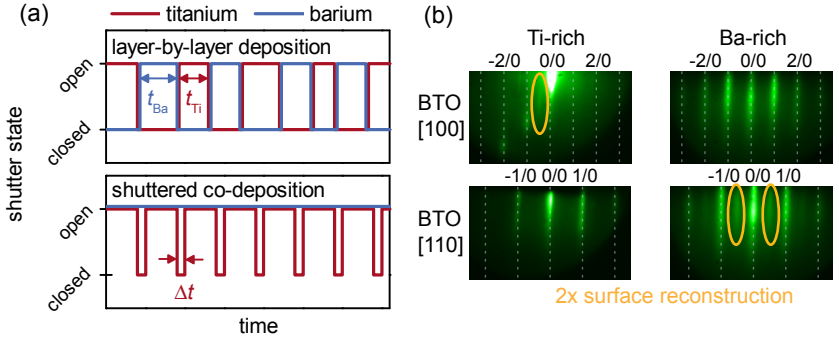

Fig. 2.20 (a) Comparison of shutter sequences for layer-by-layer growth and shuttered co-deposition. During the shuttered co-deposition, only Δt has to be controlled to ensure a stoichiometry growth. t_{Ba} and t_{Ti} are the deposition times for 1 ML of Ba and Ti, respectively, and $t_{\mathrm{Ba}} > t_{\mathrm{Ti}}$ is chosen as an example. (b) Diffraction patterns of a Ti-rich and Ba-rich $BaTiO_3$ surface, respectively, used to control Δt. The yellow ellipse highlights a x2 surface reconstruction.

maintain a 1:1 flux ratio between Ba and Ti. Therefore, either the temperature of the Ba-effusion cell can be adapted, or the ebeam filament current of the Ti-source can be changed. Adjusting the effusion cell suffers however from a rather long delay (several min) before reaching stable conditions, and changing the Ti-source requires a QCM recalibration since the Ti-flux is very sensitive to the filament current and thus hardly predictable.

Therefore, a *shuttered co-deposition* is developed to realize a stoichiometric growth without changing the source settings. Both sources, Ba and Ti, are set to roughly the same flux corresponding to ∼15 s/ML as determined via QCM calibration. The deposition times for 1 ML are t_{Ba} and t_{Ti}. For the case of $t_{\mathrm{Ba}} > t_{\mathrm{Ti}}$, as an example, both shutters are simultaneously opened for t_{Ti}. To compensate the different fluxes, only the Ba-source is afterwards kept opened for a short time $\Delta t = t_{\mathrm{Ba}} - t_{\mathrm{Ti}}$ (typically around ∼1 s), as illustrated in fig. 2.20a. If $t_{\mathrm{Ba}} < t_{\mathrm{Ti}}$, the Ti- and Ba-cycles are switched. Thus, for most of the time during the deposition both shutters are opened (co-deposition), and small deviations are compensated by a fast shutter sequence. By changing Δt during the deposition, a quick way to adjust the stoichiometry with only one parameter is given.

A feedback mechanism is required to compensate off-stoichiometric $BaTiO_3$ growth in real time. For example, the evolution of the intensity oscillations in the RHEED specular spot has been used to control the stoichiometry during

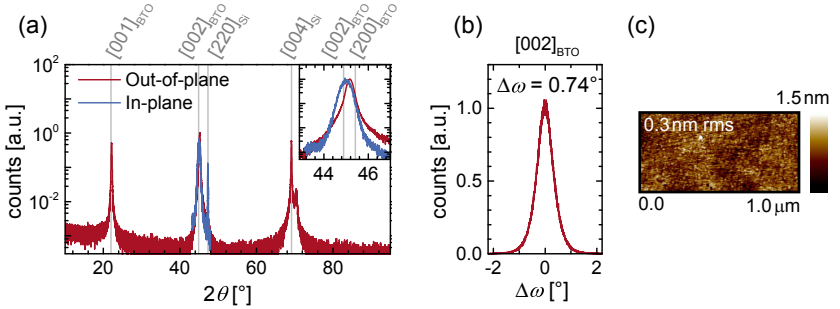

Fig. 2.21 $BaTiO_3$ film grown by the shuttered co-deposition method on a SOI substrate. (a) XRD diagram showing the epitaxial relationship between $BaTiO_3$ and Si. The in- and out-of-plane lattice constant are different due to the tetragonal crystal symmetry as seen in the inset. (b) Rocking curve of the $[002]_{BTO}$ diffraction peak. (c) Topography determined by AFM, showing a surface roughness of ∼0.3 nm rms.

the layer-by-layer growth of $SrTiO_3$ [71, 108] and could be adapted to $BaTiO_3$ growth. This technique has however several drawbacks: First, the sample cannot be rotated which causes local inhomogeneities in film thickness and stoichiometry. These might be irrelevant for small substrate sizes as often used in research laboratories, but are generally not acceptable for larger wafers. Second, the off-stoichiometry is typically only visible after some oscillations corresponding to several atomic layers. Such delay is not acceptable for the growth of $BaTiO_3$ since the time during which the onset of a precipitate formation can be reversed is extremely short ($1 - 2$ ML).

During the $SrTiO_3$ growth, a surface reconstruction with x2 symmetry becomes visible when the upper layer is non-stoichiometric [30, 106]. The symmetry of this reconstruction differs between Ti-rich and Sr-rich conditions, and hence allows to adjust the fluxes with very short delay (∼1 ML). A similar reconstruction behavior is observed during the $BaTiO_3$ growth (fig. 2.20b). Notably, the unwanted $BaTiO_3$ surface reconstructions are visible even for fast rotating samples, are very sensitive to small deviations from stoichiometry, and can be used for adjusting the Δt instantaneously. Clearly, the utilization of this feedback mechanism works only for co-deposition, where a stoichiometric surface ideally should not show any reconstruction. In case of a layer-by-layer deposition, the surface oscillates between Ti-rich and Ba-rich conditions.

As a result of the shuttered co-deposition growth, the formation of precipitates is avoided even for 50 nm thick layers, and a very flat surfaces with a roughness

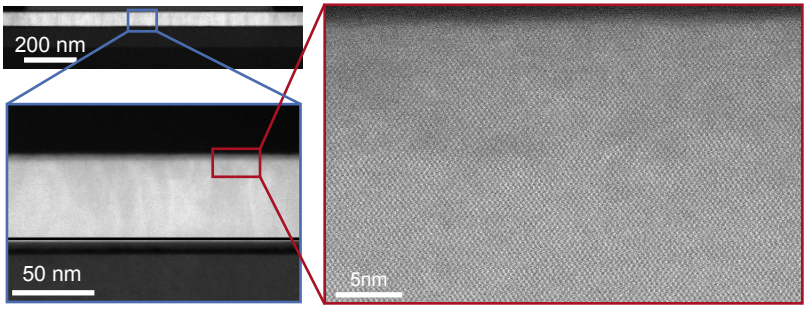

Fig. 2.22 Dark-field TEM images at various magnification levels of a 50 nm thick $BaTiO_3$ film grown via shuttered co-deposition. The film is very homogeneous and does not show any pores or islands.

of ∼0.3 nm rms and a reduced FWHM of the RC of $\Delta\omega_{BTO} = 0.74°$ is obtained (fig. 2.21) compared to the layer-by-layer deposition. The reduction of $\Delta\omega_{BTO}$ in that particular sample might also be related the utilization of $SrTiO_3$ seed layers grown with the multi-step crystallization method which yields higher $SrTiO_3$ crystalline quality (section 2.2). Nevertheless, the prevention of precipitate formation is a clear advancement to the layer-by-layer growth. Indeed, the HRTEM investigation fig. 2.22 shows a drastically improved $BaTiO_3$ quality, with no pores, no larger defects, and no island formation observable. The film appears very homogeneous in high as well as in coarse magnification, confirming the advancement of the shuttered co-deposition growth process.

2.3.3 Crystalline symmetry

Evolution of crystalline orientation The $BaTiO_3$ layers under investigation show tetragonal symmetry with the long *c*-axis oriented perpendicular to the film surface, confirmed by in- and out-of-plane XRD (fig. 2.12c) and HRTEM analysis (fig. 2.13). Previous reports claim that thin $SrTiO_3$ buffer layers lead to *a*-axis oriented $BaTiO_3$ [95] and that thicker $Ba_xSr_{1-x}TiO_3$ buffer layers ($10 - 30$ nm) are needed to obtain technologically interesting *c*-axis oriented films [41, 55, 99]. On the opposite, the present work shows that it is possible to obtain *c*-axis $BaTiO_3$ films for 4 nm-$SrTiO_3$ buffer layers, in agreement with recently published studies [48, 56]. To understand the origin of the crystalline orientations, the lattice parameters and resulting strain values are calculated for two special situations (details of the calculations in appendix B):

- The $BaTiO_3$ layer is assumed to be fully commensurate to the $SrTiO_3$

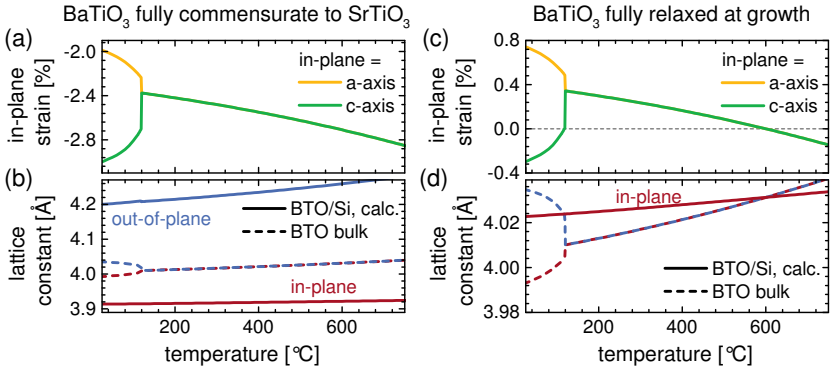

Fig. 2.23 Lattice parameters and strain values of $BaTiO_3$ on $SrTiO_3$/Si templates, calculated for two special cases. (a)/(b) $BaTiO_3$ fully commensurate to the $SrTiO_3$ layer which is assumed to be relaxed at the deposition temperature of 100 °C. (a) In-plane strain when the in-plane lattice parameter is the short (*a*-axis, yellow) or the long axis (*c*-axis, green) in the tetragonal phase. (b) In-plane lattice constant of the *c*-axis $BaTiO_3$ layer (solid red), out-of-plane parameter (solid blue) when the cell-volume is kept at the bulk value, and bulk $BaTiO_3$ lattice constants (dashed). (c)/(d) $BaTiO_3$ fully relaxed at the growth temperature of 600 °C. (c) In-plane strain and (d) lattice constants. No out-of-plane lattice parameter can be given at low temperatures to the formation of domains at the phase transition. In both cases the thermal expansion is determined by the silicon substrate, to which the $BaTiO_3$ and $SrTiO_3$ layers are clamped. Literature values are used to calculate the thermal expansion of $BaTiO_3$ [57, 109] and silicon [60] (appendix B).

buffer layer. The $SrTiO_3$ layer is considered to be relaxed at the deposition temperature of ∼100 °C, in agreement with the relaxed out-of-plane lattice constant for thin $SrTiO_3$ layers grown with the single crystallization process (fig. 2.10b). Slightly strained films as observed for different $SrTiO_3$ deposition conditions have only marginal influence on the following considerations.

Large strain levels of $\sim -2.7\%$ are present in the commensurate $BaTiO_3$ layer at the growth temperature of 600 °C, which are reduced while cooling down (fig. 2.23a). The strain is reduced when the smaller *a*-axis is oriented in-plane at the phase transition to the tetragonal phase, therefore a *c*-axis $BaTiO_3$ film establishes. As a consequence of the compressive in-plane strain, the *c*-axis would be strongly elongated compared to bulk crystals

(fig. 2.23b). In first approximation, when the volume of the $BaTiO_3$ unit cell is assumed to be bulk-like, the estimation of the out-of-plane lattice parameter shows a *c*-axis lattice constant of 4.20 Å at room temperature (fig. 2.23b). For a more realistic approximation, the change in the cell volume has to be taken into account. However, literature values for the Poisson's ratio defining this volume change are not available for $BaTiO_3$ at high growth temperatures [55].

- The $BaTiO_3$ layer is assumed to be fully relaxed at the growth temperature, and clamped to the buffer layer while cooling down. In that case, the strain level is reduced at the phase transition if the longer *c*-axis is oriented parallel to the surface (fig. 2.23c), resulting into an *a*-axis film (fig. 2.23d). In this case a simple approximation of the out-of-plane lattice constant is not possible when the crystal symmetry is considered to be tetragonal with one long *c*-axis: Both the *a*- and the *c*-axis lattice parameter are influenced by the clamping at the phase transition from cubic to tetragonal. The formation of crystalline domains rotated by 90° occurs, as discussed below. As a consequence, both lattice parameters are strongly correlated due to local strain fields, which prohibits a simple separation between *a* and *c*, unlike to *c*-axis films.

In both cases, the thermal expansion is assumed to be determined by the expansion of the silicon substrate to which the perovskite layers are clamped. A possible bending of the wafer to reduce the strain is neglected. Thin $BaTiO_3$ layers grow commensurately to the $SrTiO_3$ layer (fig. 2.13), but form edge dislocations at the $BaTiO_3/SrTiO_3$ interface to accommodate for the large lattice mismatch [56]. The $BaTiO_3$ layers are still strained compared to bulk crystals, and start to relax by forming defects above the critical thickness. This thickness was calculated by Vaithyanathan *et al.* as ∼2 nm for $BaTiO_3$ at 600 °C with in-plane strain of 2.7 % relative to the $SrTiO_3$ layer [55]. In their work [55] a thicker $Ba_xSr_{1-x}TiO_3$ buffer with larger lattice constant was required to reduce the strain to < 1 % in order to increase the critical thickness to ∼10 nm.

The reason for the reduced buffer thickness needed to obtain *c*-axis films in the current work might be the higher defect density in the $SrTiO_3$ and $BaTiO_3$ layers (FWHM of the $BaTiO_3$-RC: $\Delta\omega_{BTO} = 0.7° - 2.1°$, figs. 2.12 and 2.21) compared to the previous study ($\Delta\omega_{BTO} = 0.38°$ [55]). The defects in the $SrTiO_3$ layer might serve as centers to release strain in the $BaTiO_3$ layer at the $BaTiO_3/SrTiO_3$ interface while still maintaining a commensurate growth. The critical thickness could thus be larger than 2 nm. This conclusion is in agreement with observations of *c*-axis $BaTiO_3$ on 5 nm-thick $SrTiO_3$ buffer layers on silicon by Niu *et al.* [48], who measured FWHMs of the rocking curves

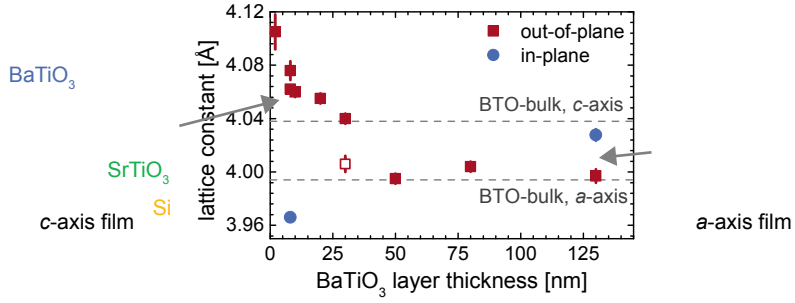

Fig. 2.24 Out-of-plane (red) and in-plane (blue) lattice parameter of $BaTiO_3$ films on $SrTiO_3$/Si grown via MBE with a critical thickness of ∼30 nm. The in-plane parameter shown for the 130 nm data point corresponds to the larger parameter when deconvoluting the data (fig. 2.25c) with two peaks. The open red square shows a second peak visible at a thickness of 30 nm, indicating a transition regime with both *a*- and *c*-axis domains. The dashed lines correspond to the bulk lattice constants. The illustrations show a *c*-axis and an *a*-axis film, respectively, where white arrows indicate the direction of the ferroelectric polarization which is parallel to the crystalline *c*-axis.

of $\Delta\omega_{BTO} = 0.7°$, which are similar to the current work and larger than those observed by Vaithyanathan *et al.* [55].

In order to experimentally determine the critical thickness, the out-of-plane lattice parameter of several $BaTiO_3$ films is measured as a function of the film thickness (fig. 2.24). Here, the critical thickness is referred to the $BaTiO_3$ layer thickness where a transition from *c*-axis to *a*-axis orientation occurs. A relaxation of the highly strained *c*-axis out-of-plane lattice constant for very thin layers (< 8 nm) is visible for an increasing film thickness up to ∼20 nm. The relaxation occurs by forming edge-dislocations (fig. 2.14) to release the large strain. For thicknesses > 50 nm, the out-of-plane lattice constant is equal to the bulk *a*-axis parameter. The *a*-axis orientation matches the expectations for thick films that grow relaxed at the high deposition temperature (fig. 2.23). The experimentally determined "critical thickness" for the transition from *c*-axis to *a*-axis oriented layers is ∼30 nm. Consistent with the behavior of the out-of-plane lattice constant, the in-plane parameter changes from *a*-axis-like in thin films to *c*-axis-like for films above the critical thickness (fig. 2.24). A fraction of $BaTiO_3$ domains with *c*-axis orientation might be present at the $BaTiO_3/SrTiO_3$ interface even for thicker *a*-axis films, as indicated by geometrical phase analysis of HR-STEM images in a recent study of identical

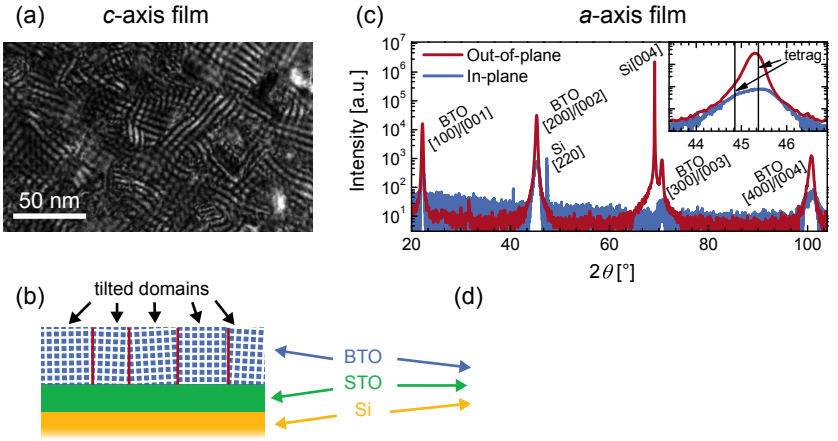

Fig. 2.25 (a) Plan-view TEM image of a 20 nm thick *c*-axis $BaTiO_3$ film showing a Moire pattern with domain sizes in the order of $10 - 50$ nm, which are illustrated in (b) as slightly tilted crystalline regions. (c) XRD diagram of a 130 nm-thick *a*-axis $BaTiO_3$ film. The inset shows a magnification of the $BaTiO_3$ as [200]/[002] peak obtained with out-of-plane and in-plane geometries. The in-plane peak is a convolution of the diffraction peaks corresponding to the *a*-axis and the *c*-axis. The vertical lines show the bulk values of tetragonal $BaTiO_3$ [58]. (d) Illustration of the domain structure in an *a*-axis film, with randomly oriented spontaneous polarization associated with the direction of the *c*-axis (white arrows in blue cuboids).

$BaTiO_3/SrTiO_3/Si$ layer stacks [56].

Domain structure Epitaxial thin films consist of many crystalline domains, which are slightly misoriented regions in the crystal. The size of these domains is assessed by imaging the Moire pattern created by the perovskite and silicon crystalline lattice for a 20 nm thick *c*-axis $BaTiO_3$ film (fig. 2.25a). The size of homogeneous areas in the Moire pattern indicates single domains with a typical size of $\sim 10 - 50$ nm. Figure 2.25b illustrates the slightly tilted crystal lattice between adjacent domains in a cross-sectional view. In plan-view geometry (not shown) the domains would be slightly rotated in respect to each other.

For thicker *a*-axis films, domains have inevitably to be formed even when any tilted domains could be avoided by perfect growth conditions: Because the template for the epitaxial growth is a cubic Si substrate, two equivalent

orientations of the elongated tetragonal *c*-axis exist. By forming domains in which the *c*-axis is rotated by 90° within the plane of the film, strain fields originating from the mismatch between the cubic Si and tetragonal $BaTiO_3$ lattice are compensated. The existence of two orthogonal domains is evidenced in a 130 nm thick $BaTiO_3$ film by the presence of the convoluted $[200]_{BTO}$ and $[002]_{BTO}$ diffraction peaks in the grazing incidence XRD data (fig. 2.25c). As no intentional miscut is present in the substrates, the population ratio of these domains is assumed to be 1:1 for symmetry reasons. The schematics of domains in an *a*-axis film (fig. 2.25d) also indicates the ferroelectric polarization of each domain (white arrows), which does not necessarily coincide with the structural domains [110]. The Moire pattern analysis for the thicker sample did not reveal distinct, domain-like areas, which prohibits a domain size assessment.

2.4 Hybrid growth of barium titanate via rf-sputtering

Due to the low deposition rate during the MBE growth (∼50 nm/h), and the requirements of films with thicknesses of several 100 nm for many applications (section 2.1), a hybrid growth approach to increase the thickness of the layers with commercially available deposition methods is developed[3]. This approach combines seed layers of $BaTiO_3$ and $SrTiO_3$ epitaxially grown on Si-substrates as described in sections 2.2 and 2.3 with rf-sputtering. Indeed, the epitaxial relationship to the silicon substrate is maintained even for larger thicknesses of > 100 nm.

2.4.1 Experimental details of the hybrid growth

After growing MBE seed layers, thicker $BaTiO_3$ layers are successively deposited by rf-sputtering at 300 W and 10^{-5} bar of Ar atmosphere containing 20 % O_2. The substrate temperature is varied in different sputtering experiments between 500 °C and 600 °C, the latter one being the maximum temperature permitted in the tool. The sputtering conditions for a reference sample without any seed layer are slightly modified: The first 10 nm of $BaTiO_3$ are sputtered in Ar atmosphere to avoid oxidation of the HF-cleaned silicon surface. The remaining 90 nm are deposited with the same conditions as described above.

3 The content of this chapter has been published in *Nanotechnology* [111]. Text excerpts and figures are reproduced by permission of IOP Publishing Limited.

To study the impact of the seed layer on the crystallinity of the sputtered layer, $BaTiO_3$ films of ∼100 nm thickness are sputtered

- directly onto a bare Si substrate at 500 °C and subsequently annealed at 650 °C
- onto MBE-$SrTiO_3$/Si seed layers with a MBE-$SrTiO_3$ thickness ranging from 4 nm to 12 nm
- onto MBE-$BaTiO_3$/4 nm MBE-$SrTiO_3$/Si seed layers with a MBE-$BaTiO_3$ thickness ranging from 2 nm to 20 nm.

For investigating the influence of the annealing conditions on the films, samples sputtered at $T = 500$ °C are annealed in atmospheric pressure of O_2 for 20 min at different temperatures, varying from 500 °C to 725 °C.

2.4.2 The role of the MBE seed layer

$BaTiO_3$ layers sputtered directly onto a Si substrate at 500 °C are amorphous. After a subsequent anneal in oxygen at 650 °C, they become polycrystalline with randomly oriented grains, as inferred from the relative peak intensities of the $\theta - 2\theta$ scan (fig. 2.26a, grey curve): A strong [110] peak is visible, similar to polycrystalline $BaTiO_3$ ceramics [58]. Likely, the formation of SiO_2 during sputtering prevents atomic ordering on the Si surface and hinders epitaxial growth during the post-sputter-deposition anneals.

A different behavior is observed for $BaTiO_3$ films sputtered and annealed onto MBE-$BaTiO_3$/$SrTiO_3$ seed layers. When sputtered and annealed onto seed layers thinner than about 6 nm, the $BaTiO_3$ consists of a majority of epitaxial [00l] domains, although domains with different orientations, for example [110], are also observed (fig. 2.26a, green curve). The situation improves for thicker seed layers. After sputtering at 500 °C onto a 8 nm $BaTiO_3$/4 nm $SrTiO_3$ template (fig. 2.26a, red curve), partially crystalline samples presents only epitaxial [00l] diffraction peaks. After annealing at 650 °C, the amount of the crystalline epitaxial phase increases and no crystalline orientations other than [00l] (or [h00]) are observed (fig. 2.26a, blue curve). $BaTiO_3$/$SrTiO_3$ seed layers with a total perovskite thickness between 6 and 24 nm behaves the same. In addition, as seen in fig. 2.26b, a $BaTiO_3$ film sputtered onto a single 12 nm $SrTiO_3$ seed layer behaved similarly to one sputtered onto a mixed 8 nm $BaTiO_3$/4 nm $SrTiO_3$ seed layer. Namely, for the same seed layer total thickness, $BaTiO_3$ layers sputtered on either $SrTiO_3$ or $BaTiO_3$ termination shows only [00l]/[h00] crystallographic directions with similar out-of-plane lattice constants.

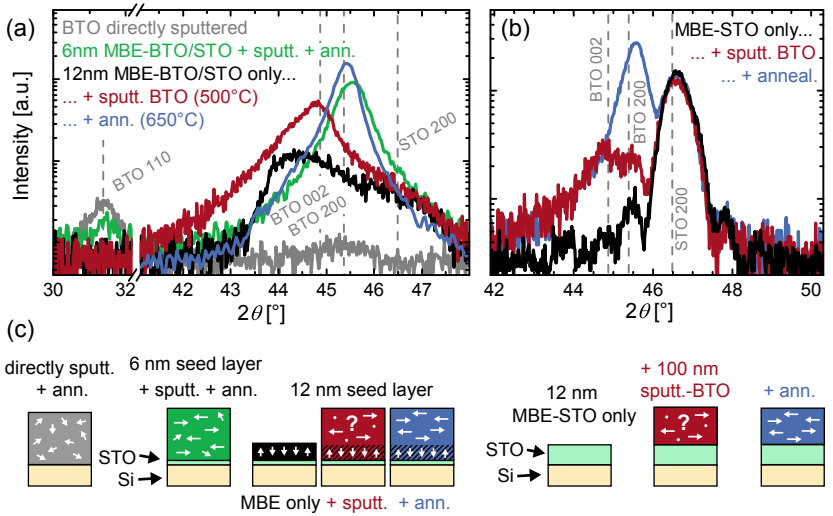

Fig. 2.26 (a) $\theta - 2\theta$ scans of 100 nm $BaTiO_3$ (i) sputtered-and-annealed on a bare Si substrate (grey), (ii) sputtered-and-annealed on a 2 nm $BaTiO_3$/4 nm $SrTiO_3$ seed layer (green), (iii) sputtered on a 8 nm $BaTiO_3$/4 nm $SrTiO_3$ MBE seed layer at 500 °C (red) and subsequently annealed at 650 °C (blue). The black curve is a 8 nm $BaTiO_3$/4 nm $SrTiO_3$ MBE seed layer only. (b) $\theta - 2\theta$ scans of 100 nm $BaTiO_3$ sputtered onto a 12 nm MBE-$SrTiO_3$ seed layer at 500 °C (red) and annealed at 650 °C (blue) (visualized in the schematics). The black curve is the $SrTiO_3$ seed only. (c) Schematics of the crystalline structure of the samples. The white arrows indicate the orientation of the $BaTiO_3$ *c*-axis.

The epitaxial relationship between $BaTiO_3$ and Si is confirmed by in-plane grazing incidence diffraction experiments discussed in section 2.4.5. A noticeable variability is found in the sputtering process, with some as-sputtered samples being amorphous and some partially crystalline. Indeed, since the sputtering temperature is close to the crystallization temperature for $BaTiO_3$ thin films, small variations in the deposition conditions might have a significant influence on the as-sputtered samples. Because air exposure between the MBE and sputtering processes may also have an impact, the time elapsed between the two steps is kept minimal. However, although some variations are visible at this intermediate stage, the samples behaves identical after the final annealing step.

The comparison of different seed layers shows that thin perovskite seed layers

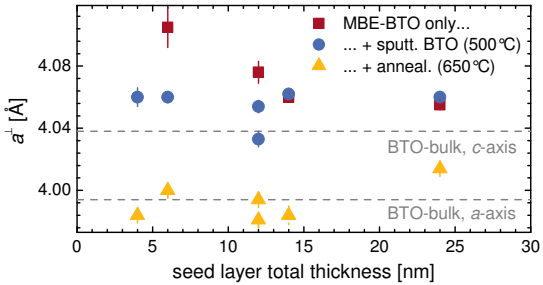

Fig. 2.27 Out-of-plane lattice constant $a^{\perp}$ as a function of the seed layer total thickness (4 nm $SrTiO_3$ + 0 − 20 nm $BaTiO_3$) for MBE-$BaTiO_3$ only (red squares, measured before sputtering), for 100 nm $BaTiO_3$ sputtered at 500 °C (blue circles), and for 100 nm sputtered $BaTiO_3$ annealed at 650 °C for 20 min in O_2 (yellow triangles).

strongly favor epitaxial $BaTiO_3$ growth during the hybrid deposition process. In particular, such layers prevent the formation of any randomly oriented phases when thicker than ∼4 nm. Due to the chemical similarity between $SrTiO_3$ and $BaTiO_3$ and due to the same in-plane lattice constant for thin, strained layers (see section 2.4.5), both seed layer terminations show a similar behavior.

2.4.3 Effect of seed layer thickness

As can be inferred from the [002]/[200] diffraction peaks reported in fig. 2.26a, the out-of-plane lattice constant $a^{\perp}$ of the initial 8 nm thick MBE-$BaTiO_3$ layer (black curve) is close to the bulk $BaTiO_3$ *c*-axis value (table 2.1). The out-of-plane orientation of $BaTiO_3$ can then be described as $[001]_{BTO} \parallel [001]_{Si}$, (*c*-axis-oriented $BaTiO_3$, $a^{\perp} = c$). In contrast, the as-sputtered $BaTiO_3$ layer (red curve) is found to be only partially crystalline and it is not possible to unambiguously define whether $BaTiO_3$ is tetragonal or cubic or a mixture of the two phases.

After an oxygen anneal at 650 °C, the total $BaTiO_3$ peak area increases, which can be attributed to the crystallization of the amorphous parts of the sputtered layer (fig. 2.26). Additionally, $a^{\perp}$ shrinks to a value closer to the bulk $BaTiO_3$ *a*-axis value (table 2.1 and fig. 2.27) and is clearly different from the bulk cubic lattice parameter ($a_{cub} = 4.031$ Å [112]). For a tetragonal crystal symmetry with one long *c*-axis, the orientation of the layer is described by $[001]_{BTO} \parallel [100]_{Si}$ (*a*-axis oriented $BaTiO_3$, $a^{\parallel} = c$). The amorphous part of

the 100 nm-thick sputtered $BaTiO_3$ layers crystallizes in a relaxed phase at the high annealing temperature. As discussed in section 2.3.3, due to the thermal expansion coefficient mismatch between $BaTiO_3$ and the silicon substrate, *a*-axis films are formed during cooling down. As shown later, the initially *c*-axis oriented $BaTiO_3$ does not relax during the anneal, maintaining its tetragonal *c*-axis orientation (schematics in fig. 2.26c).

The evolution of $a^{\perp}$ of the $BaTiO_3$ layers as function of the total seed layer thickness for a fixed sputtering temperature of 500 °C and post-annealing temperature 650 °C is reported in fig. 2.27. The seed layers consist of 4 nm MBE-$SrTiO_3$ and MBE-$BaTiO_3$ of variable thickness, while the thickness of the sputtered $BaTiO_3$ layer is kept at 100 nm. The partially crystalline as-sputtered layers (circles) are most likely *c*-axis oriented, whereas the fully crystallized annealed layers (triangles) are clearly *a*-axis oriented. This orientation is observed for all sputtered $BaTiO_3$ layers, independent of the thickness of the initial seed layer. As discussed in section 2.3.3, all MBE-$BaTiO_3$ layers (squares) in the thickness range $2 - 20$ nm are *c*-axis oriented.

2.4.4 Effects of post-deposition annealing

In order to follow the impact of the annealing temperature on the crystalline structure of the sputtered $BaTiO_3$, $\theta - 2\theta$ scans are acquired on the same sample after successively annealing steps in oxygen. The scan range includes the $[110]_{BTO}$ peak, which is the strongest diffraction peak in randomly oriented domains [58]. Only [00l] (or [h00]) diffraction peaks are observed for all annealing temperatures. The out-of-plane lattice constant $a^{\perp}$ changes monotonously from bulk *c*-axis to bulk *a*-axis values between 300 °C and 650 °C, saturating at $T \approx 650$ °C (fig. 2.28). Similarly, the area of the $[00l]_{BTO}/[h00]_{BTO}$ diffraction peaks increases and saturates in the same temperature range. As seen from the reduction of the FWHM of the $BaTiO_3$ rocking curves from $\Delta\omega_{BTO} \sim 4°$ to $\sim 2°$ (fig. 2.28), the overall crystalline quality of the $BaTiO_3$ layers increases during the annealing step. These observations show that an annealing step at $T \geq 650$ °C is required in order to fully crystallize the $BaTiO_3$ layers sputtered at 500 °C.

2.4.5 Micro-structure and strain analysis

A deeper characterization of the crystalline structure and morphology of a 100 nm thick $BaTiO_3$ layer (i) sputtered at 500 °C and (ii) subsequently annealed at 650 °C, as well as (iii) directly sputtered at 600 °C is performed by cross correlating in-plane and out-of-plane XRD with HRTEM data. The seed layer of all three samples is 8 nm $BaTiO_3$/4 nm $SrTiO_3$ grown by MBE.

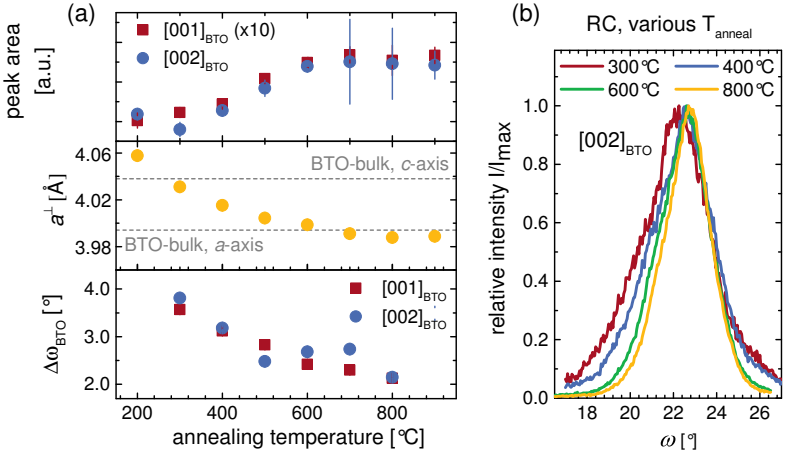

Fig. 2.28 (a) Area of the $[002]_{\mathrm{BTO}}$ and $[004]_{\mathrm{BTO}}$ diffraction peaks, out-of-plane lattice parameter $a^{\perp}$, and FWHM of the $BaTiO_3$-rocking curves $\Delta\omega_{\mathrm{BTO}}$ as function of post-sputter annealing temperature for a 100 nm $BaTiO_3$ film sputtered at 500 °C onto 8 nm $BaTiO_3$/4 nm $SrTiO_3$ MBE seed layer. The sample is kept at each temperature in O_2 for 20 min, and subsequently cooled down to room temperature for the measurements. (b) $[002]_{\mathrm{BTO}}$ rocking curves for various annealing temperatures.

The amorphous $BaTiO_3$ film of the sample sputtered at 500 °C could not be investigated as it was milled away during the sample preparation, and mainly the MBE grown seed layers remained. The remaining 8 nm-thick $BaTiO_3$ layer is tetragonal and *c*-axis oriented, in agreement with the characteristics of MBE-grown $BaTiO_3$ layers discussed in section 2.3.3. Consistently, the x-ray diffraction data of that particular sample shows a main peak originating from the tetragonal *c*-axis MBE-$BaTiO_3$, and the less intense one from the MBE-$SrTiO_3$ (fig. 2.29a, red curve). The in-plane XRD data shows only one clear peak, which corresponds to the smaller $a^{\parallel}$ of the $BaTiO_3$ and $SrTiO_3$ layer.

Three components are needed to fit the out-of-plane diffraction peak after the annealing step (fig. 2.29a, blue curve): the main one corresponding to *a*-axis $BaTiO_3$, the second one to *c*-axis $BaTiO_3$, and the third one to $SrTiO_3$. The three components suggest that the sample consists of a mainly tetragonal *a*-axis $BaTiO_3$ film mixed with some minor *c*-axis areas. Consistently, the in-plane peak (fig. 2.29b, blue curve) can be deconvoluted into two components, one

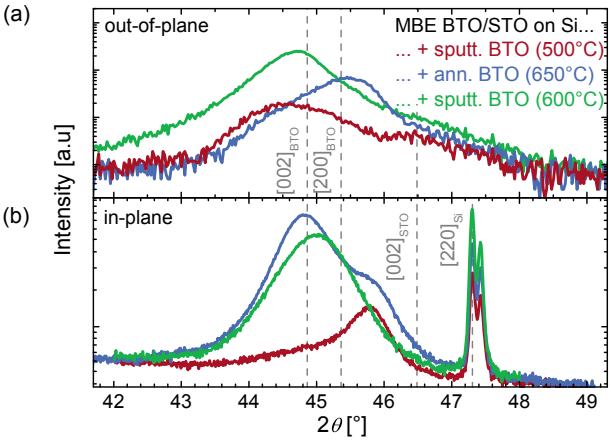

Fig. 2.29 (a) Out-of-plane and (b) in-plane $\theta - 2\theta$ scans of 100 nm $BaTiO_3$ sputtered onto a 8 nm $BaTiO_3$/4 nm $SrTiO_3$-MBE seed layer at 500 °C (red) and annealed at 650 °C (blue), or alternatively sputtered at 600 °C (green).

corresponding to the $BaTiO_3$ c-axis, and one corresponding to both the $BaTiO_3$ a-axis and the $SrTiO_3$ with same $a^{\parallel}$. Likely, the initial $BaTiO_3$ seed layer keeps its c-axis orientation, while the sputtered-and-annealed $BaTiO_3$ is mainly a-axis oriented. As discussed in section 2.3.3, the a-axis orientation originates from the relaxed growth above the critical thickness of ∼30 nm. Consistently, the average c/a-ratio in the sputtered-and-annealed sample decreases with respect to the MBE-$BaTiO_3$ (table 2.2), since the strain due to the lattice mismatch between the Si-substrate and the perovskite layers is reduced in relaxed films.

Table 2.2 Summary of the $BaTiO_3$ lattice constants as extracted from the XRD data. Values in bold correspond to the main component. Bulk lattice constants for comparison are given in table 2.1.

sample	$BaTiO_3$ $a^{\perp}$ [Å]		$BaTiO_3$ $a^{\parallel}$ [Å]		c/a
+ sputtered (500 °C)	**4.062**		**3.966**		1.024
+ sputtered (500 °C) + ann. (650 °C)	**3.984**	4.033	**4.042**	3.966	1.015
+ sputtered (600 °C)	**4.054**		**4.035**		1.005

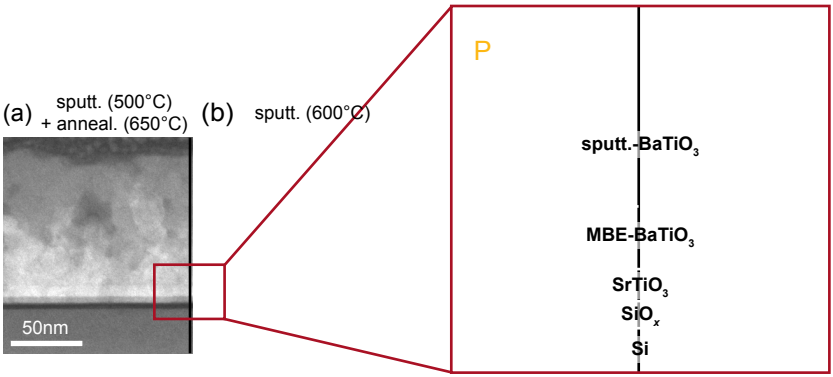

Fig. 2.30 Low-magnification and high-resolution HAADF-STEM images of (a) 100 nm $BaTiO_3$ sputtered at 500 °C and annealed at 650 °C. (b) 100 nm $BaTiO_3$ sputtered at 600 °C onto the same 8 nm $BaTiO_3$/4 nm $SrTiO_3$-MBE seed layer. "P" indicates a pore (area of darker contrast).

The cross-sectional HAADF-STEM image in fig. 2.30a reveals that the sputtered-and-annealed $BaTiO_3$ film is epitaxial but consists of many domains slightly misoriented, in particular in the upper part of the film. Porosity is occasionally visible as areas of darker contrast, but without any amorphous phase inside the pores.

The cross-sectional HAADF-STEM image of the sample sputtered at 600 °C (fig. 2.30b) exhibits a different morphology: The layer consists of nano-crystalline domains with sizes smaller than 5 nm and with small misorientation. Notably, no porosity is observed. However, the electron diffraction patterns (not shown) display no peak splitting, indicating the presence of a mainly cubic phase, or a tetragonal phase with little tetragonality. The tetragonal crystalline structure is indeed confirmed by the XRD data with $BaTiO_3$ peaks for the out-of-plane and in-plane diagram at different, but very close positions (fig. 2.29, green curves). The strong reduction of the tetragonality with almost cubic c/a-ratio (table 2.2) is likely caused by the formation of nano-domains and may originate from interface effects [97], and from the change of the Ti bonding character observed in small grains [98]. It is shown in ref. [97] that large stress fields can establish in small domains favoring the formation of a cubic phase, thus reducing the tetragonality. Such stabilization is thermodynamically explained by the "internal stress model" by Buessem *et al.* [113].

Stress at the MBE-$BaTiO_3$/sputtered $BaTiO_3$ interface could for the same

reasons influence the crystalline quality of the atomic layers at that interface. The interfacial region is clearly visible in fig. 2.30 between the MBE-$BaTiO_3$ and the sputtered $BaTiO_3$ layers. The contrast between these layers originates from differences in density and overall crystalline quality. However, despite the high resolution, any different crystalline phase at this interfacial region could not be determined.

In summary, the morphology and crystalline structure of the sputtered $BaTiO_3$ films on epitaxial seed layers is strongly dependent on the sputtering conditions: Depositing amorphous layers at rather low temperatures ($T = 500\,^{\circ}\mathrm{C}$) with an additional post-deposition annealing step creates tetragonal a-axis oriented and partially porous layers with epitaxial relationship to the silicon substrate. In contrast, layers sputtered at temperatures high enough to directly crystallize the $BaTiO_3$ layer ($T = 600\,^{\circ}\mathrm{C}$) show no pores, but epitaxially crystallize in a tetragonal phase with strongly reduced c/a-ratio. This reduced tetragonality most likely originates in the formation of nano-scale domains. Such formation does not occur in the solid phase epitaxy process when crystallizing the amorphous layer during the post-deposition anneal. The epitaxial relationship of the $BaTiO_3$ films with well-defined crystalline structure, tetragonal symmetry, and a thickness of $\geq 100\,\mathrm{nm}$ makes the layers grown with the hybrid growth process well-suited for devices that rely on the functional properties of barium titanate, such as piezo-electric and electro-optic applications.

2.5 Functional properties of barium titanate films

2.5.1 Electrical properties

Resistivity Bulk $BaTiO_3$ is an excellent electric insulator at room temperature with resistivity values of $\rho > 10^{12}\,\Omega\,\mathrm{cm}$ [114, 115]. However, doping with small amounts of foreign atoms such as La or Nb can increase the electron concentration and consequently reduce ρ by several orders of magnitude ($\rho \approx 10^{-2}\,\Omega\,\mathrm{cm}$ for 0.1 % of Nb doped $BaTiO_3$ [116]). In MBE-grown films with little impurity concentration, the conductivity is mainly determined by the concentration of oxygen vacancies [117] that can act as electron donors and can thus have a significant impact on the resistivity [118–120]. MBE is in particular prone to the formation of oxygen vacancies due to the low oxygen pressures used during the deposition.

In most applications utilizing the functional properties of $BaTiO_3$, including electro-optic devices, a highly conductive $BaTiO_3$ layer is detrimental. The current-voltage characteristics of a 8 nm-$BaTiO_3$/4 nm-$SrTiO_3$/Si layer stack

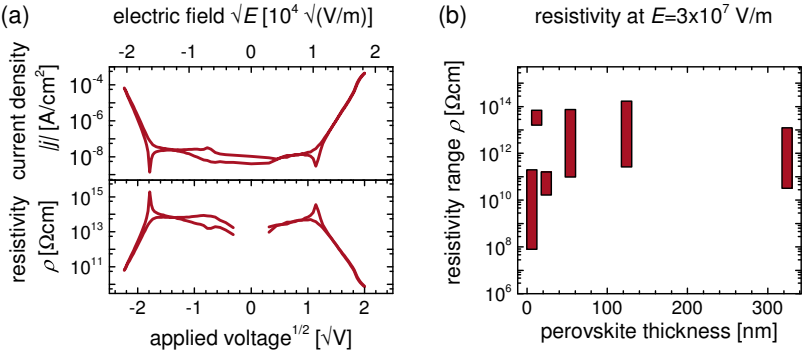

Fig. 2.31 (a) Exemplary $j(\sqrt{V})$ and resistivity curve of a 8 nm-$BaTiO_3$/4 nm-$SrTiO_3$/Si sample. The current is normalized to the size of the electrical pad (diameter of 225 µm). (b) Resistivity ranges at the same electric field $E = 3 \times 10^7$ V/m measured for various MBE-grown samples with different thicknesses d. Samples with $d > 100$ nm are grown with the hybrid growth approach (section 2.4).

shows low current densities of $|j| < 100\,\mathrm{nA/cm^2}$ for small applied voltages ($|V| < 2$ V) (fig. 2.31a). The actual current density is below the measurement range of the experimental setup. The resistivity is bulk like ($\rho > 10^{13}\,\Omega$ cm, fig. 2.31a). This is an improvement over previous studies reporting much lower resistivitiy values ($\rho < 10^9\,\Omega$ cm at 2 V for 50 nm thick, undoped $BaTiO_3$ films grown by MBE) [117]. The difference might originate from a more efficient oxygen plasma in the MBE reactor used in the current work, which results in a better oxidation of Ba and especially of Ti during the growth.

At larger electric fields, the transport mechanism in ferroelectric films is typically described by either the Poole-Frenkel or the Schottky-emission conduction [121, 122]. In both cases the current density j is exponentially dependent on the square root of the applied field E, or the applied voltage V:

$$j \propto \exp\left(\sqrt{E}\right) \propto \exp\left(\sqrt{V}\right) \tag{2.1}$$

Such behavior is observed in the $BaTiO_3$ layer for electric fields $E > 2 \times 10^8$ V/m as seen in the linear slop when plotting $j(\sqrt{V})$ (fig. 2.31a). $BaTiO_3$ films of different thicknesses between 6 and 320 nm show consistently high resistivity values at high electric fields (fig. 2.31b). The data is determined from different electrical pads and samples. The large scattering of the values (as indicated by

the bar-diagram) might be caused by not uniformly distributed pin-holes that lead to locally higher current densities.

Concluding the I/V analysis, all $BaTiO_3/SrTiO_3/Si$ samples are very resistive similar to bulk-crystals. The high resistivity confirms a low oxygen deficiency in the films even though the samples are grown at rather low oxygen partial pressures compared to the fabrication of single crystals. The $BaTiO_3$-layers are therefore well-suited for applications relying on their functional properties. The properties between $BaTiO_3$ and $SrTiO_3$ could not be separated in the experiments.

Permittivity Depending on microstructure and composition, the relative permittivity ϵ of $BaTiO_3$ can reach very high values of $\epsilon > 10^4$ close to the Curie temperature $T_C = 120\,°C$ and $\epsilon > 10^3$ at room temperature [64, 113, 114, 123]. The permittivity is of great significance when designing the electric field distribution for integrated devices (section 4.3.4) and is therefore experimentally determined via capacitance-voltage measurements in MOS structures (fig. 2.32a): Since p-doped silicon substrates are used, an accumulation of charge carriers at the semiconductor-oxide interface is reached for a negative gate bias [83]. From the corresponding capacitance C_{acc}, the relative permittivity ϵ_{ox} of the oxide can be determined via

$$C_{acc}/A = \epsilon_0 \cdot \epsilon_{ox}/d_{ox} \tag{2.2}$$

Here, d is the thickness of the film and ϵ_0 the vacuum permittivity. The ∼3 nm thick SiO_2 layer between the perovskite layer and the silicon (fig. 2.15) contributes to the measured capacitance and has to be taken into account when extracting the perovskite properties. Using $\epsilon_{SiO_2} = 3.9$ [36], the average permittivity of the $BaTiO_3/SrTiO_3$ layer stack of a 8 nm-$BaTiO_3$/4 nm-$SrTiO_3$/p-Si sample (fig. 2.32a) is calculated as $\epsilon_{per} = 35.2$, which is significantly lower than values for bulk $BaTiO_3$ ceramics [113]. The determination of the permittivity is very sensitive to the SiO_2-thickness estimation: The assumption of a 3.5 nm-thick SiO_2 layer results in a significantly higher permittivity value of $\epsilon_{per} = 56.3$.

A clear trend to an increasing permittivity for larger film thicknesses is visible, with a saturation at $\epsilon_{per} \sim 150$ (fig. 2.33). This trend, and in particular the small permittivity values for thin films ($d < 50$ nm) are consistent with the by more than one order of magnitude smaller permittivity along the c-axis compared to the a-axis-permittivity of $BaTiO_3$ [64]. The structural analysis revealed the transformation from low-permittivity-c-axis to high-permittivity-a-axis films for an increasing thickness (fig. 2.24). The permittivity values are in agreement with other reports of nanometer-scaled $Ba_xSr_{1-x}TiO_3$ layers [123]

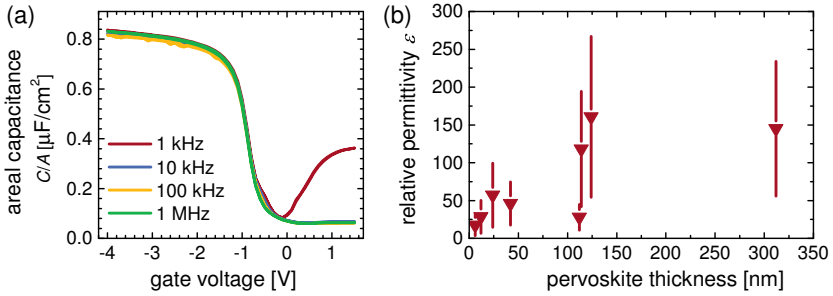

Fig. 2.32 (a) C/V characteristics of a 8 nm-$BaTiO_3$/4 nm-$SrTiO_3$/p-Si layer stack measured at different frequencies. The capacitance is normalized to the electrode area of $4 \times 10^{-4}\,cm^2$. (b) Mean permittivity of the $BaTiO_3$/$SrTiO_3$ perovskite layer stack for different film thicknesses assuming a 3 nm-thick SiO_2 layer at the $SrTiO_3$/Si interface. The error bars indicate the variation of the extracted permittivity when changing the SiO_2-thickness by ± 0.5 nm.

and provide a good data set for device simulations.

In order to separate the properties of $BaTiO_3$ and $SrTiO_3$, a systematic study would be required where both layer thicknesses are varied independently. In particular, $SrTiO_3$-films without any additional $BaTiO_3$ have to be characterized to determine ϵ_{STO}. Due to the thickness dependency of the permittivity of the perovskite layers, no separation is possible with the current data.

Finally, the similar C/V behavior at different frequencies (fig. 2.32a) indicates little trapping of charges at the interfaces or inside the oxide layer [36]. The deviation of the low-frequency data at positive gate bias is expected when reaching the inversion regime at the interface [83].

Ferroelectricity The capacitance-voltage characteristic of metal/ferroelectric/-insulator/semiconductor (MFIS) structures are expected to show a hysteresis behavior [124, 125], which has also experimentally been observed [126]. Importantly, the sense of orientation is counter-clockwise for p-doped substrates when cycling the gate bias. In contrast, a clockwise hysteresis is often observed in MOS structures on p-substrates, which can be attributed to positive, fixed charges that are trapped at or de-trapped from the oxide/semiconductor interface [36].

The $BaTiO_3$/$SrTiO_3$/SiO_2/p-Si films are also MFIS structures, and a counter-clockwise hysteresis would be expected. Most of the investigated samples show C/V curves similar to those shown in fig. 2.32, without any considerable

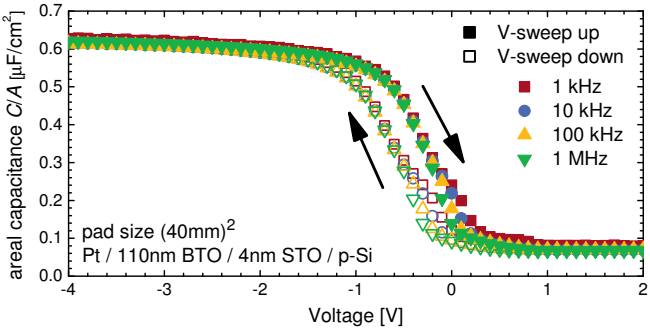

Fig. 2.33 C/V curve of a sputtered $BaTiO_3$ film of 110 nm thickness on top of 4 nm $SrTiO_3$/p-Si with an electrode size of $40 \times 40\,\mu m^2$. The counter-clock wise hysteresis loop indicates a ferroelectric behavior of the film.

hysteresis. However, some pads show a counter-clockwise hysteresis (fig. 2.33) which can be attributed to a ferroelectric behavior of the $BaTiO_3$ layer. There are several possibilities why such behavior is typically not seen for the samples:

- The $BaTiO_3$ layer is not ferroelectric. This can occur in thin films due to strong depolarization fields [127, 128], in particular when the ferroelectric material is not sandwiched between two metals but rather in contact with a dielectric. The latter is the case for the samples under investigation where the $BaTiO_3$ is grown on top of a dielectric $SrTiO_3/SiO_2$-layer.
- The hysteresis voltage is too small to be detected. Assuming the coercive field of bulk-BTO of 0.5 kV/cm, the switching voltage of a 20 nm thick perovskite layer is only 1 mV. Even taking into account the voltage drop over a 3 nm thick SiO_2 layer, the coercive voltage is still only 3 mV, and thus probably smaller than effects caused by trapped charges. On the other hand, the coercive field in thin films is typically increased by several orders of magnitude compared to bulk [127] which would raise the switching voltages.
- Leakage due to too large metalic pads might cause a de-charging of both electrodes, thus depolarizing the film.
- Only *c*-axis films should show out-of-plane ferroelectric behavior, which is in contradiction with the observations from fig. 2.33. However, the initial *c*-axis MBE-layer is still present even for thicker *a*-axis films as shown by Dubourdieu *et al.* [56] (see fig. 2.26).

Additional polarization-voltage measurements could not confirm the ferroelectricity in the films. By means of electro-optical characterization, the ferroelectricity is however unambiguously confirmed for *a*-axis films (section 3.4.4). The reason why most electric measurements performed on the films do not show ferroelectric behavior might indeed be the large voltage drop across the SiO_2 layer in combination with a strongly enhanced coercive field, which hinders domain switching at voltages accessible in the experiments.

2.5.2 Piezo-electric properties

The ferro- and piezoelectric properties of the $BaTiO_3$ thin films with different thicknesses and thus different crystalline orientations are investigated by means of PFM. In particular, a 30 nm-thin, MBE-grown film with mainly *c*-axis domains, and a 108 nm *a*-axis film, fabricated with the hybrid deposition process, are investigated. The thick film is sputtered at 500 °C and afterwards annealed at 650 °C. Details of the layer stacks are visualized in fig. 2.34.

When applying an electric field to $BaTiO_3$, ferroelectric domains whose polarization is parallel to the field can be flipped [129], whereas domains whose polarization is orthogonal to it keep their polarization state. During the PFM measurements, the applied electric field is perpendicular to the surface of the sample, resulting into a different PFM response between the two domain types: *c*-axis domains are exposed to a field parallel to their spontaneous polarization, and are therefore switchable. The amplitude of the PFM signal is sensitive to the deformation of the surface. This deformation is mainly determined by the longitudinal piezoelectric effect, which is calculated as $d_{33,f} = 35\,\mathrm{pm/V}$ along the $[001]_{\mathrm{BTO}}$ direction for *c*-axis domains in ref. [74]. In contrast, $d_{33,f}$ approaches 0 pm/V along the $[010]_{\mathrm{BTO}}$ direction [44, 74], which causes the amplitude of the PFM signal to vanish for *a*-axis domains. Furthermore, *a*-axis domains would require an electric field parallel to the surface to flip their polarization, which is not available during the PFM measurements.

For the *c*-axis $BaTiO_3$ film, domains with up/down orientation can be written (fig. 2.34). While the height signal indicates a flat topography, the structure written into the film is clearly visible in the PFM amplitude and phase image. The phase between two different domain states changes by 180°, as expected for domains oriented in opposing directions. Also, the vanishing amplitude of the PFM signal at the edges of the written structure is in agreement with the behavior at domain walls [130]. The structure is stable for more than an hour. After 12 h, the contrast decays, most likely due to relaxation effects caused by strong depolarization fields and polarization shielding, which are in particular present in MFIS structures [128].

In contrast to the *c*-axis film, no stable domain pattern could be written into

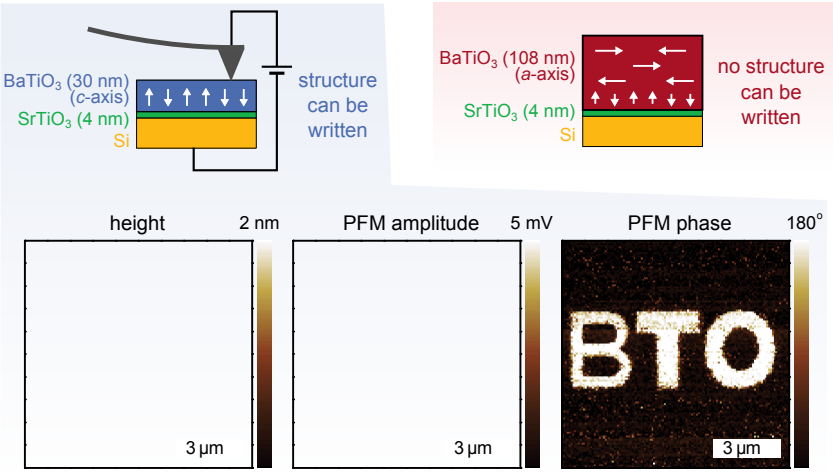

Fig. 2.34 Top: sketches indicating the sample structure investigated by PFM. Bottom: topography, amplitude and phase of the PFM signal measured on a mainly *c*-axis oriented $BaTiO_3$ thin film after initially writing the letters "BTO". No PFM contrast is observable for the thicker, *a*-axis oriented sample.

the *a*-axis film. As discussed, this behavior is due to the electric field being orthogonal to the direction of the spontaneous polarization, which does not allow switching of domains.

The PFM experiments confirm the presence of piezoelectricity and, due to the observed bistability, the presence of ferroelectricity in the thin *c*-axis film. The switching of ferroelectric domains might be promoted in PFM measurements compared to C/V-measurements as shown in section 2.5.1 due to the large electric field strength at the PFM tip compared to metallic pads. The electric field might thus be above the $BaTiO_3$ coercive field. For thicker, *a*-axis films, piezo- and ferroelectricity can neither be confirmed nor excluded with the PFM setup due to the inability of applying in-plane electric fields. By means of electro-optical characterization as described in chapter 3 the presence of ferroelectricity in *a*-axis films is however determined.

2.6 Conclusion and outlook

In the current chapter, different routes to deposit epitaxial $BaTiO_3$ and $SrTiO_3$ films on silicon substrates by means of MBE deposition and rf-sputtering are discussed. A solid phase epitaxial process is used to obtain $SrTiO_3$ seed layers by first depositing amorphous layers and subsequently annealing them. The crystalline quality of the perovskite layers is strongly enhanced if the annealing step is iteratively repeated after each deposition of ∼1 nm-thick amorphous layers, in comparison to a single crystallization step for the typically 4 nm-thick films. The cycled annealing process suppresses the formation of defects in the first $SrTiO_3$ unit cells, and results in strained layers with low surface roughness (≤ 0.4 nm rms) and sharp rocking curves ($\Delta\omega_{STO} \sim 0.3°$), indicating a good crystalline structure. To further improve the quality of the films towards bulk-like properties [41], the growth conditions of the initial $SrTiO_3$ monolayers have to be carefully investigated. In particular, the oxygen partial pressure and the temperature range have to be adjusted in order ensure full oxidation of the $SrTiO_3$ layer while avoiding the formation of SiO_2 at the same time. Furthermore, post-deposition annealing steps in oxygen might significantly improve the $SrTiO_3$ crystallinity [41].

The quality of $BaTiO_3$ thin films epitaxially grown on such $SrTiO_3$/Si templates is sensitive to the precise 1:1 stoichiometry between barium and titanium. As a consequence, the formation of islands, precipitates, and micro-structural defects such as pores and anti-phase boundaries are visible, in particular in thicker films (> 20 nm). The limitations in the precise stoichiometry control in a layer-by-layer growth approach are resolved with a *shuttered co-deposition* growth technique, which provides a quick feedback of the Ba:Ti ratio in addition to the option of almost instantaneously compensating off-stoichiometric growth conditions. The growth procedure yields high quality $BaTiO_3$ layers with sharp rocking curves ($\Delta\omega_{BTO} \sim 0.7°$), low surface roughness (≤ 0.3 nm rms), homogeneous microstructure without pores, and tetragonal crystal symmetry. The orientation of the long *c*-axis can be tuned from out-of-plane to in-plane as a function of the layer thickness, which is in agreement with the lattice constant and thermal expansion mismatches between $BaTiO_3$, $SrTiO_3$ and silicon. The transition between both orientation occurs at a film thickness of ∼30 nm. Tuning the orientation of the crystalline symmetry provides an excellent degree of freedom for engineering nano-scale devices that rely on the ferroelectric polarization of $BaTiO_3$ thin films, for example for active photonic devices as discussed in chapter 4.

In order to reach larger film thicknesses (> 100 nm), a hybrid growth process is developed combining thin MBE-grown seed layers with rf-sputtering. The

sputtered layers crystallize epitaxially to the silicon substrate, when the thickness of the MBE-grown seed layer is larger than 6 nm. Above that threshold, the crystallinity and morphology is mainly influenced by the details of the sputtering process and post annealing steps rather than the seed layer thickness or its termination. Tetragonal, *a*-axis oriented $BaTiO_3$ can be obtained with a solid phase epitaxy process, which includes an amorphous $BaTiO_3$ deposition, followed by an annealing step in oxygen. Alternatively, crystalline layers can directly be obtained by sputtering at higher temperatures. This process results in a pore-free, tetragonal $BaTiO_3$-layer with strongly reduced tetragonality, consisting of nano-domains. The systematic investigation of the role of the initial perovskite seed layer on the crystalline quality and morphology of the sputtered $BaTiO_3$ layer extends recent work, in which epitaxial $BaTiO_3$ layers were obtained on silicon combining pulsed laser deposition and MBE [48]. By using rf-sputter deposition, the feasibility of obtaining relatively thick, tetragonal $BaTiO_3$ layers on silicon substrates is shown by a rather wide-spread deposition method which is available in many research and development environments.

The $BaTiO_3$ layers show bulk-like electrical properties with large resistivity values of $\rho > 10^{13}\,\Omega\,\mathrm{cm}$ for small electric fields, indicating a good composition and little amount of oxygen vacancies. The permittivity of the layer of $\sim 50-200$ is in agreement with previously published studies. Both the permittivity and the resistivity are important parameters for the proper design of electro-optical devices (chapter 4). While no consistent electric confirmation of the ferroelectricity of the films is obtained, PFM measurements show the presence of piezo- and ferroelectricity with the spontaneous polarization along the out-of-plane direction for thin *c*-axis $BaTiO_3$ films. Piezo- and ferroelectricity are not visible in thicker, *a*-axis films, as expected for the PFM geometry used in the experiments. The presence of ferroelectricity in thin, MBE-grown $BaTiO_3$ layers is a clear advancement in obtaining functional layers on silicon compared to previous investigations, which either required a substantially thicker buffer layer [55] or which could only observe dielectric behavior in MBE-grown layers due to oxygen deficiency [48]. A recently published study confirms the presence of ferroelectricity in thin $BaTiO_3/SrTiO_3/Si$ layers as observed in this thesis [56]. Polarization measurements with metallic pads and a systematic study on films with different thicknesses should be carried out to confirm the ferroelectricity independent of the PFM measurements. As a first step towards the confirmation, the presence of ferroelectricity in *a*-axis films is shown in this thesis by means of an electro-optic characterization method, as discussed in chapter 3.

CHAPTER 3

Electro-optical characterization

Bulk barium titanate shows a strong linear electro-optical effect with Pockels coefficients of $r > 1000\,\mathrm{pm/V}$, among the largest of all oxides (fig. 1.2a and section 2.1.3). The Pockels effect describes the variation of the refractive index n of a material when applying an electric field E. In a simplified version, neglecting any tensor properties [49], it can be formulated as [27]

$$n(E) = n_0 - \frac{1}{2} r n_0^3 E, \tag{3.1}$$

where r is the Pockels coefficient and n_0 the refractive index when no electric field is applied. Thin films of $BaTiO_3$ show a large deviation from the bulk Pockels coefficients with typically much lower values as little as $22\,\mathrm{pm/V}$ for thin polycrystalline layers [131–133]. The linear electro-optical effect is even reported to completely vanish if strontium is mixed into the film [134, 135].

Due to the large variation of previously reported values, it is crucial to experimentally determine the Pockels coefficient for the films grown in this work, before starting to fabricate active devices. This is in particular important as previous studies investigated $BaTiO_3$ films grown on oxide substrates, but no study about the electro-optical properties of $BaTiO_3$ films on silicon substrates existed. However, the substrate and the deposition method has a large impact on the morphology and crystalline structure of the thin film, as discussed in chapter 2. Also the oxide/semiconductor interface might strongly impact the film properties for example by creating interfacial charges that in turn create depolarization fields. An estimation of the Pockels effect from previous studies is therefore not possible.

The following sections summarize different ways of how to characterize the

electro-optical properties of thin films, the physical background of the Pockels effect, and the setup used for the experiments, before discussing the results of the electro-optical effect in $BaTiO_3$/Si samples[1].

3.1 Electro-optical characterization methods

Light propagating through an electro-optically active material experiences a phase-shift when applying an electric field, as a consequence of the modification of the refractive index (eq. (3.1)). This phase shift can cause a change in the polarization or the intensity of the probing light, which is experimentally detectable. There are however two main challenges in the measurements:

- The change of the refractive index n is relatively small (typically, $\Delta n \sim 10^{-3} - 10^{-5}$) which often results in only small changes of the observed signal. These small changes can be at the edge of the experimental resolution, in particular for thin films where the interaction length between light and the electro-optical active material is very short.
- The tensorial nature of the electro-optical effect (section 3.2.1) makes the determination of the Pockels tensor complicated because the measurement values depend on the relative orientation between the crystal, the applied electric field, the direction of the propagation and the polarization of the light. Furthermore, the existence of ferroelectric domains has to be taken into account.

Different solutions have been reported that tackle these issues. The most common methods to electro-optical characterize thin-films are briefly compared in the following paragraphs, and their applicability to the $BaTiO_3$/Si samples is discussed.

Ellipsometry Spectroscopic ellipsometry is a wide-spread technique to characterize the optical properties of thin films. It is based on the detection of the polarization changes of light in thin films for a broad wavelength range and different angles of incidence. The detected signal is then compared with a model of the sample in order to obtain values such as the refractive index, layer thicknesses, or interface roughnesses [137]. The commercially available tools can be extended to characterize electro-optical properties by applying an

1 Parts of this chapter have been published in *Nature Communication* and *Proceedings of SPIE* [46, 136]. Text excerpts and figures are reproduced by permission of Nature Publishing Group.

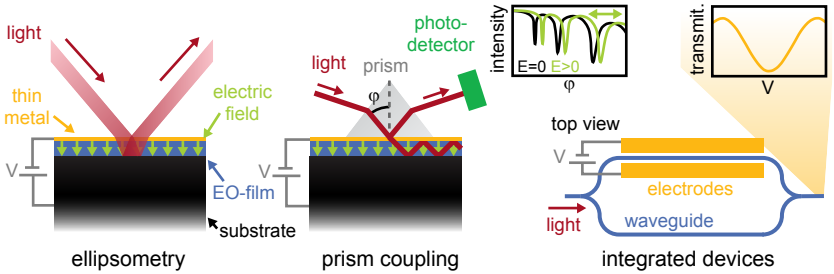

Fig. 3.1 Common methods to investigate the electro-optical properties of thin films. (a) Reflection methods sensitive to changes in the polarization, such as spectroscopic ellipsometry or the Teng-Man method. (b) Prism coupling to excite planar optical modes in the active layer. The reflected intensity drops for specific angles of incidence, which can be shifted by applying an electric field (see inset). (c) Active Mach-Zehnder interferometer as example for an integrated device. The transmission is modified for electro-optical structures when applying a voltage to the electrodes (see inset).

electric field to the sample and comparing the refractive indices as determined for different field strengths [138]. Typically, thin, semi-transparent metal top-electrodes and the grounded substrate are used to apply an field (fig. 3.1a). The method suffers however from a rather low sensitivity, as a reliable detection of $\Delta n \sim 10^{-3}$ is at the limit of the technique, in particular for very thin films of only a few 10 nm. Additionally, the electro-optical effect is not implemented in the standard modeling tools which make the tensorial analysis complicated. Still, the effective Pockels coefficients ~1 µm-thick oxides have successfully been measured with spectroscopic ellipsometry [138]. Due to the low sensitivity, especially for films < 100 nm and potentially low Pockels coefficients, other methods (see below) are preferred in this thesis.

Teng-Man reflectometry A similar method like ellipsometry with a significantly better resolution was suggested by Teng *et al.* [139] and Schildkraut [140] which is often referred to as *Teng-Man* method. The major difference to spectroscopic ellipsometry is the modulation of the electric field in combination with a lock-in detection scheme, which increases the sensitivity by several orders of magnitude. Additionally, a laser instead of a broadband light source is used. Beside this standard configuration, many modifications such as a combination of perpendicular incidence with interdigitated electrodes for in-plane electric fields have been implemented [141]. Although the Teng-Man technique is widely

spread for thin film characterization [142, 143], it is prone to misinterpretation of the measurement signals [142]. Interference effects from multiple reflections, the influence of the semi-transparent electrode, and the non-perpendicular angle of incidence that requires the consideration of all electro-optical tensor elements for a proper analysis are some of the typical error sources [142, 144]. Due to these possible measurement artifacts, the method described in the next paragraph is used in the current work.

Transmission measurements Based on the same principle of detecting changes in the polarization but by using a transmission geometry (section 3.3), the data evaluation is simplified, in particular with a perpendicular angle of incidence. Already the first electro-optical measurements of $BaTiO_3$-crystals were performed in transmission with static applied fields [75]. The drastically reduced interaction length between the light and the electro-optical material requires lock-in amplification techniques in order to study thin films [145–147]. Typically, the method is used to obtain effective Pockels values rather than single tensor elements. Transmission measurements are the method of choice in this thesis. A detailed description and mathematical treatment of the extraction of single tensor elements is discussed in section 3.3. It should be noted that the transmission measurements can be converted into the standard Teng-Man geometry with only little modifications.

Prism coupling A very sensitive method to measure the refractive index of thin films with a resolution of $\Delta n \sim 5 \times 10^{-4}$ is prism coupling [148]. With this method, a guided planar waveguide mode in the film is excited by using a prism in contact to the film and a laser beam at a specific angle of incidence (fig. 3.1b). When the angle of incidence is varied, the reflected signal shows sharp minima when film modes are excited. The refractive index can be deduced from multiple of these specific angular positions. Options for an electro-optical characterization of the film by applying an electric field between the prism and the sample [149–151] are commercially available. However, the method cannot be easily applied to $BaTiO_3$/Si samples used in the current work. First, no guided modes exist in this material stack due to the high refractive index of silicon. Second, film thicknesses of several 100 nm are required to support multiple modes, which is significantly more than the film thicknesses under consideration.

Integrated devices The fabrication of test devices such as Mach-Zehnder interferometers (fig. 3.1c) [26, 131, 152] or resonant structures like ring resonators [153] can be used to determine the electro-optical properties of a material

included in this structure. While devices can reveal even small Pockels effects ($< 2\,\mathrm{pm/V}$ [153]), the design and processing is an additional workload compared to a pure material characterization technique. This is in particular true for $BaTiO_3$/Si structures where non-typical design and process steps are involved in the device fabrication (chapter 4), which can also influence the electro-optical characteristics.

Alternative techniques Beside these most common methods, a variety of other techniques for characterizing the electro-optical properties of thin films exist, such as the utilization of diffraction patterns caused by a local variation of the refractive index with interdigitated electrodes [154], the inclusion of electro-optically active materials into cavities [155, 156], or by detecting the interference pattern of a double slit [157]. These methods are more specialized, and do not provide any obvious advantage for the $BaTiO_3$/Si analysis compared to transmission measurements.

3.2 Physical background

The simplified description of the linear electro-optical effect (eq. (3.1)) is not sufficient to describe and correctly interpret the experimental results (section 3.3). The following section provides therefore a tensorial treatment of the Pockels effect, specifically for $BaTiO_3$. A phenomenological description of the Pockels effect is used to calculate the behavior of parameters such as the orientation of the optical axis and the refractive index, which are accessible in the experiment. A microscopic model of the Pockels effect and first-principle studies of the origin of the optical nonlinearities specifically for $BaTiO_3$ are found in the literature [158–160].

3.2.1 The Pockels tensor

In nonlinear optical materials the refractive index is dependent on the applied electric field E_{ext}. The elements n_{ij} of the refractive index tensor as a function of the electric field are defined as [161]

$$n_{ij}\left(E_{\mathrm{ext}}\right) = n - \frac{1}{2} r_{ijl} n^3 E_{\mathrm{ext},l} - \frac{1}{2} \xi_{ijlm} n^3 E_{\mathrm{ext},l} E_{\mathrm{ext},m}. \tag{3.2}$$

In eq. (3.2) Einstein notation is used, r refers to the Pockels tensor, ξ to the Kerr tensor, and $E_{\mathrm{ext},l/m}$ to different components of the applied field. In the following, the second order Kerr effect will be neglected since in $BaTiO_3$ it is typically

much smaller than the Pockels effect [77] at electric field strengths accessible in the experiments discussed below. Furthermore, a simplified representation of the Pockels tensor is used: The rank of the $3 \times 3 \times 3$ Pockels tensor (27 elements) can be reduced by one to a 6×3 Pockels tensor[2] (18 elements) [49]. Due to the P4mm symmetry class of tetragonal $BaTiO_3$, the entries of this tensor can be represented by three different elements only, r_{13}, r_{33}, and r_{42} [28].

As can be deduced from eq. (3.2) the electro-optical response on the light depends on the wavevector $\boldsymbol{k}$ and the polarization relative to the electric field $\boldsymbol{E}_{\mathrm{ext}}$ and the crystalline orientation, which defines the coordinate system of the equation. The impact of the wavevector and the polarization on eq. (3.2) is reflected by the refractive index tensor n_{ij} [161]. A visualization of eq. (3.2) is shown in fig. 3.2 in which the simulated optical indicatrix $\hat{\eta} = \left(\hat{n}^{-1}\right)^2$ and its modification upon applying an electric field is plotted [161]. The polarization of light traveling through a birefringent material such as $BaTiO_3$ does not change if the polarization is oriented along one of two specific axes. The corresponding ordinary and extraordinary refractive indices n_{o} and n_{eo}, respectively, as well as the orientation of these axes can be constructed from $\hat{\eta}$ as explained in the caption of fig. 3.2.

The properties accessible through the experiment (section 3.3) are changes in n_{o} and n_{eo} and the rotation of the axes. In order to obtain these values from eq. (3.2), the optical indicatrix $\hat{\eta} = \hat{\eta}\left(\boldsymbol{E}_{\mathrm{ext}}\right)$ can be written as an eigenvalue equation using the displacement field $\boldsymbol{D}$ of the electro-magnetic light wave, the normalized wavevector $\boldsymbol{u_k} = \boldsymbol{k}/k_0$ with $k_0 = 2\pi n/\lambda$, and the refractive index n:

$$-\boldsymbol{u_k} \times \left(\boldsymbol{u_k} \times \hat{\eta}\left(\boldsymbol{E}_{\mathrm{ext}}\right) \boldsymbol{D}\right) = \frac{1}{n^2} \boldsymbol{D}. \tag{3.3}$$

A detailed derivation of this equation can be found in ref. [161]. The dependency of the tensor $\hat{\eta}\left(\boldsymbol{E}_{\mathrm{ext}}\right) = \left(\hat{n}^{-1}\left(\boldsymbol{E}_{\mathrm{ext}}\right)\right)^2$ on the static electric field $\boldsymbol{E}_{\mathrm{ext}}$ is given through equation eq. (3.2). The eigenvalues n and eigenvectors $\boldsymbol{D}$ of $\boldsymbol{u_k} \times \left(\boldsymbol{u_k} \times \boldsymbol{\eta}\left(\boldsymbol{E}_{\mathrm{ext}}\right)\right)$ correspond to the refractive indices and the direction of the major optical axes of the crystal, respectively.

3.2.2 Electro-optical response of a single domain

For the experiments (section 3.3), the angle of incidence is set to 90° and pairs of electrodes separated by a small gap are deposited on a-axis $BaTiO_3$-films in

2 a notation is used that combines two indices (i, j) into one index p, where $i, j = 1..3$ and $p = 1..6$ with special mapping rules [49]

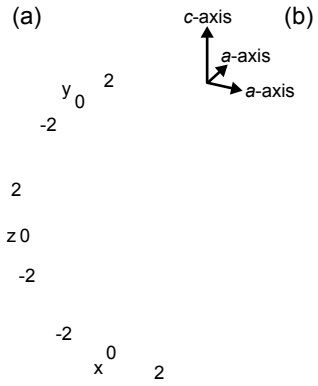

Fig. 3.2 Three-dimensional representation of the optical indicatrix $\hat{\eta} = \left(\hat{n}^{-1}\right)^2$ and the impact of an applied electric field on it, using the bulk $BaTiO_3$ Pockels tensor (compare table 3.1). The electric field strength is taken to be very large ($E_{\text{ext}} = 10^8$ V/m) for a clear visualization. (a) Illustration of the construction of the refractive indices for a specific orientation of the incoming light $\boldsymbol{k}$ (dashed, blue) and the electric field $\boldsymbol{E}_{\text{ext}}$ (yellow line): the short and long axis of the intersection ellipse (red) between the indicatrix and a plane perpendicular to $\boldsymbol{k}$ correspond to the ordinary and extraordinary index, respectively. The orientation of the $BaTiO_3$ crystalline axes is indicated by the coordinate system on the top. (b) Optical indicatrix for various orientations of the electric field.

order to create an in-plane electric field $\boldsymbol{E}_{\text{ext}}$ (fig. 3.3a). The direction of the electric field is varied in the experiment by fabricating electrodes with different orientations relative to the main crystalline axes ($[001]_{\text{BTO}}$ and $[100]_{\text{BTO}}$). However, even for a fixed electrode geometry, the relative orientation between $\boldsymbol{E}_{\text{ext}}$ and the ferroelectric polarization varies between different domains (fig. 3.3a). Therefore, the changes of the optical indicatrix as a function of the angle φ_E between $\boldsymbol{E}_{\text{ext}}$ and the ferroelectric polarization is calculated for a single domain. The results are then used to describe the response of multiple domains.

The parameters used for the simulations (table 3.1) are based on literature values for $BaTiO_3$. Since the Pockels effect in thin films is typically reduced by an order of magnitude compared to bulk $BaTiO_3$ [27, 29], the bulk literature values are scaled by a factor of 0.1 in the simulations in order to obtain more realistic results. The changes of the refractive indices $\Delta n_{\text{o/eo}} = n^0_{\text{o/eo}} - n_{\text{o/eo}}\left(\boldsymbol{E}_{\text{ext}}\right)$ and the birefringence $\Delta n_{\text{b}} = n_{\text{o}}\left(\boldsymbol{E}_{\text{ext}}\right) - n_{\text{eo}}\left(\boldsymbol{E}_{\text{ext}}\right)$, as well as the

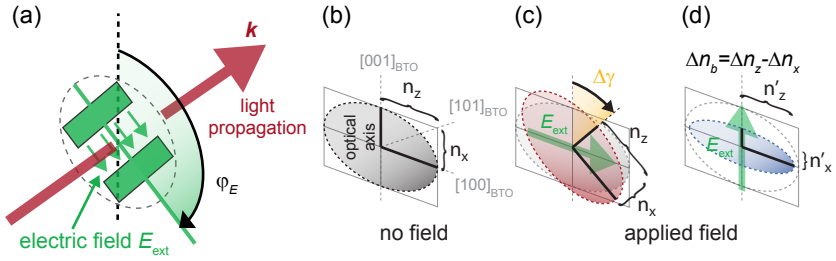

Fig. 3.3 (a) Experimental geometry: two electrodes create an in-plane electric field which is oriented at an angle φ_E relative to the main crystalline axes of the *a*-axis film (tetragonal *c*-axis parallel to the surface, see section 2.3.3). The light is transmitted perpendicular to the sample between the gap. The white arrows indicate the ferroelectric polarization of different domains. (b) Refractive index ellipse in $BaTiO_3$, showing the refractive index n_x and n_z along different crystalline directions. (c) Applying an electric field $\boldsymbol{E}_{\text{ext}}$ rotates the optical axis by $\Delta\gamma$ and (d) changes the birefringence $\Delta\,(n_{\text{b}})$ depending on the orientation of $\boldsymbol{E}_{\text{ext}}$ (not to scale).

rotation of the optical axis $\Delta\gamma$ are simulated as a function of φ_E (fig. 3.4). The largest rotation $\Delta\gamma$ of the optical axis is observed when $\boldsymbol{E}_{\text{ext}}$ is perpendicular to the crystalline *c*-axis ($\varphi_E = \pm 90°$), as illustrated in fig. 3.3c. For that geometry, the change in the refractive indices is minor. When $\boldsymbol{E}_{\text{ext}}$ is parallel to the *c*-axis ($\varphi_E = 0°/180°$) the situation is reversed: The rotation of the optical axis vanishes while the change in Δn_{b} becomes maximal (schematics in fig. 3.3d).

Table 3.1 Parameters used for simulating the electro-optical response. The refractive indices are calculated with the Sellmeier equation using parameters from ref. [162] with $\lambda = 1550\,\text{nm}$. The stress-free (unclamped) electro-optical bulk properties from ref. [28] ($\lambda = 1550\,\text{nm}$) are scaled by 0.1 to take into account the typically observed reduction of the bulk values for thin films [27, 29].

param.	n_{o}	n_{eo}	r_{13}	r_{33}	r_{42}	$\lvert E_{\text{ext}}\rvert$
value	2.297	2.268	0.8 pm/V	8 pm/V	100 pm/V	3×10^5 V/m

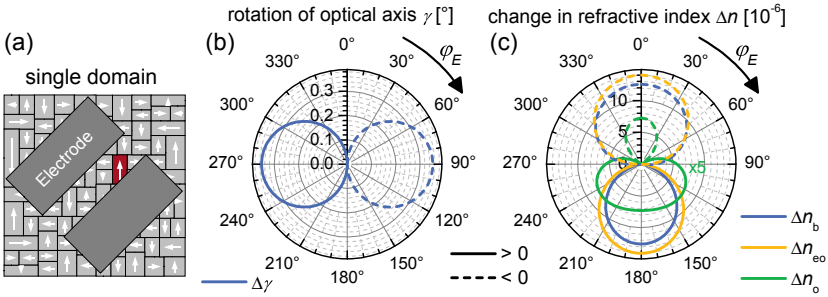

Fig. 3.4 (a) Simulated response for a single ferroelectric domain: (b) Rotation of the optical axis and (c) variation of the birefringence Δn_b and the ordinary and extraordinary refractive index Δn_o (scaled by $\times 5$) and Δn_eo, respectively, as a function of the direction of the applied field. Solid and dashed lines correspond to positive and negative values, respectively.

3.2.3 Electro-optical response of multiple domains

In a multi-domain film with various orientations of the ferroelectric polarization, different domains have a different effect on the polarization of the transmitted light. When the size of the ferroelectric domains is on the order of or smaller than the wavelength ($\lambda = 1.55\,\mu\mathrm{m}$), interference effects between the different polarization states have to be considered to describe the transmitted light. In particular, when simulating the detected power P in the experimental setup (section 3.3), the electric field vectors of the light $\boldsymbol{E_1}$ and $\boldsymbol{E_2}$ after transmission through two different domains have to be added first ($P \propto \boldsymbol{E} = (\boldsymbol{E_1} + \boldsymbol{E_2})^2$) rather than treating them separately ($\boldsymbol{E_1}^2 + \boldsymbol{E_2}^2$).

First, a set of two 180° oriented domains is considered. Applying an electric field at an arbitrary direction causes a rotation of the optical axis in the opposite direction in each domain (fig. 3.5a). Also, the change in birefringence is almost opposite between the two domains. For both domains, the polarization of the light will change after transmitting through the sample. However, the phase shift between the ordinary and extraordinary light component will be opposite. This results into the opposite sense of rotation of the elliptically polarized light. The interference of these two polarization states, being left- and right-circular polarized, respectively, will result in a zero net-change in the polarization of the transmitted light.

By applying an electric field above the ferroelectric coercive field, domains can flip their orientation and 180° domains will be eliminated. In contrast, 90°

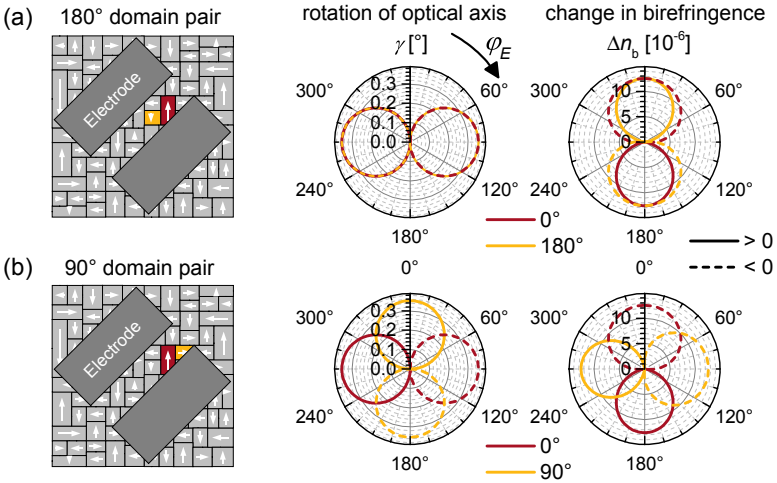

Fig. 3.5 Rotation of the optical axis and change in the birefringence for two domains with different ferroelectric polarization (white arrows in schematics on the left) as a function of direction of the electric field, (a) 180° domains and (b) 90° domains. Solid and dashed lines correspond to positive and negative values, respectively.

domains are linked to a different crystallographic orientation and still exist after such a poling process. The response of two 90° domains shows generally a different magnitude when the direction of the electric field is varied (fig. 3.5b). Thus, even if the two polarization states interfered destructively, they would not fully cancel out each other. It can be deduced from further calculations that the changes of the different polarization states even interfere constructively for 90° oriented domains (not shown here).

These consideration of multiple domains show that the net changes in the polarization due to an electric field will nearly cancel out in unpoled *a*-axis films containing 180° ferroelectric domains. In contrast, the 90° domain pattern after applying an electric field above the coercive field will effectively vary the polarization state of the transmitted beam which can eventually be measured, as described in section 3.3.

3.3 Description of setup

3.3.1 Principle of measurement

A linearly polarized laser beam will generally be elliptically polarized when transmitted through a birefringent material. As discussed in the previous chapter, applying an electric field to an electro-optical active material causes a change in that birefringence. As consequence, the polarization of the transmitted light will differ from the case without applied field. When detecting these polarization changes as a function of parameters such as magnitude and orientation of the electric field and incident polarization, it is possible to confirm or disprove the existence of a linear electro-optical effect. Furthermore, by thoroughly comparing the data with a proper model of the material system, the reconstruction of the Pockels tensor is possible.

The main experimental challenge is the small change of the polarization, in particular for thin films. The setup described in the following section is however capable of detecting small rotations δ of linearly polarized light of only $\delta \approx 10^{-5}$ degrees, which enables the analysis of very thin layers ($\sim$10 nm).

3.3.2 Electro-optical setup

The experimental setup is illustrated in fig. 3.6: A single-mode diode laser from *New Focus* operating at $\lambda = 1550$ nm is first polarized with a Glan-laser prism (extinction ratio $> 2 \times 10^5 : 1$). A successive half-wave plate mounted on a motorized stage (*Newport URS50BPP*) is used to set the incident polarization, before focusing the Gaussian-shaped beam with a spot size of $\sim$15 µm (FWHM) on the typically 7 µm-wide gap between two electrodes at an angle of incidence of 90°. Variations of the angle of incidence as a result of focusing the beam are small ($< 1°$) and are thus neglected during the analysis (section 3.3.3). To center the beam in the gap, the sample is moved with a *xyz*-stage while following the signal of a camera. The camera is focused on the sample through the same optics as the laser beam using a dichroic mirror. The alignment between the laser beam and the camera operating in the visible light regime is done by comparing the video signal with the transmitted power at the edges of large, metallic alignment pads prior to the electro-optical measurements.

Owing to the birefringence of $BaTiO_3$, the transmitted light is generally slightly elliptically polarized. A quarter-wave plate after the sample and a second Glan-laser prism, both mounted on motorized stages, are iteratively rotated to minimize the power of the transmitted light on an InGaAs detector (*Femto OE-200 IN2*). For the condition of minimal transmission, the quarter-

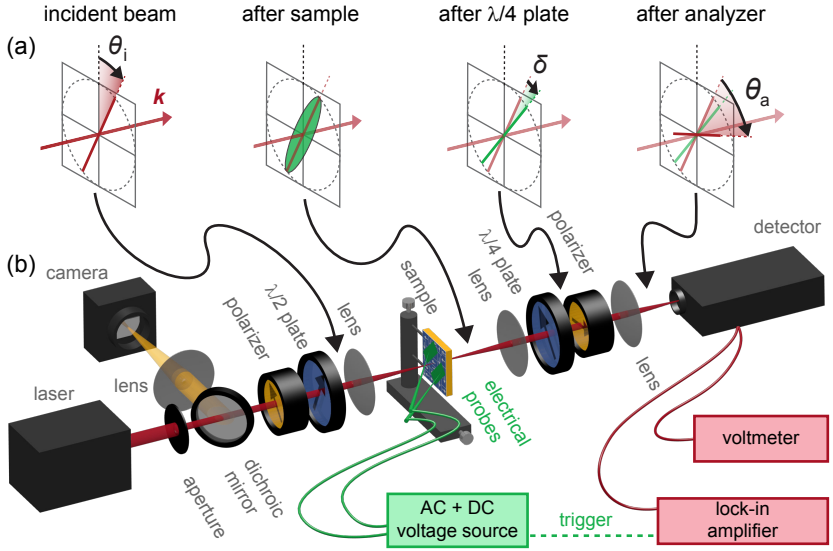

Fig. 3.6 (a) Polarization states at various positions of the laser beam in the experiment. (b) Schematics of the optical setup used for the electro-optical characterization. Details and operation principle are described in the text.

wave plate compensates the ellipticity induced by the birefringence and the transmitted light is linearly polarized.

3.3.3 Measurement and analysis procedure

After applying a voltage offset of $V_{\text{off}} = 40\,\text{V}$ for $\sim$1 min to align the ferroelectric domains, a sinusoidal, alternating voltage of $V_{\text{ac}} = 3.0\,\text{V}$ (peak-to-peak amplitude) at a frequency $f = 17.3\,\text{kHz}$ with $V_{\text{off}} = 25\,\text{V}$ is applied during the measurements. The modification of the refractive index due to the applied field leads to an elliptic polarization of the transmitted beam after the sample, which is transformed into a rotation of the linear polarization by an angle δ by the quarter-wave plate (fig. 3.6a). After passing through an analyzer oriented at an angle θ_a relative to the polarization of the incident beam (fig. 3.6a), the transmitted power is mainly determined by the angle between the two polarizers

θ_a as [49]

$$P = P_\mathrm{max} \cos^2 (\theta_\mathrm{a} - \delta) , \tag{3.4}$$

but it also depends on the induced rotation δ of the polarization. P_max is the maximum transmitted power for parallel polarizers. For small angles δ, the power variations ΔP are expected to be proportional to the derivative $\mathrm{d}P/\mathrm{d}\theta_\mathrm{a}$. Therefore, the transmitted power P and the power variations ΔP are recorded simultaneously while rotating the analyzer θ_a in small steps in combination with a lock-in detection scheme in order to gain sensitivity. The rotation of the polarization δ is determined by first obtaining the analytical function of $\tilde{P}(\theta_\mathrm{a})$ by fitting the experimental values $P(\theta_\mathrm{a})$ to

$$\tilde{P}(\theta_\mathrm{a}) \approx P_\mathrm{max} \cos^2 (\theta_\mathrm{a} - \theta_\mathrm{a,off}) + P_\mathrm{bg}, \tag{3.5}$$

which is an approximation of eq. (3.4) for small δ. The fitted values P_bg and $\theta_\mathrm{a,off}$ take into account the finite extinction ratio of the polarizing elements, and a small misalignment in the analyzer offset position, respectively. Imperfections of the quarter-wave plate are compensated by the initial iterative alignment procedure (appendix C), and do not contribute to eq. (3.5). The derivative $\mathrm{d}\tilde{P}(\theta_\mathrm{a})/\mathrm{d}\theta_\mathrm{a}$ of the fitted function is calculated to fit $\Delta P/P(\theta_\mathrm{a})$ using

$$\frac{\Delta P(\theta_\mathrm{a})}{P(\theta_\mathrm{a})} = \frac{1}{\tilde{P}(\theta_\mathrm{a})} \left(\delta \frac{\mathrm{d}\tilde{P}(\theta_\mathrm{a})}{\mathrm{d}\theta_\mathrm{a}} + A \right) \tag{3.6}$$

to obtain δ. In this equation A corresponds to background contributions, which are proportional to the transmitted power and caused by interference effects between the domains. The normalization $\Delta P/P$ improves the fit quality by eliminating artifacts that arise for example from a changing background illumination or voltage offsets between the different detector gain settings. The fitting procedure allowes the detection of rotations in the polarization down to $\delta = 10^{-5}$ degrees, which is significantly better than the mechanical resolution of the rotation stages. δ is normalized by the amplitude of the applied ac-field E_ac as

$$\delta' = \delta / E_\mathrm{ac}. \tag{3.7}$$

The magnitude of the applied electric field E is calculated by approximating the field in the gap of width d by $E = V/d$. Notably, despite the large voltages of $V_\mathrm{off} = 40\,\mathrm{V}$, only small currents of a few µA are observed between the electrodes (size $\sim$150 µm × 350 µm) when measuring the current-voltage characteristics (fig. 3.7). In particular, no electric breakdown is observed for these voltages.

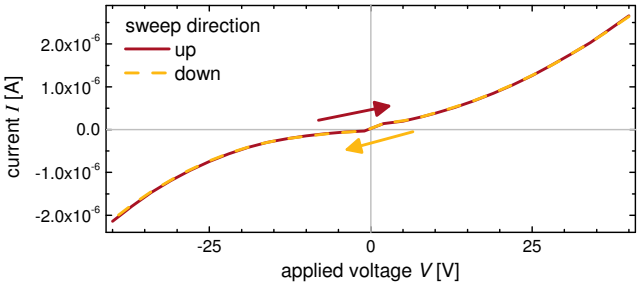

Fig. 3.7 Current-voltage characteristics: Only small currents in the µA range between two electrodes (size ∼150 µm × 350 µm) separated by a gap of 7 µm are measured. In particular, no electric break down is observed.

The c-axis Pockels coefficient r_c is often used as an effective Pockels value to describe the change of the refractive index when the electric field is parallel to the crystalline c-axis. r_c is determined at $\varphi_E = 0°$ by [146]

$$r_c = \Gamma\lambda / \left(\pi n^3 d\nu E_{ac}\right) \tag{3.8}$$

where Γ is the induced phase shift in the sample, d the thickness of the layer, and $\nu = 0.5$ is the relative volume fraction of the domains parallel to the electric field, which contribute to the electro-optical response. The phase shift can be obtained from the rotation angle of the polarization δ as $\Gamma = 2 \times \delta_{\max}$ [145] where $\delta_{\max}$ corresponds to the maximum rotation angle when varying the incident polarization θ_i. The effective Pockels coefficient r_eff is calculated at $\varphi_E = 45°$ in the same way using $\nu = 1$.

By varying the voltage offset V_off, the ferroelectric behavior of the layer can be investigated. Slowly reversing the V_off results in a reorganization of the domains, first creating 180° domains, before at even higher voltages the orientation of the initial domains is flipped. As discussed section 3.2.3, 180° domains show a vanishing electro-optical response. Thus, by looping the applied voltage, hysteresis curves can be recorded. To ensure a depolarized domain state prior to the measurements, the sample is first heated above the Curie temperature to 250 °C for 10 min, and then cooled down to room temperature. Then, for each V_off, a full sweep in θ_a is performed to determine δ, which lasts ∼10 min. The typical duration of the measurement of one hysteresis loop is ∼5 h.

A *LabVIEW* based software is developed in order to control the setup, in

particular to perform alignment procedures and systematic sweeps of several parameters such as the position of the analyzer and the applied voltage. *Wolfram Mathematica* scripts are used for analyzing the data. A more detailed discussion of both procedures is given in appendix C.

3.4 Determination of Pockels tensor

3.4.1 Description of sample

A 130 nm-$BaTiO_3$/4 nm-$SrTiO_3$/Si sample grown with the layer-by-layer deposition process (section 2.3) is used for the electro-optical measurements. A high-resistive silicon substrate ($\rho = 10^4\,\Omega\,\mathrm{cm}$) prevents the electric field between a pair of electrodes to be shortcut through the substrate, as it would be the case for conductive samples. The actual film thickness is determined by spectroscopic ellipsometry (*Woollam VASE*). X-ray analysis (data in fig. 2.25c) confirms the $BaTiO_3$ film to be a-axis oriented in agreement with the expectations for thick $BaTiO_3$ layers (fig. 2.24). The formation of 90° crystalline domains in a-axis films (fig. 2.25d) is assumed to relax strain due to the symmetry mismatch between cubic silicon and tetragonal $BaTiO_3$ (see section 2.3.3).

The backside of the wafer is polished for optical transmission measurements after the growth. Electrode pairs of 300 nm-Pt/10 nm-Ti with varying orientation between the $BaTiO_3$ crystallographic axes and the electrode gap (0° to 90°) with an accuracy of ±1° are fabricated on the samples using standard optical lithography techniques. Unless stated differently, the optical measurements are performed on devices with electrodes having a gap size of ∼7 µm.

3.4.2 Variation of analyzer angle

To qualitatively confirm the presence of the Pockels effect in the $BaTiO_3$ layer, it is necessary to test (1) if the detected power is varied by applying an electric field, (2) if the variation of the power ΔP follows eq. (3.6), and (3) if there is a linear dependence between the applied voltage and ΔP.

Indeed, the experiment shows a power modulation by the applied field, and an excellent agreement of the measured response with the expected dependence: The transmitted power P (fig. 3.8b, top) follows a $\cos^2$ behavior (eq. (3.4)), and the power variation ΔP (fig. 3.8b, bottom) is clearly proportional to the derivative of P (eq. (3.6)). The good agreement between the data and the fitted curves provides an initial validation of the model and confirms the presence of a polarization change of the transmitted light. For fitting ΔP it was taken into account that a phase shift of 180° between the applied voltage and the

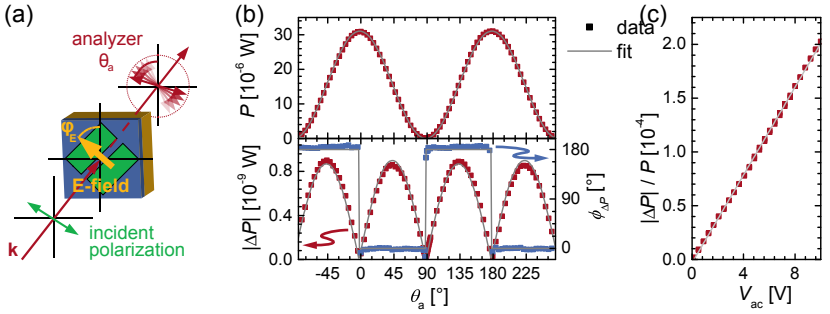

Fig. 3.8 (a) Illustration of the measurement: The analyzer position θ_a is varied for a fixed incident polarization $\theta_\mathrm{i} = 0°$, with an applied applied voltage offset of $V_\mathrm{off} = 25\,\mathrm{V}$ across a 17 µm-wide gap oriented at $\varphi_E = 45°$. (b) Transmitted power P, variation in power ΔP and the lock-in amplifier phase $\phi_{\Delta P}$ due to the electro-optical effect as a function of the analyzer position θ_a. (c) Normalized change of the transmitted power $\Delta P/P$ at $\theta_\mathrm{a} = 45°$ as a function of the peak-to-peak amplitude V_ac.

power modulation instead of measuring the negative amplitude is recorded. The field-normalized magnitude of the rotation of the polarization δ' (eq. (3.7)) is determined from the fits.

A varying absorption as the origin of the power modulation ΔP can be ruled out because in that case, ΔP would be proportional to the absolute transmitted power, in contrast to the observed electro-optical response. The linear dependence of ΔP on the applied field (fig. 3.8c) further precludes the quadratic electro-optical Kerr effect to be dominant and thus confirms the presence of the linear Pockels effect in the sample.

3.4.3 Variation of electric field orientation

To further explore the tensor nature of the Pockels effect, the dependence of δ' on the angle between the applied electric field, incident polarization, and crystallographic orientation has to be considered carefully (section 3.2.1). Applying an electric field to an anisotropic material with a linear electro-optical effect results in a rotation of the optical axis by $\Delta\gamma$ (fig. 3.3c) and a change of the birefringence by Δn_b (fig. 3.3d). In the measurement geometry used for the experiments, both effects cause a rotation of the polarization of the transmitted beam, but the magnitude of δ' depends on the incident polarization: If $\Delta\gamma$ is dominant, δ' is maximal when the incident polarization is parallel to the optical

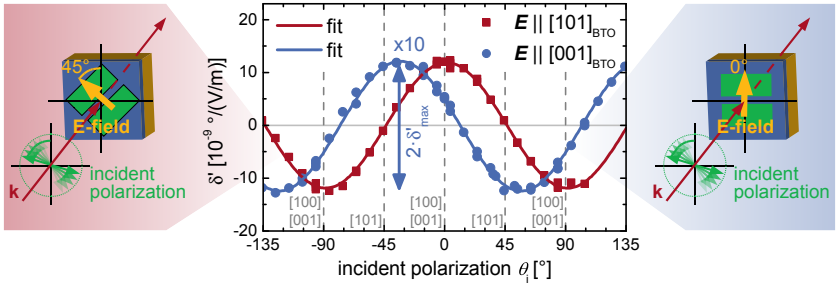

Fig. 3.9 Field-normalized rotation of the polarization δ' of the transmitted light as function of the angle of the incident polarization θ_i for two orientations of the applied field $\boldsymbol{E}$, as shown in the schematics. The dashed vertical lines correspond to the main $BaTiO_3$ crystalline directions. The data is empirically fitted by a sin-function to obtain the maximal rotation δ'_max, indicated by the blue arrow.

axis of the crystal ($\theta_\mathrm{i}|_{\delta'_\mathrm{max}} = 0°$), which is experimentally observed when the applied electric field $\boldsymbol{E}$ is oriented along the $[101]_\mathrm{BTO}$ direction (fig. 3.9). If Δn_b is dominant, on the other hand, δ' is maximal for $\left|\theta_\mathrm{i}|_{\delta'_\mathrm{max}}\right| \sim 45°$. Also this regime is observable in the measurements, when the $\boldsymbol{E}$ is oriented along the $[001]_\mathrm{BTO}/[100]_\mathrm{BTO}$ axes. The slight deviation from $\left|\theta_\mathrm{i}|_{\delta'_\mathrm{max}}\right| = 45°$ (fig. 3.9) is due to the small misorientation of the electrodes relative to the crystalline orientation, as discussed in section 3.4.6.

The modeled response of $BaTiO_3$ for a single domain (fig. 3.4) shows a vanishing rotation of the optical axis when $\boldsymbol{E}$ is parallel to $[001]_\mathrm{BTO}$ ($E \parallel [001]_\mathrm{BTO}$), whereas a change in the birefringence remains. In contrast, a strongly enhanced rotation of the optical axis is expected for $E \parallel [101]_\mathrm{BTO}$. Both features of the model agree well with the experimental results.

The dependence of the electro-optical response on the orientation of the electrodes precludes any polarization-dependent absorption or plasmonic effect from the edges of the metallic pads. Such effects would be independent of the orientation of the electrodes with respect to the $BaTiO_3$ crystalline axis, which is in contrast to the data shown in fig. 3.9. For the same reason, the potential impact from ionized particles in the air due to the high electric field strength can be ruled out to impact the measured signal.

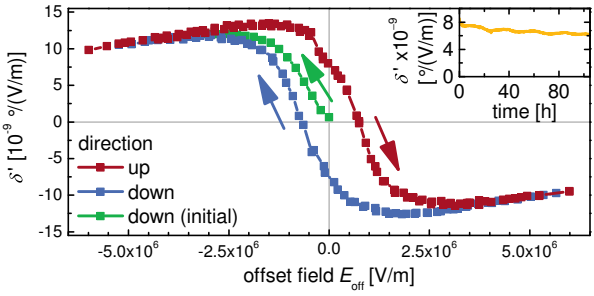

Fig. 3.10 Optical response as a function of the offset field E_{off}. The data set is collected in three successive loops measured at 25 °C after heating the film above its bulk Curie temperature (green) and sweeping E_{off} up (red) and down (blue) again. The inset shows the relaxation of the remanent δ' value at room temperature.

3.4.4 Reorientation of domains

To quantify the elements of the Pockels tensor, one must take into account not only a single domain but the overall ferroelectric domain structure of the $BaTiO_3$ film (fig. 3.3a): As discussed in section 3.2.3, the net electro-optical response of two anti-parallel domains (direction of ferroelectric polarization differs by 180°) with the same size will cancel out. However, anti-parallel domain pairs can be eliminated by flipping their ferroelectric polarization when the applied electric field component $E_{[001]}$ along the crystallographic $[001]_{\mathrm{BTO}}$ axis is above the coercive field E_{c}. Hence, a ferroelectric hysteresis loop would be expected in the optical measurements of δ' upon varying the offset of the applied electric field E_{off}. This is indeed observed experimentally (fig. 3.10).

As expected, the random domain orientation after heating the sample above the Curie temperature of $BaTiO_3$ ($T_{\mathrm{C}} = 123\,^{\circ}\mathrm{C}$ [43]) initially shows no electro-optical response at $E_{\mathrm{off}} = 0$. The presence of equally distributed 180° domain pairs cancel out any net electro-optical contribution. By increasing E_{off}, a strong enhancement in δ' is visible, resulting from the switching of the ferroelectric domains, which eliminates anti-parallel domains. The hysteresis loop monitored during the sweep of E_{off} (fig. 3.10) is a clear signature of the ferroelectric nature of the film. Once poled, the ferroelectric domain structure remains stable for several days at least, as can be seen from the small relaxation of the remanent electro-optical response (fig. 3.10, inset). From the shape of the hysteresis, a coercive field of $E_{\mathrm{c}} = 5 \times 10^5\,\mathrm{V/m}$ is extracted, which is an order of magnitude

larger than in bulk $BaTiO_3$. Such increase is typically observed for ferroelectric thin films because of domain pinning and finite depolarization fields [79, 127]. The finite, linear slope in the hysteresis loop at large electric fields E_{off} as observed in fig. 3.10 is caused by second-order electro-optical effects.

The hysteresis in the optical signal qualitatively excludes any influences from the Si-substrate on the electro-optical response of the sample. As recently shown, non-vanishing Pockels coefficients are induced in silicon if strain-gradients are present [26, 163]. However, Si remains non-ferroelectric and thus no effects of poling are visible, in clear contrast to the hysteresis behavior. The measurements shown in fig. 3.10 also allow to exclude that ferroelectric domain switching [164] has a significant contribution on the electro-optical response presented in figs. 3.8 and 3.9: These measurements are performed in the saturation regime of the hysteresis loop ($|E_{\text{off}}| > 3 \times 10^6\,\text{V/m}$). The saturation indicates that small changes in the applied field hardly change the domain population. Therefore, the modulation of the electric field by $E_{\text{ac}} = \pm 0.2 \times 10^6\,\text{V/m} \ll E_{\text{off}}$ (see section 3.3.2) for the lock-in detection induces only a negligible error in the determination of δ' and thus of the electro-optical constants. More generally, if domain switching contributed to the electro-optical response, a strong enhancement of δ' for the regime of $|E_{\text{off}} + E_{\text{ac}}| < E_{\text{c}}$ would be expected, because the relative change of the domain population is the strongest for small electric offset fields. This behavior would also be expected for the unpoled sample and is contrary to the vanishing electro-optical signal observed in that regime (fig. 3.10), thus excluding domain switching to be a major contribution to the rotation of the polarization by δ'.

3.4.5 Quantitative analysis of Pockels tensor

Determination of r_c

The hysteresis behavior is utilized for the quantitative determination of the electro-optical constants: Because the offset in the electric field $\boldsymbol{E}$ applied during the measurements (fig. 3.9) is significantly above the coercive field, the ferroelectric domains are assumed to be aligned to the electric field component $E_{[001]}$. Domains orthogonal to $\boldsymbol{E}$ experience no electric field component along their long [001] axis, thus keep their anti-parallel configuration without any net contribution to the electro-optical response. Taking this domain structure into account, it is possible to calculate the individual components of the Pockels tensor, which contains three distinct elements for tetragonal $BaTiO_3$ (section 3.2.1), r_{13}, r_{33}, and r_{42}.

For $\boldsymbol{E} \parallel [001]_{\text{BTO}}$, the optical properties are determined by r_{13} and r_{33} which

define the c-axis Pockels coefficient r_c as [49]

$$r_c = r_{33} - \left(n_\mathrm{o}/n_\mathrm{eo}\right)^3 r_{13}. \tag{3.9}$$

Using eq. (3.8), the value of $r_c = 30\,\mathrm{pm/V}$ can be determined. This r_c value is more important for the performance of electro-optical devices than the individual components r_{13} and r_{33} [29], which are correlated and cannot be independently determined with the geometry of the experiment.

Determination of r_{42}

The r_{42} Pockels coefficient is determined by simulating the expected signal for the optical setup and comparing it with the experimental results. To model the setup, the transmitted light is described using the Jones formalism with standard matrices for the incident polarizer and the quarter-wave plate [49]. Imperfections of the optical elements are neglected. The $BaTiO_3$ sample is treated as a wave retarder with a phase shift of $\Gamma\left(n_\mathrm{b}\right) = 2\pi n_\mathrm{b} d/\lambda$, where d is the thickness of the sample. The orientation of the optical axis of the retarder is set by the angle γ relative to the laboratory coordinate system. Ferroelectric domains with orthogonal optical axes, which are parallel to the crystalline c-axis (fig. 3.3), are modeled by rotating the optical axis γ of the wave retarder accordingly.

In order to obtain the Jones vector of the beam transmitted through the sample with multiple domains, the transmission for the individual domains is simulated in a first step. The resulting Jones vectors are weighted with the relative domain population and summed up in a second step. With this procedure any interference effects between different types of domains are taken into account.

The phase shift $\Gamma\left(n_\mathrm{b}\right)$ and rotation angle γ are linked to the variations in the birefringence Δn_b (fig. 3.4c) and the orientation of the optical axis $\Delta\gamma$ (fig. 3.4b) due to the electro-optical effect as a function of the applied electric field $\boldsymbol{E}$. The procedure to obtain these functions is described in section 3.2.1. By comparing the Jones vectors for two different electric fields $\boldsymbol{E_1} = \boldsymbol{E}_\mathrm{off} - \boldsymbol{E}_\mathrm{ac}/2$ and $\boldsymbol{E_2} = \boldsymbol{E}_\mathrm{off} + \boldsymbol{E}_\mathrm{ac}/2$, the normalized rotation angle δ' is determined as $\delta' = \delta'|_{E_2} - \delta'|_{E_1}$, where $\delta'|_E$ is the field-normalized angle (eq. (3.7)) of the orientation of the linear polarization after the quarter-wave plate with respect to the laboratory coordinate system. For the special case of $\boldsymbol{E} \parallel [101]_\mathrm{BTO}$, both 90° domains vary the transmitted light identically, which makes r_{42} independent of the actual domain population. This independence is validated by deliberately varying the population in simulations (not shown here).

Using the parameters listed in table 3.2, δ' is simulated as a function of r_{42}

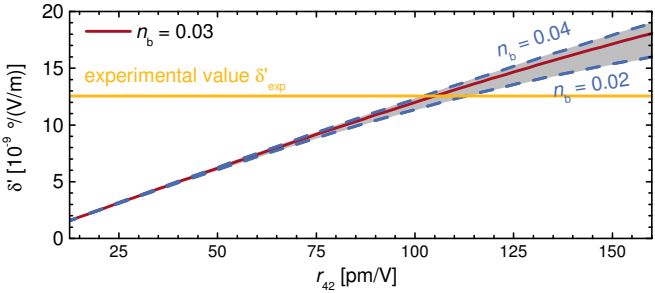

Fig. 3.11 Simulation of δ' as a function of r_{42} using parameters from table 3.2. The dashed lines indicate the influence of the birefringence on the simulation. Small deviations from the bulk value (red line) result in a similar Pockels coefficient r_{42} when comparing the simulation with the experimental value δ'_{exp} (solid, yellow).

(fig. 3.11). The refractive index of the film n is experimentally determined by spectroscopic ellipsometry. Due to the small thickness and the domain structure of the film, the birefringence n_{b} can however not be determined with that method, and the bulk value $n_{\mathrm{b}} = 0.03$ [162] is used instead. The influence of n_{b} on δ' is however small, as indicated in fig. 3.11. By comparing the simulation with the experimental value $\delta'_{\mathrm{exp}} = 12.5 \times 10^{-9}\,\mathrm{degree/(V/m)}$ for the same orientation of the electric field (fig. 3.9), the r_{42} value of the $BaTiO_3$ film is determined as $r_{42} = 105\,\mathrm{pm/V}$. Figure 3.11 shows that smaller values of n_{b} as reported for $BaTiO_3$ thin films on oxide substrates ($n_{\mathrm{b}} = 0.02$ [165])

Table 3.2 Parameters used for simulating δ' as a function of r_{42}. The birefringence n_{b} is calculated as the difference between the ordinary and extraordinary bulk refractive index (table 3.1). The Pockels coefficients r_{13} and r_{33} are scaled with r_{42}, keeping their ratio to the bulk ratio of $r_{13}/r_{42} = 0.01$ and $r_{33}/r_{42} = 0.08$ (table 3.1), respectively.

par.	domains	E_{ac}	d	θ_{i}	n	n_{b}
val.	0°/90°	3.0×10^5 V/m	130 nm	0°	2.26	0.03
par.	φ_E	E_{off}	λ	r_{13}	r_{33}	r_{42}
val.	45°	3.6×10^6 V/m	1550 nm	$0.01 \cdot r_{42}$	$0.08 \cdot r_{42}$	r_{42}

would result in even slightly higher r_{42} values.

Effective Pockels effect r_{eff}

For comparison with previous work [27, 146], an effective value $r_{\text{eff}} = 148\,\text{pm/V}$ is calculated by neglecting the tensor nature of r and simply considering the field-induced phase shift between two orthogonal components of the transmitted light (see section 3.3.2). The orientation of the electric field is chosen such that a maximal induced phase shift is obtained ($\boldsymbol{E} \parallel [101]_{\text{BTO}}$). The results represent a major improvement compared with the limited number of published data on electro-optical properties of lead-free oxides integrated on silicon [150, 153, 166].

3.4.6 Validation of measurement results

The Pockels tensor and the model with multiple domains are validated by experimentally varying the orientation of the applied electric field (fig. 3.14) and comparing the results with simulations using values for r_{42} and r_c as determined in the previous sections. For this comparison, a model is created to calculate the electro-optical response for different orientations φ_E of the applied electric field $\boldsymbol{E}$. Due to the strong influence of the ferroelectric domain structure on the electro-optical response, the reorientation process of the domains has to be taken into account by that model. The shape of the hysteresis loop obtained at $\varphi_E = 45°$ (fig. 3.10) is used for that implementation, as discussed below.

Description of model

The modeling is based on the same Jones algorithm as described in the previous section. Experimental values of the Pockels tensor are included in the simulations. Therefore, r_{13} is set to an arbitrary value r'_{13}, and r_{33} is calculated from the experimental value r_c using eq. (3.9) with $n_{\text{o}}/n_{\text{eo}} \approx 1$. As validated by simulations (not shown here), the actual value of r'_{13} does not influence δ', due to the correlation of r_{13} and r_{33} in the measurement geometry. The remaining parameters in the simulation are identical to those used in the previous section (table 3.2), except the number and population of the different domain types: In order to accommodate the reorientation of the ferroelectric domains dependent on the direction of the electric field $\boldsymbol{E}$, four domains oriented at $\gamma = 0°$, 90°, 180° and 270° (fig. 3.12a) with variable relative volume fraction ν_γ have been implemented. Completely randomly distributed ferroelectric domains correspond to $\nu_{0°} = \nu_{90°} = \nu_{180°} = \nu_{270°} = 0.25$, while $\nu_\gamma = 1$ represents a single domain state.

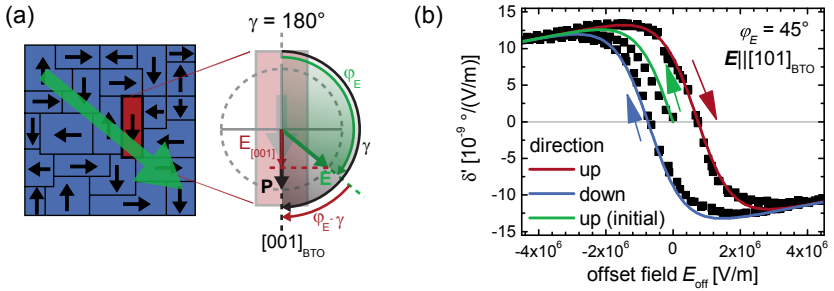

Fig. 3.12 (a) Schematics of the electric field in a single domain. A random domain distribution ($\gamma = 0°$, 90°, 180° and 270°) is exposed to an electric field (left). Angles are defined in the magnification of the red domain (right) which is oriented at $\gamma = 180°$. The projection of the electric field $\boldsymbol{E}$ (green vector) on the direction of the ferroelectric polarization $\boldsymbol{P}$ (black vector) is shown as $\boldsymbol{E}_{[001]}$ (red vector). (b) Electro-optical hysteresis loop at $\varphi_E = 45°$ ($\boldsymbol{E} \parallel [101]_{\mathrm{BTO}}$). The solid curves are calculated based on an empirical model (see text for details) where different colors correspond to different sweep directions. The same data as shown in fig. 3.10 is used.

The estimation of $\nu_\gamma(\boldsymbol{E})$ is based on the shape of the hysteresis loop for $\varphi_E = 45°$ ($\boldsymbol{E} \parallel [101]_{\mathrm{BTO}}$, fig. 3.10). The hysteresis loop is empirically modeled (fig. 3.12b) by

$$\delta' = a_1 \left(\tanh\left(a_2 \left(E_{\mathrm{off}} - E_{\mathrm{c},45°} \right) \right) + a_3 E_{\mathrm{off}} \right). \tag{3.10}$$

$E_{\mathrm{c},45°}$ is the offset field which is required to switch the mean polarization at $\varphi_E = 45°$. The point of switching the mean polarization corresponds to an equal population of all domains with no net electro-optical response ($\delta'(E_{\mathrm{c},45°}) = 0$). In order to obtain the coercive field E_{c} of a single domain, the magnitude of the electric field component $E_{[001]}$ that is parallel to the crystalline $[001]_{\mathrm{BTO}}$ axis (fig. 3.12a) has to be calculated, resulting in $E_{\mathrm{c}} = E_{\mathrm{c},45°} \cos(45°)$ for the specific data discussed in (fig. 3.12b). The parameters a_1, a_2 and a_3 in eq. (3.10) are used to adjust the shape of the model function to match the experimental data. The resulting fit values are listed in table 3.3. The initial polarization curve in fig. 3.12b is approximated by setting $E_{\mathrm{c},45°} = 0$.

Using eq. (3.10) with parameters shown in table 3.3, the fraction of aligned domains $\nu_\gamma(\boldsymbol{E})$ is calculated for an arbitrary magnitude of the applied field. For initial tests of the model, the domain structure of the sample is simplified

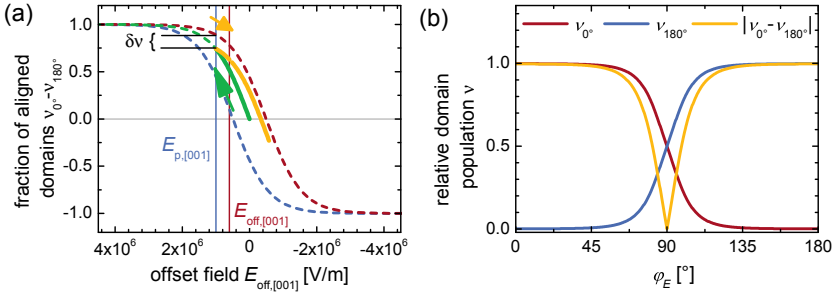

Fig. 3.13 (a) Modeled alignment process of domains for an imperfectly poled sample as function of the electric field component $E_{[001]}$ parallel to the crystalline c-axis $[001]_{\mathrm{BTO}}$. Initially, due to a strong poling field E_{p} (vertical line, solid, blue), the absolute fraction of aligned domain increases (solid, green), but is reduced (solid, yellow) upon lowering the offset field to the value $E_{\mathrm{off},[001]}$ used during the electro-optical measurements (vertical line, solid, red). The yellow curve is obtained by shifting the saturated hysteresis curve for the same sweep direction (dashed, red) by $\delta\nu$, where $\delta\nu$ corresponds to the difference between the saturated hysteresis curve and the initial curve (green) at $E = E_{\mathrm{p}}$. (b) Relative domain population in a simplified model assuming two domains only. ν_{0° and ν_{180° are the relative volume fractions of domains with a spontaneous polarization along the $\varphi_E = 0°$ and $\varphi_E = 180°$ direction, respectively.

to consist of only two domains that are polarized parallel ($\gamma = 0°$) and anti-parallel ($\gamma = 180°$) relative to the electric field at $\varphi_E = 0°$ ($\boldsymbol{E} \parallel [001]_{\mathrm{BTO}}$). The simplification is abandoned in the final simulations to account for the overall domain distribution with additional domains at $\gamma = 90°$ and $\gamma = 270°$. The parameter a_3 in eq. (3.10) originates from the nonlinear electro-optical response of a single domain at large fields and is not related to a reorientation process of the domains. It is therefore set to $a_3 = 0$ when estimating the relative domain population $\nu_\gamma(\boldsymbol{E})$.

Experimentally, a large poling field $\boldsymbol{E}_{\mathrm{p}}$ is applied prior to the electro-optical

Table 3.3 Parameters used to model modeling hysteresis curves with eq. (3.10).

param.	$E_{\mathrm{c},45°}$	E_{c}	a_1	a_2	a_3
unit	V/m	V/m	°(V/m)	$(\mathrm{V/m})^{-1}$	$(\mathrm{V/m})^{-1}$
value	7.0×10^5	4.9×10^5	1.5×10^{-9}	9.5×10^{-5}	-6×10^{-6}

measurement to align the initially randomly oriented domains. During this initial poling, the net fraction of domains $\nu_{0^\circ} - \nu_{180^\circ}$ aligned to $\boldsymbol{E}_{\mathrm{p},[\mathbf{001}]}$ is described by the initial polarization curve in the model (solid green line in fig. 3.13a). When the component $E_{\mathrm{p},[001]}$ of the poling field $\boldsymbol{E}_\mathrm{p}$ parallel to the $[001]_\mathrm{BTO}$ axis is too small to completely align all domains, the sample is not fully poled. In that case, as shown in the example of fig. 3.13a, the net fraction of aligned domains is reduced by $\delta\nu$ compared to saturated hysteresis curve (dashed red line in fig. 3.13a). Otherwise, for larger poling fields $\boldsymbol{E}_{\mathrm{p},[\mathbf{001}]}$, all domains will be re-oriented along $\boldsymbol{E}_{\mathrm{p},[\mathbf{001}]}$ and $\delta\nu$ becomes $\delta\nu = 0$. When reducing the offset field, the change of the domain population is modeled by subtracting $\delta\nu$ from the saturated hysteresis curve. The resulting curve (solid yellow) in fig. 3.13a) represents the fraction of aligned domains $\nu_{0^\circ} - \nu_{180^\circ}$ during the electro-optical measurements which are performed at an offset field of E_off, after initially poling the sample at higher fields $\boldsymbol{E}_\mathrm{p}$.

In order to obtain the domain population $\nu_\gamma(\boldsymbol{E})$ as a function of the orientation φ_E of the electric field, the component $E_{[001]}(\varphi_E, \gamma) = E\cos(\varphi_E - \gamma)$ has to be considered to describe the switching process (fig. 3.12a). By implementing this dependence into the poling mechanism described above, the relative population $\nu_\gamma(\varphi_E)$ of two domains can be calculated (fig. 3.13b) using the parameters in table 3.3 and the experimental value $E_p = 6 \times 10^6\,\mathrm{V/m}$. The simulation of δ'_max shown in fig. 3.14b additionally includes the domains at ν_{90° and ν_{270°. The total volume fractions of both domain types are adjusted accordingly ($\nu_{0^\circ} + \nu_{180^\circ} = \nu_{90^\circ} + \nu_{270^\circ} = 0.5$). This equal domain distribution is based on the cubic symmetry of the substrate (section 2.3.3) and the identical electro-optical response measured for different electrode orientations with $\Delta\varphi_E = 90^\circ$ (fig. 3.14b).

The field-dependent domain population $\nu_\gamma(\varphi_E)$ is finally implemented in the simulations of $\delta'(\varphi_E)$ as a weighting factor when summing the Jones vectors of all four domains as described above (see section of determining r_{42}). In order to obtain the maximum rotation angle $\delta'_\mathrm{max}(\varphi_E)$ and $\theta_\mathrm{i}|_{\delta'_\mathrm{max}}(\varphi_E)$, $\delta'(\varphi_E, \theta_\mathrm{i})$ is simulated as a function of the incident polarization and maximized with respect to θ_i, similar to the experimental procedure shown in fig. 3.9.

Comparison with experimental data

The experimentally determined electro-optical response for different orientations of $\boldsymbol{E}$ agrees well with the calculated response based on the model described above (fig. 3.14b). When the electric field is oriented close to the $[101]_\mathrm{BTO}$ orientation, the electro-optical response originates from a rotation of the optical axis ($\theta_\mathrm{i}|_{\delta'_\mathrm{max}} \sim 0^\circ$), and the magnitude of the response approaches a maximum. These characteristics are expected for a large r_{42} coefficient when the electric

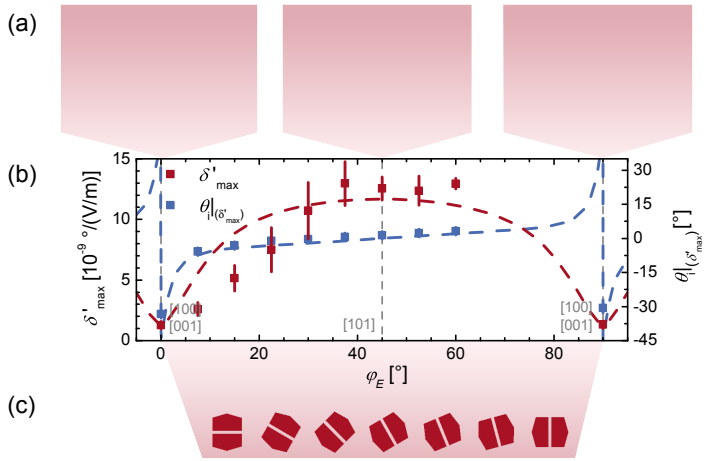

Fig. 3.14 (a) Schematics indicating the different ferroelectric domain configurations for various orientations of $\boldsymbol{E}$ (green), with domains oriented towards the field (red) and randomly oriented ones (blue). (b) Maximum rotation angle $\delta'_{\max}$ and corresponding angle of incident polarization $\theta_i|_{\delta'_{\max}}$ for various values of φ_E. The error bars show the standard deviation from several measurements on different electrode pads. The simulated curves (dashed lines) are based on the Pockels tensor that is experimentally determined. (c) Illustration of various electrode orientations used to experimentally realize different orientations of the electric field φ_E.

field is not parallel to the $[001]_{\mathrm{BTO}}$ direction (fig. 3.4). The situation is reversed when $\boldsymbol{E}$ is aligned to the $[001]_{\mathrm{BTO}}$ and $[100]_{\mathrm{BTO}}$ axes: The electro-optical response is minimal and determined by the change in birefringence ($\theta_i|_{\delta'_{\max}} \sim 45$ °) rather than by the rotation of the optical axis, in excellent agreement with the simulation. The calculations also show that $\mathrm{d}\theta_i|_{\delta'_{\max}}/\mathrm{d}\varphi_E$ is large at $\theta_i|_{\delta'_{\max}} = 45°$: A small variation of $\Delta\varphi_E = 1°$, which is below the alignment accuracy of the electrodes relative to the crystalline orientation, results in a change of $\Delta\theta_i|_{\delta'_{\max}} = 10°$. Such deviation from $\theta_i|_{\delta'_{\max}} = 45°$ is indeed experimentally observed (fig. 3.9). Finally, the identical electro-optical response when rotating the electric field by 90° matches the picture of equally distributed orthogonal domains inferred from the structural characterization (section 2.3.3). Thus, the Pockels tensor and domain structure derived in the study are consistent with the experimentally observed electro-optical behavior for various orientations of the applied electric field.

3.5 Conclusion and outlook

In order to investigate the electro-optical properties of $BaTiO_3$ films epitaxially grown on silicon substrates, an experimental setup for studying the transmission through the sample is realized. Small variations of the polarization of the light due to the electro-optical activity in $BaTiO_3$ are detected and used to reconstruct the Pockels tensor of the film. Despite the small layer thickness of ∼100 nm of the $BaTiO_3$ film and consequently a short interaction length between the laser and the active material, the sensitivity is high enough to excellently resolve the electro-optical properties of the layer.

As a result, a strong linear electro-optical effect with an effective Pockels coefficient of $r_{\text{eff}} = 148\,\text{pm/V}$ is determined for a 130 nm-thick a-axis $BaTiO_3$ layer on silicon. This value exceeds previous data reported for integrated $LiNbO_3$ by at least a factor of five, and for strained Si by a factor of 100. Additionally, the presence of ferroelectricity with a spontaneous in-plane polarization are unambiguously determined by using this electro-optical characterization method. By complementing the measurements with electro-optical simulations, a method to investigate the tensor nature of the Pockels effect of multi-domain thin films is developed. Tensor elements of $r_c = 30\,\text{pm/V}$ and $r_{42} = 105\,\text{pm/V}$ are extracted for the $BaTiO_3$ film. The knowledge of the full Pockels tensor is essential for properly designing optical devices (section 4.3). The demonstration of strong electro-optical properties in the $BaTiO_3$ layers are a fundamental step for continuing the approach of fabricating $BaTiO_3$-based, electro-optical active devices (chapter 4).

The experimental setup in combination with the opportunities in the epitaxial integration of $BaTiO_3$ on silicon (chapter 2) enables many new studies: On the one hand, the growth conditions can be varied in order to tailor the intrinsic electro-optical properties, for example by changing the layer thickness to obtain different strain levels, depositing $BaTiO_3$ layers with the hybrid sputtering process, doping the layers, or fabricating superlattices. On the other hand, the experimental conditions can be modified in order to extrinsically change the electro-optical properties even in a dynamic fashion, such as applying strain via wafer bending, or changing the temperature during the measurements. All these modifications are templates for obtaining new insight into the electro-optical properties of $BaTiO_3$ based films, and might eventually serve as a base to reach or even enhance the large Pockels coefficients of bulk $BaTiO_3$.

CHAPTER 4

Barium titanate enhanced silicon photonic devices

4.1 Background

4.1.1 Basics of silicon photonics

Silicon technology is the most mature semiconductor platform for electronic applications, which results in the smallest structures while handling the largest wafers and obtaining the highest yields. This maturity combined with the expectations for ultra-high data transmission rates, tiny footprints, co-integration with electronic circuits, and very low power consumption strongly motivated the development of complex integrated photonic circuits on silicon [1, 5, 167]. Great progress has been made over the past decade, and numerous building blocks of optical networks are already in an advanced state. One of them are silicon waveguides: The potential of guiding light in silicon at reasonably low losses has been one of the major driving forces in the research field of silicon photonics.

Two physical phenomena are the basis for silicon waveguides: First, silicon shows a transparency window in the near infrared which is compatible with important wavelength regions at $\lambda = 1.3\,\mu m$ and $1.55\,\mu m$ used for telecommunication applications. Second, the high refractive index of silicon $n_{Si} = 3.45$ at $\lambda = 1.55\,\mu m$ [168] leads to a strong light confinement in the waveguide core and consequently enables very small bending radii in the order of a few µm, which allows the design of very compact individual devices and complex optical circuits. In the simplest form, a rectangular-shaped cross section with dimensions similar to the wavelength are etched into silicon to serve as a waveguide (fig. 4.1a). To

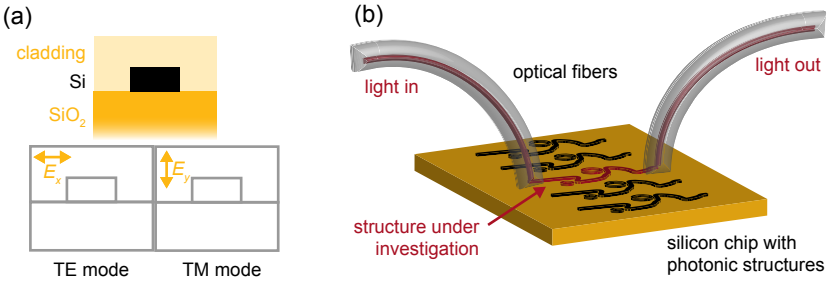

Fig. 4.1 (a) Cross section of a 400 nm-wide silicon photonic waveguide with strongly-confined modes, as seen from the power distribution of the TE and TM mode, respectively. The orientation of the main electric field component of the optical mode is indicated by a yellow arrow. (b) Schematics of a test setup to characterize integrated photonic devices.

avoid leakage into the silicon substrate, the optical mode has to be confined also in the vertical direction. Therefore, silicon-on-insulator (SOI) wafers with a thick ($2-3\,\mu$m) buried oxide (BOX) layer and a typically $\sim$220 nm-thick silicon device layer are used. Figure 4.1a shows the optical power distribution of such single-mode waveguide, supporting only one single TE (transverse-electric) and one single TM (transverse-magnetic) mode. Most optical power of the modes is stored in an electro-magnetic wave with an electric field parallel (TE) or perpendicular to the substrate plane (TM) (see yellow arrows in fig. 4.1a).

Silicon waveguides are the building blocks of many devices in integrated circuits, such as splitters, filters, and resonators. The functionality of these devices is determined by the proper design of how to arrange the waveguides on the chip. Other building blocks however require more complex design and processing steps, for example when targeting active devices such as modulators [8] or switches [169]. In order to investigate the properties of such passive and active devices, test environments as illustrated in fig. 4.1b are commonly used: Optical fibers are utilized to couple light into and out of the chip, thus allowing to probe the optical and electro-optical characteristics of individual elements of a photonic circuit.

The field of silicon photonics is constantly evolving, and many unsolved tasks exist (see section 1.1). A lot of effort is invested in the integration of other materials such as germanium for detectors [13] or III/V layers for lasing [170]. Adding an electro-optical material such as $BaTiO_3$ to silicon photonics would enable a variety of novel devices and functionalities which could drastically reduce the power consumption of tuning elements, enable

high-frequency modulators, and result in ultra-fast switches, as discussed in section 1.2. In this chapter, specific solutions for integrating $BaTiO_3$ into silicon photonic structures will be shown. In particular electro-optical active devices working at high- and low speed are designed, fabricated and experimentally characterized.

4.1.2 State-of-the art electro-optical silicon photonic devices

Due to the strong electro-optical activity (chapter 3), $BaTiO_3$ thin films are well suited for photonic devices whose functionality relies on a change of the refractive index. Examples of such devices are high-speed modulators, switches, and zero-power tuning elements. The Pockels effect offers two features, which make its exploitation for optical devices particularly appealing:

1. The Pockels effect is an ultra-fast effect peresent even in the THz-regime [22]. It therefore provides an excellent option to fabricate modulators and switches working at extremely high speed.
2. The Pockels effect is an electric field effect (eq. (3.1)) which does not require any current flow. Thus, tunable devices with ultra-low power consumption can be envisioned. It should be noted that in real devices charge has to be transferred to the electrodes in order to create an electric field, which is a major contribution to the power consumption of (any) high-speed device. This power consumption is however not an issue when tuning photonic elements: tuning is required to for example compensate temperature drifts which occur on much longer time scales.

Pockels-based high-speed $LiNbO_3$ modulator have been used for decades in the field of telecommunication [20], and are even up to now state-of-the-art [21]. In silicon photonics, such devices have hardly been considered so far because of the vanishing Pockels effect in silicon due to the centro-symmetric crystal structure, and the unavailability of electro-optical active materials on silicon. An exception is the integration of electro-optically active polymers that are spin-coated as a cladding layer on top of slot-waveguides, resulting in high modulation speeds of $\sim$40 Gb/s [152, 171]. The integration of such devices into the processing line of silicon photonic circuits is however difficult due to the low thermal budget of polymers. Therefore, other physical effects have been exploited in silicon-based electro-optical devices [8], such as the plasma dispersion-effect, the quantum-confined Stark effect (QCSE) [172], the Franz-Keldysh effect [173], or thermo-optical effects [17, 174].

The plasma dispersion-effect describes the dependence of the refractive index from the charge carrier concentration [8]. It is the most widely used effect for realizing silicon photonic modulators, mainly because no other materials

than silicon are required. This makes the process flow compatible with any CMOS fabrication line. However, such devices rely on a variation of the charge carrier profile, which involves rather slow carrier recombination processes in silicon in the ∼ns regime. By driving the modulator in the depletion regime, this limitation has been addressed and high speed modulators operating from 40 Gb/s [178] up to 60 Gb/s [14] were demonstrated (table 4.1). One major drawback of using the plasma dispersion effect is the change of the absorption when applying a voltage. The variation prevents the utilization of higher order modulation formats which are commonly used in telecommunication.

Both the QCSE and the Franz-Keldysh effect are field-effects that rely on the change of a semiconductor bandgap and thus the absorption as a function of the applied electric field. The Franz-Keldysh effect is the limit of the QCSE for very thick layers. Electro-absorption based modulators can potentially be more power efficient than plasma-dispersion based modulators [8]. Yet, another material than silicon is required for their realization, which complicates the fabrication process. The QCSE has nevertheless been explored in particular in Ge/SiGe multi-quantum wells on silicon substrates [19, 172] and high-speed modulation at 10 GHz has been shown [179]. Despite these promising results, only few waveguide-based electro-absorption devices on silicon were reported up to now [180].

Noteworthy are some recent studies of introducing a strain gradient into silicon waveguides by using a well-tuned Si_3N_4 cladding. These strain gradients

Table 4.1 State-of-the art silicon photonic Mach-Zehnder modulator with characteristic properties: voltage × length product ($V_\pi \times L$), bandwidth, extinction ratio (r_e), and insertion loss (on-chip loss). Bulk-$LiNbO_3$ modulators are listed for comparison.

	State of the art silicon photonic MZ-modulator			
year	2013 [14]	2012 [175]	2013 [152]	2009/2013
material	silicon	silicon	polymer	$LiNbO_3$
physical effect	carrier depletion	carrier depletion	Pockels	Pockels
$V_\pi \times L$ [V mm]	16-20	20-30	2.7	53.5 [176]
bandwidth [GHz]	60	20	10	33 [177]
r_e [dB]	3.6	4.2	4-11	>20 [177]
insertion loss [dB]	1.9	13.7	9	3.2[a] [177]

a off-chip insertion loss

break the symmetry in the crystalline structure and result in a non-vanishing Pockels effect in silicon [25] that has been used to fabricate electro-optical modulators [26]. The effective Pockels effect is however significantly smaller ($r_{\text{eff}} \approx 1.7\,\text{pm/V}$) [26] than in polymer or $LiNbO_3$-based devices, and in particular smaller than of $BaTiO_3$ films as presented in this work (chapter 3). Typical figures of merit for state-of-the art silicon photonic modulators based on nonlinear polymers and the plasma dispersion effect are listed in table 4.1. Bulk-$LiNbO_3$ modulators are included for comparison.

Beside these high-speed applications, low speed tuning is an important topic in silicon photonic networks. In particular resonant structures as present for example in filters require active tuning due to size variations during the fabrication and temperature variations during operation. For the latter, local variations caused by hot spots on the chip as well as global variations originating from different temperatures of the environment have to be compensated. Commonly, two approaches are followed to tackle these tasks: First, athermal cladding layers with a negative thermo-optic effect are used. When properly designed, the cladding can cancel the positive thermo-optical effect of silicon waveguides and make the device characteristics independent of the temperature [16]. Deviations in the device geometry originating from process variations can however not be compensated. Second, thermal heaters are placed on top of critical devices to shift the wavelength of resonant structures by the thermo-optic effect [17, 18]. Although this approach can also be used to compensate fabrication tolerances, it is rather power consuming ($\sim$40 mW per 10 °C [174]) and hence not suited for highly integrated devices. Nonlinear optical materials provide another way to tune the optical mode index by applying an electric field without any current flow, being a very power efficient solution. Furthermore, both directions, tuning and trimming, are addressed when the linear electro-optical effect is utilized.

$BaTiO_3$-based silicon photonic devices offer an excellent novel way to address both domains, high-speed modulation and low-speed, zero-power tuning. Possible ways to implement such layers into silicon photonic structures, as well as an analysis of the expected device performance for different geometries are discussed in detail in sections 4.3 and 4.3.4. The fabrication and characterization of first $BaTiO_3$-based silicon photonic passive and active devices is shown in the subsequent sections (sections 4.4 and 4.5.1).

4.2 Workflow and strategy

The integration of $BaTiO_3$ layers into silicon photonic devices is a novel approach, and no prior studies are available. Also no comparable electro-optical-active functional oxide has previously been utilized in silicon photonic structures.

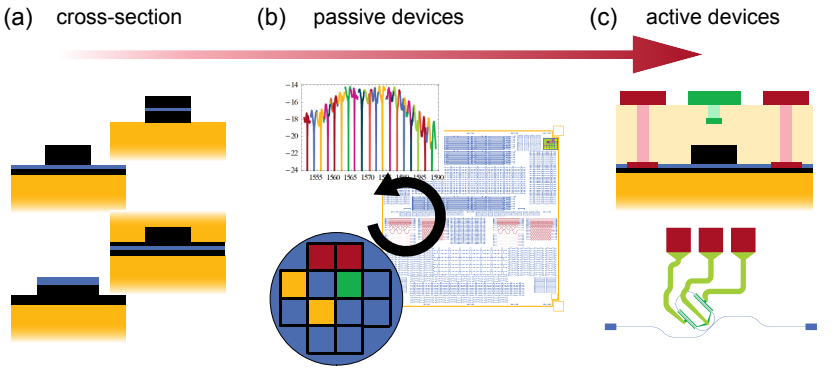

Fig. 4.2 Strategy to obtain active $BaTiO_3$-based integrated photonic devices: (a) Design of the waveguide-cross section to embed $BaTiO_3$ efficiently into silicon photonic structures. (b) Die-by-die processing and characterization of passive devices, and iterative adjustment of the mask-design. (c) Full fabrication of active devices including electrodes based on the parameters obtained from the passive measurements.

Therefore, several challenges have to be tackled when targeting a $BaTiO_3$-based electro-optical-active photonic demonstrator:

1. Design of cross section. The cross section of silicon waveguides with an embedded $BaTiO_3$ layer (fig. 4.2a) differs significantly from standard waveguides. In principle, $BaTiO_3$ could simply be used as a cladding. Due to the low refractive index, the efficiency of such structure would be rather low. Therefore, as a first step, a proper cross section is defined, taking into account the optical confinement, process compatibility, bending losses, and single mode operation. The issues and solutions are discussed in sections 4.3 and 4.3.2.
2. Realization of a "$BaTiO_3$-based photonic platform". Several passive building blocks to enable simple test devices are developed. Such building blocks are grating couplers, directional couplers, curved waveguides, ring resonators, and Mach-Zehnder interferometers (section 4.3.3). These devices are needed because the same layer stack is used for the whole photonic circuit and not only for the region of active devices, in order to keep the fabrication process as simple as possible.
3. Fabrication of active devices. Based on the results of the passive devices, more complex active structures (fig. 4.2c) involving additional process

steps are designed, fabricated, and characterized.

Two different strategies exist for handling the fabrication flow: First, a wafer-by-wafer route benefits from simplified processing steps because many tools are optimized for handling full wafers, or even require full wafers (such as laser lithography). The drawback of that strategy is the requirement of many $BaTiO_3$/Si wafers to test individual process steps and to iteratively adjust the design based on experimental results. This drawback is severe since the growth of $BaTiO_3$ layers is at the current stage a rather slow process (∼1 wafer/day), limited by the tools available for this work.

A second strategy, a die-by-die processing (fig. 4.2b), is therefore chosen in order to significantly reduce the requirements on the epitaxial growth. Only single dies are iteratively processed without dicing the wafer into pieces in order to keep the compatibility to all tools (details in section 4.4).

4.3 Device design

4.3.1 Waveguide cross section

The need of a slot waveguide structure

The simplest way to integrate barium titanate into silicon waveguides is to deposit $BaTiO_3$ as a cladding (fig. 4.3a). This configuration however suffers from a rather low confinement Γ_{BTO} of the optical power in the $BaTiO_3$ layer due to the large refractive index of silicon ($n_{Si} = 3.45$) compared to $BaTiO_3$ ($n_{BTO} \approx 2.26$, table 3.2) at $\lambda = 1.55\,\mu m$. Γ is the integrated power of the Poynting vector in a specific area of the waveguide, normalized by the total power of the mode. For typical silicon waveguide dimensions ($400\,nm \times 220\,nm$) and a $BaTiO_3$ thickness of 50 nm, the confinement is only $\Gamma_{BTO,TE} = 6.7\,\%$ for the TE, and $\Gamma_{BTO,TM} = 6.0\,\%$ for the TM mode. Hence, for active devices, the change of the effective mode index is reduced by a factor of ∼15 compared to the refractive index change in the $BaTiO_3$ layer.

The confinement factor within a material of low refractive index n can strongly be increased by embedding a thin layer between two high-n layers [181]. Figure 4.3b shows an example of such so-called “slot waveguide” applied on a $BaTiO_3$/Si material system with an additional top-silicon layer. The confinement in this structure ($\Gamma_{BTO,TM} = 24.8\,\%$, $\Gamma_{BTO,TE} = 10.9\,\%$) is significantly enhanced compared to the cladded version. Additionally, slot waveguides provide a way to apply very strong electric fields across the narrow slot by using both silicon layers as electrodes, as demonstrated with polymer filled slot waveguides [152].

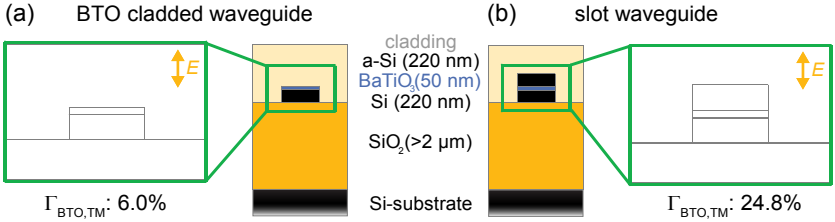

Fig. 4.3 Comparison of the light confinement Γ_{BTO} in the $BaTiO_3$ layer (a) in a standard silicon photonic waveguide with $BaTiO_3$ as a cladding and (b) in a slot-waveguide structure. In both cases, the waveguides have a width of 400 nm and support multiple TE modes, but only one TM mode. The direction of the major electric-field component of the modes is indicated in the profiles.

In the next sections, the physical background of slot waveguides and the application on the $BaTiO_3$/SOI material system is discussed. The design of possible cross sections is presented with strong considerations of the feasibility of fabricating such structures.

Physical background of slot waveguides

The concept of slot waveguides was first theoretically suggested by Almeida *et al.* [181], and experimentally realized only a short time afterwards [182]. The strong field confinement in slot waveguides results from the continuity of the $D_\perp$ component of the electric displacement field perpendicular to an (uncharged) interface between two materials, according to Maxwell's equations. For materials with different permittivity ϵ, a discontinuity of the normal component of the electric field $E_\perp$ occurs

$$\epsilon_{\mathrm{low}} E_{\perp,\mathrm{low}} = D_{\perp,\mathrm{low}} = D_{\perp,\mathrm{high}} = \epsilon_{\mathrm{high}} E_{\perp,\mathrm{high}} \tag{4.1}$$

$$E_{\perp,\mathrm{low}} = \frac{\epsilon_{\mathrm{high}}}{\epsilon_{\mathrm{low}}} E_{\perp,\mathrm{high}} = \frac{n^2_{\mathrm{high}}}{n^2_{\mathrm{low}}} E_{\perp,\mathrm{high}} \tag{4.2}$$

where the indices "low" and "high" refers to the low-n and high-n material, respectively, and where the relationship $\epsilon = n^2$ is employed [161]. The electric field at the $BaTiO_3$/Si-interface is thus enhanced by $n^2_{\mathrm{Si}}/n^2_{\mathrm{BTO}} \approx 2.3$ within the $BaTiO_3$ layer. This enhancement however decays exponentially with the distance from the interface [181]. In a slot waveguide, two symmetric interfaces are separated closer than the decay length, which results in a nearly constant high field over the full slot region, as shown in fig. 4.4. The key task in designing

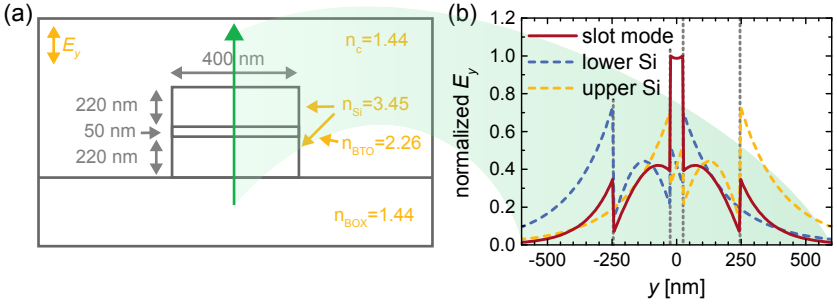

Fig. 4.4 (a) Power distribution of the TM-mode in a horizontal slot waveguide with dimensions, refractive indices, and the main component of the electric field E_y as indicated in the figure. (b) Magnitude of E_y of the optical field in the center (green arrow in (b)) of the waveguide. The dashed lines correspond to E_y of modes with the $BaTiO_3$ layer and the lower (blue) or upper (yellow) silicon block only. The second silicon block is replaced by SiO_2. The vertical dotted gray lines indicate the interfaces between the buried oxide (BOX), silicon, $BaTiO_3$, silicon, and the cladding, respectively.

a slot waveguide is to dimension the different layer thicknesses in a way to achieve a maximal power confinement in the low-n material [181].

Vertical versus horizontal slot design

Slot waveguides can be fabricated either with a horizontal [182] or with a vertical [152] slot geometry (fig. 4.5). Vertical slots benefit from the potential to fill them with liquid materials, for example to embed electro-optical active polymers [152] or to detect biological reactants [183]. Contrary, the waveguide propagation losses α_p are typically higher in vertical ($\alpha_p > 12\,\mathrm{dB/cm}$, [183, 184]) than in horizontal slots ($\alpha_p < 7\,\mathrm{dB/cm}$, [185]) due to the strong influence of the roughness of the slot interfaces on the propagation: The sidewall roughness caused by the etching steps in vertical slots is typically much larger than the interfacial roughness between two smooth layers in horizontal slot waveguides.

For silicon slot waveguides, both silicon blocks in a vertical slot can be used as electrodes, resulting in a high electric field in the slot region [152]. Contacting both silicon blocks in the horizontal configuration is more challenging. For the current work, a horizontal slot structure is followed because only this structure is compatible with the fabrication method: By means of MBE, vertical slots with high aspect ratio cause shadowing effects, and no homogenous

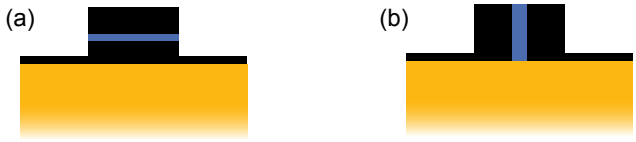

Fig. 4.5 Examples of cross-sections for a (a) horizontal and (b) vertical slot waveguide. The thin, unetched silicon layer is not needed for passive waveguides, but can be used to electrically contact the silicon block(s) in active devices.

deposition in prestructured devices is possible. Other methods such as atomic layer deposition or chemical vapor deposition would be required. In contrast, horizontal structures can be realized by growing $BaTiO_3$/Si thin films via MBE as discussed in chapter 2 and structuring them afterwards (section 4.4).

Maximizing the $BaTiO_3$-light confinement

The mode profile of slot waveguides is calculated by systematically varying the geometry in order to optimize the cross section. The targets of this optimization procedure are

- Maximization of the optical confinement in the $BaTiO_3$ layer
- Single TM-mode operation
- Compatibility of the fabrication route to available processing tools
- Reasonable robustness of the waveguides against variations of the geometry during fabrication.

The simulations are predominantly performed with the commercial mode solver *FieldDesigner* by *PhoeniX Software* using a field-mode-matching and finite difference solving method. The latter is applied when propagation losses due to metal electrodes or bent waveguides are calculated.

Type of waveguide The starting layer stack for all simulations consists of a SOI wafer with a thick BOX layer (2 µm), a device silicon layer of variable thickness, a 50 nm-thick $BaTiO_3$-layer, a top-silicon layer of variable thickness, and a SiO_2-cladding (fig. 4.6a). The 4 nm-thick $SrTiO_3$ film is included in the $BaTiO_3$ layer in the simulations due to the similar refractive index ($n_{STO} = 2.28$ at $\lambda = 1.55$ µm [168]) compared to $BaTiO_3$ ($n_{BTO} \approx 2.26$, table 3.2). 5 nm-thick SiO_2 layers are embedded at both interfaces of the $BaTiO_3$ layer to account for interfacial SiO_2 that establishes during the growth (fig. 2.15), and to account

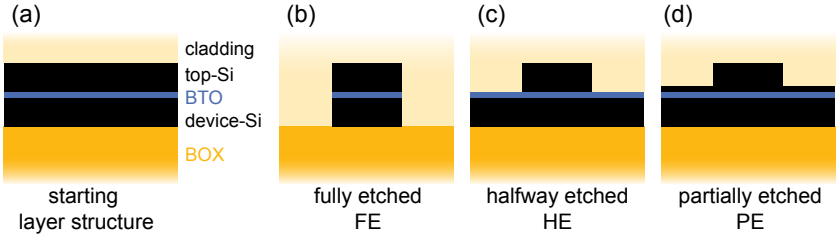

Fig. 4.6 (a) Starting structure for all waveguide simulations. Cross section of a (a) fully etched (FE), (b) halfway etched (HE), and (c) partially etched waveguide (PE).

for a SiO_2 layer that is deposited prior to the top-silicon deposition to avoid contamination of the Si-deposition chamber (see section 4.4). Depending on the processing route, the top-silicon layer is hydrogenated amorphous silicon (*a*-Si:H), or crystalline silicon (*c*-Si) (section 4.4). Literature values of the refractive indices are used, except for $BaTiO_3$ and *a*-Si:H for which experimental values obtained via spectroscopic ellipsometry are applied.

Etch-depth First, different etch stop levels within the initial layer stack (fig. 4.6a) are considered. Notably, no etch process for $BaTiO_3$ has been reported that yields smooth sidewalls as required for low-loss waveguiding. Studies on etching $Ba_xSr_{1-x}TiO_3$ thin films are focused on isotropic wet chemical processes, which would under-etch the slot, Ar-sputtering [186] with low selectivity against silicon, and dry etching [187, 188] with low selectivity against HSQ (hydrogen silsesquioxane), which is used as etching mask (section 4.4). Therefore, cross sections that do not rely on a $BaTiO_3$ etching step are preferred among the possible waveguide layouts:

- Fully etched waveguides ("FE", fig. 4.6b). The high optical confinement in the waveguide core of fully etched waveguides allows small bending radii. However, the unexplored etching process for $BaTiO_3$ might result in a high sidewall roughness and consequently in high propagation losses. Furthermore, fully etched structures suffer from a low electric field strength inside the $BaTiO_3$ slot due to its high permittivity (section 2.5) compared to the SiO_2-cladding layer (discussed later, in fig. 4.14).
- Halfway etched waveguides ("HE", fig. 4.6c). Etching only the top-silicon layer results in strip loaded waveguides that generally have lower propagation losses than fully etched waveguides. On the other hand HE-type waveguides suffer from higher bending losses at the same bending radius

compared to FE-type waveguides. Compared to FE waveguides, the electric field produced by two electrodes parallel to the waveguide is rather strong since no voltage drop in the cladding occurs (discussed later, in fig. 4.14). This cross section is the structure of choice for most of the fabricated devices throughout this thesis.

- Partially etched waveguides ("PE", fig. 4.6d). Compared to HE waveguides, not completely etching the top-silicon results in a laterally less confined mode and thus in larger bending losses. The main advantage of this structure is the possibility to utilize the top-silicon block as an electrode which is contacted next to the waveguide via the thin, unetched top-silicon layer. Applying a voltage relative to the device silicon layer results in large electric fields across the thin $BaTiO_3$ layer. Structures of this type are experimentally realized in this work.

Due to their good process compatibility without any $BaTiO_3$ etching step, the properties of both HE and PE waveguides is simulated in more detail in the following sections.

Thickness of device-silicon Numerous geometrical parameters can be varied in the cross sections discussed above (fig. 4.6). The thickness of the device-silicon (fig. 4.6a) layer $t_{\text{d-Si}}$ is defined by the initial SOI-wafer, and cannot be changed during the processing simply by varying the mask layouts or the deposition conditions. As a first step of the waveguide optimization, the influence of $t_{\text{d-Si}}$ is investigated to allow a proper choice of the SOI substrate.

To reduce the parameter space, the thickness of the $BaTiO_3$ layer is fixed to $t_{\text{BTO}} = 50\,\text{nm}$ as typically used during the growth. The waveguide width is set to $w_{\text{WG}} = 400\,\text{nm}$, which is similar to commonly used silicon waveguides. Variations of these parameters did not yield radically different conclusions. When varying the experimentally easily changeable top-silicon thickness $t_{\text{t-Si}}$ simultaneously with the device silicon thickness $t_{\text{d-Si}}$ in HE-type waveguides (fig. 4.7), a large regime without any supported TM modes is visible. In particular no TM modes are guided for thick device-Si layers, where the lateral confinement in the waveguides is small. Single TM-mode operation is only possible in a small regime (highlighted in yellow, fig. 4.7). This regime is very similar for PE-type waveguides (not shown).

The experimental realization of the structures is limited by the availability of substrates with proper dimensions in $t_{\text{d-Si}}$. The only two commercially available substrate types in that thickness regime with a $> 2\,\mu\text{m}$-thick BOX layer are indicated in fig. 4.7 (dashed, red lines). The SOI wafer type with $t_{\text{d-Si}} = 70\,\text{nm}$ is compatible with single mode operation and is therefore used for the experiments.

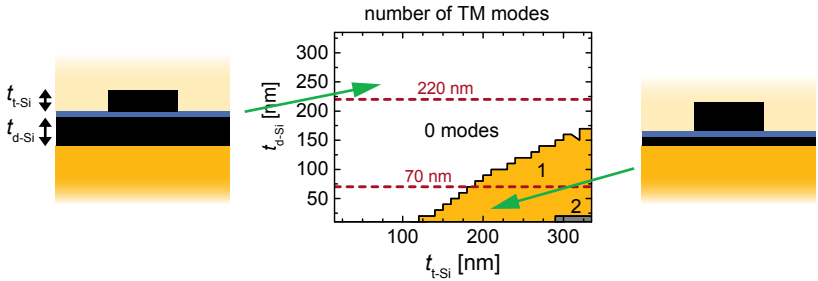

Fig. 4.7 Effect of the thicknesses of the device- and top-silicon layers on the presence of TM modes. The $BaTiO_3$ thickness and waveguide width is fixed to $t_{BTO} = 50\,nm$ and $w_{WG} = 400\,nm$, respectively. The dashed lines indicate commercially available SOI wafers with a thick ($> 2\,\mu m$) BOX layer. Cross sections for two regimes marked with the green arrows are illustrated on the sides.

Variation of waveguide dimensions While keeping $t_{BTO} = 50\,nm$ and $t_{d\text{-}Si} = 70\,nm$, the thickness of the top-silicon layer $t_{t\text{-}Si}$ and the waveguide width w_{WG} are varied since they can easily be modified in the experiment. As shown in the highlighted region in fig. 4.8b, the waveguide only guides a single TM-mode in a certain regime of both parameters. Outside this regime, either no or multiple TM-modes are guided.

The confinement factor Γ_{BTO} for the single-TM mode region is color encoded in fig. 4.8b: Γ_{BTO} becomes large for thin top-silicon layers and wide waveguides. However, the process window to obtain single-TM-mode operation also becomes smaller in that range, which means an additional risk for the fabrication. Not only is it hard to control the *a*-Si:H layer thickness better than $\Delta t_{t\text{-}Si} < 10\,nm$, also the refractive index of the layer can vary depending on the hydrogen content and deposition conditions. The refractive index has direct impact on the region of single-mode operation. Therefore, the design point is set to $t_{t\text{-}Si} = 210\,nm$ and $w_{WG} = 575\,nm$ (green lines in fig. 4.8b), which provides a good tradeoff between a strong confinement ($\Gamma_{BTO} = 19.9\,\%$) and reasonably high process tolerances. The effective index and the group index of the TM-mode for such geometry is $n_{eff,TM} = 2.21$ and $n_{g,TM} = 3.67$, respectively.

When calculating Γ_{BTO} for a specific waveguide width ($w_{WG} = 575\,nm$) as a function of the thickness of the top-silicon layer (fig. 4.8d), a clear maximum for the TM mode is found. Also the much larger confinement compared to the TE-modes is visible, for which no field enhancement due the refractive index contrast is present. The different mode profiles (fig. 4.8c) for specific

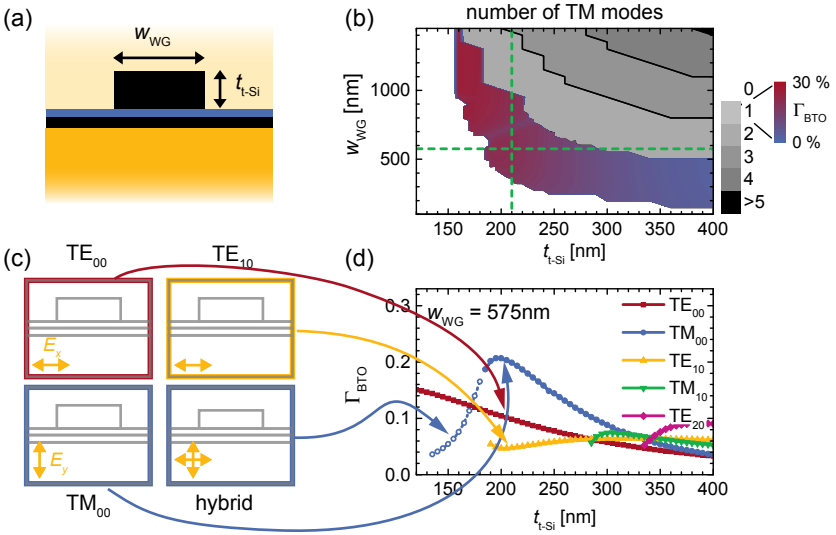

Fig. 4.8 Variation of the HE-waveguide cross section. (a) Change of the waveguide width w_{WG} and the thickness of the top-silicon $t_{t\text{-}Si}$ layer. (b) Regions with different numbers of TM modes. The colored area corresponds to the single-TM-mode regime where the confinement factor Γ_{BTO} is color-encoded. The dashed green lines are the targeted design point. (c) Magnitude of the Poynting vector of modes corresponding to different waveguide geometries, and different polarizations. The yellow arrows indicate the direction of the major electric field component of the modes. The hybrid mode contains similar power in the E_x (TE) and E_y (TM) field. (d) Γ_{BTO} for a 575 nm-wide waveguide. Open symbols corresponds to poorly confined hybrid TE/TM modes.

$t_{t\text{-}Si}$-thicknesses show the field enhancement in the $BaTiO_3$ layer and the low optical confinement in the waveguide for modes simulated at the edges to the cut-off condition. These modes might disappear if the fabricated waveguide is slightly different from the simulations due to process variations. The low mode confinement also prohibits small bending radii and hence makes the waveguides not applicable for small photonic structures.

Partially-etched (PE) waveguides In contrast to HE-waveguides discussed in the previous section, PE waveguides provide a way to use the upper silicon block

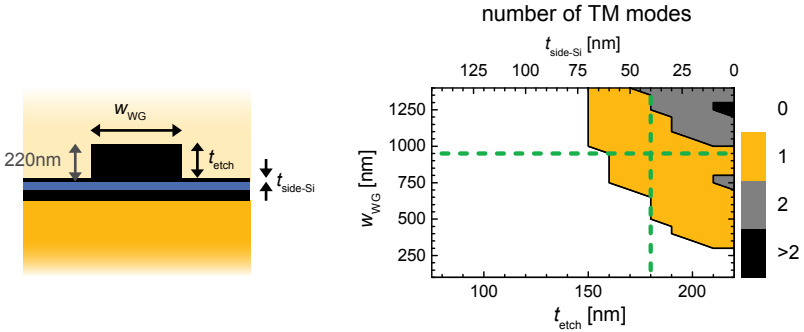

Fig. 4.9 Number of modes for a partially-etched (PE) waveguide as a function of the etch depth t_{etch} and the width of the waveguide w_{WG}. The total thickness of the device silicon is fixed at $t_{\text{t-Si}} = 220\,\mathrm{nm}$ ($t_{\mathrm{etch}} + t_{\text{side-Si}} = t_{\text{t-Si}}$). The green lines indicate the design point for PE-waveguides.

as an electrode. The block can be electrically contacted with metal electrodes on the side of the waveguide via a thin, unetched silicon layer (fig. 4.9). By doping the top-silicon layer properly, a balance between high-speed (highly doped) and low absorption (lowly doped) has to be found. For low speed operation, the slightly doped silicon of a standard photonics SOI wafers ($\rho \approx 10\,\Omega\,\mathrm{cm}$) could be used as electrodes to create a strong electric field in the $BaTiO_3$ layer, which has a significantly higher resistivity ($\rho \approx 10^{10}\,\Omega\,\mathrm{cm}$, section 2.5).

On the one hand, the thickness $t_{\text{side-Si}}$ of the unetched silicon should be as large as possible in order to minimize the series resistance between the metal pads and the waveguide core. On the other hand, the TM-mode will laterally be less confined and eventually not be guided anymore if $t_{\text{side-Si}}$ is too high. Figure 4.9 shows the region of single-TM operation, for different etch depth t_{etch} and waveguide width w_{WG}. The top-silicon thickness is kept at $t_{\text{t-Si}} = 220\,\mathrm{nm}$. This restriction originates from the availability of regular SOI wafers, which are needed in order to obtain a slightly conductive top-silicon layer via wafer bonding (section 4.4). To ensure single TM mode operation, the un-etched silicon layer has to be kept thin, and the waveguide width has to be increased compared to HE-waveguides. The design point is set to $w_{\mathrm{WG}} = 950\,\mathrm{nm}$ and $t_{\text{side-Si}} = 40\,\mathrm{nm}$, as a compromise between process robustness, a reasonable thickness for electrical contacts, and a large $\Gamma_{\mathrm{BTO}} = 21\,\%$ (not shown here).

Conclusion for geometry variations The previous paragraphs discuss different aspects for designing an "optimized" waveguide cross section for $BaTiO_3$-based

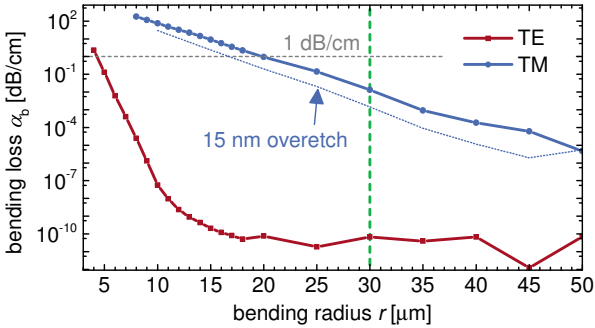

Fig. 4.10 Simulated bending losses for waveguides with HE cross section profile. $\alpha_b = 1\,\mathrm{dB/cm}$ serves as upper limit when analyzing the bending losses, and is indicated with a dashed gray line. The dashed blue line shows a reduction of the losses by over-etching 15 nm into the $BaTiO_3$ layer. The dashed green line indicates the design point for active devices ($r = 30\,\mu\mathrm{m}$).

slot waveguides. Two solutions are developed, a halfway-etched (HE, fig. 4.6c), and a partially-etched (PE, fig. 4.6d) slot waveguide. Both structures provide a strong field enhancement in the $BaTiO_3$ slot region, single-TM mode operation, a decent tolerance to variations of the dimensions during the fabrication, and avoid any $BaTiO_3$-etching steps.

Bending losses of waveguides

Compared to fully etched waveguides (fig. 4.6b), the modes in halfway etched waveguides are laterally less confined. This is in particular true for TM-modes. The simulated losses for HE-type waveguides for different bending radii r confirm this behavior (fig. 4.10): While TE modes exhibit low bending losses of $\alpha_b = 1\,\mathrm{dB/cm}$ for $r \sim 4.5\,\mu\mathrm{m}$, TM-modes require a significantly larger bending radius of $r \sim 20\,\mu\mathrm{m}$ to achieve similar bending losses. As indicated in fig. 4.10, slightly over-etching into the $BaTiO_3$ layer can be utilized to reduce the bending radii while keeping the losses constant due to a better mode confinement.

Since a high integration density with aggressively scaled devices is not in the focus of this thesis, the bending radii in active devices are designed as $r \geq 30\,\mu\mathrm{m}$ with negligible bending losses ($\alpha_{b,TM} \approx 0.01\,\mathrm{dB/cm}$). The absolute losses for a 90° bend are as low as $6 \times 10^{-5}\,\mathrm{dB}$. The modal overlap between a 30 µm-bend and a straight waveguide is very high (99.92 %), and consequently no significant additional losses are expected. For non-active devices, such as

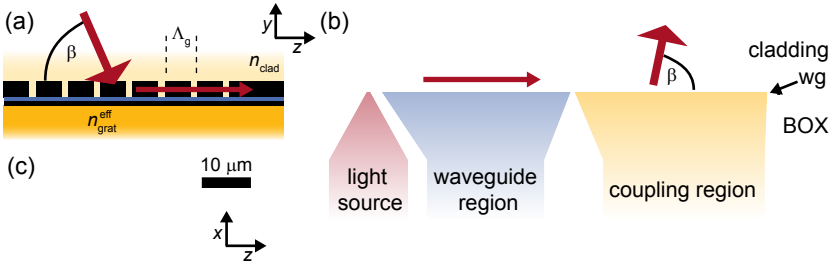

Fig. 4.11 (a) Cross section of a grating coupler: Light directed at an angle β onto the grating is diffracted into the plane of the waveguide. (b) FDTD-simulation using MEEP for a grating coupler with a duty cycle of $D = 0.8$ and a HE-waveguide cross section. For the simulation, a point source is placed in the waveguide, and the light coupled out of the grating is considered. The color code red/blue indicates the magnitude and phase of the electric E_y field. (c) Mask layout of a focusing grating coupler used in the experiments. Anti-reflection wedges on the left side reduce back reflections into the waveguide [10].

connecting waveguides, very large bending radii of 100 µm are used.

4.3.2 Grating couplers

Grating coupler provide a way to couple light into and out of a silicon photonic circuit with optical fibers in close proximity to the surface (fig. 4.1b). In contrast to butt coupling, they enable the characterization of individual devices placed anywhere on a chip. The untypical cross section of the $BaTiO_3$ slot waveguides prohibited the usage of standard silicon photonic couplers, but required a redesign of the grating dimensions as explained in the following section.

Cross sectional design

The key design parameters for the grating couplers used in this work are the grating period Λ_g (fig. 4.11a) and the duty cycle D. The duty cycle is defined as ratio between the length of an unetched grating tooth and Λ_g. The etching depth, as well as the cladding are defined by the waveguide cross section and are not modified in the coupling region to avoid additional processing steps.

Different strategies can be followed to properly design photonic grating couplers. One of them is the utilization of finite-difference time-domain simulation

tools in combination with photonic Eigenmode solvers [10, 189] to take into account the exact two dimensional cross-sectional structure. Alternatively, the grating region can be treated as an effective material with refractive index $n_{\mathrm{grat}}^{\mathrm{eff}}$. An analytical solution to describe the diffraction of a wave at a grating can be applied [190]

$$n_{\mathrm{grat}}^{\mathrm{eff}} = n_{\mathrm{clad}} \cos(\beta) + \lambda/\Lambda_{\mathrm{g}}, \tag{4.3}$$

where β is the angle of incidence as defined in fig. 4.11a and n_{clad} the refractive index of the cladding. The approximation of the grating region with a homogeneous "effective" material results in a deviation between the two simulation approaches. Both calculation strategies are followed in the current work, but only small differences for the structure under investigation are found. Motivated by the much smaller computational effort, the algebraic solution is thus used for the design process.

In a first step, $n_{\mathrm{grat}}^{\mathrm{eff}}$ is calculated as a function of the duty cycle using a mode solver. The effective refractive indices of the etched layers $n_{\mathrm{etched}}^{\mathrm{eff}}$ are therefore defined as mixtures between the refractive index of the unetched layers in the grating teeth and the cladding in the gaps of the grating:

$$n_{\mathrm{etched}}^{\mathrm{eff}}(D) = D \times n_{\mathrm{unetched}} + (1 - D)\, n_{\mathrm{clad}}. \tag{4.4}$$

Depending on the etch depth, this approximation is applied for the top-silicon, $BaTiO_3$, and device-silicon layer. Layers that are not etched in the grating region are treated similar to the previous simulations of the waveguide geometry. The cross section in the coupling area is considered as a planar waveguide because of the large width of the couplers ($\sim 10\,\mu\mathrm{m} \gg \lambda$). Hence, a one-dimensional mode solver is used.

$\Lambda_{\mathrm{g}}(\lambda, D, \beta)$ is obtained by replacing $n_{\mathrm{grat}}^{\mathrm{eff}}$ in eq. (4.3) with the solutions of the mode solver where D is embedded via eq. (4.4). The center wavelength is fixed at $\lambda = 1550\,\mathrm{nm}$, and the angle of incidence is set to $\beta = 80°$ to reduce reflections from the fiber back into the grating compared to a perpendicular angle of incidence. The duty cycle determines the diffraction strength of a single tooth, and the reflection of the grating [189]. The grating is simulated for different values of D using the FDTD (finite-difference time-domain) simulation software MEEP [191]. A value of $D \approx 0.8$ results in planar waves in the coupling region, and is therefore used in the following considerations. No full quantitative analysis is performed per FDTD, in particular the spot size of the diffracted light is not further adjusted in order to match the size of the fiber core for example by chirping the grating [6].

The grating period Λ_{g} is calculated as a function of the etch depth t_{etch} in

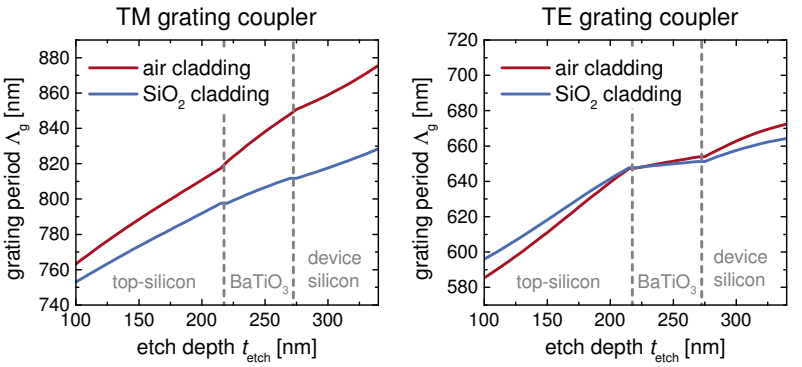

Fig. 4.12 Simulated grating period Λ_g of grating couplers as a function of the etching depth. The simulation is based on HE-waveguides with varying etch depth. The couplers are designed for the wavelength $\lambda = 1550\,\text{nm}$, a coupling angle of $\beta = 80°$, and a duty cycle of $D = 0.8$.

order to take into account both the HE and PE waveguide structures, as well as effects of potential under- and over etching during the fabrication (fig. 4.12). Solutions for TE and TM modes, and different cladding materials are shown. Due to the higher mode index, the grating period of the TE couplers is smaller than the TM couplers.

Mask layout

Focusing grating couplers are used to keep the footprint of the couplers low and thus to obtain a high density of test devices and a low exposure time during the ebeam lithography step. For an optimal design, the bending of the grating teeth has satisfy an algebraic equation of the sixth order as described by Waldhäusl *et al.* [190]. A simplified elliptical equation [190] is used to design the mask layout of the couplers (fig. 4.11c). Anti-reflection wedges are added at the end of the couplers in order reduce back reflection into the waveguide [10], which eventually results in unwanted interference patterns in the transmission spectra.

4.3.3 Directional couplers

Directional couplers provide a way to transfer optical power between two adjacent waveguides. They can be used as basic building block of Mach-

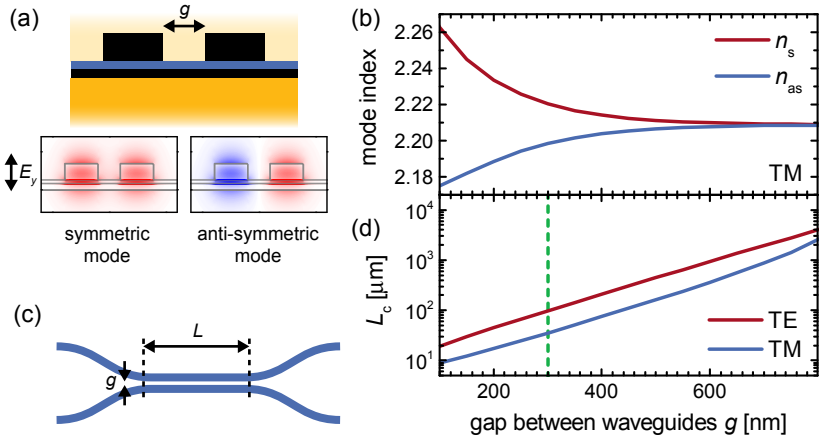

Fig. 4.13 Simulation of directional couplers. (a) Two symmetric waveguides separated by a gap g guide a symmetric and an anti-symmetric supermode. The red/blue colors represent the sign and magnitude of the electric field component E_y perpendicular to the film, as indicated on the left. (b) Mode index n_s and n_{as} of the symmetric and the anti-symmetric TM-mode, respectively, as a function of the gap size. (c) Illustration of the top view of a directional coupler. (d) Calculated coupling length L_c for TE and TM couplers, respectively. The green line indicates the design point for active TM-devices.

Zehnder (MZ) interferometers, which are among the different types active device that are targeted in this thesis. The specific cross section of the $BaTiO_3$ slot waveguides requires a customized design of the couplers.

Directional couplers are well described by coupled mode theory, which can be used to obtain coupling coefficients and energy transfer functions for even complex, asymmetric couplers with multiple waveguides [192]. In the case of a symmetric coupler with two waveguides, a simplified treatment is possible [192]: In close proximity of two single-mode waveguides, a symmetric and an anti-symmetric supermode are formed (fig. 4.13a). Their effective indices n_s and n_{as} depend on the gap size g between both waveguides and are generally different (fig. 4.13a). The superposition of both modes with the same phase φ_0 corresponds to the situation when all power is confined in one of the two waveguides. After propagating a distance L along the waveguide pairs, a phase delay of $\Delta\varphi$ establishes between both modes due to the different propagation constants. When the phase shift is $\Delta\varphi = \pi$, the relative phase of the electric

field between both modes is reversed compared to the initial situation at φ_0. The optical power of the superposition of both modes is thus confined in the other waveguide.

The length L_c (fig. 4.13c) of a coupler that transfers all energy from one waveguide to the other can be calculated by [193]

$$L_c = \frac{\lambda}{2|n_s - n_{as}|}. \tag{4.5}$$

The coupling length for $BaTiO_3$-waveguides is plotted in fig. 4.13c: The TM-mode is laterally more expanded than the TE-mode, which results in a stronger coupling coefficient and thus in shorter L_c. Longer couplers are more tolerant to small size variations during the fabrication. Therefore, $g = 300\,\text{nm}$ and accordingly $L_c = 36\,\mu\text{m}$ is targeted for active TM-devices. For passive devices also smaller gap sizes are tested (section 4.5.5).

Notably, symmetric directional couplers can ideally transfer 100 % of the power from one waveguide to the other one. While eq. (4.5) only represents the shortest coupling length, it can be increased by multiples of $2L_c$ [192].

4.3.4 Active devices

In the following section the design and estimated performance of electro-optical active devices that utilize the Pockels effect of the $BaTiO_3$ layer are discussed. If not mentioned differently, waveguide cross sections of HE-type (fig. 4.6) are used. The behavior of PE-waveguides differs significantly only for specific electric field configurations, as highlighted accordingly.

Placement of electrodes

In order to vary the effective index of the optical mode, an electric field has to be applied to the $BaTiO_3$ region within the waveguide core. Two substantially different electrode geometries can be designed, resulting in a horizontal, in-plane electric field (fig. 4.14a), or in a vertical out-of-plane electric field (fig. 4.14b). The proper choice of the electric field configuration depends on the type of application and on the details of the $BaTiO_3$ microstructure, as discussed below.

In-plane electric field A horizontal electric field is obtained by placing two electrodes parallel to the waveguide on top of the $BaTiO_3$ layer (fig. 4.14a). A waveguide having such in-plane (x-direction) electric field configuration is marked with a $\parallel$-sign in the following. The distance d_{el} between the electrodes and the waveguide has to be large enough to avoid high optical losses due to the

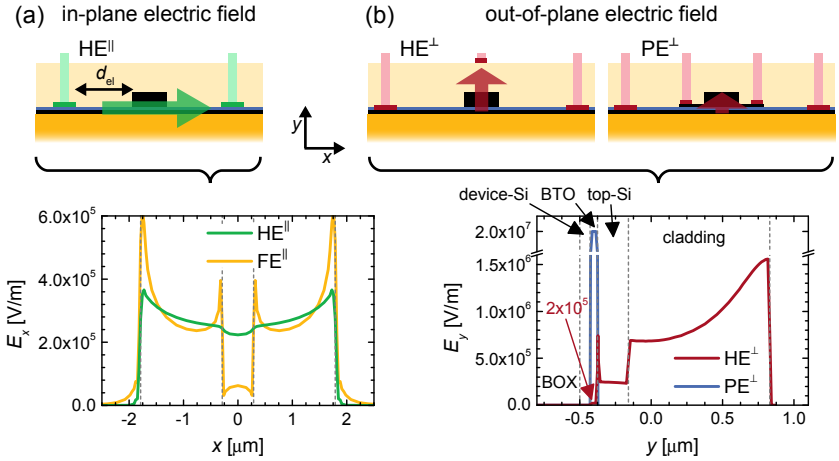

Fig. 4.14 Electric field in the $BaTiO_3$ layer in the core of slot waveguides when applying a voltage of $V = 1\,\text{V}$ to the electrodes. (a) $\text{HE}^{\parallel}$-waveguides with in-plane component E_x of the electric field originating from $1.5\,\mu\text{m} \times 50\,\text{nm}$ electrodes separated by $d_{\text{el}} = 1.5\,\mu\text{m}$ from the waveguide. The field distribution for a $\text{FE}^{\parallel}$-waveguides is shown for comparison. (b) Electrodes to obtain an out-of-plane electric field in a $\text{HE}^{\perp}$-waveguide. A large drop of the voltage occurs in the low-permittivity SiO_2-cladding. When directly applying the voltage to the device-silicon layer in $\text{PE}^{\perp}$-waveguides, the electric field in the $BaTiO_3$ core is significantly enhanced. The dimensions of the bottom electrodes are identical to (a), with an additional $0.5\,\mu\text{m} \times 50\,\text{nm}$ metal electrode on top of the $1.0\,\mu\text{m}$-thick SiO_2-cladding. Dashed gray lines indicate the interfaces between the layers.

absorption of the metal. For a low-loss configuration with $d_{\text{el}} = 1.5\,\mu\text{m}$, the electric field in the $BaTiO_3$ layer can be approximated by $E \approx \Delta V/(2d_{\text{el}} + w_{\text{WG}})$ when applying a voltage ΔV between both electrodes. Figure 4.14a shows a more accurate simulation of the x-component of the electric field $\boldsymbol{E}$ in the center of the $BaTiO_3$ layer in a $\text{HE}^{\parallel}$-waveguide, calculated with *FielDesigner* by *Phoenix*. All materials but the platinum metals are treated as dielectrics with permittivity values as shown in table 4.2. Platinum is chosen due its excellent conductivity for high speed applications, but can be replaced by other metals such as aluminum.

In contrast to $\text{HE}^{\parallel}$-waveguides, the field distribution in fully etched $\text{FE}^{\parallel}$-waveguides shows a large drop of the electric field within the $BaTiO_3$ layer in

the waveguide core (fig. 4.14a). This drop is caused by the large permittivity of $BaTiO_3$ compared to the SiO_2 cladding, which leads to a reduction of the electric field across the $BaTiO_3/SiO_2$ interface by

$$E_{x,\mathrm{BTO}} = \frac{\epsilon_{\mathrm{SiO_2}}}{\epsilon_{\mathrm{BTO}}} E_{x,\mathrm{SiO_2}} \approx 0.1 E_{x,\mathrm{SiO_2}}, \tag{4.6}$$

due to the boundary conditions of the electric field component, as described in eqs. (4.1) and (4.2). The drop of the electric field at the $BaTiO_3/SiO_2$-interface in $FE^{\parallel}$-waveguides leads to a reduction of the mean electric field $\hat{E}_x$-component in the center of the waveguide by a factor of ∼4 compared to $HE^{\parallel}$-waveguides. Due to the stronger lateral optical confinement in the $FE^{\parallel}$-waveguides, the electrodes could however be fabricated closer to the waveguide while keeping the losses low, thus increasing the electric field in the center. A quantitative analysis is not performed, because FE-waveguides are not targeted due higher processing challenges (section 4.3.1).

The *Phoenix* software package used for the simulation does not take into account the semiconducting nature of the device-silicon layer and the silicon handle wafer. The real electric field distribution might vary from the discussion above due to compensation of the electric field by charge separation in these layers. However, due to the small concentration of the dopants (∼$10^{15}/\mathrm{cm}^3$ boron atoms) in the silicon layers ($\rho_{\mathrm{Si}} \approx 10\,\Omega\,\mathrm{cm}$) [36], the concentration of charges and their influence on compensating the electric field is considered to be low.

Out-of-plane electric field By applying a voltage between the device-silicon layer (lower silicon layer, see fig. 4.6a) and an electrode placed on the cladding on top of the waveguide, an out-of-plane electric field is created in the $BaTiO_3$ layer (fig. 4.14b). Such out-of-plane configuration is labeled with a $\perp$-sign in this work. The top electrode has to be separated from the waveguide via the cladding to avoid high losses in $HE^{\perp}$-waveguide due to the metal electrode. This separation results however in a large drop of the voltage in the cladding due to the low permittivity of SiO_2 compared to $BaTiO_3$, as discussed in the previous paragraph. The influence of the permittivity on the field distribution is

Table 4.2 Permittivity values used for simulating the static electric field distribution (from [36] and section 2.5).

param.	ϵ_{Si}	$\epsilon_{\mathrm{SiO_2}}$	ϵ_{BTO}
value	11.68	3.9	50

visible in the strong enhancement of the magnitude of the out-of-plane electric field component E_y in the 5 nm-thick SiO_2 layer between the $BaTiO_3$ and the top-silicon layer (fig. 4.14b). Despite the large voltage drop across the cladding, the out-of-plane electric field $E_y = 2 \times 10^5$ V/m in $BaTiO_3$ in the waveguide core for an applied voltage of $V = 1$ V is by a factor of ∼5 larger than the bulk coercive field of barium titanate [194]. It is thus suitable for switching the domains. However, as discussed in section 3.4.4, the actual coercive field in thin films might be higher than in bulk crystals.

Therefore, $PE^{\perp}$-type waveguides are considered, where the top-silicon is contacted via the unetched thin silicon layer. This electrode configuration leads to extremely high electric fields of $E_y = 2 \times 10^7$ V/m for $V = 1$ V (fig. 4.14b) within the $BaTiO_3$ layer in the waveguide core. The strong field for small voltages in $PE^{\perp}$-waveguides is very appealing for zero-power tuning and slow switching applications. For high-speed applications, the resistance of the thin silicon layer which electrically connects to the metal pads with the waveguide has to be lowered through doping while taking care of keeping the absorption losses low. Alternatively, low-absorbing transparent electrodes such as indium-tin-oxide (ITO) can be brought much closer to the waveguide. However, such electrodes still have a rather high absorption in the infrared [195] and a lower conductivity than metals which might limit high-speed operation.

Requirements from $BaTiO_3$ symmetry The actual preferred field configuration is strongly dependent on the crystalline orientation of the $BaTiO_3$ layer. The 50 nm-thick $BaTiO_3$/Si films are *a*-axis-oriented (fig. 2.24) and thus require the electric field to be in-plane in order to pole the ferroelectric domains. The poling is necessary since the electro-optical response of two 180° domains cancels out (section 3.2). In order to achieve a maximal electro-optical effect in poled films, the electric field must be oriented along the $[101]_{BTO}$ direction (fig. 3.14). Such field orientation can be achieved by depositing the electrodes at an angle of 45° relative to the main crystalline axes of the epitaxial $BaTiO_3$ layer. Generally, in-plane electrodes allow a rather simple processing route because both electrodes can be fabricated with the same lithography step.

In contrast, two separate processing steps are required to obtain an out-of-plane electric field: One electrode is placed on top of the cladding, whereas the other is below the cladding. Additionally, an out-of-plane field cannot be used to pole *a*-axis-oriented films. It can however eliminate 180° domains in a *c*-axis $BaTiO_3$ layers. For *c*-axis $BaTiO_3$ and vertical electric field, only the r_c rather than the larger r_{42} coefficient of the Pockels tensor is exploited. Nevertheless, r_c in bulk $BaTiO_3$ ($r_c = 108$ pm/V) is still significantly higher than in many other materials, such as $LiNbO_3$. To obtain *c*-axis films with

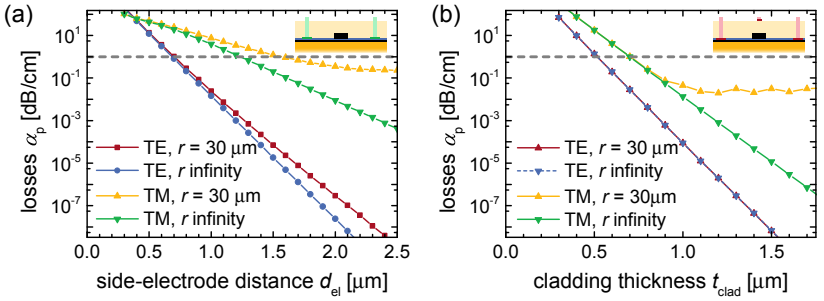

Fig. 4.15 Simulated propagation losses α_p for different distances between the platinum electrodes and the waveguide core for straight and bent waveguides. (a) Side electrodes with variable separation d_{el} from the waveguide. (b) Top-electrode sitting on the cladding of variable thickness t_{clad}. The ground electrodes are separated from the waveguide to not influence the modes. The insets illustrate the different electrode configurations.

the growth process described in section 2.3, the $BaTiO_3$-thickness has to be thinner than $t_{BTO} \leq 30\,nm$. Using different growth procedures, c-axis oriented layers with $t_{BTO} \geq 50\,nm$ on silicon substrates are feasible [196].

In summary, the crystalline structure has to be considered for obtaining the optimal electrode configuration. For the case of 50 nm-thick $BaTiO_3$ films as grown in the current work, electrodes creating an in-plane electric field have to be fabricated.

Losses due to electrodes While bringing the electrodes closer to the waveguide core is beneficial for obtaining large electric fields, the propagation losses α_p will increase due to the absorption of the metal. Because of the larger lateral dimensions, the TM mode is stronger influenced by metallic side electrodes than the TE mode (fig. 4.15a): a separation of $d_{el} \geq 1.2\,\mu m$ between the waveguide core and the electrodes is required to keep the TM-losses low ($\alpha_p \leq 1\,dB/cm$). Bent waveguides, as for example present in ring resonators, require even larger separations of $d_{el} \geq 1.5\,\mu m$ to keep the losses at the same level for a radius of $r = 30\,\mu m$. This requirement is a consequence of the additional bending losses and the slightly asymmetric mode profile resulting in a stronger modal overlap with the metal region at the outer face of the bend. Platinum electrodes with dimensions as described in fig. 4.14 are used for the loss simulations with a refractive index of $n = 5$ and an extinction coefficient of $k = 7$ at $\lambda = 1.55\,\mu m$ [197].

To keep the losses below $\alpha_\mathrm{p} \leq 1\,\mathrm{dB/cm}$ for an electrode configuration with out-of-plane electric field, the cladding thickness t_clad has to be at least $t_\mathrm{clad} = 0.7\,\mu\mathrm{m}$ for TM-modes (fig. 4.15b). Bent waveguides with $r = 30\,\mu\mathrm{m}$ are purely dominated by bending losses for cladding thicknesses $t_\mathrm{clad} > 1.0\,\mu\mathrm{m}$. Again, the TE modes suffer from lower losses due to the better optical confinement.

Variation of mode index

The electric-field-induced change of the refractive index n_BTO varies the effective index n_eff of the optical mode when applying a voltage. The change of n_eff is dependent on the overlap of the optical mode with the $BaTiO_3$ layer, described by the confinement factor Γ_BTO. Neglecting the tensor nature of the Pockels effect and using the simplified representation of the electro-optical effect (eq. (3.1)) with an effective Pockels coefficient r_eff, the change of the mode index on the applied voltage V is

$$\frac{\mathrm{d}n_\mathrm{eff}}{\mathrm{d}V} = \frac{\partial n_\mathrm{eff}}{\partial n_\mathrm{BTO}} \frac{\mathrm{d}n_\mathrm{BTO}}{\mathrm{d}V} \approx \Gamma_\mathrm{BTO} \times \frac{1}{2} n_\mathrm{BTO}^3 r_\mathrm{eff} \times \frac{\mathrm{d}\hat{E}}{\mathrm{d}V}. \tag{4.7}$$

The mean electric field $\hat{E}$ in the $BaTiO_3$ region is estimated from the electric field distribution shown in fig. 4.14 as

$$\hat{E}_{x,\mathrm{HE}^\parallel}(V) \approx 2.3 \times 10^5\,\mathrm{V/m} \times V/\mathrm{V} \tag{4.8}$$

$$\hat{E}_{y,\mathrm{PE}^\perp}(V) \approx 2 \times 10^7\,\mathrm{V/m} \times V/\mathrm{V} \tag{4.9}$$

for the in-plane field in $\mathrm{HE}^\parallel$-waveguides and the out-of-plane electric field in $\mathrm{PE}^\perp$-waveguides, respectively. Using these electric field strengths, the experimental values for the effective Pockels coefficient ($r_\mathrm{eff} = 148\,\mathrm{pm/V}$, section 3.4) and n_BTO (table 3.2), as well as the simulated confinement factors (section 4.3.1), the shift of the optical mode index when changing the applied voltage by ΔV is described by eq. (4.7) as

$$\Delta n_{\mathrm{eff},\mathrm{HE}^\parallel} \approx 3.9 \times 10^{-5} \Delta V/\mathrm{V} \tag{4.10}$$

$$\Delta n_{\mathrm{eff},\mathrm{PE}^\perp} \approx 3.6 \times 10^{-3} \Delta V/\mathrm{V}. \tag{4.11}$$

In order to properly treat spectral characteristics of devices, for example in ring resonators, the dispersion of the waveguide has to be taken into account by using the group index [198]

$$n_\mathrm{g} = n_\mathrm{eff} - \lambda \frac{\mathrm{d}n_\mathrm{eff}}{\mathrm{d}\lambda}. \tag{4.12}$$

The dependence of n_g (n_{eff}) is determined by simulating the group index and the effective index for small variations in the refractive index of $BaTiO_3$ in HE and PE waveguide cross sections. For both waveguides, the variations of the group index can be approximated by

$$\Delta n_g \approx 0.8 \Delta n_{eff}. \tag{4.13}$$

Equations (4.10) and (4.11) are based on effective Pockels values, and any rotation of the optical axis of $BaTiO_3$ is neglected. For a more accurate description, the tensor nature of the electro-optical effect has to be considered. In particular for ring resonators with circular electrodes, the dependence of the electro-optical-response on the in-plane direction of the electric field has to be taken into account, because ring resonators cover a large range of angles between the electric field and the $BaTiO_3$ main crystalline axes. These tensor-based calculations of the expected performance are however omitted in this thesis.

To increase the device performance, the changes of the effective index as calculated in eqs. (4.10) and (4.11) can be enhanced by:

- utilizing less absorbing electrodes, such as ITO, which can be brought closer to the waveguide core (Δn_{eff} enhanced by a factor of $f \times \sim 2$).
- replacing the SiO_2-cladding by a high-k material to reduce the voltage drop in the cladding in $HE^{\perp}$ and $FE^{\parallel}$ waveguides ($f \times \sim 2-5$).
- increasing Γ_{BTO} by growing thicker $BaTiO_3$ layers ($f \times \sim 2$ for $HE^{\parallel}$-waveguides).
- improving the electro-optical properties of $BaTiO_3$ towards bulk values ($f \times \sim 10$)

The combination of these measures could thus result in a $f \sim 4-200$ times improved performance.

Equation (4.11) strongly motivates the usage of $PE^{\perp}$-like waveguides as tuning elements to compensate thermal drifts of resonant structures. The thermal induced change of the refractive index of silicon [15]

$$\frac{dn_{Si}}{dT} = 2 \times 10^{-4}/\mathrm{K} \tag{4.14}$$

is compensated with a voltage of $V = 56\,\mathrm{mV/°C}$. For bulk-like $BaTiO_3$ properties, a temperature range of 100 °C can thus be covered by applying only $\pm 0.28\,\mathrm{V}$, assuming a thermo-optic effect of $BaTiO_3$ similar to silicon ($dn_o/dT < 3 \times 10^{-5}/\mathrm{K}$, $dn_{eo}/dT \approx 2.5 \times 10^{-4}/\mathrm{K}$ [199]).

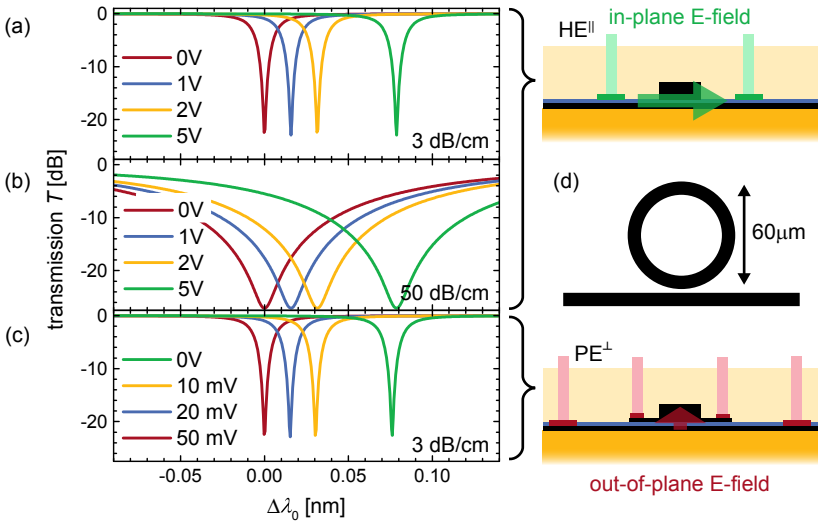

Fig. 4.16 Simulated transmission spectrum of ring resonators for different applied voltages, different propagation losses α_p (indicated in the plots), and a fixed coupling strenght to the waveguide. (a) and (b) correspond to $HE^{\parallel}$-waveguides, and (c) to $PE^{\perp}$-waveguides, respectively. (d) Illustration of the top view of a ring resonator device.

Ring resonators

Bending a waveguide to a closed ring adjacent to a straight waveguide forms a ring resonator structure (fig. 4.16d), which can be resonantly excited. The resonances result in periodic dips in the transmission spectra of the straight waveguides, which can be described analytically [198, 200]. The extinction ratio r_e at a resonance is determined by the coupling between the waveguide and the ring, and the losses in the ring. When the amount of energy coupled into the ring is equal to the energy lost during one roundtrip, the ring is "critically coupled" to the waveguide, and the extinction ratio $r_e = T_{max}/T_{min}$ between the maximal and minimal transmission T_{max} and T_{min}, respectively, becomes $r_e \to \infty$ [200].

The spectral positions λ_0 of the resonance peaks are determined by the optical path length of the ring. A change of n_g modifies this optical path length, and thus shifts the spectral positions of the resonances. Using $n_g(V)$ derived from eqs. (4.10), (4.11) and (4.13), the estimated shift of the resonances

in rings with radius $r = 30\,\mu m$ is estimated (fig. 4.16) based on the analytic solutions given in the literature [198]. The coupling coefficient is adjusted to obtain an extinction ratio of $r_e \approx 25\,dB$ as typically observed in the experiments (section 4.5.4).

Figures 4.16a and 4.16b show a shift of the resonance by $\Delta\lambda_0 \sim 80\,pm$ for $\Delta V = 5\,V$ in $HE^{\parallel}$ waveguides at $\lambda \approx 1550\,nm$. The transmission of the rings is strongly influenced by the propagation losses α_p: When using a ring resonator as active switch, the wavelength is fixed at a resonance $\lambda = \lambda_0$, which results in a low transmission of the device. By applying a voltage ΔV, λ_0 is shifted and the transmission T at λ becomes ideally $T_{on} = 1\ (= 0\,dB)$. For $\Delta V = 5\,V$, a transmission of $T_{on} \approx -5\,dB$ is visible in the "on-state" for $\alpha_p = 50\,dB/cm$ (compare red and green curve in fig. 4.16b). Either larger shifts or lower propagation losses are required. The latter leads to sharper resonances, as seen in fig. 4.16a ($T_{on} \approx 0\,dB$ with $\alpha_p = 3\,dB/cm$ and $\Delta V = 5\,V$).

For $PE^{\perp}$-waveguides, where the top-silicon is used as electrode, a much stronger change in n_g results in significantly larger shifts of the resonance wavelength λ_0 (fig. 4.16c): Only $\Delta V \sim 50\,mV$ is required to change λ_0 by $\Delta\lambda \sim 80\,pm$. The voltage requirement is thus by ~100 lower than in $HE^{\parallel}$-waveguides.

The calculated shifts of the resonances shown in fig. 4.16 are significantly larger than the spectral resolution of $\Delta\lambda \approx 10\,pm$ of the measurement equipment used for characterizing the devices (section 4.5.1). A confirmation or disapproval of the electro-optical-effect in active $BaTiO_3$-based ring resonators is thus expected to be possible.

Mach-Zehnder interferometer

In a Mach-Zehnder interferometer (MZI) light is first split into two separate arms and then, after some distance, recombined again. If the arms have a different optical path length (fig. 4.17c), the optical field will exhibit a relative phase shift between the two arms, and interference effects are visible at the output ports. MZIs can be used as passive devices such as cascaded filters [7], and as active devices such as modulators [201]. The latter relies on a variable phase shift between the arms that is used to modulate the power at one single output port, or switch the power between two ports. Compared to modulators based on ring resonators, Mach-Zehnder modulator are broadband and suffer less from thermal drifts and size variations during the fabrication, on the cost of a larger footprint. They are widely used as high-speed modulators in silicon photonics [14, 175, 201] as well as in telecommunication [20, 21].

Analytical transfer functions of MZIs can be derived dependent on the symmetry and perfection of the couplers and the phase shift between the two

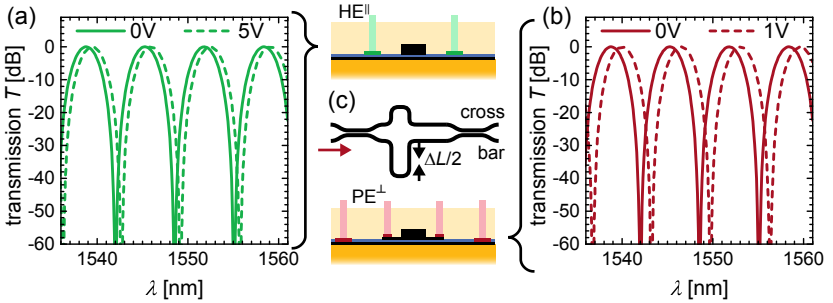

Fig. 4.17 Simulated transmission spectrum for the bar port of a $BaTiO_3$-based MZI with a delay line of $\Delta L = 100\,\mu m$ and different applied voltages. (a) 1000 µm-long MZI with $HE^{\parallel}$ cross section. (b) 100 µm-long MZI with $PE^{\perp}$-type cross section. (c) Schematics of the top view of a Mach-Zehnder interferometer with symmetric bends in both arms and a delay line of length ΔL. The "bar" and "cross" ports are labeled accordingly.

arms due to their different physical length ΔL [192]. Using the transfer function of a MZI with two identical, ideal 50:50 couplers [192], the transmission spectrum at the "bar" port (fig. 4.17c) is calculated for a delay line of $\Delta L = 100\,\mu m$ (fig. 4.17a). Applying a voltage of $V = 5\,V$ to electrodes along the shorter arm shifts the transmission spectrum as a consequence of the change in n_g and the resulting phase shift $\Delta\varphi$ between both arms (fig. 4.17a). The length of the shorter arm is fixed to $L = 1000\,\mu m$. For $PE^{\perp}$-waveguides with a much stronger electric field, similar shifts can already be obtained for short devices ($L = 100\,\mu m$) and lower voltages ($V = 1\,V$), as indicated in fig. 4.17b. For both estimations the electric field is only applied to one of the two arms.

The figure of merit for active MZI at low frequency is the product between the voltage V_π inducing a phase shift $\Delta\varphi = \pi$ between the arms and the length of the arms L. $L \times V_\pi$ is defined by

$$\pi = \Delta\varphi = \frac{2\pi}{\lambda} \times L \times \Delta n_g\,(V_\pi)\,. \tag{4.15}$$

Applying the voltage induced change $\Delta n_g\,(V)$ from eqs. (4.10), (4.11) and (4.13), values of

$$V_\pi \times L = 25\,V\,mm \text{ } (HE^{\parallel} \text{ waveguide}) \tag{4.16}$$

$$V_\pi \times L = 0.27\,V\,mm \text{ } (PE^{\perp} \text{ waveguide}) \tag{4.17}$$

are obtained at a wavelength of $\lambda = 1550\,\text{nm}$ for $\text{HE}^{\parallel}$- and $\text{PE}^{\perp}$-waveguides, respectively. As discussed in the next section, these figures of merit are very promising in comparison with alternative modulator designs.

4.3.5 Benchmarking active barium-titanate devices

The previous discussion shows a strong dependence of the performance of active $BaTiO_3$-based slot waveguide devices on the actual geometry of the cross section and the electrodes. $\text{HE}^{\parallel}$-waveguide structures can be used for high-speed modulation because no limitations are given for the lateral size and thickness of the metal connections. Thus the electrode design can be tuned for rf-operation with thick metal layers. The performance of MZIs with $V_\pi \times L = 25\,\text{V}\,\text{mm}$ is almost identical to state-of-the-art silicon photonic modulators based on the plasma dispersion effect, and by a factor of ∼3 better than $LiNbO_3$-based modulators (table 4.1). The best polymer based modulators are however ∼10-times more efficient than the expected $BaTiO_3$ performance due to a strong electric field confinement in the slot region in those devices [152]. In principle there is no inherent limitation of the operation speed of $BaTiO_3$/Si-modulators since the Pockels effect does not vanish even at THz-frequencies. The actual bandwidth is therefore determined by the design of the electrodes, and phase matching between electrical and optical waves. The proper rf-design is a similar challenge to non-$BaTiO_3$-based devices, which has for example been addressed in traveling wave electrode designs.

When benchmarking the expected performance, it has to be considered that the $BaTiO_3$-slot waveguide design is novel and much less mature than $LiNbO_3$ or silicon photonic modulators. The shift of the n_g can be increased by different electrode layouts, stronger optical confinements, and improved $BaTiO_3$ quality with bulk-like Pockels coefficients. Those measures could lower the $V_\pi \times L$ product by a factor of up to 200, as discussed in section 4.3.4. Such increase would provide a significant performance boost in the field of modulators. Clearly, research on silicon photonic modulators is still ongoing and further improvements are expected. The progress for $LiNbO_3$ devices has however already faded in the recent years [21].

$\text{PE}^{\perp}$-waveguides are expected to show already in the current design stage a superior figure of merit with $V_\pi \times L = 0.27\,\text{V}\,\text{mm}$. This value is by a factor of $\sim 100 - 200$ lower than in current state-of-the-art plasma-dispersion-based modulators, and by ∼10 lower than in polymer-based modulators. The geometry used to derived eq. (4.17) assumes electrodes adjacent to the $BaTiO_3$ layer. Therefore, the electric field is assumed to be maximal and the figure of merit further cannot be improved by an optimized electrode design. Still, increasing the confinement factor and approaching bulk-like Pockels values would enhance

the performance by ∼10 to $V_\pi \times L = 0.027\,\mathrm{V\,mm}$.

The drawback in the $\mathrm{PE}^{\perp}$-waveguide geometry is the rather large capacitance and high series resistance of the electrodes, which limits the maximal operation frequency. By properly adjusting doping profiles, and using different electrodes in a closer vicinity to the waveguide core, the bandwidth can be increased, similar to vertical slot waveguide modulators [152]. Rf-simulations are however not performed in the frame of this thesis. Devices with the current layout can be operated at lower frequencies and are usable as tuning elements. Temperature drifts of 10 °C can be compensated with low voltages of $V^2_{\Delta 10\,^\circ\mathrm{C}} \sim 0.5\,\mathrm{V}$. The static power consumption $P_{\mathrm{el},\Delta 10\,^\circ\mathrm{C}}$ due to leakage currents required to balance such temperature variation can be calculated per length L of the waveguide as

$$P_{\mathrm{el},\Delta 10\,^\circ\mathrm{C}} = \frac{V^2_{\Delta 10\,^\circ\mathrm{C}}}{R} = \frac{w_{\mathrm{el}} \times L}{t_{\mathrm{BTO}} \times \rho_{\mathrm{BTO}}} V^2_{\Delta 10\,^\circ\mathrm{C}} = 2.5 \times 10^{-9}\,\mathrm{W/m} \times L. \quad (4.18)$$

The experimental resistivity $\rho_{\mathrm{BTO}} = 10^{10}\,\Omega\,\mathrm{cm}$, a $BaTiO_3$ thickness of $t_{\mathrm{BTO}} = 50\,\mathrm{nm}$ and a width of the top-silicon electrode of $w_{\mathrm{el}} = 5\,\mu\mathrm{m}$ are used in that equation. The absolute power consumption is extremely low: To compensate the phase shift in a 500 µm-long waveguide induced by a temperature variation of $\Delta T = 10\,^\circ\mathrm{C}$, only $P_{\mathrm{el}} \approx 1\,\mathrm{pW}$ is required. This power consumption is more than 10 orders of magnitude below typical values for thermal tuners with similar dimensions (∼40 mW [174], section 4.1.2). $BaTiO_3$-tuning elements can thus be considered as zero-power tuning devices.

4.4 Fabrication

The fabrication of passive and active $BaTiO_3$-based waveguide structures involves the development of a processing route, the design of lithography masks, and the preparation of the $BaTiO_3$/SOI starting wafers. The fabrication route from a $BaTiO_3$/SOI starting wafer into photonic devices can be split into three major blocks, as visualized in fig. 4.18

(A) Preparation of slot-waveguide layer stack. The top-silicon layer is either integrated by depositing an amorphous silicon layer, or alternatively by bonding another SOI wafer and back-etching the handle-wafer.

(B) Fabrication of passive waveguides. In a first step, only the top-silicon layer is structured, and optionally covered with a SiO_2 cladding in order to obtain passive devices.

(C) Fabrication of active devices. In several additional steps, metal electrodes connected to larger pads for the electrical characterization are deposited on the wafer.

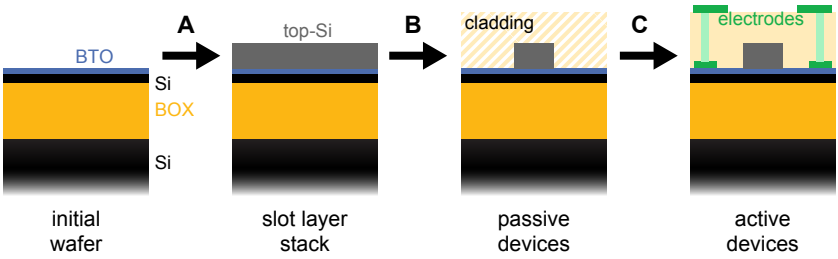

Fig. 4.18 General processing route of $BaTiO_3$/SOI photonic devices: First, a top-silicon layer is deposited on an initial $BaTiO_3$/SOI wafer (step "A"), before passive devices ("B") and finally electrodes ("C") are fabricated. For passive devices the deposition of a cladding is optional during step B.

These different processing blocks are discussed in detail in the next sections, after the initial description of the mask design procedure.

4.4.1 Mask design

Several different device types are designed in order to benchmark the $BaTiO_3$-slot waveguide platform. The designs are based on calculations discussed in section 4.3, but iterative adjustments depending on intermediate experimental results are performed. Some design parameters are solely determined by analyzing fabricated structures, such as the gap between ring and straight waveguide in ring resonators. A theoretical determination of the target gap size is not possible due to unknown parameters such as the losses in the structures. The main structures under investigation are listed in table 4.3. These devices are typically arranged in dense arrays with slightly different geometrical parameters within a $1 \times 1\,\text{cm}$ die as indicated in fig. 4.19a. The density of active devices is significantly reduced due to the space requirements of the large electrical pads for contacting the electrodes (fig. 4.19b).

In order to facilitate the variation of the numerous parameters, all device layouts are programmed fully parametrized with the open source mask design software package *IPKISS*, which is developed by the *Ghent University* and *imec*. The parametrized approach is in particular beneficial for designing active devices where a strong correlation between different elements exist. For example, the position of the electrodes, vias and pad connections in a ring resonator have to be properly adjusted when varying the gap size between the ring and the straight waveguide. Functions to automatically generate data files containing all device

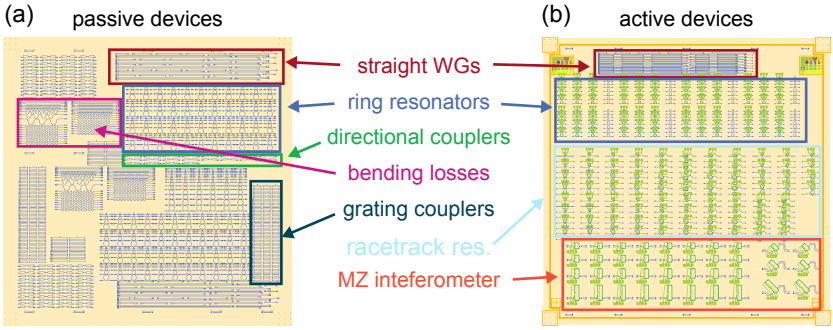

Fig. 4.19 Typical mask layouts for (a) passive and (b) active devices. Sections for different device types with a variety of device geometries are designed.

parameters are implemented in the design scripts. These data files are used to generate measurement procedures in the fiber-optical-setup (section 4.5.1) and to analyze the experimental results.

4.4.2 Fabrication of Si/$BaTiO_3$/Si layer stack

50 nm-thick $BaTiO_3$ layers on SOI substrates are used as initial wafers for the device fabrication, following both MBE-growth recipes as described in

Table 4.3 Devices types, purpose and varied parameters for $BaTiO_3$-slot waveguide structures.

device type	purpose/analysis	parameters varied
straight waveguide	propagation losses	length (250 µm - 9 mm)
spiral	propagation losses	length (1 cm - 5 cm)
bent waveguide	bending losses	bending radius
grating coupler	input/output coupler	grating period, duty cycle
directional coupler	design of MZI	coupling length, gap size
MZ-interferometer	active switching	couplers, delay length, arm length, electrode layout
ring resonator	active switching	radius, coupling gap, coupling shape, ring shape, electrode layout

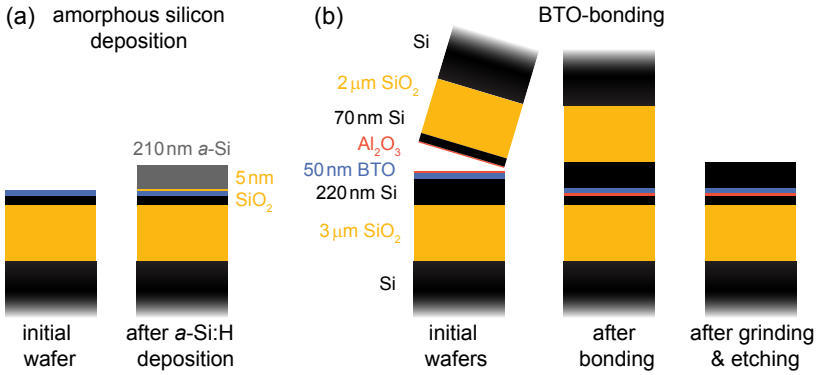

Fig. 4.20 Fabrication of the Si/$BaTiO_3$/Si layer stack. (a) Deposition of 210 nm *a*-Si:H by VHF-PECVD on top of a $BaTiO_3$/SOI wafer coated with a 5 nm-thin SiO_2 protection layer. (b) Transfer of a crystalline silicon layer via molecular bonding: a SOI wafer is bonded on top of a $BaTiO_3$/SOI wafer, both coated with 5 nm of Al_2O_3. The handle wafer and the BOX is afterwards ground and etched away. The bonded wafer stack is flipped during the process, and the handle wafer of the initial wafer is removed.

section 2.3. If not stated differently, all SOI wafers consist of a 70 nm-thick device silicon layer on top of a 2 µm-thick buried oxide (BOX) layer. The silicon layer on top of the $BaTiO_3$ layer is either deposited in a plasma-enhanced vapor deposition process (PECVD) (fig. 4.20a) or transferred via bonding (fig. 4.20b), as described below.

Amorphous silicon deposition

Hydrogenated amorphous silicon (*a*-Si:H) layers are deposited by PECVD at 200 °C with a 1:1 mixture between H_2 and SiH_4 in an *Octopus I* cluster tool developed by *INDEOtec SA*. The tool is operated at very high frequency (VHF) of 40.68 MHz. The low temperature is necessary to avoid hydrogen diffusion out of the film. The hydrogen serves as passivation for dangling bonds in silicon, which are strongly absorbing in the infrared [202]. To avoid contamination of the tool with $BaTiO_3$, a 5 nm-thin SiO_2 layer is deposited by PECVD on top of the $BaTiO_3$/SOI-stack prior to the *a*-Si:H process in a *Oxford Plasmalab System 100 PECVD* tool.

The low adhesion of the *a*-Si:H layer on top of the SiO_2/$BaTiO_3$-layer is a major challenge for this processing route: Bubbles are formed during the

a-Si:H deposition and in successive process steps due to local delamination of the silicon layer. The delamination might be triggered by degasing of hydrogen from the *a*-Si:H films. The density of the bubbles with a typical diameter of $\sim$100 µm is low enough ($<$ 1000 per 2inch-wafer) to still yield many functional devices, such as ring resonators. However, the bubbles serve as nucleation center to delaminate larger parts of the *a*-Si:H-film, for example when performing mega-sonic cleans. Therefore, the bubbles are individually etched away, and trenches to confine possible delamination processes in small areas are structured into the *a*-Si:H layer. With this procedure, the wafers could be well-processed with all required subsequent steps.

Transfer of crystalline silicon

In an alternative approach, a molecular bonding process is developed in order to transfer a thin crystalline silicon (*c*-Si) layer onto the $BaTiO_3$-layer, leading to a novel *c*-Si/$BaTiO_3$/*c*-Si layer stack. In contrast to *a*-Si:H, the *c*-Si-layer is slightly doped ($\rho \approx 10\,\Omega\,\mathrm{cm}$) and can thus be used as top electrode in $PE^{\perp}$-waveguides while avoiding high absorption losses. The fabrication of $PE^{\perp}$-waveguides with *a*-Si:H as top-silicon is not possible due to the low conductivity of these layers.

A $BaTiO_3$-layer grown on a SOI wafer with 220 nm device silicon and a blanked SOI wafer with 70 nm device silicon serve as templates for the bonding process (fig. 4.20b). After thoroughly cleaning both wafers to remove any particles and organic contaminants, $5-10$ nm-thick Al_2O_3-layers are deposited at 250 °C by atomic layer deposition (ALD) on both surfaces. Ozone cleaning ensures a molecular water film on both wafers that activates the successive direct bonding process. The bonded stack is annealed at 250 °C, before grinding one of the handle-wafers down to a thickness of 50 µm. The remaining silicon is then etched away with a 25 %-concentrated TMAH (tetramethylammonium hydroxide) solution, which is very selective to the buried SiO_2 (BOX) layer below the silicon. The BOX is removed in a final step by a long buffered-HF (BHF) dip to obtain a layer stack as shown in fig. 4.20b.

The bonding process is very sensitive to clean surfaces with low roughness below 0.5 nm rms (root mean square). Polishing of rougher surfaces is not possible due to the low $BaTiO_3$ layer thickness. High bonding yields ($>$ 90 %) could only be obtained for $BaTiO_3$-layers grown with the improved shuttered co-deposition process, which reduces the surface roughness by suppressing the formation of islands (section 2.3).

The *c*-Si/$BaTiO_3$/*c*-Si layer stack shows very smooth interfaces without any voids, and a homogeneous $BaTiO_3$-layer of high quality (fig. 4.21b). The waveguide cross section shown in fig. 4.21a is discussed in section 4.4.3.

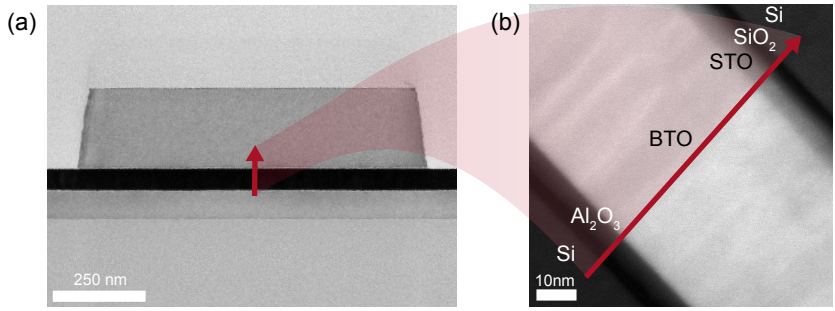

Fig. 4.21 STEM cross section of a waveguide fabricated from a *c*-Si/$BaTiO_3$/*c*-Si layer stack. (a) Overview of the waveguide in BF-STEM mode. (b) The magnification of the interface in DF-STEM mode shows smooth interfaces. The red arrow indicates the orientation of the magnified image.

4.4.3 Fabrication of waveguide structures

Die-by-die processing

A strategy was devised to re-use the 2 inch-wafers for several, iterative processing rounds in order to reduce the effort in growing $BaTiO_3$/SOI layers (see section 4.2). After fabricating a set of devices on a specific die, the waveguides are characterized and the designs of the successive dies are adjusted accordingly (fig. 4.2b). Since most of the processing tools are optimized for handling full wafers (for example homogenous dry etching or PECVD), or even required full wafers (such as laser lithography), the 2 inch-wafers are not diced into single dies.

However, the handling of full wafers requires an adjustment of the process flow to protect the wafer while processing only individual dies. Figure 4.22 schematically shows the fabrication of passive devices in a single die while keeping the remaining wafer in its initial state for further process iterations. The principle is also applied when additional steps such as the fabrication of electrodes are performed. Metallic alignment markers are the only exception of the die-by-die handling: They are fabricated prior to any photonic structures on the full 2 inch-wafer as shown in fig. 4.22a.

Etching of waveguides

170 nm-thick HSQ, which serves as etching mask for fabricating the waveguide structures, is exposed in a *Vistec EBPG 5200* ebeam lithography tool operating

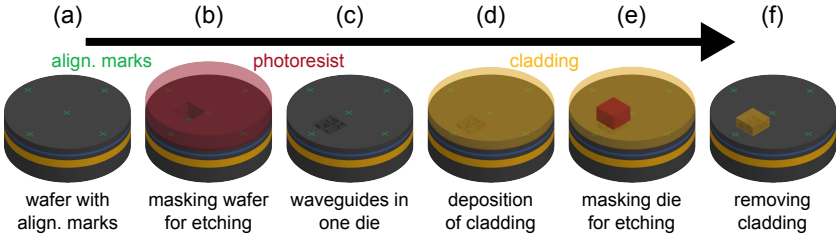

Fig. 4.22 Schematic of the die-by-die processing without dicing the wafer into small pieces. (a) Alignment marks are fabricated on the full wafer. (b) The wafer except the dies being processed are protected with photoresist before (c) etching the silicon layer. (d) The cladding is first deposited on the full wafer before (e) masking the dies being processed and (f) removing the cladding from the remaining wafer again.

at 100 kV. Subsequently, ∼1.2 µm-thick positive optical photoresist (*AZ6612*) is spun on the wafer, exposed with a *DWL 2000* laser writer (*Heidelberg instruments*), and developed with standard recipes. The mask used for this laser lithography step is designed to only expose dies that contain HSQ structures and thus protect the remaining wafer as depicted in fig. 4.22b.

The top-silicon layer is then dry etched in a *Oxford Instruments Plasmalab System 100 ICP-RIE* using a 2-step HBr process as described in table 4.4. An initial short HBr step is used to etch the native SiO_2 layer on top of the wafer, before adding O_2 into the plasma. The mixture between O_2 and HBr strongly impacts the selectivity between etching SiO_2 and Si and the sidewalls of the structures [203]. If O_2 is used, a passivation layer is formed at the surface of the etched silicon, preventing a lateral etch process. A well-tuned O_2/HBr mixture yields perpendicular waveguide sidewalls. An example of a HE-waveguide that was etched with too little O_2 admixture, resulting into ∼83° sidewall angle, is shown in fig. 4.21.

The HBr process is controlled by end-point detection when fabricating HE-waveguides, where the full top-silicon layer is removed. Time-based etching is used for PE-waveguides since a ∼40 nm-thin top-silicon layer has to be retained rather than etching down to the $BaTiO_3$ surface.

Generally, the process conditions in the ICP-RIE (inductively coupled plasma - reactive-ion etching) tool vary between the runs, resulting in fluctuations of the etch quality. The variation is on the one hand due to issues with properly conditioning the chamber prior to the process. On the other hand, the initially used HBr-etch recipe operating at low ICP-powers (400 W) is at the edge of

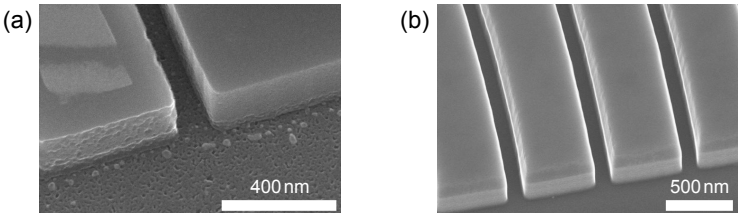

Fig. 4.23 SEM images of grating couplers after etching the top-silicon with HBr. (a) Rough and smooth sidewalls adjacent to each other on the same device due to locally varying plasma conditions with an ICP power of 400 W. Residuals of HSQ are visible on top of the left structure. (b) Smooth side walls when etching with a stable plasma at an ICP power of 800 W. The HSQ layer has not been removed for that sample.

obtaining a stable plasma. Figure 4.23a shows an example where even local variations of the plasma conditions are observed in two adjacent waveguides with rough and smooth sidewalls, respectively. The process is stabilized by increasing the ICP power on the cost of a higher etch rate and thus less control for PE-waveguides. Nevertheless, the modified process is better reproducible and results in smooth sidewalls as visible via scanning electron microscopy (SEM) (fig. 4.23b). A quantitative measurement of the sidewall roughness is not performed, but optical loss measurements indicated a low roughness comparable with state-of-the-art silicon photonic structures (section 4.5.2).

After the etching process, the HSQ layer is typically not removed. Due to the similar optical properties of exposed HSQ and SiO_2, the remaining HSQ layer is nearly invisible for the guided light when a SiO_2 cladding is used. The removal of the exposed HSQ layer by BHF is avoided because of the non-uniform etching of the $BaTiO_3$ film, which results in a roughening of the surface, as seen in

Table 4.4 Typical process parameters when etching the top-silicon layer by ICP-RIE. The table temperature is kept at 50 °C, and the chamber pressure at 4 mTorr

step	purpose	time	O_2	HBr	RF	ICP
1	pump out	180 s				
2	SiO_2 + Si etch	10 s		40 sccm	80 W	800 W
3	Si etch	∼65 s	2 sccm	38 sccm	80 W	800 W
4	pump purge	5 × 60 s				

fig. 4.23a. Figure 4.24a illustrates the cross section after the HBr etching step, including the mask design and an optical microscopy image of a ring resonator at that processing stage.

Cladding layer

A cladding layer is required for active devices in order to fabricate metallic bridges over the waveguides to contact the electrodes. Because the cladding influences the mode profiles and thus the device parameters of couplers and resonators, the cladding is typically also fabricated on passive waveguide structures in order not to maintain two different designs. Several requirements have to be fulfilled when depositing the ∼1 µm-thick cladding:

- Low deposition temperature, preferable below 200 °C to avoid de-hydrogenation of the *a*-Si:H layer, and delamination of the bonded device silicon.
- Low stress in the cladding layer to avoid cracks or delamination of the top-Si layers.
- Uniform coverage around the waveguiding structures.

Different methods are tested, including spin-coating thick HSQ and subsequent post-annealing, as well as PECVD using SiH_4, and PECVD using TEOS (tetraethoxysilane) precursors. All of these processes yield to SiO_2-like layers. The TEOS process proved to be the best solution: It neither shows the formation of cracks as observed in HSQ claddings, nor are any voids at the edges of the waveguides visible as seen with SiO_2 grown by PECVD (SiH_4). A smooth coverage around the waveguides is obtained (fig. 4.21). Additionally, the stress in the cladding could be tuned to low values ($\sigma < 10\,\mathrm{MPa}$), which reduces to risk of delaminating the waveguiding layers. The potential influence of the TEOS-SiO_2 cladding on the propagation losses due to O-H-bondings [204] is tested by comparing standard silicon waveguides with and without the cladding. No increased propagation losses are observable.

4.4.4 Fabrication of electrical connections

Active devices require the fabrication of electrodes in addition to the passive waveguides. Supplementary processing steps are discussed for the example of $HE^{\parallel}$-waveguides with side electrodes. Additional remarks will be made on small deviations in the process flow of active $PE^{\perp}$- and $HE^{\perp}$-waveguides.

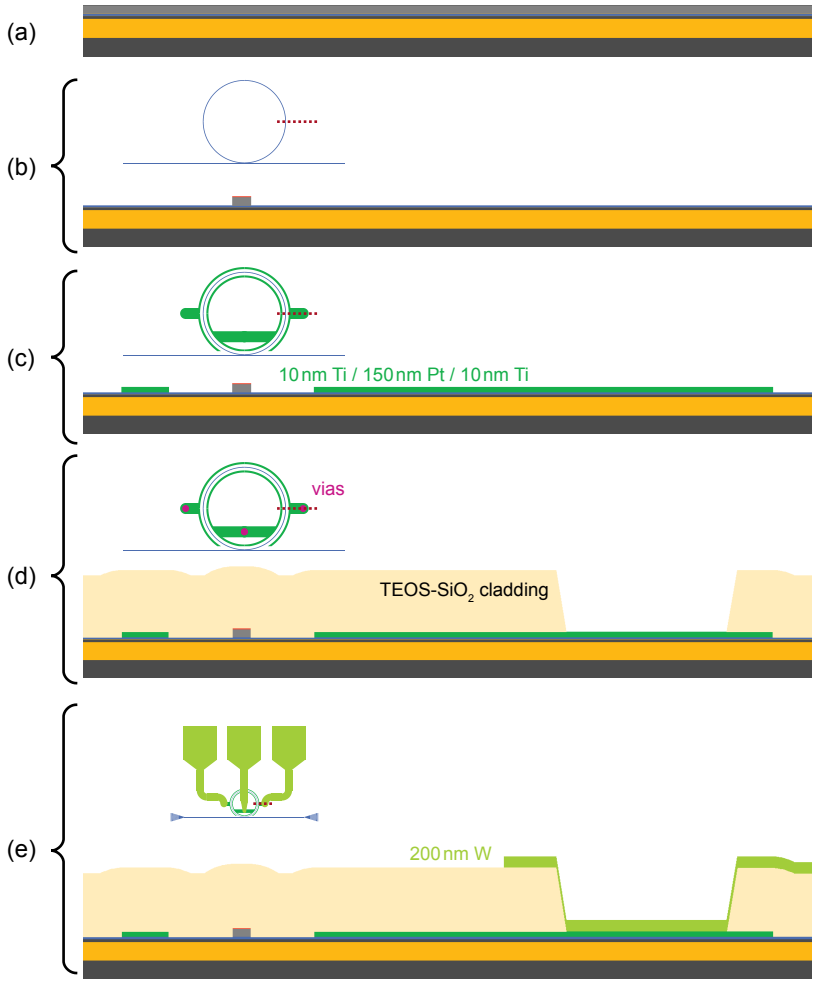

Fig. 4.24 Evolution of the mask design, top view, and schematics of the cross section, when fabricating active $HE^{\parallel}$-waveguide devices with in-plane electric field. The cross section corresponds to the dashed red line shown in the mask designs. (a) The initial layer stack is (b) dry-etched using a HBr plasma to form waveguides. (c) Side electrodes are deposited on top of the $BaTiO_3$ layer using a lift-off process, before (d) depositing a TEOS-SiO_2-cladding and etching openings to the electrodes. (e) The electrodes are connected to larger pads with a 200 nm-thick tungsten layer.

Side electrodes

Figure 4.24c shows the mask layout for a pair of electrodes parallel to the waveguide in a ring resonator. The widths of the electrodes is kept small (∼1 µm) to avoid a large capacitance that could limit the performance of the devices during high-speed operation. Larger pads connected to the electrodes serve as bottom contact for vias through the cladding, as shown in the next step. The electrodes are fabricated with a lift-off process before depositing the cladding layer. Therefore, a ∼150 nm-PMMA (polymethyl methacrylate) and a ∼250 nm-MMA (methyl methacrylate) layer are first spin coated on the wafer and baked for 5 min at 180 °C, then exposed by ebeam lithography, and finally developed with MIBK (methyl isobutyl ketone) dissolved in isopropanol. Ebeam lithography is required to ensure a good alignment of the metal pads to the waveguide, which are separated by $1 - 3$ µm. A combination of 10 nm-Ti/150 nm-Pt/10 nm-Ti is evaporated on the wafer, before a lift-off step in hot NMP (N-methyl pyrrolidone). Ultrasonic cleaning is used only at low powers to reduce the risk of delaminating the *a*-Si:H layer. The titanium layers are used to promote a good adhesion of the electrode to $BaTiO_3$ and the following cladding layer, while the rather thick platinum layer ensures low resistance for high-speed operation. In principle, also CMOS-compatible metals can be used for that step. A schematics of the cross section and an optical microscopy image after the metal deposition is shown in fig. 4.24c.

To obtain an out-of-plane electric field, a BHF (buffered HF) dip is performed prior to the metal evaporation in order to locally remove the $BaTiO_3$ layer and thus contact the device silicon layer. The PMMA/MMA resist stack is etched at extremely low rates by BHF and thus protects the waveguiding structures.

Vias

After depositing the TEOS-SiO_2-cladding layer as described in section 4.4.3, vias are etched through the cladding in order to connect the electrodes with the probing pads for the electro-optical characterization. Circular structures with a diameter of 5 µm are written by laser lithography into an optical photoresist (*AZ6612*). Laser lithography is the method of choice since no physical masks are required. Thus, the designs can quickly be adjusted and directly be written on the wafer without contacting the surface. The size of the vias is kept small to reduce the capacitance of the device, analogous to the electrode design.

After the development, the resist is baked for 3 min at 130 °C: the reflow process lowers the angle between the resist sidewalls and the surface of the wafer to ∼60°. This beveled shape is transferred into the SiO_2-cladding with a dry etch process in a *Oxford RIE PlasmaPro NGP 80* etching tool. The

combination of O_2 and CHF_3 with rf-powers of 200 W is very selective to the metal pads with a negligible platinum etch rate. The cross section, mask layout and resulting structure is shown in fig. 4.24d.

The top electrode in $HE^{\perp}$-waveguides is deposited onto the cladding prior to the fabrication of the vias. The wafer is then coated with another thin cladding layer to allow the connections to both electrodes to be crossed. Subsequently, both vias for the bottom electrode as well as the top electrode are etched in a single step.

Probing pads

Finally, the side electrodes are connected through the vias with larger metal pads on the cladding (fig. 4.24e): first, a 200 nm thick tungsten layer is therefore deposited via magnetron sputtering on the full wafer. Insulating TiO_2 on the electrodes is removed with a short argon sputtering step prior to the metal deposition. Laser lithography is used on a 1.2 µm-thick *AZ6612*-photoresist layer to define the electrical connections and the contact pads. The tungsten layer is dry-etched via RIE with identical parameters as used when etching the alignment markers. A short Ar-etch is performed on the contact pads as a final step to remove any insulating oxide layer. The mask designs is adjusted for $HE^{\perp}$ and $PE^{\perp}$ waveguides. Figure 4.24e shows the final cross section and top view of a fully processed $HE^{\parallel}$-type device with in-plane electrodes.

4.4.5 Fabrication of reference waveguides

Several waveguide structures with other layer stacks than Si/$BaTiO_3$/SOI are fabricated in order to separate the impact of the prpoerties of the waveguide materials from the impact of the slot waveguide design on the device performance. In particular, as will be discussed in section 4.5.2, unforeseen high propagation losses in the $BaTiO_3$ waveguides are observed. The following waveguides are used to identify the loss channel:

- SOI waveguides (fig. 4.25a). Standard, fully etched silicon photonic waveguides are fabricated from SOI wafers with 220 nm-thick device silicon layer in order to obtain propagation losses mainly caused by sidewall roughness to be compared with literature values. This comparison allows to judge the quality of the HBr-etching conditions.
- Fully etched *a*-Si:H waveguides (fig. 4.25b). The losses in amorphous silicon are strongly dependent on the deposition conditions and can vary by several orders of magnitude [205]. Since no process for obtaining low-loss *a*-Si:H layers has been available for this work, various deposition

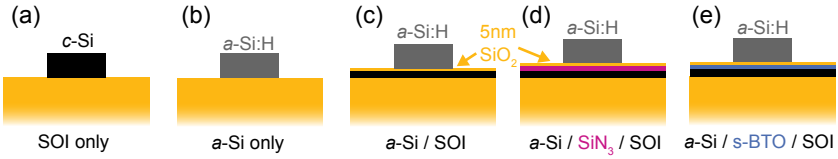

Fig. 4.25 Reference samples fabricated to determine losses (a) in standard SOI waveguides, (b) in FE *a*-Si:H waveguides, and (c) in PE *a*-Si:H waveguides. (d) The $BaTiO_3$ layer is replaced by a 50 nm-thick Si_3N_4 layer to verify the existence of a TM mode, and to analyze the propagation losses. (e) PE-waveguides samples with sputtered, polycrystalline $BaTiO_3$.

methods are compared by fabricating fully etched waveguiding structures. Amorphous silicon is fabricated (1) by MBE-deposition in hydrogen plasma, (2) by rf-sputtering, (3) by rf-PECVD operating at 13.56 MHz with 2 %-SiH_4 precursor gas diluted in He, and (4) by the VHF-PECVD process as described above. The sputtered and rf-PECVD deposited films are post-annealed at 200 °C in forming gas (10 %-H_2/90 %-N_2) to incorporate additional hydrogen into the layers.

- Halfway etched *a*-Si:H waveguides on SOI wafers with 70 nm-thick device silicon layers (fig. 4.25c). Therefore, *a*-Si:H is deposited by means of VHF-PECVD on top of a 5 nm-thick SiO_2 layer protection layer, similar to *a*-Si:H/$BaTiO_3$/SOI structures.

- Slot-waveguide structures with dimensions identical to those of $BaTiO_3$-waveguides, but where the $BaTiO_3$ layer is replaced with a Si_3N_4 layer grown by PECVD (fig. 4.25d). By increasing the Si-content, the refractive index of the Si_3N_4 layer is tuned to ∼2.2, similar to the index of $BaTiO_3$-thin films.

- *a*-Si:H/$BaTiO_3$/SOI waveguide structures with sputtered, and subsequently post annealed $BaTiO_3$ at 700 °C in oxygen fig. 4.25e. Since no MBE seed layer is used, the $BaTiO_3$ films are polycrystalline.

Beside identifying the origin of the high propagation losses, Si_3N_4 slot waveguides are also used to verify the simulations of the optical modes. In particular, the existence of a TM mode for the designed slot waveguide geometry is verified experimentally.

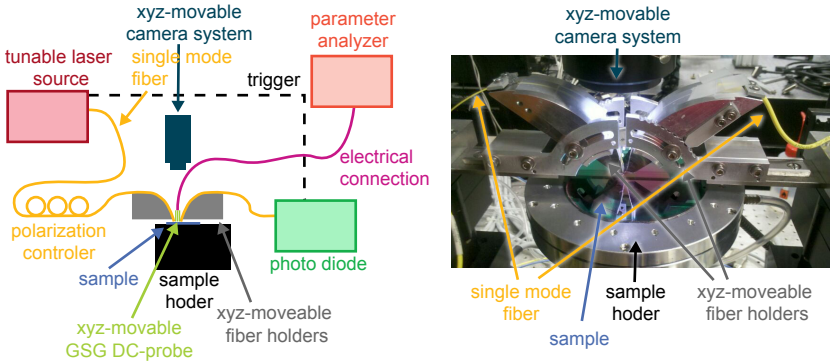

Fig. 4.26 (a) Schematics of the experimental setup for optically characterizing integrated devices. (b) Photograph of the system.

4.5 Characterization

4.5.1 Experimental procedure

Electro-optical fiber setup

Figure 4.26 shows the setup used to optically and electro-optically characterize the integrated devices: An *EXFO optical test system IQ-203* with a tunable (1510 – 1610 nm) laser (*IQ-2600B*) having a maximum output power of −3 dBm serves as light source. The *EXFO* system also contains an InGaAs photo diode (lower detection limit of −90 dBm) (*IQ-1600*), which is electrically triggered by the source when performing wavelength sweeps. After passing a polarization controller, the light is coupled into the waveguides via grating couplers using a cleaved single-mode fiber mounted at an angle of ∼10° relative to the surface normal. The light transmitted through the devices is collected with a second cleaved fiber. Both fibers are mounted on motorized xyz-stages, which are movable with a step size of 50 nm and controlled by a computer system. A camera provides feedback for positioning the fibers above the grating couplers. Electrical and low-speed electro-optical measurements are performed with a parameter analyzer (*Agilent Technologies B1500A*) and ground-signal-ground probes mounted on a manual xyz stage.

Measurement and analysis procedure

Automated fiber alignment The fibers are roughly placed on top of the grating couplers using the video camera, before iteratively varying the x and y axes of the fiber holder in small steps and maximizing the transmitted power. The procedure is repeated multiple times for an accurate alignment. The fibers are placed 10 µm above the sample surface close to the device under investigation using video feedback. Once the fibers are well aligned, optical measurement such as recording transmission spectra are started.

In this work hundreds of irregularly arranged devices distributed over the wafer are characterized. The existing *LabVIEW* control software is therefore extended to fully automate the measurement procedure for passive devices. Recipes to measure, for example, only specific ring resonator structures are directly created during the mask generation. For each wafer, three devices have to be aligned manually. From these alignment positions the transformation matrices between the coordinate system of the mask and the stages are determined. These matrices are used to directly move the fibers to any device on the wafer. An automated fine-alignment to maximize the transmission is performed prior to any measurement. Long term drifts for example due to temperature variations are compensated by automatically recalibrating the transformation matrices during the measurement procedures. The placement of the electrical probes is performed manually when characterizing active devices.

Analysis of transmission spectra During many experiments transmission spectra are recorded to obtain characteristics such as quality factors of resonators or propagation losses. For non-resonant devices, the spectra are fitted with a Gaussian function

$$P(\lambda) = P_0 \exp\left(-\frac{(\lambda - \lambda_0)^2}{2\sigma^2}\right) \tag{4.19}$$

where λ_0 is the center wavelength (fig. 4.27a), $2\sqrt{2\ln 2}\sigma$ the full width at half maximum (FWHM) of the transmission peak and P_0 the maximal transmitted power. P_0 measured for different waveguide lengths L is then used to determine the propagation losses α_p by applying

$$P_0(L) = 2\alpha_\mathrm{g} \times P_\mathrm{s} \times 10^{-\left(\alpha_\mathrm{p}/10\right)L} \tag{4.20}$$

where α_g is the insertion loss of one grating coupler in dB, P_s the power delivered from the source to the first grating coupler, and α_p the losses in dB/m. Larger defects on the wafer, such as bubbles in the *a*-Si:H layer or badly bonded parts, lower the transmission through the waveguides unrelated to the

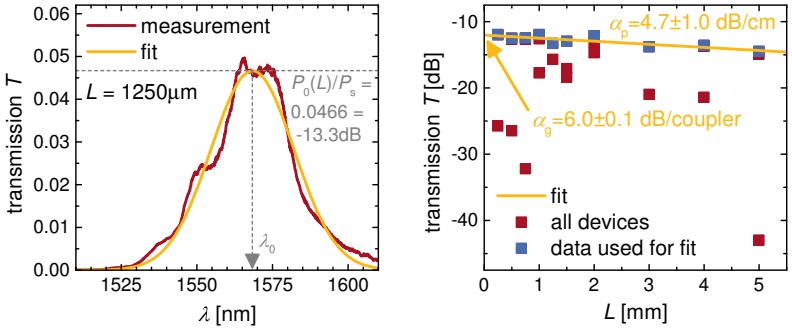

Fig. 4.27 (a) Fitted transmission spectrum of a waveguide with two grating couplers coupling the light in and out of the device. The maximal transmission P_0 and the center wavelength λ_0, both determined from the fit, are indicated with dashed, gray lines. (b) Transmission T of several waveguides of different length. Only the maximal values for each L are used for fitting the data with eq. (4.20) to determine the propagation losses α_p and coupling losses α_g.

propagation losses. Straight waveguides are placed at several positions all over the wafer, and multiple waveguides are measured for each length L. Rather than calculating the mean value, which would also include losses caused by rare, larger defects, only the maximal $P_0\,(L)$ is used for determining α_p with eq. (4.20). Figure 4.27b shows the transmission $T = P_0\,(L)/P_\mathrm{s}$ for all devices (red) and those actually used for the fitting procedure (blue) measured of a specific sample. The slope of the linear fit in the logarithmic representation of T corresponds to α_p, and the extrapolation for $L = 0$ to $\frac{1}{2}\alpha_\mathrm{g}$. Any losses within the fibers and connectors of the optical setup contribute to α_g, but are neglected since they are typically much smaller ($< 1\,\mathrm{dB}$) than the coupling losses. In the following sections, only the maximal values T for each L are plotted in the figures.

4.5.2 Straight waveguides

Reference waveguides

SOI waveguides Fully etched SOI waveguides with air cladding show propagation losses of $\alpha_\mathrm{p} = (2.8 \pm 1.0)\,\mathrm{dB/cm}$ for the TE mode (fig. 4.28a). This value is in the same range as typical losses in fully etched silicon waveguides ($2 - 4\,\mathrm{dB/cm}$, [206, 207]), and only slightly higher than in the best waveguides

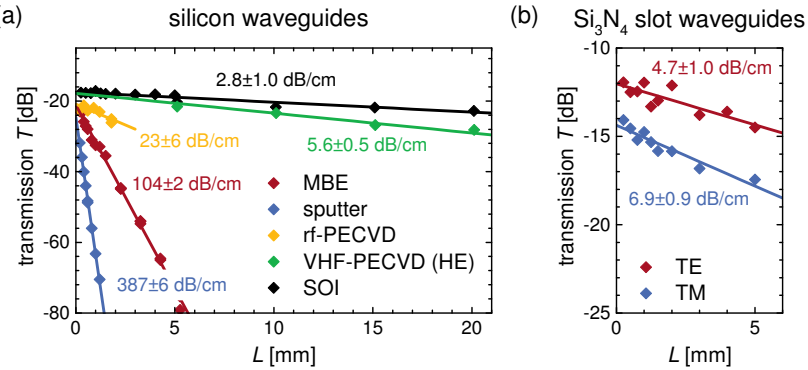

Fig. 4.28 (a) Transmission T of differently fabricated FE a-Si-waveguides (fig. 4.25b), and standard FE SOI waveguides (fig. 4.25a) of different length L. The VHF-PECVD waveguides are halfway etched (HE) (fig. 4.25c). (b) T for TE and TM modes in Si_3N_4 slot waveguides with a-Si:H as top-silicon grown via VHF-PECVD. The propagation losses α_p are indicated in the figures. All waveguides are characterized without cladding.

with similar geometry published in the literature (0.9 dB/cm, [208]). This good agreement with previous studies confirms that the processing route used in this work results in good waveguiding structures. In particular, it confirms the sidewall roughness after the silicon etch step to be similar to state-of-the-art waveguides.

SOI waveguides are used to measure the influence of different cladding layers on the propagation losses (not shown). Both unbaked-HSQ-cladding ($\alpha_p = (3.3 \pm 0.1)$ dB/cm) and TEOS cladding layers ($\alpha_p = (2.6 \pm 0.1)$ dB/cm) show almost identical propagation losses to those of air-cladded waveguides. HSQ can thus be utilized as a cladding that is simply spin coat on the waveguides for intermediately characterizing devices. Since non-exposed HSQ can easily be removed afterwards by acetone, the fabrication process can be continued, for example to add electrodes.

Amorphous silicon layers The losses of the a-Si:H-waveguides strongly depend on the fabrication methods: values between (387 ± 6) dB/cm and (5.6 ± 0.5) dB/cm are measured for TE modes in air-cladded waveguides (fig. 4.28a). The large losses in sputtered and MBE-grown a-Si films are likely due a low saturation of dangling Si-bonds [202]. This assumption is supported by the

even higher losses for these films (∼150 dB/cm more than shown in fig. 4.28a) when no additional H_2/N_2 anneal to saturate dangling bonds is performed after the deposition.

The significantly lower losses in VHF-PECVD grown films compared to rf-PECVD films can also be related to the large hydrogen content in the VHF-PECVD process (50 %) and the utilization of pure SiH_4-gas. The rf-PECVD tool is limited to only 2 % concentrated SiH_4. These process parameters severely impact the losses of *a*-Si layers [209]. Additionally the data of the VHF-PECVD sample corresponds to HE-like waveguides (fig. 4.25c) with less influence of the sidewall-roughness on the propagation losses, while all other *a*-Si waveguides are fully etched (fig. 4.25b). The propagation losses of the VHF-PECVD are close to those of the best amorphous silicon waveguides with similar dimensions (∼3.4 dB/cm for fully etched, and ∼1.4 dB/cm for shallow rip-waveguides [209]). By increasing the width of the waveguides to 2.5 µm, the effect of sidewall roughness is reduced in the VHF-PECVD waveguides and losses as low as (3.0 ± 0.7) dB/cm are measured (not shown).

Layers of *a*-Si:H deposited via VHF-PECVD thus provide a good material system to fabricate low-absorbing $BaTiO_3$-slot waveguides, and are therefore used for all samples described in the following sections.

Si_3N_4 slot-waveguides Slot waveguides with Si_3N_4 in the slot region (fig. 4.25d) have low TE-propagation losses of only $\alpha_p = (4.7 \pm 1.0)$ dB/cm (fig. 4.28b). Importantly, the structures show the existence of a TM-mode, which confirms the results of the simulations of the cross section (section 4.3.1). The propagation losses of the TM mode having a strong field enhancement in the Si_3N_4 regions are $\alpha_p = (6.9 \pm 0.9)$ dB/cm. They are comparable to those of previously reported slot Si-slot waveguides [185, 210].

Conclusion from reference structures The various test waveguides indicate the process route to be well-suited for fabricating $BaTiO_3$-slot waveguides with reasonably low losses: The Si-etch process results in a good sidewall roughness, the *a*-Si:H layers show low absorption, and the cladding does not increase the propagation losses. Furthermore, the existence of highly confined TM-modes in the slot waveguide cross sections is experimentally confirmed. The measured losses of ∼7 dB/cm for that mode might be reduced by further optimizing the *a*-Si:H-deposition and -etching process.

Barium titanate-slot-waveguides

Sputtered $BaTiO_3$ Compared to the reference structures, air-cladded slot waveguides with sputtered $BaTiO_3$ instead of Si_3N_4 show significantly higher propagation losses of $\alpha_p \approx 64\,dB/cm$ and $\alpha_p \approx 133\,dB/cm$ for TE and TM modes, respectively (fig. 4.29a). Since bulk-$BaTiO_3$ is non-absorbing at $\lambda = 1550\,nm$, the high losses are mainly attributed to scattering losses in the polycrystalline $BaTiO_3$-layer. Scattering of light can occur at the $BaTiO_3$ surface, which shows a roughness of typically $> 4\,nm$ (rms) on the sputtered layers, and at local inhomogeneities with a characteristic size of $\sim 2 - 10\,\mu m$ as visible in the optical microscope (fig. 4.29b). Also the high porosity of $> 10\,\%$ measured with ellipsometry might contribute to scattering losses. Generally, large variations in the propagation losses ($\Delta\alpha_p \sim 50\,dB/cm$) between several, independently processed samples are observed. The variation might in fact be caused by different grain, pore and crack sizes due to the strong dependence of the morphology of sputtered $BaTiO_3$ layers on the annealing conditions.

MBE-grown $BaTiO_3$ In contrast to sputtered $BaTiO_3$ layers, epitaxial barium titanate shows a very uniform, crack-free surface with a roughness below 0.5 nm (rms) (section 2.3). However, the propagation losses obtained for slot waveguide structures with MBE-grown $BaTiO_3$ films are unexpectedly high (fig. 4.29a): HE-waveguides with *a*-Si:H as top-silicon layer show TE-losses of $\alpha_{p,TE} \sim (319 \pm 7)\,dB/cm$, while PE-waveguides capped with *c*-Si result in even higher losses of $\alpha_{p,TE} \sim (575 \pm 21)\,dB/cm$. Due to the low absorption of lowly-doped *c*-Si a better performance than with *a*-Si:H layers would be expected. The deposition of a SiO_2 cladding reduces α_p only marginally as shown in fig. 4.29a by the dashed green line. The propagation losses measured on several samples with different MBE-$BaTiO_3$ layers show large variations but are consistently high ($\alpha_{p,TE} = 200 - 400\,dB/cm$). The propagation losses of TM modes are even higher, typically $\alpha_{p,TM} \gg 500\,dB/cm$.

Origin of high losses From the relatively low losses of the reference waveguides, several possible mechanisms can be exclude as the dominant loss channel in the MBE-$BaTiO_3$ waveguides:

- The top VHF-PECVD-grown *a*-Si:H layer is only slightly absorbing and does not result in propagation losses of $\alpha_p > 200\,dB/cm$. Also, the high losses in *c*-Si capped PE-slot waveguides confirm the minor influence of the top-silicon on α_p: The *c*-Si layer is lowly doped and shows thus a low absorption.

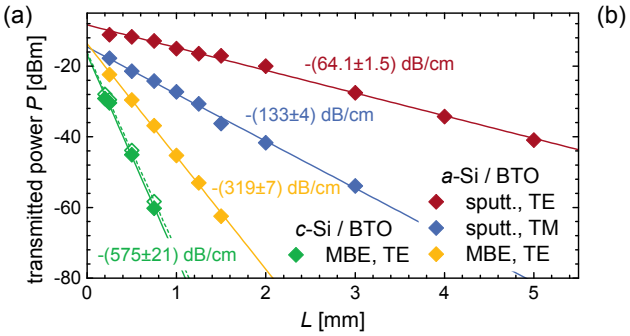

Fig. 4.29 (a) Transmitted power P through air-cladded slot waveguides of various length L with differently deposited $BaTiO_3$ layers. Waveguides with a-Si:H as top-silicon layer are HE-type, while c-Si capped waveguides are PE-type. c-Si waveguides with SiO_2 cladding (open green symbols, dashed line) show very a similar propagation loss ($\alpha_p = (559 \pm 15)$ dB/cm) to the uncladded ones. (b) Bright-field (top) and dark-field (bottom) optical microscopy images of sputtered $BaTiO_3$ layers showing a non-uniform, grainy morphology.

- Sidewall roughness limits the losses to ~3 dB/cm in FE SOI reference waveguides. The Si-etch process thus does not result in such high losses as measured for MBE-$BaTiO_3$ structures. Simulations of the propagation losses show that even very rough waveguides (standard deviation of 10 nm with a correlation length of 50 nm) result in much lower propagation losses (< 40 dB/cm) for fully etched waveguides of similar size [211]. Even higher roughness values would be required to account for the observed propagation losses. Such high roughness is in contrast to the smooth sidewalls seen in the SEM investigation (fig. 4.23b).
- Possibly, TM modes are not guided in the waveguide cross section and radiate into the device-silicon layer. This would however be in contrast to the rather low TM losses in Si_3N_4-slot waveguides, and could also not account for the high losses of the TE modes, which cannot be cut off due to the symmetry structure of cladded waveguides.
- Scattering effects in the MBE-$BaTiO_3$ layers can be neglected compared to sputtered $BaTiO_3$ due to a significantly higher crystalline quality and very homogeneous morphology in the MBE-$BaTiO_3$ layers.

Previous studies show that the absorption in undoped $BaTiO_3$ at $\lambda = 1550$ nm is negligible [212]. Waveguides made from epitaxial barium titanate on MgO

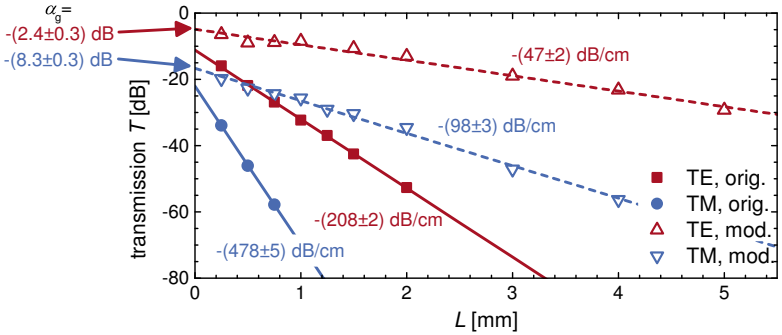

Fig. 4.30 Transmission T for MBE-$BaTiO_3$ slot waveguides of different length L, fabricated with the original process as described in section 4.4 without cladding ("orig."), and with a slightly modified process with TEOS-SiO_2-cladding ("mod."). The losses per grating coupler α_g for the modified process are indicated on the left.

substrates show low propagation losses of $2-4\,\mathrm{dB/cm}$ [131, 165, 213] which are mainly determined by scattering losses. Losses due to abortion in the $BaTiO_3$-layers are therefore considered to be very unlikely, but provide on the other hand the only reasonable explanation for the high losses of MBE-$BaTiO_3$ slot waveguides. The reason why $BaTiO_3$ shows a rather high absorption despite the excellent crystallinity is not clear.

Reduction of propagation losses With additional experiments and careful analyses, the origin of the high absorption losses could finally be identified, and a way to strongly reduce them with few additional process steps was found. Figure 4.30 shows the lowest α_p-values for HE slot waveguides fabricated with the original process. Additionally, data for MBE-$BaTiO_3$ slot waveguides with the modified fabrication process are shown[1]. The cross section of the waveguides is not altered and still a a-Si:H/$BaTiO_3$/SOI stack with the same dimensions as described above. With the modified process, the losses are reduced to $\alpha_{p,TE} = (47 \pm 2)\,\mathrm{dB/cm}$ and $\alpha_{p,TM} = (98 \pm 3)\,\mathrm{dB/cm}$ for TE and TM modes in cladded structures, respectively. The sample to sample variation is still high, and losses as low as $\alpha_{p,TM} = (67 \pm 4)\,\mathrm{dB/cm}$ are observed for the TM mode.

1 Due to a pending patent application, no further details on the slightly modified process can be given here.

All $BaTiO_3$-waveguides discussed in the following sections are fabricated with the modified process.

Grating couplers

Using eq. (4.20), the coupling losses α_g at $L = 0\,\mu m$ are determined from the data shown in fig. 4.30 as $\alpha_{g,TE} = (2.4 \pm 0.3)\,dB$ and $\alpha_{g,TM} = (8.3 \pm 0.3)\,dB$ for TE and TM grating couplers, respectively. Waveguides fabricated with the original process that are shown in fig. 4.30 show slightly higher coupling losses since no cladding was used for these particular devices.

The coupling efficiency of the TE-couplers is comparable with state of the art grating couplers, while the insertion loss for the TM couplers is by ~4 dB higher [10, 214]. By chirping the duty cycle of the gratings, and adjusting the design iteratively based on experimental results, the efficiency of both couplers might be increased. In the same way, reflections from the couplers back into the waveguide can be reduced. Such undesired reflections are visible as periodic modulation of the transmitted power due to interference effects (see fig. 4.27a). The efficiency of the couplers is however sufficient at the current state in order to characterize electro-optical active devices.

4.5.3 Bent waveguides

Bending losses are determined using several MBE-$BaTiO_3$-slot waveguides consisting of multiple 180° bends with different bending radius r (fig. 4.31a, inset). The total length of the bent waveguides is kept constant at $L \sim 2\,mm$. To reduce losses due to mode mismatch between the differently curved parts, short straight waveguides ($L_\Delta = 2.5\,\mu m$) are placed in between bends with opposing bending directions. For both the TE and the TM mode, a transition from a regime dominated by bending losses ($r < 10\,\mu m$) and one dominated by propagation losses independent of the bending ($r > 20\,\mu m$) is visible (fig. 4.31a).

The transmission T of the devices is calculated based on the experimentally determined propagation losses α_p of straight waveguides (fig. 4.30) and the simulated bending losses α_b (fig. 4.10):

$$T = \frac{1}{2} \times \alpha_g \times 10^{-\alpha_p\left(L + mL_\Delta\right) - \alpha_b L}. \tag{4.21}$$

In this equation, $m \approx L/(\pi r)$ is the number of 180° bends and α_g the coupling losses as determined from fig. 4.30. The losses of the TE mode are higher than the calculated bending losses (fig. 4.31a), which is likely caused by an increased sidewall roughness for small curvatures due to the finite pixel size in the ebeam lithography process. In contrast, the TM mode shows lower

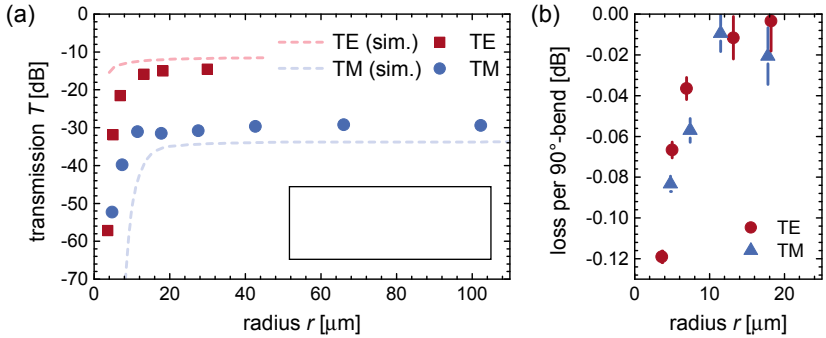

Fig. 4.31 (a) Experimental and simulated transmission for waveguides with different bending radii r. The total length of the waveguides is ∼2 mm. The inset schematically shows the mask design of devices with different bending radii. (b) Bending losses per 90°-bend calculated from the data shown in (a). The error bar is based on the uncertainty in determining the transmission in waveguides without significant contribution of bending losses ($r > 20\,\mu m$).

losses than expected. This reduction might originate from a better confinement due to overetching and thus lower bending losses (fig. 4.10). Because of the large propagation losses α_p, only few data points are collected in the regime where bending losses dominate the transmission of the waveguides. An accurate comparison between the simulations and experimental data is therefore not possible.

The losses per 90°-bend $\alpha_{b,90°}$ for small bending radii are estimated using eq. (4.21), experimental values of α_g (fig. 4.30) and T (fig. 4.31a), and

$$\alpha_{b,90°} = \frac{\alpha_b}{\pi r/2}. \tag{4.22}$$

α_p is determined from the data shown in fig. 4.31a in the regime where bending losses are negligible ($r > 20\,\mu m$). For small radii, the bending losses per 90°-bend are $\alpha_{b,90°} < 0.02\,dB$ (fig. 4.31b), which is significantly smaller than the propagation losses along a straight waveguide with the same length (∼0.3 dB for $r = 20\,\mu m$ and $\alpha_p = 98\,dB/cm$ (TM-mode, see fig. 4.30)). Bending losses are therefore negligible in ring resonators with $r = 30\,\mu m$, which is the design point for devices discussed in the following sections.

4.5.4 Ring resonators

Ring resonators from both Si_3N_4-slot waveguides as well as $BaTiO_3$-slot waveguides show sharp resonances for TM-modes, depending on the actual device geometry. At a resonance, the transmitted power $P(\lambda)$ is approximated with a Lorentzian peak function in order to analyze typical figures of merit such as the quality factor and propagation losses in the ring:

$$P(\lambda) = P_0 - (P_0 - P_{\min}) \frac{(\delta\lambda/2)^2}{(\lambda - \lambda_0)^2 + (\delta\lambda/2)^2}. \tag{4.23}$$

In this equation, λ_0 is the center wavelength of the resonance, $\delta\lambda$ the full width at half transmission, P_0 the transmitted power next to the resonance, and $P_{\min}$ the transmission at the resonance. From the fitted parameters, the extinction ratio $r_e = P_0/P_{\min}$ can be calculated, as well as the quality factor Q [161]:

$$Q \approx \frac{\lambda_0}{\delta\lambda} \tag{4.24}$$

For critically coupled rings, the quality factor Q_{cr} is used to estimate the propagation losses α_p in the rings with group index n_g [198, 215]

$$\alpha_p = \frac{\pi n_g}{Q_{cr}\lambda_0}. \tag{4.25}$$

The condition of critical coupling is fulfilled when the extinction ratio approaches infinity. The group index can experimentally be determined by measuring the free spectral range FSR between two resonances, and using [198]

$$\mathrm{FSR} \approx \frac{\lambda^2}{n_g L}, \tag{4.26}$$

where $L = 2r\pi$ is the cavity length in the ring with radius r. A more general determination of the losses for arbitrary coupled rings [198] is not needed here because the gap of the waveguide and the ring is varied to reach critical coupling.

Si_3N_4 slot waveguides Figure 4.32 shows the TM-transmission spectrum of a Si_3N_4-slot waveguide ring resonator with radius $r = 30\,\mu m$. The resonances show an extinction ratio of $r_e > 15\,dB$, which corresponds to nearly critically coupled rings. The finesse of the resonator is $\mathcal{F} = \mathrm{FSR}/\delta\lambda \approx 38$ [216]. From the quality factor $Q = 2.0 \times 10^4$ and the group index $n_g = 3.89$, the propagation losses in the ring are estimated as $\alpha_p = 17\,dB/cm$. The propagation losses are higher than in straight waveguides ($\alpha_p = (6.9 \pm 0.9)\,dB/cm$, section 4.5.2).

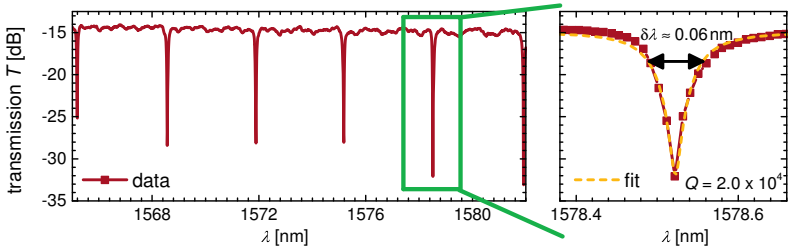

Fig. 4.32 TM-transmission spectrum of a Si_3N_4-slot waveguide ring resonator with $r = 30\,\mu m$. Resonances with quality factors of $Q = 2.0 \times 10^4$ are measured. The width of the resonance $\delta\lambda$ at half transmission (-3dB) is indicated in the right plot.

Bending losses are supposed to be $< 0.1\,dB/cm$ for waveguides with $30\,\mu m$ bending radius and do not account for the higher losses. The deviations between both measurements might rather be related to local inhomogeneities on the wafer. Investigating multiple rings combined with a better statistical analysis could reduce the measurement uncertainty. Such an in-depth analysis is not performed in this work. The sharp resonances with $\delta\lambda \approx 0.06\,nm$ (fig. 4.32) are sufficient to resolve the resonance shifts which are expected for electro-optical-active $BaTiO_3$-based devices (fig. 4.16).

$BaTiO_3$ slot waveguides Due to the higher propagation losses in $BaTiO_3$ slot waveguides compared to those with Si_3N_4 core, the resonances of ring resonators with identical dimensions show lower quality factors of $Q \approx 5.4 \times 10^3$ and lower finesses of $\mathcal{F} \approx 12$ for TM-modes (fig. 4.33). The group index of the TM mode is $n_g = 3.90$. This value is close to the simulated index ($n_{g,TM} = 3.67$, section 4.3.1) and the index of Si_3N_4-slot waveguides, and confirms a good match of the geometry and index profiles between simulations, reference structures and $BaTiO_3$-waveguides. The propagation losses obtained from the rings ($\alpha_p = 64\,dB/cm$) are similar to the values obtained from straight waveguides (lowest values measured $\alpha_{p,TM} = (67 \pm 4)\,dB/cm$, section 4.5.2). The analysis of several rings shows a variation of $\Delta\alpha_p > 20\,dB/cm$. These rather strong fluctuations between different devices are in agreement with local inhomogeneities due to defects, which are also visible when measuring multiple straight waveguides as shown in fig. 4.27b. The width of the resonances $\delta\lambda \approx 0.25\,nm$ (fig. 4.33) makes the $BaTiO_3$-devices suited to sense shifts of $\Delta\lambda_0 = 0.1\,nm$ in subsequent electro-optical-measurements.

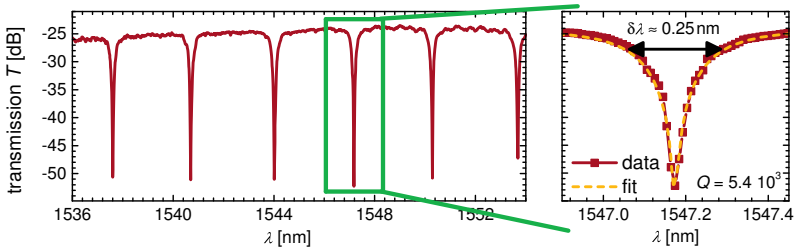

Fig. 4.33 TM-transmission spectrum of a critically coupled $BaTiO_3$-slot waveguide ring resonator. The quality factor of the magnified resonance is $Q = 5.4 \times 10^3$. The width of the resonance $\delta\lambda$ at half transmission ($-3\,\mathrm{dB}$) is indicated in the right plot.

The extinction factor r_e at the resonances is strongly dependent on the losses in the ring and on the coupling coefficient [216]. The latter is systematically varied by changing the gap size g between the ring and the straight waveguide in order to find the condition of critical coupling (fig. 4.34a): While for small gap sizes ($g < 80\,\mathrm{nm}$), too much light is coupled to the rings, resulting into broad resonances, the resonances disappear for large distances ($g > 350\,\mathrm{nm}$). For intermediate gap sizes $g_{cr} \approx 190\,\mathrm{nm}$, the extinction factor shows a maximum of $r_e > 25\,\mathrm{dB}$ (fig. 4.34b). Rings fabricated with g_{cr} are critically coupled to the waveguides. The parameter g_{cr} is used for fabricating active devices, and therefore determined for all waveguide geometries used in this work, such as race track resonators, or rings with different radii and different coupling geometries.

In addition to the TM ring resonators discussed above, TE modes are analyzed: Generally, higher quality factors of $Q \sim 1.0 \times 10^4$ and smaller g_{cr} are observed, which is in agreement with the lower propagation losses, and the stronger lateral confinement and consequently the lower coupling strength of TE modes.

4.5.5 Directional couplers

As a prerequisite for properly designing Mach-Zehnder interferometers, the dimensions for symmetric directional couplers calculated in section 4.3.3 are experimentally verified for $BaTiO_3$-slot waveguide structures. Couplers with a gap size of $g = 200\,\mathrm{nm}$ show an oscillating power transfer between the bar and the cross port (fig. 4.35b) when the length L of the parallel waveguides in the

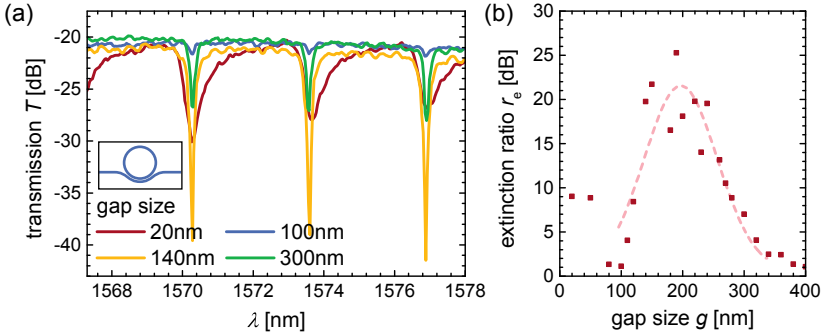

Fig. 4.34 Analysis of the coupling between ring resonators and straight waveguides. (a) TM-transmission spectra for various gap sizes g. The spectra are slightly shifted in order to match the resonance wavelength, which differed between the devices due to fabrication variations. (b) Extinction ratio r_e for various gap sizes obtained from fitting the resonances at $\lambda \approx 1570\,\text{nm}$, the wavelength of maximal transmission of the grating couplers. The dashed line is a guide for the eye. All Data corresponds to rings with $r = 30\,\mu\text{m}$ and with slightly curved (see inset in (a)) $BaTiO_3$-slot waveguides.

coupling region is varied (fig. 4.35a), as expected for directional couplers [192]. The data is fitted with

$$P(L) = P_0 \sin\left(2\pi \frac{L - L_0}{2L_c}\right)^2, \tag{4.27}$$

where L_c is the minimal length of the coupler to transfer all energy into the other waveguide, L_0 the offset, and P_0 the total transmitted power through both ports. The offset L_0 originates from the energy transfer in the bent waveguides before and after the parallel waveguides. Due to the large bending radius of $r = 100\,\mu\text{m}$ in that region, most energy is transferred into the bar state already for $L = 0$. The period of the oscillation of the power between both ports is $2L_c = 2 \times (17.9 \pm 0.2)\,\mu\text{m}$, which is in excellent agreement with calculated coupling length of $17.3\,\mu\text{m}$ (fig. 4.13). This agreement indicates a good match between the targeted design and the actual fabricated waveguide geometry.

Other gap sizes between 100 and 400 nm for TM coupler as well as TE coupler are investigated. Because of the stronger confinement and thus lower coupling strength between the waveguides, TE couplers are generally longer,

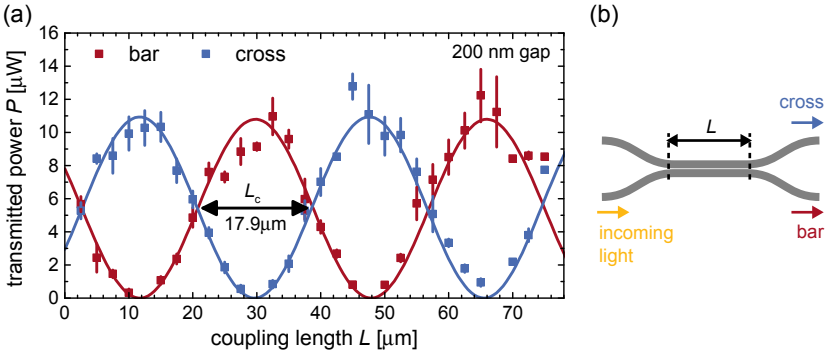

Fig. 4.35 (a) Transmitted power P in the bar and the cross port of symmetric directional couplers with different length L. The error bars show the standard deviation between several identically designed couplers. The fits (solid lines) reveal a coupling length of $L_c = (17.9 \pm 0.2)\,\mu m$ to transfer all power from one waveguide to the other one. (b) Schematics of measurement geometry.

with $L_c = (55 \pm 10)\,\mu m$ for a gap size of $g = 200\,nm$. Since small gap sizes are more prone to process variations due to the exponential dependence of the coupling strength on g, a larger gap size than shown in fig. 4.35 is used for fabricating Mach-Zehnder interferometers ($g = 300\,nm$ and $L_c = (38 \pm 3)\,\mu m$).

4.5.6 Mach-Zehnder interferometers

However, due to a mistake in the design process, the actual couplers used in subsequently fabricated MZIs are not accurate 50:50 splitters. The asymmetric splitting ratio results in different extinction ratios in the bar and cross port for MZIs with a delay line of $\Delta L = 200\,\mu m$ (fig. 4.36a). The good extinction in the cross port ($r_e > 25\,dB$) shows that both couplers in the MZI are identical [192], and indicates a good etching homogeneity on local scale. The extinction ratio in the bar port decreases for larger wavelengths, where the coupling strength is generally higher. The couplers are thus over-coupled. Shorter couplers or larger gap sizes have to be designed to obtain symmetric conditions in the bar and cross ports.

Such symmetric behavior is obtained despite the non-symmetric couplers for MZIs devices with longer delay lines of $\Delta L = 800\,\mu m$ (fig. 4.36b): the rather high losses in the waveguides of several dB/mm require over-coupled splitters in order to compensate the additional losses in the longer arm. These

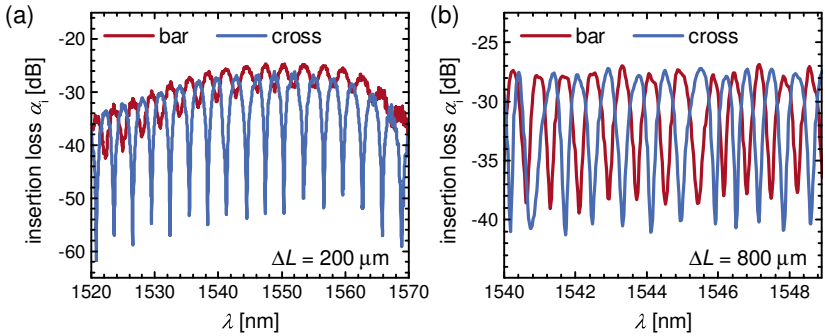

Fig. 4.36 Mach-Zehnder interferometer with a delay line length of (a) $\Delta L = 200\,\mu m$ and (b) $\Delta L = 800\,\mu m$. In both cases, the shorter arm has a length of $\sim$350 µm. The directional couplers used for the interferometers are not perfect 50:50 splitters, which results in a relatively low extinction ratio in the bar configuration in (a). The unbalanced splitting is compensated by the propagation losses in longer delay lines as seen in (b).

results show the importance of including the outcome of the measurements of directional couplers (section 4.5.5) as well as the propagation loss measurements (section 4.5.2) in the design of future $BaTiO_3$-slot waveguide MZI devices.

4.5.7 Active devices - current state and future work

Active $HE^{\parallel}$-slot waveguide ring resonators with in-plane electrodes are manufactured based on geometrical parameters obtained from the optimization of passive devices. The presence of the electrodes separated by $d_{el} = 1.0 - 3.0\,\mu m$ from the waveguide core does not alter the transmission spectra of the devices. This behavior is expected from the simulations which show propagation losses of $\alpha_p < 10\,dB/cm$ in bent waveguides with $d_{el} = 1.0\,\mu m$ and radius $r = 30\,\mu m$ (fig. 4.15). These propagation losses only marginally influence the total propagation losses of TM modes with $\alpha_p > 50 - 100\,dB/cm$ as measured in straight waveguides (section 4.5.2).

In the frame of this thesis only few devices could be investigated and no complete analysis can be provided here. In particular, many device parameters which were varied during the device design and many external parameters during the characterization such as temperature variations could not be considered. The following discussion indicates the state of the current work and provides an outlook for future experiments.

The initial electro-optical measurement are performed on racetrack ring resonators with electrodes only along the straight "tracks" (figs. 4.37a and 4.37c). The electric field in these devices is homogeneous along the full active region relative to the $BaTiO_3$ crystalline axes. Due to the tensor nature of the electro-optical effect (section 3.2.1), a different performance of the devices is expected for differently oriented race track resonators. The influence of the orientation of the electric field is visible in the characterization of thin films in chapter 3, where a maximal electro-optical response is observed when the the electric field is oriented parallel to the $[101]_{\mathrm{BTO}}$ direction (fig. 3.14).

Shift of resonance wavelength

Indeed, devices with differently oriented electrodes show a different electro-optical response: Hardly any shift of the resonance wavelengths λ_0 is visible when the electrodes are parallel to the $[001]_{\mathrm{BTO}}/[100]_{\mathrm{BTO}}$-axes (figs. 4.37a and 4.37b). For this configuration only the rather small r_{13} and r_{33} elements of the Pockels tensor contribute to the electro-optical response, which might thus be below the experimental resolution of $\Delta\lambda \approx 0.01\,\mathrm{nm}$.

When the electrodes are oriented along the $[101]_{\mathrm{BTO}}$ axes, a different behavior is observed: By applying a voltage V to the electrodes, λ_0 increases (figs. 4.37c and 4.37d). The shift of λ_0 is caused by a change of the group index Δn_{g}, which can be calculated as

$$2\pi \frac{n_{\mathrm{g},0} L}{\lambda_0} = 2\pi m \tag{4.28}$$

$$2\pi \frac{n_{\mathrm{g},V} L}{\lambda_V} = 2\pi \frac{(n_{\mathrm{g},0} + \Delta n_{\mathrm{g}})\, L}{\lambda_0 + \Delta\lambda_0} = 2\pi m \tag{4.29}$$

$$\Delta n_{\mathrm{g}} = n_{\mathrm{g},0} \frac{\Delta\lambda_0}{\lambda_0} = 3.91 \frac{0.34\,\mathrm{nm}}{1552.5\,\mathrm{nm}} = 8.6 \times 10^{-4}. \tag{4.30}$$

In this derivation, m is the order of the resonance, $\Delta\lambda_0 = 0.34\,\mathrm{nm}$ the shift of the resonance extracted from fig. 4.37d, and $n_{\mathrm{g},0} = 3.91$ the group index of the TM-mode in HE-waveguides which was determined from the free spectral range using eq. (4.26). The indices "V" and "0" indicate the applied voltage ($V = 18\,\mathrm{V}$ and $V = 0\,\mathrm{V}$, respectively). The shift per applied voltage is

$$\Delta n_{\mathrm{g}} = 4.8 \times 10^{-5} \Delta V/\mathrm{V}. \tag{4.31}$$

This change of the group index Δn_{g} is in the same order of magnitude than the expected performance, which is calculated as $\Delta n_{\mathrm{g}} = 2.0 \times 10^{-5} \Delta V/\mathrm{V}$ from eqs. (4.10) and (4.13) when assuming a linear scaling of the electric field with the inverse distance of the electrodes.

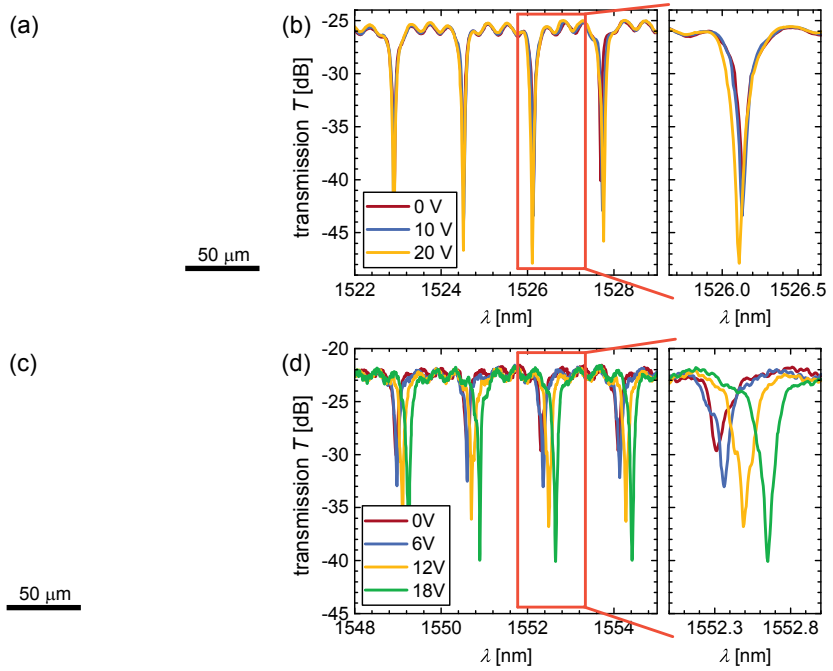

Fig. 4.37 (a) Optical microscopy image and (b) transmission spectra for various applied voltages of an active racetrack resonator with electrodes parallel to the $[100]_{\mathrm{BTO}}$ direction or parallel to the $[101]_{\mathrm{BTO}}$ direction ((c) and (d)) seperated by 2.5 µm from the waveguide. The radius of the bends is $r = 30$ µm with 75 µm-long tracks and 10 µm-long straight coupling regions. The directions of the main crystalline axes of $BaTiO_3$ are indicated in the microscopy images. The spectra shown in (d) are normalized by ∼1 dB to match the slightly varying background levels which might have been caused by a drift of the fiber position relative to the grating couplers. Different spectral ranges are used during the measurements due to a mistake in the measurement scripts, which however is not expected to alter the results.

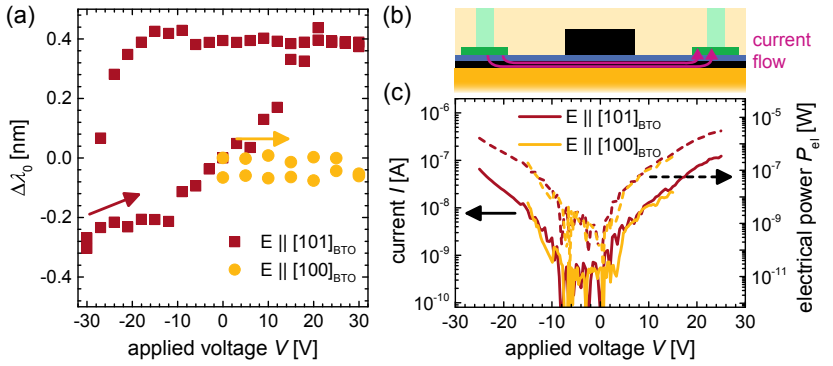

Fig. 4.38 (a) Change of the resonance wavelength λ_0 for various applied voltages in devices with an electric field along the $[100]_{\mathrm{BTO}}/[001]_{\mathrm{BTO}}$ and $[101]_{\mathrm{BTO}}$ direction, respectively. The arrows show the direction of the voltage sweeps. No data points with negative bias are obtained for the device with $\boldsymbol{E} \parallel [100]_{\mathrm{BTO}}$. (b) Illustration of a possible path of electric current (pink lines), which could flow vertically through the $BaTiO_3$ layer below the electrodes and horizontally in the device-silicon layer due to the high resistivity of $BaTiO_3$. (c) Current-voltage characteristics (solid lines) for both devices shown in (a). The dashed lines show the corresponding power consumption P_{el}.

A systematic variation of the applied voltage confirms the different electro-optical response for the devices with differently oriented electrodes (fig. 4.38a). However, the device with the electric field oriented along the $[101]_{\mathrm{BTO}}$ shows a hysteretic behavior in $\Delta\lambda_0$ when sweeping the applied voltage, which is not expected when the shift of the resonance wavelength is solely caused by the Pockels effect. The hysteretic behavior indicates the presence of another electro-optical process in the device. In order to identify such process, several mechanisms that can cause a shift of λ_0 are discussed in the following. In particular, the magnitude and a possible hysteretic response of those effects are compared with the current data.

- Plasma dispersion effect. The influence of the charge carrier concentration on the optical properties can be estimated from the current-voltage characteristics of the devices: Only small currents $I < 100\,\mathrm{nA}$ at voltages of $V = 25\,\mathrm{V}$ are observed (fig. 4.38c). The exponential $I(V)$ behavior seen in fig. 4.38c is expected for charge transport through the $BaTiO_3$ layer (section 2.5.1). Most likely, the current flows vertically through the

$BaTiO_3$ film below the electrodes, and horizontally through the device-silicon layer (fig. 4.38b) because silicon has the lowest resistivity among all layers in the waveguide core. Since there is no *pn* or *pin* junction in the structure, the charge carrier concentration in the silicon layer will not increase by the low current, and the plasma dispersion effect has thus no influence on the transmission spectra.

Alternatively, due to the strong electric field, charge carriers in the silicon layer could be pulled out of the active region. The equilibrium concentration of free carriers when no field is applied is limited by the low doping ($\sim 10^{15}/\mathrm{cm}^3$), which results in only a small change of the refractive index ($\Delta n_{\mathrm{Si}} < 10^{-5}$) when the structure is fully depleted [217]. This change is more than one order of magnitude lower than observed in the measurement (see eq. (4.30)).

Additionally, due to the symmetric electrode configuration, the plasma dispersion effect should be symmetric for positive and negative applied voltages ($\Delta\lambda_0(V) = \Delta\lambda_0(-V)$), independent of the orientation of the electric field, and without hysteretic behavior. Such symmetric behavior is in contradiction to the measurements shown in fig. 4.38a. All of these three aspects rule out the plasma dispersion as the dominant electro-optical effect in the $BaTiO_3$-slot waveguide devices.

- Thermo-optic effect. Joule heating might change the temperature of the waveguide, which could influence the optical properties due to the thermo-optic effect. In order to achieve a change of the effective index $\Delta n_{\mathrm{g}} = 8.6 \times 10^{-4}$ (eq. (4.30)), a temperature variation of $\Delta T = 4.3\,^{\circ}\mathrm{C}$ is required (eqs. (4.13) and (4.14)). The calculation is based on the similar thermo-optic effect in $BaTiO_3$ and silicon (section 4.3.4). It seems unlikely to reach such temperature variation with the low electric power consumption of $P_{\mathrm{el}} \sim 1\,\mu\mathrm{W}$ (fig. 4.38c), particularly when considering previous studies: A three orders of magnitude higher electrical power ($P_{\mathrm{el}} \sim 1\,\mathrm{mW}$) is needed to tune the resonance of ring resonators ($r = 15\,\mu\mathrm{m}$) with metallic heaters by the same magnitude ($\Delta\lambda_0 \approx 0.34\,\mathrm{nm}$) [17].

  Furthermore, the thermo-optic effect would neither depend on the orientation of the electrodes nor on the direction of the current flow, in contrast to the observations in fig. 4.38a. Also, no significant hysteresis of the temperature would be expected due to the slow measurement speed ($\sim$1 min per data point in fig. 4.38a), and the good thermal contact of the waveguide to the substrate, which ensures that thermal equilibrium is quickly reached.

- Pockels effect. The magnitude of $\Delta\lambda_0$ as well as the different behavior

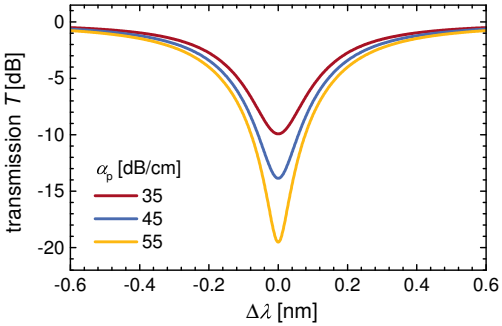

Fig. 4.39 Simulated transmission spectrum for a ring resonator with the same cavity length as the race track resonators shown in fig. 4.37. The simulations were performed at $\lambda \approx 1550\,\text{nm}$ for different propagation losses α_p based on the method described in section 4.3.4. The coupling between the ring and the straight waveguide was set to obtain an extinction ratio of $r_\text{e} \approx 20\,\text{dB}$.

for differently oriented electrodes are in agreement with the Pockels effect. The electro-optical response when applying positive or negative voltages might generally be different due to poling of ferroelectric domains in the $BaTiO_3$ layer. However, a symmetric hysteresis ($\Delta\lambda_0(V) = \Delta\lambda_0(-V)$) would be expected. In particular, the same position of the resonance for $V = 0\,\text{V}$ should be observed, in contrast to the data shown in fig. 4.38a.

Thus, none of these effects can account for all features seen in the shift of the resonance wavelength. A combination of several mechanisms, or an additional process has to be present in the samples. One possible effect would be the diffusion of ions within the $BaTiO_3$ layer, which could create or move charged defects. The space charge region around such defects creates an electric field which changes the refractive index of $BaTiO_3$ via the Pockels effect. Such two-step process is called "photorefractive effect" and is observed in ferroelectric materials [218, 219]. Additional experiments that could confirm or exclude such ion diffusion as origin of the electro-optical response are discussed at the end of this section.

Influence of propagation losses

Beside the shift of the resonance wavelength, the device with the electric field oriented along the $[101]_\text{BTO}$ axis shows a change in the extinction ratio from $r_\text{e} \approx 8\,\text{dB}$ to $18\,\text{dB}$ when increasing the voltage (fig. 4.37d). Variations of r_e

are hardly visible in the device with electrodes along the $[100]_{BTO}/[001]_{BTO}$ axes (fig. 4.37b). A change of r_e results either from a variation of the losses in the ring, or from a modified coupling between the resonator and the waveguide. The latter is unlikely since the electrodes are at a large distance to the coupling region (figs. 4.37a and 4.37c) and should thus not have any significant effect on it.

To estimate the effect of variable losses on the measurements, the transmission of a racetrack resonator is calculated based on the method described in section 4.3.4. Therefore, the experimental propagation losses are first obtained from the data set in fig. 4.37d with the highest extinction ratio. The procedure described in section 4.5.4, which is valid for critically coupled rings, results in $\alpha_p \sim 55\,\mathrm{dB/cm}$. For non-critically coupled rings with lower extinction ratio, the propagation losses and coupling losses are strongly correlated and could thus not unambiguously be distinguished when fitting the spectra with the analytic description of a ring resonator [198]. To calculate the transmission spectra, the coupling coefficient between the resonator and the waveguide is fixed at a value that yields an extinction ratio of $r_e \approx 20\,\mathrm{dB}$, as observed in the experiments fig. 4.37d. The extinction ratio varies by $\Delta r_e \sim 10\,\mathrm{dB}$ when the propagation losses are changed by $\Delta\alpha_p \sim 10\,\mathrm{dB/cm}$ (fig. 4.39). These simulated changes of Δr_e reproduce the experimental observation in the device with the electric field oriented along the $[101]_{BTO}$ direction (fig. 4.37d).

In principle, a varying concentration of charge carriers can change the absorption in the waveguide, and hence, account for a change in the extinction ratio. For carrier depletion in the low-doped device-silicon layer, the effect would be $\Delta\alpha_p < 0.01\,\mathrm{dB/cm}$ [217], which is much smaller than $\Delta\alpha_p \sim 10$ dB/cm as used in the simulations (fig. 4.39). To reach changes of 10 dB/cm, a ∼1000-fold increase of the carrier concentration to $\sim 10^{18}/\mathrm{cm}^3$ [217] would be required, which is unlikely due to the absence of a *pn* or *pin* region in the waveguide. Furthermore, a modulation of the charge carrier concentration would be independent of the orientation of the electrodes relative to the crystalline axes, in contrast to the observations from fig. 4.37.

Temperature variations ΔT are also considered not to influence the extinction ratio as they do hardly impact the absorption of silicon at low temperatures. The little influence on r_e is evidenced by previously reported experiments on ring resonators covered with metal heaters to tune the resonances: The extinction ratio of the rings hardly changes from room temperature to high temperatures of $\Delta T > 100\,°\mathrm{C}$ [17].

The Pockels effect only influences the real part of the refractive index and has no effect on the propagation losses. However, a variation of the birefringence in $BaTiO_3$ might change the polarization of the optical mode, and thus create an additional loss channel by converting TM into TE-like modes. Such effect

would be dependent on the relative orientation between the electric field and the crystalline axes, as observed in fig. 4.37. Alternatively, the variation of ionic defects in the $BaTiO_3$ layer might alter the absorption of the crystal ("photochromic effect") [219]. However, due to the limited amount of data, the analysis of the variation in the extinction ratio is restricted to the previous discussion, without definite conclusion. Possible future experiments to further understand the origin of the variations in r_e are discussed below.

Conclusion of electro-optical active devices

Optical switching in active race track resonators has been observed when applying an electric field. The order of magnitude of the response as well as the different behavior between differently oriented race track resonators match the expected performance of $BaTiO_3$-slot waveguides with strong Pockels effect. Artifacts such as a variation of the temperature or charge carrier concentrations in the silicon layer have been shown to be unlikely. However, the observed hysteresis in the shift of the resonance wavelength and the change of the extinction ratio cannot be attributed to a nonlinear optical response caused by the Pockels effect in $BaTiO_3$. Hence, a combination of several physical effects has to be considered in order to conclude the experiments, such as the coupling between TE and TM modes due to the birefringence of $BaTiO_3$, or the drift of ions in the $BaTiO_3$ layer which modifies the refractive index via the Pockels effect.

Future experiments

Additional experiments are required to identify the electro-optical process in the $BaTiO_3$ slot waveguide structures. A selection of important experiments is given below:

- Frequency dependent measurements. By changing the frequency of the applied voltage from $\sim$0 Hz to several GHz, the time constant τ of the electro-optical process can be analyzed. It allows to separate effects from ion diffusion ($\tau >$ ms, [219]) and thermo-optical effects ($\tau >$ µs) from the much faster Plasma-dispersion and Pockels-effect ($\tau <$ ns). If the operation speed of the device is not electrically limited by the electrode design, the Pockels effect ($\tau \sim$ ps) might be distinguished from charge carrier effects ($\tau \sim 0.1$ ns). As a first step, the limitations due to the electrodes can be estimated by simulating the rf-performance for the specific device layout.
- Variation of the applied voltage profile. The dependence of the hysteresis in $\Delta\lambda_0$ on the initially applied voltage should be investigated. In particular,

it has to be tested whether the hysteresis is already visible for the first measurements with small applied voltages, or only created after applying large voltages. The latter would indicate that a poling process of the ferroelectric domains might occur or that ionic filaments are created. In contrast to drifted ions, the poling of domains should be fully reversible by heating the sample above the Curie temperature, as seen during the electro-optical characterization of the $BaTiO_3$ layers (section 3.4.4). The experiment would hence give indications about the physical origin of the observed hysteresis.

- Direct correlation between $\Delta\lambda_0$ and I. By simultaneously measuring the current I and the optical response, it might be possible to separate the influence of the Pockels effect, which does not require any current flow, and charge carrier and temperature effects. In particular it is important to see whether the strong change in $\Delta\lambda_0$ at large voltages (fig. 4.38) is related to a similar increase in the current flow.

- Variation of device layout. Several device parameters should systematically be varied: (1) The dependence of the electro-optical response on the orientation of the electric field can be tested by characterizing devices with differently oriented electrodes. In particular other directions than $[001]_{BTO}$ and $[101]_{BTO}$ should be investigated. (2) By changing the distance between the electrodes and the waveguides, the response due to the electric field and due to current flow can be further separated due to the different scaling of the current and the field. (3) MZIs provide a way to characterize the electro-optical response independently of any resonant conditions and are thus less dependent on parameters such as temperature drifts. (4) The potential change of the polarization of the optical mode might be investigated by fabricating several straight waveguides with side electrodes and different combinations of grating couplers (for TE and TM-modes, respectively). It might thus be tested if by applying a voltage the total transmission is reduced, or if power is redistributed between the TE and TM mode.

- Temperature dependent measurements. By varying the sample temperature in a controlled way, the effective thermo-optic effect of $BaTiO_3$/SOI waveguides can be accessed. The influence of temperature changes on the resonant wavelength and the extinction ratio can thus be concluded or excluded.

4.6 Conclusion and outlook

This chapter discusses the implementation of thin epitaxial $BaTiO_3$ films on SOI wafers into silicon photonic structures for electro-optical active devices. Cross sections of horizontal slot waveguides with $BaTiO_3$ embedded between two silicon layers are designed to achieve a strong mode confinement in the active region and single-mode operation, and to provide compatibility with common processing routes. Components such as grating couplers and directional couplers are designed to enable basic test structures for passive and electro-optical active operation.

Active devices can be optimized for low speed or high speed operation: Compared to state of the art electro-optical devices in silicon photonics (table 4.1), $BaTiO_3$-based low-speed tuning structures promise by 2-3 orders of magnitude larger wavelength shifts for the same drive voltage (table 4.5). In terms of power consumption, $BaTiO_3$-based devices exceed the performance of current solutions using metallic heaters by up to 10 orders of magnitude.

For high-speed operation, similar figures of merit to state-of-the art modulators regarding voltage requirements are expected (table 4.5). Ways to lower the driving voltage in $BaTiO_3$ slot waveguides by one order of magnitude are discussed. The major benefits for high-speed operation are the low power requirements and the ultra-high modulation speed enabled by the Pockels effect.

Table 4.5 Calculated $V_\pi \times L$ for $BaTiO_3$-based Mach-Zehnder silicon photonic modulators, based on the Pockels effect of $BaTiO_3$/Si structures (section 3.4). The values in parenthesis are estimations for the maximal device performance after optimizing the cross sectional design and the material properties (see section 4.3.4). The $V_\pi \times L$ product of experimentally realized devices is calculated from the voltage induced change of the refractive index (eq. (4.31)) of a race track resonator, using eq. (4.15). State-of-the-art silicon photonic modulators are listed in table 4.1 for comparison.

	properties of $BaTiO_3$-based MZ modulators		
origin	calculated	calculated	from experiment
cross section	$HE^{\parallel}$	$PE^{\perp}$	$HE^{\parallel}$
physical effect	Pockels	Pockels	ambiguous
$V_\pi \times L$ [V mm]	25 (0.2)	0.27 (0.03)	16
bandwidth	rf	limited by $BaTiO_3$ capacitance / Si-series-resistance	not determined

Rf-simulations are needed to properly design the geometry of the electrodes and leads in order to reach these high modulation speeds. In particular, speed limitations due to the large permittivity of $BaTiO_3$ and therefore the potentially large capacitance between the electrodes have to be evaluated. Such simulations are not performed in the frame of this thesis.

Besides the design of the waveguides, a processing route is developed that relies mainly on standard fabrication steps. One major challenge is to obtain the Si/$BaTiO_3$/SOI layer stack with a low-loss top-silicon layer. Two solutions are successfully applied, based on the deposition of *a*-Si:H and on the layer transfer of a *c*-Si layer via molecular wafer bonding.

Passive waveguides show unexpectedly high propagation losses of >200 dB/cm. The origin of theses losses can be identified as absorption effects in the $BaTiO_3$ layer, and a way to strongly reduce them is established. From these optimized waveguide structures, passive devices such as ring resonators, couplers, and Mach-Zehnder-interferometers are successfully fabricated. First active ring resonators show promising results with a shift of the resonance wavelengths when applying a voltage (table 4.5). However, some features of the experimental results are not yet understood, such as a hysteretic behavior when sweeping the applied voltage. The Pockels effect can thus not be identified as the origin of this electro-optical response. By varying parameters in the design as well as external parameters such as the temperature or the frequency of the applied voltage, possible measurement artifacts on the electro-optical performance have to be excluded in future experiments.

The complete route from designing, fabricating and characterizing $BaTiO_3$-based active devices presented here opens the door for a new generation of silicon photonics devices enhanced by the unique properties of advanced oxides. In order to establish and further optimize the electro-optic properties, three topics should be addressed in future device designs: First, the electric field distribution for different frequencies has to be analyzed more carefully. In particular, the semiconducting nature of the silicon layers has to be taken into account. Second, the crystalline symmetry and domain structure of the $BaTiO_3$ layer must be considered for a proper estimation of the device performance. Third, the waveguide cross section should be designed in a way to achieve a maximal shift of the propagation constant rather than a maximal optical confinement in the $BaTiO_3$ layer. Therefore, an algorithm taking into account the mode profile, electric field profile and the propagation losses at the same time should be used, rather than separately optimizing the individual parameters.

To improve the processing yield, the reduction of defects in the top-silicon layer has to be further investigated, in particular the poor adhesion of the *a*-Si:H layer. Additionally, despite the reduction of the absorption losses in the $BaTiO_3$ slot waveguides, low losses as obtained for Si_3N_4 slot waveguides have

not yet been reached and further improvements are desirable.

Before optimizing the device design and the process flow, the origin of the electro-optical response has to be identified unambiguously as the very first step. Various important measurements to get more insight into the physical nature of the observed switching behavior are described in detail in section 4.5.7.

CHAPTER 5

Conclusion and Outlook

5.1 Conclusion

This thesis presents a novel approach to obtain active, integrated silicon photonic devices based on barium titanate thin films. Due to the strong nonlinear optical properties of $BaTiO_3$ and the absence of a linear electro-optical effect in silicon, these devices offer new solutions for ultra-high speed modulators, fast switches, and extremely low-power tuning elements. In order to exploit these benefits of barium titanate thin films in silicon photonic devices, a full route for the fabrication of such devices is established, starting from a bare silicon wafer.

Thin strontium titanate layers epitaxially grown on silicon substrates by means of molecular beam epitaxy serve as crystalline template for the $BaTiO_3$ deposition. The comparison of different growth processes shows a clear enhancement of the crystalline quality of the $SrTiO_3$-template when utilizing multiple rather than a single crystallization step of thin amorphously deposited layers. $BaTiO_3$ films grown on top of these seed layers are epitaxial, but tend to form crystalline defects and pores, most likely due to small deviations from stoichiometric growth conditions. The structural quality is strongly enhanced by a shuttered co-deposition growth technique. The analysis of RHEED patterns during the growth allows an improved composition control between Ba and Ti, and ultimately results in homogeneous films with low surface roughness and a high crystalline quality. Such $BaTiO_3$ layers show tetragonal symmetry, high resistivity, ferroelectric properties, and a low surface roughness. These key features are a prerequisite for most electro-optical applications. In addition to the MBE deposition, a hybrid growth method combining epitaxial seed layers

with rf-sputtering is developed. This method provides a way to grow rather thick ($\geq 100\,\mathrm{nm}$) epitaxial $BaTiO_3$ layers as needed for many optical but also piezo-electrical applications with a simple, commercially available deposition method.

The properties of thin films can vary significantly from bulk properties, and so far, no study on the electro-optical activity of $BaTiO_3$ thin films on silicon substrates has been performed. Previous studies of similar $Ba_xSr_{1-x}TiO_3$ thin films on different substrates show a large scattering of the electro-optical properties [131, 133, 220]. Even vanishing Pockels coefficients were reported [135]. Therefore, an electro-optical characterization setup is built capable of sensing the tensor nature of the optical response in the films. The effective Pockels coefficient $r_{\mathrm{eff}} = 148\,\mathrm{pm/V}$ of $BaTiO_3$-layers on silicon substrates is determined in this work. The large Pockels coefficient is a major improvement compared to the limited number of published data on electro-optical properties of lead-free oxides integrated on silicon [150, 153, 166] and thus makes $BaTiO_3$/Si layers very appealing for integrated photonic devices.

Until today, no other concept of utilizing epitaxial complex oxides in combination with silicon photonic structures has been demonstrated. As a first step, a novel waveguiding structure with $BaTiO_3$ embedded between two silicon layers is developed. A platform of devices including couplers, splitters, and interferometers based on such slot waveguides is designed and finally fabricated. These passive devices show the targeted characteristics and demonstrates the usability of $BaTiO_3$ in photonic circuits. The origin of unforeseen high propagation losses is identified and subsequently removed by a modified fabrication process.

Finally, active devices relying on the strong Pockels effect in $BaTiO_3$, in particular tunable ring resonators and Mach-Zehnder interferometers, are targeted. Here, the expected performance is strongly dependent on the kind of application: The characteristics for high-speed operation in terms of voltage requirements are similar to state-of-the-art silicon photonic modulators. The Pockels effect is however present even in the THz-regime and could thus break the speed barrier of current modulator designs based on the plasma dispersion effect. For low-speed operation, $BaTiO_3$ devices promise to reduce the voltage requirements of current tuning solutions by $2-3$ orders of magnitudes, and the power requirements by up to 10 orders of magnitude. Such expected performance is a clear enhancement compared to state-of-the-art devices. This thesis shows a first implementation of actively tunable ring resonators. These active devices are fabricated successfully and indeed show a shift of the resonance wavelengths when applying a voltage, indicating electro-optical activity in the devices. Although a conclusive interpretation of the experimental data is not possible within the scope of this thesis, the results represent a promising first

step towards understanding the behavior of $BaTiO_3$-based slot-waveguides and pave the way for future implementations of electro-optically active materials into silicon photonic devices.

5.2 Outlook

Electro-optically active $BaTiO_3$ films epitaxially grown on silicon substrates form a platform to engineer novel devices in the field of silicon photonics. Exciting challenges for material scientists lie in tailoring the electro-optical properties of such functional oxides, which could be realized by strain engineering or fabrication of superlattice structures [221]. Molecular beam epitaxy is a deposition method perfectly suited to address these tasks, since different strain levels can already be obtained by changing the film thickness (chapter 2). Stacks of multiple layers can retain large strain even in thick layers beyond the critical thickness of $BaTiO_3$. Furthermore, doping can be used to change the chemistry in the layers and thus alter their optical properties. Understanding the correlation between the crystalline structure and the Pockels tensor could ultimately lead to another boost of the electro-optical response, and eventually result in thin films that are superior to bulk crystals. This vision is also motivated by reports of perovskite thin films on silicon substrates exceeding the crystalline quality of bulk single crystals [41].

Integrated photonic devices as suggested in this thesis will clearly benefit by such enhanced electro-optical activity in the $BaTiO_3$ layer. Their performance can also be improved by further engineering the waveguide design, such as varying the electrode layout or altering the $BaTiO_3$ thickness. $BaTiO_3$-based waveguides could finally add various features to the current silicon photonic platform: First, they offer a different, potentially extremely fast way to modulate light compared to current solutions. Second, they could solve the problem of the high sensitivity of silicon photonic circuits on temperature variations and small size variations during the fabrication. Third, $BaTiO_3$-waveguides can be used as static tuning elements of resonant structures or filters with extremely low voltage and power requirements compared to current solutions based on local heaters. Fourth, completely new non-volatile optical switches or memories can be envisioned when the ferroelectric properties of $BaTiO_3$ or the diffusion of ions in the perovskite layer are exploited. Finally, the variations of the birefringence could be used to implement new device types to actively change the polarization of the optical modes, in particularly to convert TE and TM modes.

It can be foreseen that a local integration of $BaTiO_3$ slot waveguides into current silicon photonic solutions based on 220 nm SOI wafers is possible by

proper adjustment of the design of the waveguide cross section. Couplers between the standard-Si waveguides and $BaTiO_3$-slot waveguides as well as additional processing steps such as etching of $BaTiO_3$ might be necessary, but do not imply fundamental limitations. Alternatively, the photonic circuits could be fabricated entirely out of $BaTiO_3$-based structures. Providing the currently observed losses are reduced, such a platform enables the realization of complex, integrated photonic circuits - with a design toolbox that is enriched by the class of strong electro-optically active materials.

Appendices

APPENDIX A

French summary

A.1 Chapitre 1 : introduction

La constante amélioration des performances des puces électroniques se traduit par une difficulté croissante à gérer les transferts de données par le biais de câbles électriques [5], non seulement à cause des contraintes en puissance mais aussi à cause de la demande grandissante en bande passante. Dans ce contexte, des dispositifs optiques ont vu le jour et des éléments tels que des détecteurs [222] ou des modulateurs [8] sont d'ores et déjà intégrés sur des plateformes de silicium. Toutefois, il est intéressant de constater qu'à ce jour la technologie photonique sur silicium n'ait pas encore exploité les propriétés électro-optiques linéaires des oxydes.

En effet, l'énorme potentiel des matériaux à fort coefficient électro-optique linéaire (plus connu sous le nom de coefficient de Pockels) dans les systèmes de communications optiques est parfaitement illustré par les dispositifs à base de niobate de lithium ($LiNbO_3$). Au cours des dernières décennies, le niobate de lithium a été utilisé en tant que modulateur de lumière à hautes fréquences [20], et est jusqu'à présent un composant majeur de la grande majorité des réseaux de télécommunication [21]. L'effet Pockels, qui décrit la variation d'indice de réfraction d'un matériau soumis à un champ électrique, a lieu à des fréquences de l'ordre du Terahertz [22]. L'aspect linéaire de cet effet a été fondamental pour exploiter des formats de modulation avancée, comme par exemple la modulation d'amplitude quadratique qui augmente la bande passante des liaisons optiques [21, 23]. Malheureusement, tous ces dispositifs sont déposés sur des substrats de $LiNbO_3$ cristallins et sont donc incompatibles

avec les circuits photoniques sur silicium.

Utiliser un matériau présentant un fort coefficient électro-optique dans des circuits optiques sur silicium permettrait d'une part de dupliquer la technique de modulation du $LiNbO_3$ qui est maintenant parfaitement maîtrisée, et d'autre part d'élaborer de nouveaux dispositifs qui, grâce à la variation d'indice optique en l'absence de courant, seraient réglables sans avoir à fournir d'énergie. Enfin, la création de mémoires optiques non volatiles pourrait être envisagée en utilisant les propriétés ferroélectriques de nombreux matériaux actifs électro-optiquement. Pour ces applications il n'est pas possible d'utiliser du silicium car son coefficient de Pockels est très faible, dû à la structure centro symétrique de son cristal [24]. Quand bien même cette symétrie pourrait être rompue en appliquant des gradients de contraintes [25, 26], l'effet Pockels alors obtenu resterait à peu près 20 fois plus petit que celui du $LiNbO_3$. Par conséquent, il est nécessaire d'intégrer d'autres matériaux afin de créer des dispositifs tirant avantage de l'effet Pockels.

Ainsi, le titanate de baryum ($BaTiO_3$) représente un excellent candidat pour l'intégration en photonique à base de silicium car il remplit les critères suivants :

1. Épais, il a l'un des plus fort coefficient de Pockels connu parmi les matériaux actifs électro-optiquement supérieur à ($r_{BTO} > 1000\,pm/V$), voir fig. A.1a). En particulier, les coefficients électro-optiques du titanate de baryum épais sont 30 fois supérieurs à ceux du $LiNbO_3$ et à peu près $\sim$600 fois supérieurs à ceux du silicium contraint.
2. Déposé en fines couches sur des substrats d'oxyde de magnésium, il permet de faire des modulateurs à grande vitesse [29, 31, 32] (voir fig. A.1b).
3. L'intégration d'oxydes cristallins épitaxiés, comme le $BaTiO_3$ ou le titanate de strontium ($SrTiO_3$) sur silicium a déjà été démontrée (voir fig. A.1c) [33, 34].

Afin d'utiliser le $BaTiO_3$ intégré sur des dispositifs photoniques à base de silicium, il est nécessaire de réunir les 3 conditions précédentes qui n'ont été jusqu'à présent démontrées que séparément. Cette thèse s'est donc intéressée à définir un moyen de développer des dispositifs photoniques actifs électro-optiquement à partir de substrats de silicium. Au cours des différents chapitres, les points suivants ont tout particulièrement été abordés (fig. A.1d) :

- La croissance par épitaxie (chapitre 2) : afin de croître des couches minces de titanate de baryum cristallin aussi proche que possible du cristal parfait, différents protocoles de croissance par épitaxie à jet moléculaire ont été développés.
- La caractérisation électro-optique de couches minces de $BaTiO_3$ (chapitre 3) : les propriétés des couches minces cristallines peuvent sensiblement

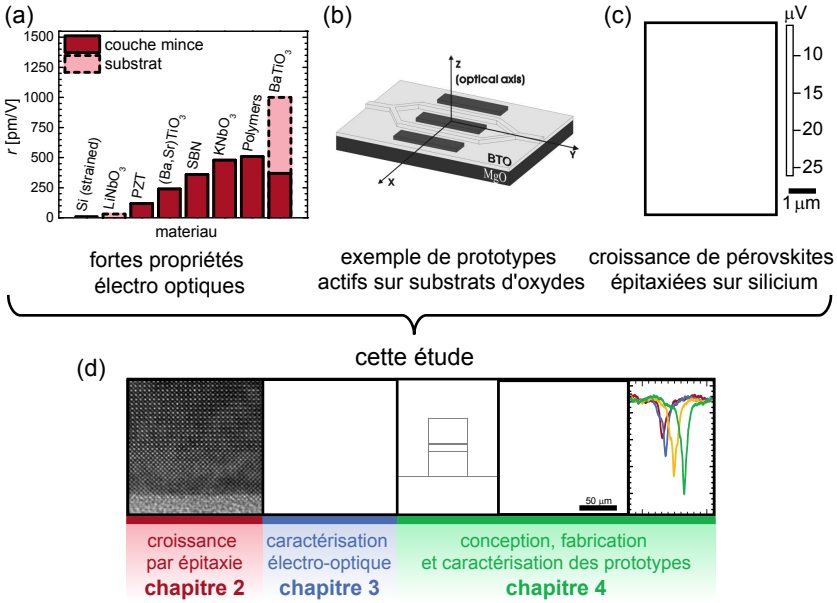

Fig. A.1 (a) Comparaison des coefficients de Pockels de differents matériaux (d'après les [26–28]), le $BaTiO_3$ épais présente la plus forte valeur. (b) Exemple de modulateur optique à base de $BaTiO_3$ déposé sur substrat de MgO [29] (schéma reporté avec la permission d'AIP Publishing LLC). (c) Croissance épitaxiée de $SrTiO_3$ ferroélectrique sur silicium [30] (schéma reporté avec la permission de l'association américaine pour l'avancée de la science). (d) Sujet et plan de la thèse.

varier de celles du même matériau épais. Ainsi, le $SrTiO_3$ en couches minces est ferroélectrique alors que sous forme de cristal épais, il ne l'est pas. De même, les propriétés du $BaTiO_3$ ont généralement tendance à se dégrader lorsqu'il est déposé sur des substrats oxydes, par rapport au cristal épais [27]. Par ailleurs, aucune étude des coefficients de Pockels du $BaTiO_3$ déposé sur substrat de silicium n'a été publiée à ce jour. Afin de caractériser des couches minces de $BaTiO_3$, un banc de mesures électro-optiques a été élaboré et une étude systématique de la réponse électro-optique d'échantillons de $BaTiO_3$ sur silicium a été menée.

- Dispositifs photoniques à base de $BaTiO_3$ sur silicium (chapitre 4): enfin, un concept de couches minces de $BaTiO_3$ électro-optiquement actives

intégrées sur une plateforme de silicium photonique a été développé. Ce développement inclut l'ingénierie de guides d'ondes avec un fort confinement du mode optique dans le BTO, la conception de composants photoniques tels que des coupleurs et des résonateurs, et l'analyse comparative de leur performance avec des dispositifs photoniques à base de silicium. Des dispositifs actifs et passifs à base de BTO ont été fabriqués et caractérisés par des moyens optiques et électro-optiques.

A.2 Chapitre 2 : fabrication des films minces

Dans le chapitre 2 les différentes routes suivies pour déposer des films épitaxiés de $BaTiO_3$ et $SrTiO_3$ sur substrat de silicium par MBE et pulvérisation rf sont discutées. Un processus d'épitaxie en phase solide est utilisé pour obtenir des couches tampons de $SrTiO_3$, en déposant tout d'abord des couches amorphes suivi d'un recuit de cristallisation. La qualité cristalline des films de phase perovskite est fortement améliorée si un recuit est effectué après les dépositions successives de couches amorphes de $\sim$1 nm plutôt que de croître un film plus épais, typiquement 4 nm, en une seule étape de cristallisation. Les cycles de recuit suppriment la formation de défauts dans les premières cellules unité du $SrTiO_3$, ce qui conduit à des couches sous contrainte avec faible rugosité de surface (≤ 0.4 nm rms) et des largeurs de balayage en omega étroites (rocking curves, $\Delta\omega_{\mathrm{STO}} \sim 0.3°$), ce qui indique une bonne cristallinité. Pour améliorer la qualité des films au niveau des propriétés de volume [41], les conditions de croissance des monocouches initiales de $SrTiO_3$ doivent être étudiées avec attention. En particulier la pression partielle d'oxygène et le domaine de température doivent être ajustés pour assurer une oxydation de $SrTiO_3$ tout en évitant la formation simultanée de SiO_2. De plus les recuits après dépôt sous oxygène peuvent améliorer la cristallinité de $SrTiO_3$ de manière significative [41].

La qualité des films minces de $BaTiO_3$ épitaxiés sur les matrices $SrTiO_3$/Si est sensible à la stœchiométrie exacte 1:1 entre le barium et le titane. Une conséquence est la formation d'ilôts, de précipités et autres défauts microstructuraux tels que pores et parois d'antiphase qui sont visibles en particulier dans les films plus épais (> 20 nm). Les limitations dans le contrôle de la stœchiométrie exacte lors de la croissance couche-par-couche sont résolues par une méthode de co-déposition avec obturateur qui donne une information rapide sur le ratio Ba:Ti en plus de l'option de pouvoir compenser de manière presque instantanée les conditions de croissance hors-stœchiométrie. Cette procédure de croissance produit des films de $BaTiO_3$ de haute qualité avec largeurs de balayage en omega étroites ($\Delta\omega_{\mathrm{BTO}} \sim 0.7°$), faibles rugosité de surface (≤ 0.3 nm rms), microstructure homogène sans pores et de symétrie cristalline tétragonale. L'orientation de l'axe c peut être ajustée entre axe c parallele ou perpendiculaire au plan de croissance en augmentant l'épaisseur de la couche, ce qui est en accord avec la disparité des paramètres de maille et des coefficients d'expansion thermique du $SrTiO_3$, $BaTiO_3$ et du silicium. La transition entre les deux orientations se produit à l'épaisseur d'environ $\sim$30 nm. L'ajustement de l'orientation cristalline procure un excellent degré de liberté pour la conception de dispositifs nanométriques qui reposent sur la polarisation

ferroélectrique de films minces de $BaTiO_3$. Un exemple est les composants photoniques actifs qui sont discutés dans le chapitre 4.

Pour atteindre des épaisseurs de film plus grandes ($> 100\,nm$), un processus de croissance hybride est développé, qui combine la croissance de couches de nucléation par MBE avec la pulvérisation rf. Les couches par pulvérisation rf croissent épitaxialement sur le substrat de silicium, lorsque l'épaisseur de la couche tampon par MBE dépasse 6 nm. Au dessus de ce seuil, la cristallinité et morphologie sont influencées d'avantage par les détails du processus de pulvérisation et les cycles de recuit que par l'épaisseur de la couche de nucléation ou de sa terminaison. $BaTiO_3$ en phase quadratique et d'orientation selon l'axe a peut être obtenu par un procédé d'épitaxie en phase solide qui inclut la déposition de $BaTiO_3$ amorphe suivit d'un recuit sous oxygène. En outre, des couches cristallines peuvent être aussi obtenues directement par pulvérisation à hautes températures, une méthode qui conduit à du $BaTiO_3$ à tétragonalité réduite, sans pores mais sous forme de nano-domaines. L'étude systématique du rôle de la couche de nucléation sur la qualité cristalline et la morphologie des couches de $BaTiO_3$ par pulvérisation est une extension d'un travail récent où des couches épitaxiées ont été fabriquées par la méthode d'ablation laser combinée avec la MBE [48]. La fabrication de films relativement épais de $BaTiO_3$ tétragonal sur silicium par pulvérisation rf est démontrée, une méthode largement utilisé en recherche et développement.

Les couches de $BaTiO_3$ ont des propriétés électriques similaires aux échantillons massifs avec des résistivités élevées $\rho > 10^{13}\,\Omega\,cm$ à faible champ électrique, indiquant une bonne composition et peu de lacunes d'oxygène. La permittivité des couches $\sim 50 - 200$ est en accord avec la littérature. La permittivité et résistivité sont deux paramètres importants pour la conception de composants électro-optiques (chapitre 4). Bien que la ferroelectricité des films ne soit pas confirmée de manière consistante par les données électriques, les mesures PFM montrent la présence de piézo- et ferroélectricité avec une polarisation spontanée hors-plan pour les films minces de $BaTiO_3$ orientés selon l'axe c (fig. A.2). Par contre piézo- et ferroelectricité ne sont pas visibles dans les films plus épais, orientés selon l'axe a, comme attendu avec la géométrie utilisée pour les mesures PFM. La présence de ferroélectricité dans les couches minces de $BaTiO_3$ par MBE est un réel progrès dans l'obtention de couches fonctionnelles sur silicium. Par comparaison les études précédentes nécessitaient soit une couche tampon bien plus épaisse [55] ou alors seul un comportement diélectrique pouvait être observé à cause d'un défaut important en oxygène [48]. Une publication récente confirme les résultats de notre travail avec la présence de ferroélectricité dans des films minces de $BaTiO_3/SrTiO_3/Si$ [56]. Des mesures de polarisation avec des contacts métalliques et une étude systématique sur des films d'épaisseur variable devraient être effectuées pour confirmer indépendamment les résultats

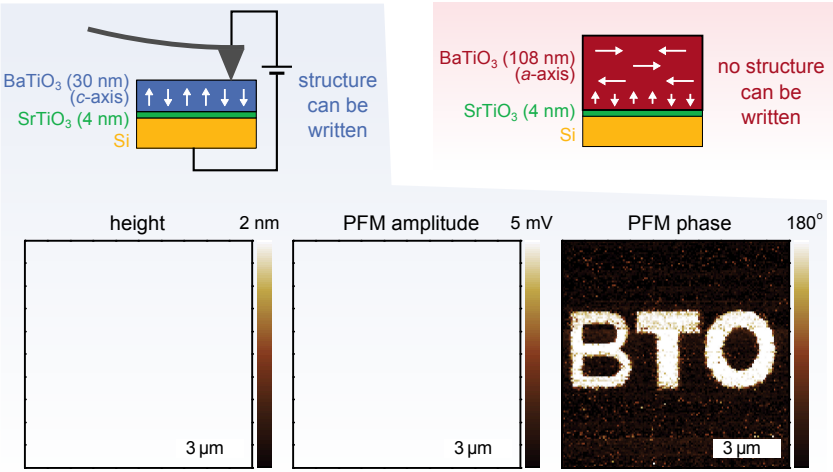

Fig. A.2 Haut : schémas de la structure des échantillons mesurés par PFM. Bas : topographie, amplitude et phase du signal PFM mesuré sur film mince de $BaTiO_3$ orienté selon l'axe *c* après écriture des lettres "BTO". Aucun contraste du signal PFM n'est observable sur le film plus épais orienté selon l'axe a.

de PFM. Un premier pas dans ce sens est la démonstration dans ce travail de thèse de la ferroélectricité dans les films en orientation selon l'axe a par la méthode de caractérisation électro-optique discutée dans le chapitre 2.

A.3 Chapitre 3 : caractérisation électro-optique

Afin d'étudier les propriétés électro-optiques de films de $BaTiO_3$, épitaxiés sur des substrats de Silicium, un plan expérimental analysant la transmission de la lumière à travers l'échantillon a été réalisé. De faibles variations de la polarisation de la lumière, causées par l'activité électro-optique dans le $BaTiO_3$, sont observées et utilisées pour reconstruire le tenseur des coefficients de Pockels du film épitaxié. Malgré la faible épaisseur du film de $BaTiO_3$ (environ $\sim$100 nm) et par conséquent une faible longueur d'interaction entre le laser et le film, la sensibilité est suffisamment élevée pour déterminer, de façon très précise, les propriétés électro-optiques du film.

Un effet électro-optique fortement linéaire avec un coefficient de Pockels $r_{\text{eff}} = 148\,\text{pm/V}$ a été déterminé, pour une couche de $BaTiO_3$ de 130 nm d'épaisseur, orientée selon l'axe cristallographique a et épitaxié sur un substrat de silicium. Cette valeur dépasse les données reportées dans la littérature, dans le cas de films de $LiNbO_3$, d'au minimum un facteur 5 et d'un facteur 100 dans le cas de films de Silicium contraints. De plus, la présence d'effet ferroélectrique avec une polarisation spontanée dans le plan a été déterminée sans aucune ambiguïté grâce à cette technique de caractérisation électro-optique (fig. A.3).

A l'aide de simulations électro-optiques complétant les mesures expérimentales, une méthode d'investigation est développée pour étudier la nature du tenseur des effets de Pockels d'un film mince. Pour un film de $BaTiO_3$, les éléments du tenseur $r_c = 30\,\text{pm/V}$ et $r_{42} = 105\,\text{pm/V}$ ont été déterminés. La connaissance du tenseur complet de Pockels est essentielle pour concevoir de façon optimale les composants optiques (section 4.3). La preuve expérimentale d'effets électro-optiques intenses dans des couches de $BaTiO_3$ est une étape déterminante, permettant de continuer la fabrication de composants actifs électro-optiques (chapitre 4).

Le plan expérimental et les possibilités d'intégration par épitaxie du $BaTiO_3$ sur Silicium (chapitre 2) permettent d'envisager de nombreuses nouvelles études: d'une part, les conditions de croissance peuvent être modifiées dans le but d'adapter les caractéristiques électro-optiques intrinsèques du film, par exemple en changeant son épaisseur pour obtenir différents niveaux de contraintes dans le film, en déposant les films de $BaTiO_3$ par le processus hybride de pulvérisation, en dopant les films, ou encore en fabriquant des super-réseaux. D'autre part, les conditions expérimentales peuvent être modifiées dans le but de changer les propriétés électro-optiques extrinsèques, comme par exemple en appliquant une contrainte par déformation du substrat ou en faisant varier la température durant les mesures. Toutes ces modifications offrent de nouvelles possibilités pour mieux comprendre les caractéristiques électro-optiques des films de $BaTiO_3$

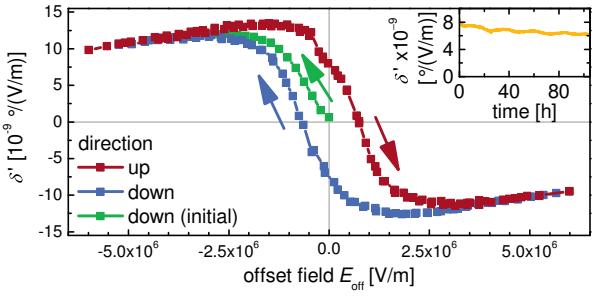

Fig. A.3 Réponse optique en fonction du champ électrique E_{off}. Les données sont collectées lors de 3 boucles successives à 25 °C après avoir chauffé l'échantillon au-dessus de la température de Curie du cristal massif (en vert) et en balayant E_{off} vers le haut (rouge) et vers le bas (bleue) de nouveau. L'encart montre la relaxation de la valeur rémanente δ' à température ambiante.

et pourront potentiellement servir à améliorer les coefficients de Pockels de cristaux massifs de $BaTiO_3$.

A.4 Chapitre 4 : dispositifs photoniques sur silicium améliorés avec du titanate de baryum

Le chapitre 4 traite de l'introduction de couches minces de $BaTiO_3$ epitaxiées sur substrat SOI dans des structures photoniques à base de Si afin de réaliser des composants electro-optiques actifs. La géométrie de guides d'ondes horizontaux composés comprenant une couche de $BaTiO_3$ entre deux couches de Si est optimisée afin d'obtenir un fort confinement du mode optique dans la region active, afin de ne supporter qu'un mode optique, et de rester compatible avec les procédés de fabrication standards. Des composants tels que des structures de couplage directionnelles et coupleurs de Bragg sont réalisées afin de permettre la caractérisation optique des structures de test basiques passives tout comme celle des composants electro-optiques actifs.

Les composants actifs peuvent être optimisés pour un fonctionnement à basse ou à très haute fréquence : contrairement à l'état de l'art des composants electro-optiques à base de photonique sur Si (table 4.1), les structures de réglage à base de $BaTiO_3$ doivent permettre 2 à 3 ordres de grandeur d'amelioration de la gamme de réglage en longueur d'onde pour la même tension d'alimentation (table A.1). En terme de consommation d'énergie, les composants à base de $BaTiO_3$ peuvent dépasser les performances des solutions utilisant des systèmes de chauffage métallique de près de 10 ordres de grandeur.

Pour le fonctionnement à très haute fréquence, il est attendu d'obtenir des tensions d'opération similaires aux meilleurs modulateurs reportés dans l'état de l'art (table A.1). Toutefois, certaines méthodes pour réduire d'un ordre de grandeur la tension d'opération pour des guide d'ondes composés à base de $BaTiO_3$ sont actuellement a l'etude. Les avantages principaux de ces structures pour l'opération à très haute fréquence sont inherents a l'effet Pockels : vitesse de modulation extrêmement élevée pour une très faible consommation.

Pour pouvoir atteindre de très hautes fréquences de fonctionnement, des simulations RF sont nécessaires afin d'optimiser la géométrie des électrodes. En particulier, la grande constante diélectrique du $BaTiO_3$ induit de grandes capacités parasites entre les électrodes. Cette effet doit être pris en compte. Cependant, ce type de simulations ne fait pas partie du cadre de cette thèse.

Au delà des simulations de la géométrie des guides d'ondes, un procédé de fabrication se basant sur des étapes standards est également proposé (fig. A.4). La difficulté la plus importante est d'obtenir une couche supérieure de Si ayant de faibles pertes optiques. Deux solutions sont proposées et réalisées avec succès, basées sur la déposition de *a*-Si:H ou sur le transfert par collage moléculaire d'une couche de *c*-Si.

Des mesures sur les guides d'ondes passifs révèlent des pertes optiques de

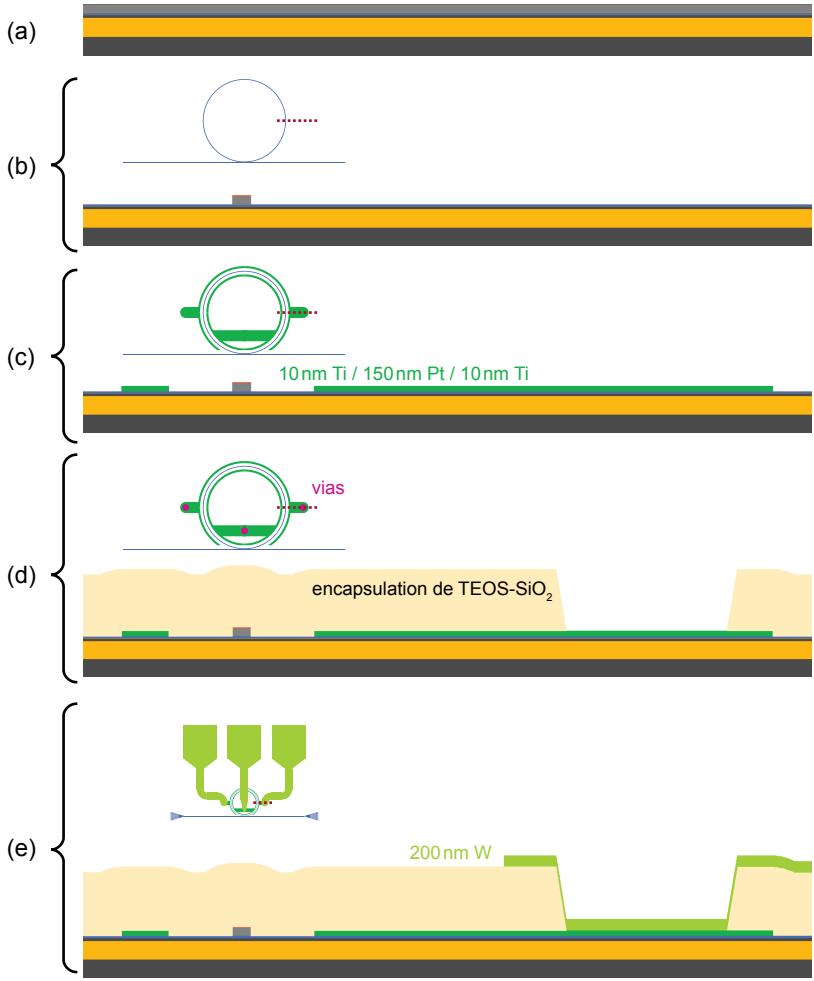

Fig. A.4 Evolution des niveaux de masque, de la vue de dessus et de la vue en coupe schematique. La vue en coupe dorrespond a la ligne en pointillé rouge dans les niveaux de masque. (a) L'empilement initial de couches est (b) gravé avec un plasma d'HBr pour former des guides d'ondes. (c) Des électrodes latérales sont déposées sur le $BaTiO_3$, puis une encapsulation de TEOS-SiO_2 est déposée et des ouvertures sont gravées pour accéder aux électrodes. (e) Les électrodes sont ensuite connectées à des bornes de contact plus grandes au moyen d'une couche de 200 nm de tungstène.

propagation extrêmement élevées, supérieures a 200 dB/cm. L'origine de ces pertes est identifiee comme venant de la couche de $BaTiO_3$. Une méthode pour réduire ces pertes est proposée et réalisée avec succès. Grace à ces guides d'ondes optimisés, des composants passifs fonctionnels tels que des résonateurs circulaires (fig. A.5), des coupleurs et des interféromètres Mach-Zehnder sont démontrés. Les premières mesures sur des résonateurs circulaires actifs démontrent des résultats prometteurs puisqu'une variation de la longueur d'onde de résonnance en fonction de la tension d'opération a pu être atteint (table 4.5). Cependant, certains aspects des résultats expérimentaux ne sont pas encore complètement compris, comme le comportement à hystérèse en fonction de la tension appliquée. L'effet Pockels ne peut donc pas être clairement identifié comme étant à l'origine de la réponse electro-optique. En variant des paramètres géométriques et extérieurs tels que la température ou la fréquence de la tension appliquée, l'origine exacte de la réponse electro-optique pourra être mieux identifiée.

Le procédé complet proposé ci-après qui consiste a optimiser la géométrie des structures, fabriquer et caractériser les composants actifs à base de $BaTiO_3$ ouvre la voie vers une nouvelle génération de composants photoniques à base de Si boostés par les propriétés uniques des oxydes fonctionnels. Afin de repousser les limites des composants electro-optiques présentés dans ce travail, trois sujets

Table A.1 Valeur calculées $V_\pi \times L$ pour des modulateurs photoniques sur Si de type Mach-Zehnder à base de $BaTiO_3$, en utilisant l'effet Pockels des structures $BaTiO_3$/Si (section 3.4). Les valeurs entre parenthèse sont des estimations de la performance maximale des composants après avoir optimisé leur géométrie et les propriétés des matériaux (voir section 4.3.4). Le produit $V_\pi \times L$ est calculé pour des résonateurs experimentaux de type "race-track" a partir du changement d'indice de réfraction en fonction de la tension appliquée (éq. 4.31) en utilisant l'équation 4.15. Les valeurs de l'etat de l'art pour des modulateurs photonique a base de silicium sont reportées dans la table 4.1 pour comparaison.

	proprietes des modulateurs MZ a base de $BaTiO_3$		
origine	calculé	calculé	experimental
coupe	$HE^{\parallel}$	$PE^{\perp}$	$HE^{\parallel}$
effet physique	Pockels	Pockels	ambigüe
$V_\pi \times L$ [V mm]	25 (0.2)	0.27 (0.03)	16
bande passante	rf	limité par la capacité du $BaTiO_3$ / résistance série du Si	indeterminé

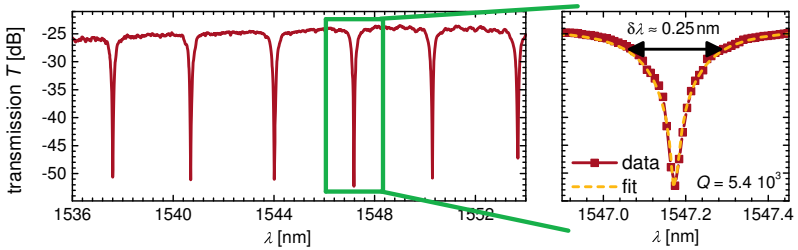

Fig. A.5 Spectre de transmission TM d'un résonateur circulaire à base de guides d'ondes composés comprenant du $BaTiO_3$, étant couplé au point critique. Le facteur de qualite extrait de la resonnance agrandie a droite est $Q = 5.4 \times 10^3$. La largeur de la résonance a mi-transmission $\delta\lambda$ (-3 dB) est indiquée dans la figure de droite.

doivent être traités dans le future : premièrement, la distribution du champ électrique en fonction de la fréquence de fonctionnement doit être prise en compte. En particulier, le Si doit être réellement traité comme un matériau semi-conducteur. Deuxièmement, la symétrie cristalline et l'organisation des domaines de la couche de $BaTiO_3$ doit être pris en compte afin d'extraire correctement la réelle performance des composants mesurés. Troisièmement, la géométrie des guides d'ondes ne doit pas être optimisée pour confiner au mieux le mode optique dans la région active, mais plutôt pour maximiser la variation des constantes de propagation. L'algorithme d'optimisation doit prendre en compte simultanément le profil du mode optique, la distribution du champ électrique et les pertes de propagation, et non pas optimiser ces différents aspects séparément.

Afin d'améliorer rendement de fabrication, la densité de défauts dans la couche supérieure de Si doit être réduite et l'origine des problèmes d'adhésion du *a*-Si:H doit être identifiée. Egalement, bien que la stratégie proposée pour réduire les pertes optiques dans les guides d'ondes à base de $BaTiO_3$ fut un succès, ces pertes doivent encore être réduites afin d'approcher celles mesurées dans les échantillons de référence avec Si_3N_4.

Avant de chercher a ré-optimiser la structure des composants et le procédé de fabrication, l'origine exacte de la réponse electro-optique observée doit être comprise de manière in-ambigüe. Plusieurs mesures importantes doivent être conduites (comme décrites en détail dans la section 4.5.7) afin de mieux comprendre l'origine physique de l'effet de commutation observé.

A.5 Chapitre 5 : conclusion et perspectives

Cette thèse présente une nouvelle approche pour l'obtention de dispositifs actifs basés sur des films minces de titanate de baryum, intégrés dans une technologie photonique silicium. En raison des excellentes propriétés optiques non linéaires de $BaTiO_3$ et à cause de l'absence d'un tel effet dans le silicium, ces dispositifs apportent de nouvelles solutions pour la fabrication de modulateurs ultra-rapides, des commutateurs rapides, et de dispositifs d'ajustement de très faible puissance. Afin d'exploiter les propriétés des couches minces de $BaTiO_3$ dans des dispositifs photoniques sur silicium, un procédé complet est établi, en partant de substrat de silicium.

Des couches tampons de titanate de strontium sont tout d'abord obtenues par croissance épitaxiale sur le silicium en utilisant l'épitaxie par jets moléculaires (EJM) et l'épitaxie en phase solide. La comparaison des différents processus de croissance montre clairement une amélioration de la qualité structurale des couches lorsque l'étape de cristallisation est effectuée de manière séquentielle. Ces films servent ensuite de couche de nucléation pour le dépôt de $BaTiO_3$ monocristallin. Les films de $BaTiO_3$ sont épitaxiés, mais la densité de défauts cristallins et la porosité est dépendante de leur stœchiométrie. La qualité structurale est notamment fortement améliorée en utilisant une technique de croissance par co-déposition alternée. L'analyse en temps réel pendant la croissance (par diffraction électronique rasante) permet un contrôle de composition fin pour optimiser le rapport Ba/Ti. Cette étude aboutit finalement à l'obtention de films homogènes ayant une faible rugosité de surface et une bonne qualité cristalline. Ces couches $BaTiO_3$ cristallisent dans une symétrie quadratique, ont une résistivité élevée et des propriétés ferroélectriques. Ces caractéristiques sont une condition préalable pour la plupart des applications électro-optiques. En plus du dépôt par EJM, un procédé de croissance hybride incluant une déposition par pulvérisation cathodique est également développé. Cette méthode simple et industrielle permet de faire croître des couches épitaxiales de $BaTiO_3$ avec des épaisseurs ($\geq 100\,nm$) adaptées aux applications optiques mais également piézo-électriques.

Les propriétés des couches minces peuvent dévier considérablement des propriétés des matériaux massifs. A ce jour dependant, aucune étude sur l'activité électro-optique des couches minces de $BaTiO_3$ sur des substrats de silicium n'a été effectuée. Des études antérieures basées sur des films minces de $Ba_xSr_{1-x}TiO_3$ montrent une grande dispersion des propriétés électro-optiques [131, 133, 220]. Des coefficients Pockels proche de zéro ont même été rapportés [135]. Un système de caractérisation électro-optique est donc construit afin de déterminer le tenseur electro-optique dans les films. Un coefficient de Pockels

$r_{\text{eff}} = 148\,\text{pm/V}$ est extrait pour des couches de $BaTiO_3$ sur des substrats de silicium. Cette valeur représente une amélioration majeure par rapport aux données publiées sur les propriétés électro-optiques d'oxydes sans plomb intégrés sur silicium [150, 153, 166]. Ce résultat rend donc le système $BaTiO_3$/Si très attractif pour la réalisation de dispositifs photoniques intégrés.

Dans un premier temps, un guide d'ondes à fente avec $BaTiO_3$ incorporé entre deux couches de silicium est développé. Une plate-forme incluant différents dispositifs (coupleurs , diviseurs, interféromètres..) et basée sur de tels guides d'ondes est finalement conçue et fabriquée. Les dispositifs passifs présentent les caractéristiques souhaitées et démontre la facilité d'utilisation de $BaTiO_3$ dans les circuits photoniques. L'origine des pertes de propagation élevées est également identifiée, et éliminée en utilisant un procédé de fabrication modifié.

Enfin, des dispositifs actifs s'appuyant sur l'effet Pockels dans $BaTiO_3$ sont fabriqués, en particulier des résonateurs en anneau et des interféromètres de Mach-Zehnder. Pour de tels dispositifs, les objectifs de performances dependent de l'application: Les caractéristiques de fonctionnement en tension à haute fréquence sont similaires aux modulateurs photoniques sur silicium à l'état de l'art. L'effet Pockels est cependant présent même jusque dans la gamme THz, et pourrait ainsi offrir des vitesses de modulation supérieures aux modulateurs actuels basés sur l'effet de dispersion plasma. Pour un fonctionnement à basse fréquence, par exemple pour des dispositifs d'ajustement, les tensions de travail pourraient être réduites par $2-3$ ordres de grandeur, et les besoins en énergie de près de 10 ordres de grandeur. Ce gain en performance serait une amélioration nette par rapport à des dispositifs à l'état de l'art. Cette thèse montre donc une première mise en œuvre de résonateurs en anneau activement accordables. Ces dispositifs actifs sont fabriqués avec succès et présentent un décalage des longueurs d'onde de résonance en fonction de la direction et de l'intensité du champ appliqué, ce qui indique clairement une activité électro-optique liée au $BaTiO_3$. Une interprétation complète des données expérimentales à ce niveau des travaux n'est pas possible dans le cadre de cette thèse. Ces résultats représentent cependant une étape prometteuse vers la compréhension du comportement de dispositifs photoniques basés sur $BaTiO_3$, et ouvrent la voie à de futures implémentations de matériaux électro-optiquement actifs pour la photonique intégrée sur silicium.

APPENDIX B

Calculation of barium titanate lattice constants

The in-plane strain $\epsilon_{\parallel}$ in $BaTiO_3$ thin films grown on $SrTiO_3$/Si substrates shown in fig. 2.23 is calculated by

$$\epsilon^{\parallel}(T) = \frac{a^{\parallel}_{\mathrm{BTO,f}}(T)}{a^{\parallel}_{\mathrm{BTO,b}}(T)} - 1 \tag{B.1}$$

where $a^{\parallel}_{\mathrm{BTO,b}}(T)$ is the lattice constants of bulk-$BaTiO_3$. $a^{\parallel}_{\mathrm{BTO,f}}(T)$ is the in-plane lattice parameter of the $BaTiO_3$ film, which is calculated for two different situations: If the $BaTiO_3$ layer is completely strained to the $SrTiO_3$ seed layer (fig. 2.23b), the $BaTiO_3$ in-plane lattice constant at temperature T is determined as

$$a^{\parallel}_{\mathrm{BTO,f}}(T) = \left(a_{\mathrm{STO,b}}(T_{\mathrm{g,STO}}) \frac{a_{\mathrm{Si,b}}(T)}{a_{\mathrm{Si,b}}(T_{\mathrm{g,STO}})} \right). \tag{B.2}$$

Here, $a_{\mathrm{STO,b}}(T_{\mathrm{g,STO}})$ is the bulk-$SrTiO_3$ lattice constant at the $SrTiO_3$ deposition temperature $T_{\mathrm{g,STO}} \approx 100\,^{\circ}\mathrm{C}$ and $a_{\mathrm{Si,b}}(T)$ the lattice constant of bulk-Si. The out-of-plane lattice constant $a^{\perp}_{\mathrm{BTO,f}}(T)$ of the $BaTiO_3$ film is calculated as

$$a^{\perp}_{\mathrm{BTO,f}}(T) = \sqrt{\frac{V_{\mathrm{BTO,b}}(T)}{a^{\parallel}_{\mathrm{BTO,f}}(T)}} \tag{B.3}$$

where $V_{\mathrm{BTO,b}}(T)$ is the volume of the unit cell of bulk $BaTiO_3$.

In the second case, the $BaTiO_3$ film is assumed to be fully relaxed at the $BaTiO_3$ deposition temperature of $T_{\mathrm{g,BTO}} \approx 600\,^{\circ}\mathrm{C}$. Hence, the in-plane lattice

constant is determined as

$$a^{\parallel}_{\mathrm{BTO,f}}(T) = a_{\mathrm{BTO,b}}(T_{\mathrm{g,BTO}})\,\frac{a_{\mathrm{Si,b}}(T)}{a_{\mathrm{Si,b}}(T_{\mathrm{g,BTO}})}. \tag{B.4}$$

In all cases, the literature values are used for calculating the temperature dependent lattice constants of $BaTiO_3$ [57, 109], $SrTiO_3$ [59], and Si [60].

APPENDIX C

Electro-optical software and analysis tools

C.1 Software to control electro-optical setup

A *National Instruments LabVIEW* based software is developed in order to control the measurement setup described in section 3.3. A screenshot and a description of the user interface is shown in fig. C.1. The program is used to communicate with all relevant instruments in the measurement setup, in particular the ac- and the dc-voltage source, three motorized stages, the detector, the locking-in amplifier, and the analog-digital converter. The sample alignment is performed manually on a non-motorized xyz-stage. Several design aspects and specific challenges are addressed in the *LabVIEW* program, as described in the following paragraphs.

Measurement flexibility Measurement flexibility is given high priority in the software design. The standard measurement routine is defined as a "parameters sweep" which includes the following steps

1. The "measurement procedure" is set. The measurement procedure defines which signals will be recorded (such as transmitted power P, power variations ΔP, or both), the parameters used for the data recording (such as data averaging, or target values for the standard deviation of the measured signal), and how the data is processed (such as subtraction of background signals).
2. The inital device parameters are set, such as the frequency f and voltages of the applied field, integration times for the lock-in amplifier, and gain settings.

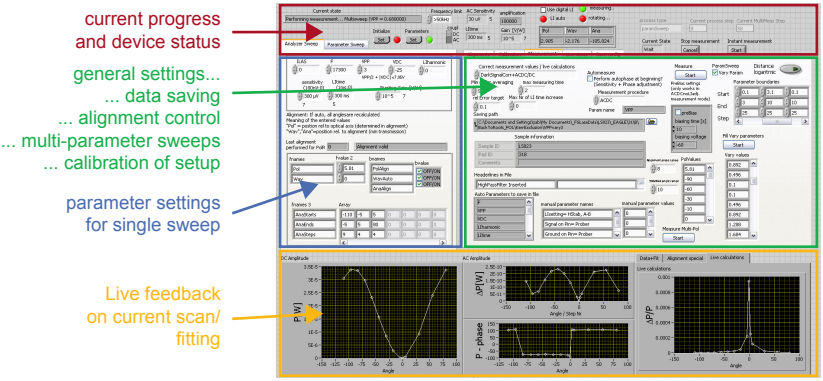

Fig. C.1 Screenshot of the user-interface of the *LabVIEW* program developed for controlling the measurement hardware. The purpose of several different blocks is indicated on the right.

3. The parameter to be varied during the sweep is defined, as well as the setpoints for this parameter by a range of values (or multiple ranges).

With this procedure, many different dependencies such as $\Delta P\,(f)$, $\Delta P\,(V_{\mathrm{off}})$, or analyzer scans $\Delta P/P\,(\theta_{\mathrm{a}})$ can be analyzed with ease. Optionally, a second parameter can be varied in the same way, resulting into two dimensional data arrays. Examples are the determination of analyzer scans $\Delta P/P\,(\theta_{\mathrm{a}})$ at various angles of the incident polarization θ_{i} or at various voltage offsets V_{off}, as required for measuring hysteresis loops.

The approach of flexibly defining the actual parameter to scan also allows the setup to be easily extended for future measurements, for example including temperature variations or a motorized sample stage.

Quarter-wave plate alignment As discussed in section 3.3.2, the quarter-wave plate compensates the ellipticity of polarization of the light after the sample. The position has to be set accurately depending on the sample orientation and the incident polarization. An automated routine is programmed that iteratively varies the angle of the quarter-wave plate and the analyzer, or both of them simultaneously. The elements are set to the minimum position of the transmitted light, which is determined by fitting the angular scans. The alignment is either stopped by reaching a maximum number of iterations or by crossing a threshold of minimal transmission.

Automated gain settings The high extinction ratios of the polarizers results in a large range of the detected power signal covering 5 orders of magnitude when rotating the analyzer. Therefore, the detector gain as well as the gain of the lock-in amplifier has to be adjusted continuously during the measurement. The device-specific auto-tune functions are rather slow, in particular for the lock-in amplifier with an integration time on the order of $\sim$1 s. A much faster, manual auto-tuning routine is programmed which takes into account the measurement history and a set of well-defined switching thresholds specific to the devices in use.

Calibration of polarizing elements The various polarizing elements (two polarizers, one quarter-wave and one half-wave plate, fig. 3.6) have to be well-aligned in respect to each other in order to achieve good extinction ratios. Automated routines are programmed to calibrate the angular offset of the motorized stages in respect to the first polarizing element. Therefore, the optical elements have to be inserted and calibrated successively. These calibration procedures work similar to the above mentioned alignment procedure, and facilitate the exchange of optical elements.

C.2 Data analysis

The analysis of the measurement data is performed with scripts written in *Wolfram Mathematica*. Similar to controlling the measurement hardware, great care is taken on a flexible way of evaluating the data. The core of gaining large flexibility is the introduction of a specific data format, that separates the data values, the description of the data, and the parameters for the measurement in defined form. Functions in order to manipulate and evaluate the data with models defined in section 3.3.2 are developed based on the specific data format. Thus, newly added parameters in the original data files as obtained from the *LabVIEW* module can be handled without changing any of the analysis-functions.

List of Figures

List of Tables

Bibliography

1. Deen, M. J. & Basu, P. *Silicon Photonics - Fundamentals and Devices* (John Wiley & Sons, 2012).
2. Haurylau, M. *et al.* "On-Chip Optical Interconnect Roadmap: Challenges and Critical Directions". *IEEE J. Sel. Topics Quantum Electron.* **12,** 1699–1705 (2006).
3. Chen, G. *et al.* "Predictions of CMOS compatible on-chip optical interconnect". *Integr VLSI J* **40,** 434–446 (2007).
4. Beausoleil, R., Kuekes, P., Snider, G. S., Wang, S.-Y. & Williams, R. S. "Nanoelectronic and Nanophotonic Interconnect". *Proc. IEEE* **96,** 230–247 (2008).
5. Miller, D. A. B. "Device Requirements for Optical Interconnects to Silicon Chips". *Proc. IEEE* **87,** 1166–1185 (2009).
6. Taillaert, D. *et al.* "Grating Couplers for Coupling between Optical Fibers and Nanophotonic Waveguides". *Jpn. J. Appl. Phys.* **45,** 6071–6077 (2006).
7. Horst, F. *et al.* "Cascaded Mach-Zehnder wavelength filters in silicon photonics for low loss and flat pass-band WDM (de-)multiplexing". *Opt. Express* **21,** 11652–11658 (2013).
8. Reed, G. T., Mashanovich, G., Gardes, F. Y. & Thomson, D. J. "Silicon optical modulators". *Nature Photon.* **4,** 518–526 (2010).

9. Luxtera. *Press release - Luxtera Delivers Worlds First Single Chip 100Gbps Integrated Opto-Electronic Transceiver*. <http://www.luxtera.com/20111108239/luxtera-delivers-world%E2%80%99s-first-single-chip-100gbps-integrated-opto-electronic-transceiver.html> (2011).
10. Hofrichter, J. *InP Microdisks for Optical Signal Processing and Data Transmission*. PhD thesis (Technische Universität Eindhoven, 2013).
11. Yu, Z. & Fan, S. "Complete optical isolation created by indirect interband photonic transitions". *Nat Photon* **3,** 91–94 (2009).
12. Liu, J., Sun, X., Camacho-Aguilera, R., Kimerling, L. C. & Michel, J. "Ge-on-Si laser operating at room temperature". *Opt. Lett.* **35,** 679–681 (2010).
13. Michel, J., Liu, J. & Kimerling, L. C. "High-performance Ge-on-Si photodetectors". *Nature Photon.* **4,** 527–534 (2010).
14. Xiao, X. *et al.* "High-speed, low-loss silicon Mach-Zehnder modulators with doping optimization". *Opt. Express* **21,** 4116–4125 (2013).
15. Cocorullo, G., Della Corte, F. G. & Rendina, I. "Temperature dependence of the thermo-optic coefficient in crystalline silicon between room temperature and 550 K at the wavelength of 1523 nm". *Appl. Phys. Lett.* **74,** 3338–3340 (1999).
16. Teng, J. *et al.* "Athermal Silicon-on-insulator ring resonators byoverlaying a polymer cladding on narrowedwaveguides". *Opt. Express* **17,** 14627–14633 (2009).
17. Gan, F. *et al. Maximizing the Thermo-Optic Tuning Range of Silicon Photonic Structures*. in *Photonics in Switching, 2007* (2007), 67–68.
18. Atabaki, A. H., Shah Hosseini, E., Eftekhar, A. A., Yegnanarayanan, S. & Adibi, A. "Optimization of metallic microheaters for high-speed reconfigurable silicon photonics". *Opt. Express* **18,** 18312–18323 (2010).
19. Chaisakul, P. *et al.* "Strong quantum-confined Stark effect from light hole related direct-gap transitions in Ge quantum wells". *Appl. Phys. Lett.* **102,** 191107 (2013).

20. Wooten, E. *et al.* "A Review of Lithium Niobate Modulators for Fiber-Optic Communications Systems". *J. Sel. Topics Quantum Electron.* **6,** 69–82 (2000).

21. Janner, D., Tulli, D., Garcia-Ruperez, M. J.-Granda, Belmonte, M. & Pruneri, V. "Micro-structured integrated electro-optic $LiNbO_3$ modulators". *Laser & Photonics Reviews* **3,** 301–313 (2009).

22. Valdmanis, J. A. *Measurement of High-Speed Signals in Solid State Devices (Chapter 4)* (ed Marcus, R. B.) (Academic Press, INC., San Diego, 1990).

23. Wu, X., Peng, W.-R., Arbab, V., Wang, J. & Willner, A. "Tunable optical wavelength conversion of OFDM signal using a periodically-poled lithium niobate waveguide". *Opt. Express* **17,** 9177–9182 (2009).

24. Nye, J. F. *Physical properties of crystals* (Oxford University Press, 1960).

25. Jacobsen, R. S. *et al.* "Strained silicon as a new electro-optic material". *Nature* **441,** 199–202 (2006).

26. Chmielak, B. *et al.* "Pockels effect based fully integrated, strained silicon electro-optic modulator". *Opt. Express* **19,** 17212–17219 (2011).

27. Wessels, B. W. "Ferroelectric Epitaxial Thin Films for Integrated Optics". *Annu. Rev. Mater. Res.* **37,** 659–679 (2007).

28. Bernasconi, P., Zgonik, M. & Gunter, P. "Temperature dependence and dispersion of electro-optic and elasto-optic effect in perovskite crystals". *J. Appl. Phys.* **78,** 2651–2658 (1995).

29. Petraru, A., Schubert, J., Schmid, M. & Buchal, C. "Ferroelectric $BaTiO_3$ thin-film optical waveguide modulators". *Appl. Phys. Lett.* **81,** 1375–1377 (2002).

30. Warusawithana, M. P. *et al.* "A Ferroelectric Oxide Made Directly on Silicon". *Science* **324,** 367–370 (2009).

31. Gill, D. M., Conrad, C. W., Ford, G., Wessels, B. W. & Ho, S. T. "Thin-film channel waveguide electro-optic modulator in epitaxial $BaTiO_3$". *Appl. Phys. Lett.* **71,** 1783–1785 (1997).

32. Tang, P., Towner, D., Hamano, T., Meier, A. & Wessels, B. "Electrooptic modulation up to 40 GHz in a barium titanate thin film waveguide modulator". *Opt. Express* **12,** 5962–5967 (2004).

33. McKee, R. A., Walker, F. J., Conner, J. R., Specht, E. D. & Zelmon, D. E. "Molecular beam epitaxy growth of epitaxial barium silicide, barium oxide, and barium titanate on silicon". *Appl. Phys. Lett.* **59,** 782–784 (1991).

34. Baek, S.-H. & Eom, C.-B. "Epitaxial integration of perovskite-based multifunctional oxides on silicon". *Acta Mater.* **61,** 2734–2750 (2013).

35. Herman, M. A., Richter, W. & Sitter, H. *Epitaxy* (eds Hull, R., Parisi, J., R M Osgood, J. & Warlimont, H.) (Springer-Verlag, 2004).

36. Sze, S. M. *Physics of Semiconductor Devices* (John Wiley & Sons, 1981).

37. Reiner, J. W., Garrity, K. F., Walker, F. J., Ismail-Beigi, S. & Ahn, C. H. "Role of Strontium in Oxide Epitaxy on Silicon (001)". *Phys. Rev. Lett.* **101,** 105503 (2008).

38. Marchiori, C. *et al.* "Thermal stability of the $SrTiO_3$/(Ba,Sr)O stacks epitaxially grown on Si". *Appl. Phys. Lett.* **88,** 072913 (2006).

39. Norga, G. J. *et al.* "Phase of reflection high-energy electron diffraction oscillations during (Ba,Sr)O epitaxy on Si(100): A marker of Sr barrier integrity". *Appl. Phys. Lett.* **87,** 262905 (2005).

40. Gu, X. *et al.* "Commercial molecular beam epitaxy production of high quality $SrTiO_3$ on large diameter Si substrates". *J. Vac. Sci. Technol., B* **27,** 1195 (2009).

41. Park, J. W., Baek, S. H., Bark, C. W., Biegalski, M. D. & Eom, C. B. "Quasi-single-crystal (001) $SrTiO_3$ templates on Si". *Appl. Phys. Lett.* **95,** 061902 (2009).

42. Park, J. *et al.* "Creation of a two-dimensional electron gas at an oxide interface on silicon". *Nat. Commun.* **1,** 94 (2010).

43. Sakayori, K.-i. *et al.* "Curie Temperature of $BaTiO_3$". *Jpn. J. Appl. Phys.* **34,** 5443–5445 (1995).

44. Damjanovic, D., Brem, F. & Setter, N. "Crystal orientation dependence of the piezoelectric d_{33} coefficient in tetragonal $BaTiO_3$ as a function of temperature". *Appl. Phys. Lett.* **80,** 652–654 (2002).

45. Choi, K. J. *et al.* "Enhancement of Ferroelectricity in Strained BaTiO3 Thin Films". *Science* **306,** 1005–1009 (2004).

46. Abel, S. *et al.* "A strong electro-optically active lead-free ferroelectric integrated on silicon". *Nat. Commun.* **4,** 1671 (2013).

47. Abe, K., Uchino, K. & Nomura, S. "Barium titanate-based actuator with ceramic internal electrodes". *Ferroelectrics* **68,** 215–223 (1986).

48. Niu, G. *et al.* "Epitaxy of $BaTiO_3$ thin film on Si(001) using a $SrTiO_3$ buffer layer for non-volatile memory application". *Microelectron. Eng.* **88,** 1232–1235 (2011).

49. Yariv, A. & Yeh, P. *Optical Waves in Crystals* (John Wiley & Sons, New York, 1984).

50. Kay, H. F. & Vousden, F. "Symmetry Changes in Barium Titanate at Low Temperatures and their Relation to its Ferroelectric Properties". *Philos. Mag.* **40,** 1019 –1040 (1949).

51. Jang, J. W., Chung, S. J., Cho, W. J., Hahn, T. S. & Choi, S. S. "Thickness dependence of room temperature permittivity of polycrystalline $BaTiO_3$ thin films by radio-frequency magnetron sputtering". *J. Appl. Phys.* **81,** 6322–6327 (1997).

52. Salama, C. A. T. & Siciunas, E. "Characteristics of rf Sputtered Barium Titanate Films on Silicon". *J. Vac. Sci. Technol. A* **9,** 91–96 (1972).

53. Ashman, C. R., Först, C. J., Schwarz, K. & Blöchl, P. E. "First-principles calculations of strontium on Si(001)". *Phys. Rev. B* **69,** 075309 (2004).

54. Hellberg, C. S., Andersen, K. E., Li, H., Ryan, P. J. & Woicik, J. C. "Structure of STO_3 Films on Si". *Phys. Rev. Lett.* **108,** 166101 (16 2012).

55. Vaithyanathan, V. *et al.* "c-axis oriented epitaxial $BaTiO_3$ films on (001) Si". *J. Appl. Phys.* **100,** 024108–9 (2006).

56. Dubourdieu, C. *et al.* "Switching of ferroelectric polarization in epitaxial $BaTiO_3$ films on silicon without a conducting bottom electrode". *Nat. Nanotechnol.* **8,** 748–754 (2013).

57. Bland, J. A. "The thermal expansion of cubic barium titanate ($BaTiO_3$) from 350C to 1050C". *Can. J. Phys.* **37,** 417–421 (1959).

58. Swanson, H. E. & Fuyat, R. K. "Standard X-ray Diffraction Powder Patterns". *Natl. Bur. Stand. (U.S.)* **3,** 45 (1954).

59. De Ligny, D. & Richet, P. "High-temperature heat capacity and thermal expansion of $SrTiO_3$ and $SrZrO_3$ perovskites". *Phys. Rev. B* **53,** 3013–3022 (1996).

60. Okada, Y. & Tokumaru, Y. "Precise determination of lattice parameter and thermal expansion coefficient of silicon between 300 and 1500 K". *J. Appl. Phys.* **56,** 314–320 (1984).

61. Baek, S. H. *et al.* "Giant Piezoelectricity on Si for Hyperactive MEMS". *Science* **334,** 958–961 (2011).

62. Isarakorn, D. *et al.* "Epitaxial piezoelectric MEMS on silicon". *J. Micromech. Microeng.* **20,** 055008 (2010).

63. Trolier-McKinstry, S. & Muralt, P. "Thin Film Piezoelectrics for MEMS". *J. Electroceram.* **12,** 7–17 (1-2 2004).

64. Merz, W. J. "The Electric and Optical Behavior of $BaTiO_3$ Single-Domain Crystals". *Phys. Rev.* **76,** 1221 (1949).

65. Hooton, J. A. & Merz, W. J. "Etch Patterns and Ferroelectric Domains in $BaTiO_3$ Single Crystals". *Phys. Rev.* **98,** 409–413 (1955).

66. Junquera, J. & Ghosez, P. "Critical thickness for ferroelectricity in perovskite ultrathin films". *Nature* **422,** 506–509 (2003).

67. Tenne, D. A. *et al.* "Probing Nanoscale Ferroelectricity by Ultraviolet Raman Spectroscopy". *Science* **313,** 1614–1616 (2006).

68. Polking, M. J. *et al.* "Ferroelectric order in individual nanometre-scale crystals". *Nature Mater.* **11,** 700–709 (2012).

69. Dicken, M. J. *et al.* "Electrooptic Modulation in Thin Film Barium Titanate Plasmonic Interferometers". *Nano Lett.* **8,** 4048–4052 (2008).

70. Marssi, M. E., Marrec, F. L., Lukyanchuk, I. A. & Karkut, M. G. "Ferroelectric transition in an epitaxial barium titanate thin film: Raman spectroscopy and x-ray diffraction study". *J. Appl. Phys.* **94,** 3307–3312 (2003).

71. Brooks, C. M. *et al.* "Growth of homoepitaxial $SrTiO_3$ thin films by molecular-beam epitaxy". *Appl. Phys. Lett.* **94,** 162905 (2009).

72. Lee, S., Randall, C. A. & Liu, Z.-K. "Modified Phase Diagram for the Barium Oxide-Titanium Dioxide System for the Ferroelectric Barium Titanate". *J. Am. Ceram. Soc.* **90,** 2589–2594 (2007).

73. Matthias, B. & von Hippel, A. "Domain Structure and Dielectric Response of Barium Titanate Single Crystals". *Phys. Rev.* **73,** 1378–1384 (1948).

74. Ouyang, J., Ramesh, R. & Roytburd, A. "Theoretical investigation of the intrinsic piezoelectric properties for tetragonal $BaTiO_3$ epitaxial films". *Appl. Surf. Sci.* **252,** 3394–3400 (2006).

75. Johnston, A. R. & Weingart, J. M. "Determination of the Low-Frequency Linear Electro-Optic Effect in Tetragonal $BaTiO_3$". *J. Opt. Soc. Am.* **55,** 828–833 (1965).

76. Johnston, A. R. "The strain-free electro-optic effect in single-crystal barium titanate". *Appl. Phys. Lett.* **7,** 195–198 (1965).

77. Zgonik, M. *et al.* "Dielectric, elastic, piezoelectric, electro-optic, and elasto-optic tensors of $BaTiO_3$ crystals". *Phys. Rev. B* **50,** 5941–5949 (1994).

78. Yin, Y. W. *et al.* "Enhanced tunnelling electroresistance effect due to a ferroelectrically induced phase transition at a magnetic complex oxide interface". *Nat. Mater.* **12,** 397–402 (2013).

79. Rabe, K. M., Ahn, C. H. & Triscone, J.-M. *Physics of Ferroelectrics* (eds Ascheron, C. E. & Skolaut, W.) (Springer-Verlag, Berlin Heidelberg, 2007).

80. Braun, W. *Applied RHEED Reflection High-Energy Electron Diffraction During Crystal Growth* (Springer, 1999).

81. Klug, H. P. & Alexander, L. E. *X-ray diffraction procedures* 2nd (John Wiley & Sons, 1974).

82. Proksch, R. *Piezoresponse Force Microscopy with Asylum Research AFMs*. Tech. rep. (Asylum Research and Sergei Kalinin, Center for Nanophase Materials Sciences (CNMS) at Oak Ridge National Laboratory).

83. Schroder, D. K. *Semiconductor material and device characterization* (John, 2006).

84. McKee, R. A., Walker, F. J. & Chisholm, M. F. "Crystalline Oxides on Silicon: The First Five Monolayers". *Phys. Rev. Lett.* **81,** 3014–3017 (1998).

85. McKee, R. A., Walker, F. J. & Chisholm, M. F. "Physical Structure and Inversion Charge at a Semiconductor Interface with a Crystalline Oxide". *Science* **293,** 468–471 (2001).

86. Niu, G. *et al.* "Molecular beam epitaxy of $SrTiO_3$ on Si (001): Early stages of the growth and strain relaxation". *Appl. Phys. Lett.* **95,** 062902 (2009).

87. Norga, G. J. *et al.* "Growth of Perovskites with Crystalline Interfaces on Si(100)". *Mat. Res. Soc. Symp. Proc.* **786,** E7.3.1–E7.3.8 (2003).

88. Goncharova, L. V. *et al.* "Interface structure and thermal stability of epitaxial $SrTiO_3$ thin films on Si (001)". *J. Appl. Phys.* **100,** 014912 (2006).

89. Niu, G. *Epitaxy of crystalline oxides for functional materials integration on silicon*. PhD thesis (Ecole centrale de Lyon, 2010).

90. Li, H. *et al.* "Two-dimensional growth of high-quality strontium titanate thin films on Si". *J. Appl. Phys.* **93,** 4521–4525 (2003).

91. Cho, Y. W., Choi, S. K. & Rao, G. V. "The influence of an extrinsic interfacial layer on the polarization of sputtered $BaTiO_3$ film". *Appl. Phys. Lett.* **86,** 202905 (2005).

92. Terada, J. "An X-Ray Study of Barium-Strontium-Calcium Triple Oxide". *J. Phys. Soc. Jpn.* **10,** 555–565 (1955).

93. Sturm, J. & Reaves, C. "Silicon temperature measurement by infrared absorption. Fundamental processes and doping effects". *IEEE Trans. Electron Devices* **39,** 81–88 (1992).

94. Meier, A., Niu, F. & Wessels, B. "Integration of $BaTiO_3$ on Si (001) using MgO/STO buffer layers by molecular beam epitaxy". *J. Cryst. Growth* **294,** 401–406 (2006).

95. Niu, F. & Wessels, B. W. "Epitaxial growth and strain relaxation of $BaTiO_3$ thin films on $SrTiO_3$ buffered (001) Si by molecular beam epitaxy". *J. Vac. Sci. Technol. B* **25,** 1053–1057 (2007).

96. Yu, Z. *et al.* "Epitaxial oxide thin films on Si(001)". *J. Vac. Sci. Technol. B* **18,** 2139–2145 (2000).

97. Chattopadhyay, S., Ayyub, P., Palkar, V. R. & Multani, M. "Size-induced diffuse phase transition in the nanocrystalline ferroelectric $PbTiO_3$". *Phys. Rev. B* **52,** 13177–13183 (1995).

98. Tsunekawa, S. *et al.* "Critical size and anomalous lattice expansion in nanocrystalline $BaTiO_3$ particles". *Phys. Rev. B* **62,** 3065–3070 (2000).

99. Qiao, L. & Bi, X. "Origin of compressive strain and phase transition characteristics of thin $BaTiO_3$ film grown on $LaNiO_3$/Si substrate". *Phys. Status Solidi a* **207,** 2511–2516 (2010).

100. Norga, G. J. *et al.* "Solid phase epitaxy of $SrTiO_3$ on (Ba,Sr)O/Si(100): The relationship between oxygen stoichiometry and interface stability". *J. Appl. Phys.* **99,** 084102–7 (2006).

101. Delhaye, G. *et al.* "Structural properties of epitaxial $SrTiO_3$ thin films grown by molecular beam epitaxy on Si(001)". *J. Appl. Phys.* **100,** 124109–5 (2006).

102. Stemmer, S. *et al.* "Oxidation states of titanium in bulk barium titanates and in (100) fiber-textured $(Ba_xSr_{1-x})Ti_{1+y}O_{3+z}$ thin films". *Appl. Phys. Lett.* **79,** 3149–3151 (2001).

103. Holloway, K. & Sinclair, R. "Amorphous Ti-Si alloy formed by interdiffusion of amorphous Si and crystalline Ti multilayers". *J. Appl. Phys.* **61,** 1359–1364 (1987).

104. Lebedev, O. I. *et al.* "A study of the domain structure of epitaxial $La_{1-x}Ca_xMnO_3$ films by high-resolution transmission electron microscopy". *Philos. Mag. A* **79,** 1461–1478 (1999).

105. Zheng, H., Salamanca-Riba, L., Ramesh, R. & Li, H. "Suppression of antiphase domain boundary formation in $Ba_{0.5}Sr_{0.5}TiO_3$ films grown on vicinal MgO substrates". *Appl. Phys. Lett.* **85,** 2905–2907 (2004).

106. Yu, Z. *et al.* "Advances in heteroepitaxy of oxides on silicon". *Thin Solid Films* **462-463,** 51–56 (2004).

107. Liang, Y. *et al.* "Heteroepitaxy of $SrTiO_3$ on vicinal Si(001): Growth and kinetic effects". *J. Appl. Phys.* **96,** 3413–3416 (2004).

108. Haeni, J., Theis, C. & Schlom, D. "RHEED Intensity Oscillations for the Stoichiometric Growth of $SrTiO_3$ Thin Films by Reactive Molecular Beam Epitaxy". *J. Electroceram.* **4,** 385–391 (2000).

109. Shebanov, L. A. "X-ray temperature study of crystallographic characteristics of Barium Titanate". *Phys. Status Solidi a* **65,** 321–325 (1981).

110. Waser, R. *Polar Oxides: Properties, Characterization, and Imaging* 1st (eds Waser, R., Buettger, U. & Tiedke, S.) 391 (Wiley, 2005).

111. Abel, S *et al.* "Controlling tetragonality and crystalline orientation in BaTiO 3 nano-layers grown on Si". *Nanotechnology* **24,** 285701 (2013).

112. Naka, S., Nakakita, F., Suwa, Y. & Inagaki, M. "Change from Metastable Cubic to Stable Tetragonal Form of Submicron Barium Titanate". *Bull. Chem. Soc. Jpn.* **47,** 1168–1171 (1974).

113. Buessem, W. R., Cross, L. E. & Goswami, A. K. "Phenomenological Theory of High Permittivity in Fine-Grained Barium Titanate". *J. Am. Ceram. Soc.* **49,** 33–36 (1966).

114. "$BaTiO_3$ transport properties". in *Landolt-Börnstein - Group III Condensed Matter* (eds Madelung, O., Rössler, U. & Schulz, M.) (Springer).

115. Panwar, N. S. & Semwal, B. S. "Study of electrical conductivity of barium titanate ceramics". *Ferroelectrics* **115,** 1–6 (1991).

116. Brown, F. & Taylor, C. E. "Electrical Conductivity of Niobium-Doped Barium Titanate". *J. Appl. Phys.* **35,** 2554–2556 (1964).

117. Niu, G. *et al.* "Molecular beam epitaxy growth of $BaTiO_3$ thin films and crucial impact of oxygen content conditions on the electrical characteristics". *Thin Solid Films* **520,** 4595 –4599 (2012).

118. Erhart, P. & Albe, K. "Modeling the electrical conductivity in BaTiO3 on the basis of first-principles calculations". *J. Appl. Phys.* **104,** 044315 (2008).

119. Ridpath, D. & Wright, D. "Electrical conductivity of reduced barium titanate crystals". *J. Mater. Sci.* **5,** 487–491 (1970).

120. Choi, G. M., Tuller, H. L. & Goldschmidt, D. "Electronic-transport behavior in single-crystalline $Ba_{0.03}Sr_{0.97}TiO_3$". *Phys. Rev. B* **34,** 6972–6979 (10 1986).

121. Ieda, M., Sawa, G. & Kato, S. "A Consideration of Poole-Frenkel Effect on Electric Conduction in Insulators". *J. Appl. Phys.* **42,** 3737–3740 (1971).

122. Wang, Y.-P. & Tseng, T.-Y. "Electronic defect and trap-related current of $(Ba_{0.4}Sr_{0.6})TiO_3$ thin films". *J. Appl. Phys.* **81,** 6762–6766 (1997).

123. Padmini, P. *et al.* "Realization of high tunability barium strontium titanate thin films by rf magnetron sputtering". *Appl. Phys. Lett.* **75,** 3186–3188 (1999).

124. Miller, S. L. & McWhorter, P. J. "Physics of the ferroelectric nonvolatile memory field effect transistor". *J. Appl. Phys.* **72,** 5999–6010 (1992).

125. Lue, H.-T., Wu, C.-J. & Tseng, T.-Y. "Device modeling of ferroelectric memory field-effect transistor (FeMFET)". *IEEE Trans. Electron Devices* **49,** 1790–1798 (2002).

126. Liu, M., Kim, H. K. & Blachere, J. "Lead–zirconate–titanate-based metal/ferroelectric/insulator/semiconductor structure for nonvolatile memories". *J. Appl. Phys.* **91,** 5985–5996 (2002).

127. Dawber, M., Chandra, P., Littlewood, P. B. & Scott, J. F. "Depolarization corrections to the coercive field in thin-film ferroelectrics". *J. Phys.: Condens. Matter* **15,** L393–L398 (2003).

128. *Ferroelectric Thin Films - Basic Properties and Device Physics for Memory Application* (eds Okuyama, M. & Ishibashi, Y.) (Springer, 2005).

129. Pertsev, N. A. *et al.* "Dynamics of ferroelectric nanodomains in $BaTiO_3$ epitaxial thin films via piezoresponse force microscopy". *Nanotechnology* **19,** 375703 (2008).

130. Rodriguez, B. J. *et al.* "Domain growth kinetics in lithium niobate single crystals studied by piezoresponse force microscopy". *Appl. Phys. Lett.* **86,** 012906 (2005).

131. Petraru, A., Schubert, J., Schmid, M., Trithaveesak, O. & Buchal, C. "Integrated optical Mach Zehnder modulator based on polycrystalline $BaTiO_3$". *Opt. Lett.* **28,** 2527–2529 (2003).

132. Niu, F., Teren, A. R., Hoerman, B. H. & Wessels, B. W. "Epitaxial Ferroelectric $BaTiO_3$ Thin Films on Silicon (001) for Microphotonic Applications". *Mat. Res. Soc. Symp. Proc.* **637,** E1.9 (2000).

133. Tang, P., Meier, A. L., Towner, D. J. & Wessels, B. W. "$BaTiO_3$ thin-filmwaveguide modulator with a low voltage-lengthproduct at near-infraredwavelengths of 0.98 and 1.55 um". *Opt. Lett.* **30,** 254–256 (2005).

134. Kim, D.-Y. *et al.* "Electro-optic characteristics of (001)-oriented $Ba_{0.6}Sr_{0.4}TiO_3$ thin films". *Appl. Phys. Lett.* **82,** 1455–1457 (2003).

135. Takeda, K., Muraishi, T., Hoshina, T., Kakemoto, H. & Tsurumi, T. "Birefringence and electro-optic effect in epitaxial BST thin films". *Mat. Sci. Eng. B* **161,** 61–65 (2009).

136. Abel, S. *et al. Electro-optical properties of barium titanate films epitaxially grown on silicon*. in *Proc. SPIE* (eds Teherani, F. H., Look, D. C. & Rogers, D. J.) **8263** (SPIE, San Francisco, California, USA, 2012), 82630Y.

137. *Handbook of Ellipsometry* (eds Tompkins, H. G. & Irene, E. A.) (William Andrew Inc., 2005).

138. Kang, T. D. *et al.* "Large electro-optic effect in single-crystal $Pb(Zr,Ti)O_3$ (001) measured by spectroscopic ellipsometry". *J. Appl. Phys.* **104,** 093103 (2008).

139. Teng, C. C. & Man, H. T. "Simple reflection technique for measuring the electro-optic coefficient of poled polymers". *Appl. Phys. Lett.* **56,** 1734–1736 (1990).

140. Schildkraut, J. S. "Determination of the electrooptic coefficient of a poled polymer film". *Appl. Opt.* **29,** 2839–2841 (1990).

141. Ma, H., Levy, J., Biegalski, M. D., Trolier-McKinstry, S. & Schlom, D. G. "Room-temperature electro-optic properties of strained $SrTiO_3$ films grown on $DyScO_3$". *J. Appl. Phys.* **105,** 014102 (2009).

142. Park, D. H. *Characterization of Linear Electro-Optic Effect of Poled Organic Thin Films.* PhD thesis (University of Maryland, 2008).

143. Enami, Y. *et al.* "Hybrid polymer/sol-gel waveguide modulators with exceptionally large electro-optic coefficients". *Nat Photon* **1,** 180–185 (2007).

144. Wang, F., Furman, E. & Haertling, G. H. "Electro-optic measurements of thin-film materials by means of reflection differential ellipsometry". *J. Appl. Phys.* **78,** 9–15 (1995).

145. Adachi, H., Kawaguchi, T., Setsune, K., Ohji, K. & Wasa, K. "Electro-optic effects of (Pb, La)(Zr, Ti)O_3 thin films prepared by rf planar magnetron sputtering". *Appl. Phys. Lett.* **42,** 867–868 (1983).

146. Reitze, D. H. *et al.* "Electro-optic properties of single crystalline ferroelectric thin films". *Appl. Phys. Lett.* **63,** 596–598 (1993).

147. Hoerman, B. H., Nichols, B. M., Nystrom, M. J. & Wessels, B. W. "Dynamic response of the electro-optic effect in epitaxial $KNbO_3$". *Appl. Phys. Lett.* **75,** 2707–2709 (1999).

148. Hunsperger, R. G. *Integrated Optics - Theory and Technology* 6th edition (Springer Science+Business Media, 2009).

149. Herminghaus, S., Smith, B. A. & Swalen, J. D. "Electro-optic coefficients in electric-field-poled polymer waveguides". *J. Opt. Soc. Am. B* **8,** 2311–2317 (1991).

150. Rabiei, P. & Gunter, P. "Optical and electro-optical properties of submicrometer lithium niobate slab waveguides prepared by crystal ion slicing and wafer bonding". *Appl. Phys. Lett.* **85,** 4603–4605 (2004).

151. Liu, W. C., Mak, C. L. & Wong, K. H. "$Sr_{1.8}Ca_{0.2}NaNb_5O_{15}$ films for electro-optic modulator application". *J. Phys. D: Appl. Phys.* **42,** 105114 (2009).

152. Palmer, R. *et al.* "Low Power Mach-Zehnder Modulator in Silicon-Organic Hybrid Technology". *IEEE Photon. Technol. Lett.* **25,** 1226–1229 (2013).

153. Lee, Y. S. *et al.* "Hybrid Si-$LiNbO_3$ microring electro-optically tunable resonators for active photonic devices". *Opt. Lett.* **36,** 1119–1121 (2011).

154. Tayebati, P., Trivedi, D. & Tabat, M. "Pulsed laser deposition of SBN:75 thin films with electro-optic coefficient of 844 pm/V". *Appl. Phys. Lett.* **69,** 1023–1025 (1996).

155. Uchiki, H. & Kobayashi, T. "New determination method of electro-optic constants and relevant nonlinear susceptibilities and its application to doped polymer". *J. Appl. Phys.* **64,** 2625–2629 (1988).

156. Hou, A., Liu, H., Sun, J., Zhang, D. & Yi, M. "Measurement of the electro-optic coefficient of polymer thin films with better spatial resolution". *Optics & Laser Technology* **39,** 411–414 (2007).

157. Kalluri, S. *et al.* "Simple two-slit interference electro-optic coefficients measurement technique and efficient coplanar electrode poling of polymer thin films". *Appl. Phys. Lett.* **69,** 275–277 (1996).

158. Khatib, D., Jannot, B. & Jullien, P. "Theory of electro-optic effect in the tetragonal phase of $BaTiO_3$". *Ferroelectrics Lett.* **15,** 1–7 (1993).

159. Veithen, M., Gonze, X. & Ghosez, P. "First-Principles Study of the Electro-Optic Effect in Ferroelectric Oxides". *Phys. Rev. Lett.* **93,** 187401 (2004).

160. Hermet, P, Veithen, M & Ghosez, P. "Raman scattering intensities in $BaTiO_3$ and $PbTiO_3$ prototypical ferroelectrics from density functional theory". *J. Phys.: Condens. Matter* **21,** 215901 (2009).

161. Saleh, B. E. A. & Teich, M. C. *Fundamentals of Photonics* second (eds Saleh, B. E. A. & Teich, M. C.) 1177 (John Wiley & Sons, Inc., Hoboken, New Jersey, 2007).

162. Cook jr, W. R. "5.3.4.16 Tetragonal, 4mm (C4v)". in *Landolt-Börnstein - Group III Condensed Matter* (Springer).

163. Cazzanelli, M. *et al.* "Second-harmonic generation in silicon waveguides strained by silicon nitride". *Nat. Mater.* **11,** 148–154 (2012).

164. Liu, Z., Meier, A. L. & Wessels, B. W. "Dynamic response of polydomain ferroelectric barium titanate epitaxial thin films and its field dependence". *J. Appl. Phys.* **104,** 064115 (2008).

165. Beckers, L. *et al.* "Structural and optical characterization of epitaxial waveguiding $BaTiO_3$ thin films on MgO". *J. Appl. Phys.* **83,** 3305–3310 (1998).

166. Akazawa, H. & Shimada, M. "Electro-optic properties of c-axis oriented $LiNbO_3$ films grown on Si(100) substrate". *Mater. Sci. Eng. B* **120,** 50–54 (2005).

167. *Silicon photonics* (ed Reed, G. T.) (John Wiley & Sons, 2008).

168. Bass, M. *et al. Handbook of Optics* Third Edition (McGraw Hill Professional, 2009).

169. Biberman, A. *et al.* "Broadband Silicon Photonic Electrooptic Switch for Photonic Interconnection Networks". *IEEE Photon. Technol. Lett.* **23,** 504–506 (2011).

170. Hofrichter, J. *et al.* "A single InP-on-SOI microdisk for high-speed half-duplex on-chip optical links". *Opt. Express* **20,** B365–B370 (2012).

171. Alloatti, L. *et al.* "42.7 Gbit/s electro-optic modulator in silicon technology". *Opt. Express* **19,** 11841–11851 (2011).

172. Kuo, Y.-H. *et al.* "Strong quantum-confined Stark effect in germanium quantum-well structures on silicon". *Nature* **437,** 1334–1336 (2005).

173. Liu, J. *et al.* "Design of monolithically integrated GeSi electro-absorption modulators and photodetectors on a SOI platform". *Opt. Express* **15,** 623–628 (2007).

174. Kiyat, I., Aydinli, A. & Dagli, N. "Low-power thermooptical tuning of SOI resonator switch". *IEEE Photon. Technol. Lett.* **18,** 364–366 (2006).

175. Baehr-Jones, T. *et al.* "Ultralow drive voltage silicon traveling-wave modulator". *Opt. Express* **20,** 12014–12020 (2012).

176. Garcia-Granda, M., Hu, H., Rodriguez-Garcia, J. & Sohler, W. "Design and Fabrication of Novel Ridge Guide Modulators in Lithium Niobate". *J. Lightw. Technol.* **27,** 5690–5697 (2009).

177. *PowPower SD-40 40 GBs Intensity Modulator*. http://www.oclaro.com/product_pages/Powerbit_SD-40.php. Oct. 2013.

178. Liao, L. *et al.* "40 Gbit/s silicon optical modulator for highspeed applications". *Electronics Lett.* **43** (2007).

179. Rong, Y. *et al.* "Quantum-Confined Stark Effect in Ge/SiGe Quantum Wells on Si". *IEEE J. Sel. Topics Quantum Electron.* **16,** 85–92 (2010).

180. Hao Kuo, Y., Chen, H.-W. & Bowers, J. E. "High speed hybrid silicon evanescent electroabsorption modulator". *Opt. Express* **16,** 9936–9941 (2008).

181. Almeida, V. R., Xu, Q., Barrios, C. A. & Lipson, M. "Guiding and confining light in void nanostructure". *Opt. Lett.* **29,** 1209–1211 (2004).

182. Baehr-Jones, T., Hochberg, M., Walker, C. & Scherer, A. "High-Q optical resonators in silicon-on-insulator-based slot waveguides". *Appl. Phys. Lett.* **86,** 081101 (2005).

183. Claes, T. *et al.* "Label-Free Biosensing With a Slot-Waveguide-Based Ring Resonator in Silicon on Insulator". *IEEE Photon. J.* **1,** 197–204 (2009).

184. Vivien, L. *et al.* "Vertical multiple-slot waveguide ring resonators in silicon nitride". *Opt. Express* **16,** 17237–17242 (2008).

185. Sun, R *et al.* "Horizontal single and multiple slot waveguides: optical transmission at $\lambda = 1550$ nm." *Opt. Express* **15,** 17967–17972 (2007).

186. Petraru, A. I. *Optical and electro-optical properties of $BaTiO_3$ thin films and Mach-Zehnder waveguide modulators.* PhD thesis (Universität zu Köln, 2003).

187. Kang, P.-S., Kim, K.-T., Kim, D.-P., Kim, C.-I. & Efremov, A. M. "Dry etching characteristics of $(Ba_{0.6},Sr_{0.4})TiO_3$ thin films in high density CF_4/Ar plasma". *Surf. Coat. Technol.* **171,** 273–279 (2002).

188. Kim, G.-H., Kim, K.-T. & Kim, C.-I. "Dry etching of (Ba,Sr)TiO_3 thin films using an inductively coupled plasma". *J. Vac. Sci. Technol. A* **23,** 894–897 (2005).

189. Taillaert, D. *et al.* "An out-of-plane grating coupler for efficient butt-coupling between compact planar waveguides and single-mode fibers". *IEEE J. Quantum Electron.* **38,** 949–955 (2002).

190. Waldhäusl, R. *et al.* "Efficient Coupling into Polymer Waveguides by Gratings". *Appl. Opt.* **36,** 9383–9390 (1997).

191. Oskooi, A. F. *et al.* "Meep: A flexible free-software package for electromagnetic simulations by the FDTD method". *Comp. Phys. Commun.* **181,** 687 –702 (2010).

192. März, R. *Integrated Optics - Design and Modeling* (Artech House, inc, 1994).

193. Delage, A. *et al.* "Wavelength-Dependent Model of a Ring Resonator Sensor Excited by a Directional Coupler". *J. Lightwave Technol.* **27,** 1172–1180 (2009).

194. Merz, W. J. "Double Hysteresis Loop of $BaTiO_3$ at the Curie Point". *Phys. Rev.* **91,** 513– (1953).

195. Rao, S., Corte, F. G. D. & Summonte, C. "Low-loss amorphous silicon waveguides grown by PECVD on indium tin oxide". *J. Europ. Opt. Soc. Rap. Public.* **5,** 100395 (2010).

196. Scigaj, M. *et al.* "Ultra-flat $BaTiO_3$ epitaxial films on Si(001) with large out-of-plane polarization". *Appl. Phys. Lett.* **102,** 112905 (2013).

197. Palik, E. *Handbook of Optical Constants of Solids, Volumes I, II, and III: Subject Index and Contributor Index* (Elsevier Science & Tech, 1985).

198. Bogaerts, W. *et al.* "Silicon microring resonators". *Laser & Photonics Reviews* **6,** 47–73 (2012).

199. Buse, K. *et al.* "Refractive Indices of Single Domain $BaTiO_3$ for Different Wavelengths and Temperatures". *Phys. Status Solidi a* **135,** K87–K89 (1993).

200. Vorckel, A., Monster, M., Henschel, W., Bolivar, P. & Kurz, H. "Asymmetrically coupled silicon-on-insulator microring resonators for compact add-drop multiplexers". *IEEE Photon. Technol. Lett.* **15,** 921–923 (2003).

201. Green, W. M., Rooks, M. J., Sekaric, L. & Vlasov, Y. A. "Ultra-compact, low RF power, 10 Gb/s siliconMach-Zehnder modulator". *Opt. Express* **15,** 17106–17113 (2007).

202. De Dood, M. J. A., Polman, A., Zijlstra, T. & van der Drift, E. W. J. M. "Amorphous silicon waveguides for microphotonics". *J. Appl. Phys.* **92,** 649–653 (2002).

203. Wahlbrink, T. *et al.* "Highly selective etch process for silicon-on-insulator nano-devices". *Microelectron. Eng.* **78-79,** 212–217 (2005).

204. Henry, C. H., Kazarinov, R. F., Lee, H. J., Orlowsky, K. J. & Katz, L. E. "Low loss Si_3N_4-SiO_2 optical waveguides on Si". *Appl. Opt.* **26,** 2621–2624 (1987).

205. Jackson, W. B. & Amer, N. M. "Direct measurement of gap-state absorption in hydrogenated amorphous silicon by photothermal deflection spectroscopy". *Phys. Rev. B* **25,** 5559–5562 (1982).

206. Vlasov, Y. & McNab, S. "Losses in single-mode silicon-on-insulator strip waveguides and bends". *Opt. Express* **12,** 1622–1631 (2004).

207. Dumon, P. *et al.* "Low-loss SOI photonic wires and ring resonators fabricated with deep UV lithography". *IEEE Photon. Technol. Lett.* **16,** 1328–1330 (2004).

208. Gnan, M., Thoms, S., Macintyre, D., De La Rue, R. & Sorel, M. "Fabrication of low-loss photonic wires in silicon-on-insulator using hydrogen silsesquioxane electron-beam resist". *Electronics Lett.* **44,** 115–116 (2008).

209. Selvaraja, S. K. *et al.* "Low-loss amorphous silicon-on-insulator technology for photonic integrated circuitry". *Opt. Commun.* **282,** 1767 –1770 (2009).

210. Gould, M. *et al.* "Silicon-polymer hybrid slot waveguide ring-resonator modulator". *Opt. Express* **19,** 3952–3961 (2011).

211. Grillot, F., Vivien, L., Laval, S., Pascal, D. & Cassan, E. "Size influence on the propagation loss induced by sidewall roughness in ultrasmall SOI waveguides". *IEEE Photon. Technol. Lett.* **16,** 1661–1663 (2004).

212. "$BaTiO_3$ optical properties, dielectric constant". in *Landolt-Börnstein - Group III Condensed Matter* (eds Madelung, O., Rössler, U. & Schulz, M.) (Springer).

213. Gill, D. M., Block, B. A., Conrad, C. W., Wessels, B. W. & Ho, S. T. "Thin film channel waveguides fabricated in metalorganic chemical vapor deposition grown $BaTiO_3$ on MgO". *Appl. Phys. Lett.* **69,** 2968–2970 (1996).

214. Bolten, J. *et al.* "CMOS compatible cost-efficient fabrication of SOI grating couplers". *Microelectron. Eng.* **86,** 1114–1116 (2009).

215. Niehusmann, J. *et al.* "Ultrahigh-quality-factor silicon-on-insulator microringresonator". *Opt. Lett.* **29,** 2861–2863 (2004).

216. *Integrated Ring Resonators* (ed Rabus, D. G.) (Springer, 2007).

217. Soref, R. & Bennett, B. "Electrooptical effects in silicon". *IEEE J. Quantum Electron.* **23,** 123–129 (1987).

218. Korkishko, Y. N. & Fedorov, V. A. *Ion Exchange in Single Crystals for Integrated Optics and Optoelectronics* (Cambridge International Science Publishing, 1999).

219. *Photorefractive Materials and Their Applications 2 - Materials* (eds Günter, P. & Huignard, J.-P.) (Springer, 2007).

220. Wang, D. Y., Li, S., Chan, H. L. W. & Choy, C. L. "Optical and electro-optic anisotropy of epitaxial $Ba_{0.7}Sr_{0.e}TiO_3$ thin films". *Appl. Phys. Lett.* **96,** 061905 (2010).

221. Hiltunen, J., Lappalainen, J., Puustinen, J., Lantto, V. & Tuller, H. "Size-dependent optical properties of $BaTiO_3$ - $SrTiO_3$ superlattices". *Opt. Express* **16,** 8219–8228 (2008).

222. Michel, J. *Active Ge Based Devices for Silicon Photonics.* Foils of a talk. 2010.

Contribution to this work

With some exceptions, all the work shown in my thesis was performed at IBM Research - Zurich. This section briefly highlights my contribution to the results, and indicates where my colleagues provided strong support. Conceptional guidance was given throughout the work by my managers Jean Fompeyrine and Bert Offrein, my academic supervisor Alexei Tchelnokov, and my supervisors at IBM, Chiara Marchiori and Thilo Stöferle.

The MBE-depositions were performed by myself except few $SrTiO_3$/Si samples grown with the multi-step crystallization method in the *DCA* chamber. Mario El Kazzi was leading these experiments. Heinz Siegwart maintained both MBE chambers with my strong support. Daniele Caimi took care of cleaning the samples and the rf-sputtering of $BaTiO_3$ films on perovskite seed layers. To analyze the films, I performed most x-ray, AFM, and electrical measurements, and all PFM measurements. The electrical contacts for the C/V and I/V measurements were typically fabricated by Daniele Caimi. TEM-related investigations were performed by Marta Rossell, Rolf Erni (both EMPA, Dübendorf, Switzerland), and Teya Topuria and Philip Rice (IBM Research - Almaden). Marilyne Sousa prepared the samples for the TEM experiments.

The electro-optical characterization of the $BaTiO_3$ thin films were done almost exclusively by myself, including the design and realization of the electro-optical setup, the automation of the measurement routines, data analysis, and simulations of the expected response of the samples. Thilo Stöferle guided me through the first steps of setting up the experiment with free space optics. I created all electrode layouts. The fabrication of the metallic pads and the polishing of the backside of the samples,

however, was mainly performed by Daniele Caimi and by Ute Drechsler, respectively.

I furthermore simulated all cross sections of the $BaTiO_3$-based waveguides, and designed all device geometries and mask sets. The grating couplers of some initial test structures were calculated by Jens Hofrichter. I adapted the design, and I simulated all of the couplers for the $BaTiO_3$-slot waveguides with optimized waveguide cross section, using Phoenix, MPB, and MEEP. I carried out most steps during the fabrication of the devices independently, including the lithography steps, the etching and the deposition of several layers. Daniele Caimi and Lukas Czornomaz supported my work and the design of the process flow. Some fabrication steps, however, were solely performed by my colleagues: The e-beam lithography (Kevin Lister and Lukas Czornomaz), sputter deposition and metal evaporation (mainly Daniele Caimi), molecular bonding (Nicolas Daix), and the *a*-Si:H-deposition via HF-PECVD (Michael Stückelberger, Neuchatel). I optically and electro-optically characterized all devices using an existing motorized fiber-optical setup. Based on existing measurement scripts, I extended the control software for automated measurements of randomly distributed devices on the sample. The data analysis of the measurements was done by myself.

Acknowledgments

I really enjoyed doing my PhD at IBM Research - Zurich, which I got to know as a place with excellent opportunities for developing and realizing ideas. Not only because of the good equipment and extensive network in the scientific world, but mainly because of the great people at the lab who ensure an inspiring and motivating research atmosphere. Their openness for discussions and their willingness to share their knowledge helped me a lot throughout my PhD time.

My special thanks goes to Jean Fompeyrine, who scientifically guided me through the world of epitaxy, opened so many doors for me, and kept my back free from unnecessary administrative tasks. In particular, I appreciate his trust in my work from the very beginning and his backup in all situations. Similarly, I would like to thank Bert Offrein, who made sure that I feel at home in the Photonics group. His support made the great link between my work on materials science and photonic devices possible. I also enjoyed having Alexei Tchelnokov as my PhD supervisor in Grenoble, who provided good scientific ideas, and helped me a lot with the French administration (which can be really difficult for foreigners). Also, his confidence and optimism about the outcome of my PhD was a steady motivation for my work. I also owe my gratitude to Walter Riess who does an outstanding job in supporting the PhD students in the Science & Technology department at IBM Research - Zurich by always keeping a close connection to us. I really appreciate his advice for big strategic decisions as well as smaller scientific problems for example when discussing about lock-in amplifiers in the lab late in the evenings.

Chiara Marchiori deserves special mentioning: She greatly supported me in all aspects regarding materials science, helped me a lot when it

came to writing manuscripts, and always motivated me by keeping her enthusiasm about the $BaTiO_3$ work. In the same way, Thilo Stöferle did an excellent job of guiding my work on optics and photonic devices and improving my manuscripts, and always had time for discussions, which typically ended fruitfully with many new ideas. My work would not have been possible without the great support of the Advanced Functional Materials and the Photonics team. In particular, I would like to thank Heinz Siegwart for keeping Daisy and Natasha in good shape and teaching me all the technical details of how to keep UHV systems at UHV, Daniele Caimi for his great support in- and out-side the cleanroom at any time, Lukas Czornomaz for excellent processing hints, his willingness to help me with FIRE, SKY, GOBIG, GOHOME and GOSOUTH, as well as special ebeam exposure shifts, Nicolas Daix for providing his bonding expertise to the EBIDO project. Also thanks to Marilyne Sousa for doing a great job in the TEM sample preparation and helping me with XRD analyses, to Jens Hofrichter for providing designs of grating couplers which enabled a quick start into the the world of devices as well as for taking care of our platform for MEEP and MPB simulations together with the rest of the Aquasarli team, and to Mario El Kazzi for various fun day and night shifts bringing epitaxial $SrTiO_3$ to Natasha. Furthermore, I like to show my gratitude to Folkert Horst who gave me great advice when it came to integrated photonic devices, Christophe Rossel who introduced me to our electrical characterization facilities, Kevin Lister for his outstanding job writing the EBIDO structures, and Paul Seidler who was a pleasant partner for sharing our fiber optical setup. I would also like to thank the whole operational team of the new cleanroom and Ute Drechsler for their good support and great hints when I processed the optical devices. Special thanks also to the "French connection" in our group with Marilyne, Christophe, Nicolas, Lukas, and Jean for helping me with French translations.

There are numerous people outside IBM Research - Zurich who I share the credit of my work with: Rolf Erni and Marta Rossell for their quick and brilliant TEM investigations, Michael Stückelberger for depositing the world-best *a*-Si:H-layers with ultra-short delay and personal delivery to the Zurich main station, and Teya Topuria and Philip Rice at IBM Almaden for the first HRTEM images of the $BaTiO_3$ samples. Many thanks also to Chuck Wade and Matt Copel who organized very open

and interesting tours for me through the IBM Research labs in Almaden and Yorktown.

In addition to the support in science-related questions, I enjoyed a fun time with many colleagues in plenty of coffee breaks and lunches. I enjoyed a good start with Mirja who welcomed me with some very motivating PhD comics that turned out to be reality, the entertaining chats in the breaks with Rainer and Gabriele, the IBM soccer team, and our Bavarian Schafkopf-team with Armin, Peter, Christian, and as the latest member Felix (even though being from the Ländle). Felix and many other PhD students and post-docs, in particular Fabian, Bruno, Robby, Daniel, Antje, Luc, Cyrill, Philipp, Flo, and Frank were a great company throughout the past years, in- and outside the lab. Special thanks to Philipp, for the fun time from the first till the last days, and to Martina, for fighting for our own office, so many coffees, the quick help for my manuscript, and the great atmosphere every day!

I will always be grateful to my friends outside IBM, in particular Lukas with his help in strategic decisions and Basti for struggling with my manuscript, and the endless support of my sister, my parents, and Theresa throughout the time of my thesis. Thank you very much!

Curriculum vitae

Personal details and contact

Name	Stefan Abel
Date of birth	21. August 1983
Place of birth	Augsburg, Germany
Nationality	German
E-mail	mail@stefanabel.com

Work and education

Dec 09 - spring 14	PhD thesis at IBM Research - Zurich, Rüschlikon, Switzerland, in the groups of Jean Fompeyrine (Advanced Functional Materials) and Bert Offrein (Photonics) • Topic: Electro-optical silicon photonic devices based on $BaTiO_3$-thin films • Academic supervision: Alexei Tchelnokov (Characterization and Photonic Systems, CEA-Leti, Grenoble, France)
Oct 03 - Jun 09	Study of Nanostrukturtechnik at the University of Würzburg, Germany (similar to a M. Sc. in physics with focus on nanostructures)
Jun 08 - Jun 09	Diplomarbeit (equivalent of a Master's thesis) at the Corporate Sector Research of the Robert Bosch GmbH, Schillerhöhe, Germany

	• Topic: Electrical conductivity of doped, nanocrystalline zirconium dioxide • Supervision: Prof. Ralph Claessen (Experimental Physics 4, University of Würzburg, Germany)
Aug 06 - May 07	Visiting scholar at the University of California, Berkeley, USA • Member in the group of Prof. Ramamoorthy Ramesh (Department of Materials Science and Engineering) • Focus: Measurement of local magneto-optical properties of thin films

List of publications

Published journal papers and proceedings

- Rossel, C., Sousa, M., Abel, S., Caimi, D., Suhm, A., Abergel, J., Le Rhun, G. & Defay, E., Temperature dependence of the transverse piezoelectric coefficient of thin films and aging effects, *Journal of Applied Physics*, 115 (2014)

- Marchiori, C., Kazzi, M. E., Czornomaz, L., Pierucci, D., Silly, M., Sirotti, F., Abel, S., Uccelli, E., Sousa, M. & Fompeyrine, J., Nanoscale physics and defect state chemistry at amorphous-Si/$In_{0.53}Ga_{0.47}$ As interfaces, *Journal of Physics D*, 47, 055101 (2014)

- Abel, S., Stöferle, T., Marchiori, C., Caimi, D., Czornomaz, L., Rossel, C., Rossell, M., Erni, R., Sousa, M., Siegwart, H., Hofrichter, J., Stuckelberger, M., Chelnokov, A., Offrein, B. J. & Fompeyrine, J., Electro-Optical Active Barium Titanate Thin Films in Silicon Photonics Devices, *Advanced Photonics 2013, Optical Society of America*, IW4A.5 (2013)

- Abel, S., Sousa, M., Rossel, C., Caimi, D., Rossell, M. D., Erni, R., Fompeyrine, J. & Marchiori, C., Controlling tetragonality and crystalline orientation in $BaTiO_3$ nano-layers grown on Si, *Nanotechnology* **24**, 285701 (2013)

- Abel, S., Stöferle, T., Marchiori, C., Rossel, C., Rossell, M., Erni, R., Caimi, D., Sousa, M., Chelnokov, A., Offrein, B. & Fompeyrine,

J., A strong electro-optically active lead-free ferroelectric integrated on silicon, *Nature Communications* **4**, 1671 (2013)

- Abel, S., Caimi, D., Sousa, M., Stöferle, T., Rossel, C., Marchiori, C., Chelnokov, A. & Fompeyrine, J., Electro-optical properties of barium titanate films epitaxially grown on silicon, *Proc. SPIE*, **8263**, 82630Y (2012)

Presentations at scientific conferences

- Abel, S., Stöferle, T., Marchiori, C., Caimi, D., Czornomaz, L., Rossel, C., Rossell, M., Erni, R., Sousa, M., Siegwart, H., Hofrichter, J., Stuckelberger, M., Chelnokov, A., Offrein, B. J. & Fompeyrine, J., Electro-Optical Active Barium Titanate Thin Films in Silicon Photonics Devices, *Integrated Photonics Research, Silicon and Nanophotonics*, IW4A.5 (2013)

- Abel, S., Stöferle, T., Marchiori, C., Rossel, C., Caimi, D., Sousa, M. & Fompeyrine, J., Electro-optical Properties of Barium Titanate Thin Films Epitaxially Grown on Silicon, *MRS Fall Meeting*, 2012, Boston, Session AA17.06 (2012)

- Abel, S., Marchiori, C., Sousa, M., Caimi, D., Siegwart, H., Rossel, C. & Fompeyrine, J., Integration of Epitaxial Barium Titanate onto Silicon via RF-Sputtering using MBE-grown Seed Layers, *E-MRS*, Nice, P2 53 (2011)